Localized Investigations of the Electrochemical Properties of Lithium-ion Battery Materials Using Scanning Micropipette Contact Method

Malak Dayeh, M.Sc.

A thesis submitted to McGill University
in partial fulfillment of the requirements of the degree of
Doctor of Philosophy

Department of Chemistry, McGill University
Montreal, Quebec, Canada

بِسْمِ اللَّهِ الرَّحْمَنِ الرَّحِيمِ

﴿ يَرْفَعِ اللَّهُ الَّذِينَ آمَنُوا مِنكُمْ وَالَّذِينَ أُوتُوا العِلْمَ دَرَجَاتٍ وَاللَّهُ بِمَا تَعْمَلُونَ خَبِير﴾ [سورة المجادلة: ١١]

"لِكُلِّ شَيءٍ زَكاةً وزَكاةُ العِلمِ أن يُعَلِّمَهُ أهلَه"

الإمام جعفر الصادق (ع) – ملهم الكيمياء

Abstract

With the ever-growing demand for energy storage devices, rechargeable lithium-ion batteries (LIBs) are being considered as the leading candidates in the fields of portable electronics, and in hybrid, plug-in hybrid, and all electrical vehicles. They are a commercial success offering uniquely high volumetric and gravimetric energy density, as well as, longer lifetime than comparable battery technologies. Yet, electrode materials with improved energy capacity and charge/discharge rates are still highly desirable and in some instances required for LIBs to meet their full application potential; the electric vehicle being a case in point.

The development of new cathode materials for LIBs is an active field of research. These investigations range from discovering new battery materials, seeking alternative synthesis routes for existing compounds, and altering cathode film compositions. The performance of the battery material is typically tested in coin cells. However, many factors during the assembly of the coin cell can influence the test performance of the novel material. Additionally, the testing of a full cell assembly requires a significant period of time to run charge/discharge cycles. Moreover, the mechanism of lithium intercalation and deintercalation at the surface of the electrode involves spatial heterogeneous reactions that are difficult to be resolved by using composite films. Data from these tests also convolute the responses from a large ensemble of particles; therefore, only average properties of battery materials are detected. As an alternative approach, the ability to visualize the localized redox activity of electrode materials under *in-situ* condition at sub-micrometer scale is of significant importance.

This thesis presents step-by-step development of an analytical tool, namely the scanning micropipette contact method (SMCM) for localized investigations of active LIBs materials. The proposed technique was designed in an anaerobic environment to use true battery electrolytes, thus providing the opportunity to study microscopic features on air sensitive materials. Developed probes provided microscale resolution, allowed the assessment of battery materials without the need to assemble a full cell, reducing analysis time and cost, and increasing experimental accuracy. In other words, SMCM was employed as a “battery within a pipette”, where the cathode is the working electrode with the electrolyte and anode in the pipette. When the pipette wets the working electrode, a miniature battery is created, and local electrochemical responses can be probed. Once the electrochemical investigation at a specific position on the working electrode is completed, the pipette can be withdrawn and positioned on a new section of the working electrode. Multiple measurements were carried out across a working electrode to probe key properties of a battery material such as capacity, efficiency, and local heterogeneities in material properties distribution. A correlation between the electrochemical responses and the complementary techniques, such as scanning electron microscopy and atomic force microscopy, was also established.

Also presented is a proof-of-concept experiments that were first performed on the commonly used lithium iron phosphate (LFP) active particles using carbonate-based solution. Electrochemical measurements from SMCM were compared to conventional coin cells data to critically assess the similarities between film and particle measurements, and determine the viability of the SMCM technique to elucidate key electrochemical properties.

SMCM was successfully extended to ionic liquid as an alternative electrolyte solution to the conventional organic electrolytes. This enabled studying higher energy cathode materials that require higher oxidation potentials such as the layered lithium nickel manganese cobalt oxide (NMC). Introducing carbon black as a conducting phase between the NMC particles was also demonstrated in an attempt to enhance the electronic resistance between the active material and the working substrate. This was achieved via ball milling of NMC with carbon at different conditions. The effect of ball milling conditions on the morphology and the crystallinity of NMC samples was characterized. The electrochemical performance of NMC samples before and after ball milling was also explored via coin cells measurements.

Résumé

Avec la demande toujours croissante de dispositifs de stockage d'énergie, les batteries rechargeables lithium-ion (LIB) sont considérées comme les principales candidates dans les domaines de l'électronique portable et des véhicules hybrides, hybrides rechargeables et électriques. C’est un succès commercial qui offre une densité d’énergie volumétrique et gravimétrique unique, ainsi qu’une durée de vie supérieure à celle des technologies de batterie comparables. Cependant, les matériaux d'électrode avec une capacité énergétique et des taux de charge / décharge améliorés restent hautement souhaitables et, dans certains cas, sont nécessaires pour que les LIB atteignent leur plein potentiel d'application; le véhicule électrique en est un exemple.

Le développement de nouveaux matériaux cathodiques pour les LIB est un domaine de recherche actif. Ces recherches vont de la découverte de nouveaux matériaux de batterie, à la recherche de voies de synthèse alternatives pour les composés existants et à la modification de la composition des films cathodiques. Les performances du matériau de la batterie sont généralement testées dans des piles bouton. Cependant, de nombreux facteurs lors de l'assemblage de la pile bouton peuvent influer sur les performances du nouveau matériau lors des tests. De plus, le test d'un assemblage de cellules complet nécessite une période de temps importante pour exécuter des cycles de charge / décharge. De plus, le mécanisme d'intercalation et de désintercalation du lithium à la surface de l'électrode implique des réactions hétérogènes dans l'espace qui sont difficiles à résoudre en utilisant des films composites. Les données de ces tests sont une convolution des réponses d'un grand ensemble de particules; par conséquent, seules les propriétés moyennes des matériaux de la batterie sont détectées. À titre d’approche alternative, la possibilité de visualiser l’activité redox localisée des matériaux d’électrode dans des conditions in situ à une échelle inférieure au micromètre revêt une importance considérable.

Cette thèse présente le développement étape par étape d'un outil analytique, à savoir la méthode de contact à micropipette à balayage (SMCM) pour des investigations localisées de matériaux de LIB actifs. La technique proposée a été conçue dans un environnement anaérobie pour utiliser de vrais électrolytes de batterie, offrant ainsi la possibilité d'étudier les caractéristiques microscopiques sur des matériaux sensibles à l'air. Les sondes développées ont fourni une résolution à l'échelle microscopique et elles ont permis d'évaluer les matériaux de la batterie sans avoir à assembler une cellule complète, ce qui a permis de réduire le temps et les coûts d'analyse ainsi que d'accroître la précision expérimentale. En d'autres termes, le SMCM a été utilisé comme «pile dans une pipette», la cathode étant l'électrode de travail avec l'électrolyte et l'anode dans la pipette. Lorsque la pipette mouille l'électrode de travail, une pile miniature est créée et les réponses électrochimiques locales peuvent être sondées. Une fois que l'investigation électrochimique en un point spécifique de l'électrode de travail est terminée, la pipette peut être retirée et positionnée sur une nouvelle section de l'électrode de travail. Plusieurs mesures ont été effectuées sur une électrode de travail pour sonder les propriétés clés d'un matériau de batterie, telles que la capacité, l'efficacité et les hétérogénéités locales dans la distribution des propriétés du matériau. Une corrélation entre les réponses électrochimiques et les techniques complémentaires, telles que la microscopie électronique à balayage et la microscopie à force atomique, a également été établie.

On présente également des expériences de validation de principe qui ont d'abord été réalisées sur les particules actives de phosphate de fer et de lithium (LFP) couramment utilisées à l'aide d'une solution à base de carbonate. Les mesures électrochimiques issues de la SMCM ont été comparées aux données relatives aux piles bouton classiques pour évaluer de manière critique les similitudes entre les mesures de film et de particules et déterminer la viabilité de la technique SMCM pour élucider les propriétés électrochimiques essentielles.

La SMCM a été étendue avec succès au liquide ionique en tant que solution électrolytique alternative aux électrolytes organiques conventionnels. Cela a permis d'étudier des matériaux cathodiques à haute énergie nécessitant des potentiels d'oxydation plus élevés tels que l'oxyde de lithium-nickel-manganèse-cobalt (NMC) en couches. L'introduction du noir de carbone en tant que phase conductrice entre les particules de NMC a également été démontrée dans le but d'améliorer la résistance électronique entre le matériau actif et le substrat de travail. Ceci a été réalisé par broyage à billes de NMC avec du carbone dans différentes conditions. L'effet des conditions de broyage à billes sur la morphologie et la cristallinité des échantillons de NMC a été caractérisé. Les performances électrochimiques des échantillons NMC avant et après le broyage à billes ont également été explorées via des mesures de piles bouton.

Acknowledgments

It is with profound joy that I present this thesis and I will take this opportunity to express my sincere acknowledgments to those who have helped me to accomplish this work.

First and foremost, I would like to thank God Almighty for giving me the strength, knowledge, and opportunity to undertake this research study and for granting me the capability to proceed successfully. I am truly grateful for his blessings and guidance especially during all the challenging moments in completing this thesis.

With a deep sense of gratitude, I express my respect and appreciation to my supervisor, Prof. Janine Mauzeroll, for her valuable advice, availability, patience, and unceasing encouragement. I would like to thank Janine for her continuous academic support and concern from time to time during scientific investigations. Her professionalism and wise supervision always made me proud to be a member in her group. I also extend my gratitude to Prof. Steen Schougaard for his permanent research supervision and constructive criticism over the last years. I thank him also for granting me a hospitable atmosphere to carry out my research in his lab and providing me with necessary resources.

I have great pleasure in acknowledging any effort or assistance granted to me by all McGill faculty and staff members throughout my residency at the chemistry department. I am especially grateful to Chantal Marotte for her assistance with the administrative tasks necessary for completing my PhD program.

Collective and individual thanks are owed to all members of the Mauzeroll group for their fruitful cooperation, interaction, and support during my graduate studies. I am grateful to Nicholas Payne and Lisa Stephens for the long and helpful discussions we had before reviews. I convey my sincere thanks to Dr. Michael Snowden, who introduced me to the world of electrochemistry research, and who trained me to work in the glovebox and directed me in the early stage of my PhD. I will forever be grateful for the stimulating work we have performed together; his patience, guidance, and profuse assistance were the bases for the success of this research. Very special thanks also goes to Dr. Mohammadreza Ghavidel for his technical assistance, insightful discussion, and skillful suggestions. I am very thankful for the long hours we spent together preparing and reviewing our manuscript to submit on time. His continuous support and encouragements are hard to put into words.

Many thanks to all my friends at McGill who made my graduate experience much more enjoyable. I am very appreciative to Ghada Ayoub and Siba Moussa who were always ready for quick chats and funny conversations away from research throughout these years. Special thanks to my best friend Majid Rasool for sharing with me the stress and complaints in my PhD journey and for motivating me during the last days when writing this thesis.

Words fail me to express my indebtedness and gratitude to my family. I salute their ultimate sacrifices as I proudly dedicate this work:

To the soft touch in my life, to the candle that shines my way and to the moon that guards my nights, to my Mom, whose endless love and deep kindness was my weapon throughout my life. She helped me sculpture my character through her everlasting support and care, and encouraged me to fulfill my goals.

To the first and great man in my life, to my Dad, whose blessings have paved the way for my dreams to come true. His unequivocal confidence in my character and abilities are the reason behind my accomplishments today.

To the source of joy and optimism in my life, to my brothers, whose support, cooperation, and advice were my road to this fruitful work.

To my better half and to the love of my life, to my fiancé, who gave me the positive energy to pass all the hardships with his care and patience. He has been a true and great supporter and has unconditionally loved me during my good and bad times. I feel throughout this experience we both learned a lot about life and we strengthened our commitment and determination to each other. I am looking forward to live with you a life full of affection and mercy that God Almighty has placed between us.

Thank you all for making this possible and I hope I make you all proud.

۞ وَمَا تَوْفِيقِي إِلاَّ بِاللّهِ عَلَيْهِ تَوَكَّلْتُ وَهُوَ رَبُّ الْعَرْشِ الْعَظِيمِ ۞

Author Contributions

The work presented in this thesis were performed under the direct supervision of Professor Janine Mauzeroll at McGill University. All the research work and performed experiments presented in this thesis were conducted in the laboratory of Professor Steen Brian Schougaard at Université du Québec à Montréal (UQAM). Details are given below for each chapter to outline individual contributions of all collaborators.

Chapter 2

The author designed and performed all the experiments, which included three-electrode cell measurements with different electrolytes and working electrodes (Figures 2.1 and 2.2), calibration and silanization of the pipettes (Table 2.1), fabrication of $Al_{1-x}Li_x$ QRCE (Figure 2.9), as well as droplet stability measurements performed on the glassy carbon substrate using the SMCM technique (Figure 2.8). The cyclic voltammograms data performed with the redox mediator MPT (Figure 2.5), the SMCM measurements performed with different salinization agents (Figure 2.7), as well as the droplet stability measurements performed on the gold substrate using the SMCM technique (Figure A5) were performed by Dr. M.E. Snowden (Postdoctoral Fellow at McGill University, Mauzeroll Group).

Chapter 3

The author performed parts of the experiments and data analysis of the published manuscript, which included galvanostatic measurements (Figure 3.2A), SMCM measurements (Figure 3.3A), and parts of the data treatment (Figures 3.3C, 3.4, and 3.5B). The experiments were designed by Dr. M.E. Snowden who performed part of the SMCM measurements and stability tests as well (Figure 3.6A and Figure B2). Scanning electron microscopy imaging and the numerical modeling on the experimental data in COMSOL (Figure 3.4 and Figure B1) were performed by N. Payne (Ph. D. student at McGill University, Mauzeroll Group) with the assistance of Dr. M.E. Snowden.

Coin cell measurements (Figure 3.2B) were performed by Simon Gervais (Master's student at UQAM, Schougaard group). The manuscript was written and reviewed by Dr. M.E. Snowden.

Chapter 4

The author designed and performed all the experiments and data analysis of the published manuscript, which included system optimization (Figure 4.2), three-electrode cell measurements (Figure 4.3), and SMCM measurements (Figure 4.4A). The author also wrote and reviewed the manuscript. Scanning electron microscopy imaging was performed with the assistance of Dr. M. R. Zamanzad Ghavidel (Postdoctoral Fellow at McGill University, Mauzeroll Group) who also provided valuable input for the preparation and the correction of the manuscript. Atomic force microscopy imaging was conducted by the technical assistance of M. Ramkaran (McGill University).

Chapter 5

The author designed and performed all the experiments and data analysis, which included XRD and TGA analysis (Figures 5.3 and 5.5), coin cells measurements (Figure 5.8), and SMCM measurements (Figure 5.9). The preparation of coin cells was carried out with the assistance of Dr. M. R. Zamanzad Ghavidel who helped in the final assembly. The ball milling experiments were performed with the assistance of A. Jonderian (Ph.D. student at McGill University, McCalla group) to prepare the milling jars, and Dr. H. M. Titi (Postdoctoral Fellow at McGill University, Friščić Group) to run the mill with appropriate conditions. Transmission electron microscopy imaging was conducted by the technical assistance of D. Liu (McGill University).

The work in **Chapters 3** and **4** has been previously published.

Table of Contents

List of Figures

List of Tables

List of Symbols

Symbol	Description	Units
A	Area of working electrode	cm^2
α	Transfer coefficient	
C_O	Concentration of the oxidant species	$mol\ cm^{-3}$
C_R	Concentration of the reductant species	$mol\ cm^{-3}$
D_O	Diffusion coefficient of the oxidant species	$cm^2\ s^{-1}$
E	Electrode potential	V
$E^{0'}$	Formal electrode potential	V
ΔE	Redox potential difference	V
F	Faraday's constant	$C\ mol^{-1}$
ΔG	Gibbs free energy	J
i	Current	A
i_p	Peak current	A
J_O	Flux of species O	$mol\ s^{-1}\ cm^{-2}$
$J_{O,d}$	Diffusional component of the flux of species O	$mol\ s^{-1}\ cm^{-2}$
$J_{O,m}$	Migrational component of the flux of species O	$mol\ s^{-1}\ cm^{-2}$
$J_{O,c}$	Convectional component of the flux of species O	$mol\ s^{-1}\ cm^{-2}$
k^0	Standard heterogeneous rate constant	$cm\ s^{-1}$
k_b	Heterogeneous rate constant for oxidation	$cm\ s^{-1}$
k_f	Heterogeneous rate constant for reduction	$cm\ s^{-1}$
k_r	Electron transfer rate constant	$cm\ s^{-1}$
k_t	Mass transport limitation rate constant	$cm\ s^{-1}$
K	Scherrer constant	
L	Crystallite size	nm
n	Number of electrons	
O	Oxidized form of the standard system	

R	Reduced form of the standard system	
R	Universal gas constant	J mol^{-1} K^{-1}
T	Absolute temperature	K
t	Time	s
υ	Velocity of solution flow	cm s^{-1}
υ	Potential scan rate	V s^{-1}
z_O	Charge on the species O	
β	Full width at half maximum	radians
θ	Bragg angle	degree
λ	Wavelength of the X-ray	nm
ϕ	Electrostatic potential	V

List of Abbreviations

AFM	Atomic Force Microscopy
DEC	Diethyl Carbonate
DMC	Dimethyl Carbonate
EC	Ethylene Carbonate
EDX	Energy Dispersive X-ray Spectroscopy
EMC	Ethyl Methyl Carbonate
EMI TFSI	1-ethyl-3-methylimidazolium bis(trifluoromethylsulfonyl)imide
LIBs	Lithium-ion Batteries
LFP	Lithium Iron Phosphate
MPT	10-Methylphenothiazine
NMC	Lithium Nickel Manganese Cobalt Oxide
PC	Propylene Carbonate
QRCE	Quasi-Reference Counter Electrode
SECM	Scanning Electrochemical Microscopy
SEM	Scanning Electron Microscopy
SICM	Scanning Ion Conductance Microscopy
SMCM	Scanning Micropipette Contact Method
TEM	Transmission Electron Microscopy
TGA	Thermogravimetric Analysis
XRD	X-ray Diffraction

Chapter 1

Introduction

The following introduction discusses the principles and the theory of LIBs and highlights briefly the structure and performance characteristics of commonly used positive electrode materials and their applications. The fundamentals of the scanning electrochemical probe techniques that have been successfully applied in the field of LIBs are also reviewed.

1.1 Introduction to Batteries

During the past decade, the world has witnessed a tremendous increase in the population and technology advances. This led to an increase in the energy demand that is expected to double by the year 2050.[1-2] About 80% to 85% of our energy comes from fossil fuels, a product of ancient biomass stored beneath Earth's surface for up to 200 million years.[3] However, this natural reserve will be depleted shortly. Moreover, fossil fuels have limited supplies and hazardous environmental impact.[4] Therefore, research is driven today to seek environmentally clean alternative energy resources that can meet the increasing energy demands. Among the different options of energy resources, electrochemical storage systems, such as batteries and super capacitors, are playing an important role in this field as they can efficiently store and deliver energy on demand.[5]

Batteries are electrochemical devices that convert stored chemical energy into useful electrical energy and have a history of nearly 2000 years. They consist of three main components: two electrodes, the anode and the cathode, made up of different chemicals (typically metals); and the electrolyte, which promotes the movement of ions between these two terminals. During a discharge process, an oxidation reaction proceeds at the battery's negative terminal. The anode material releases electrons in the external circuit and ions in the electrolyte and becomes more positive. Meanwhile, at the positive terminal, the cathode material accepts electrons and ions and becomes more negative through what is called a reduction reaction, thereby completing the electrical circuit.

The battery operates by providing separate pathways for electrons and ions to pass between the oxidation and reduction sites (see Figure 1.1). The electrons flow in the external circuit where they can provide useful work, for example, powering a cellular phone or lighting a light bulb. The ions, on the other hand, transport current through the ionically conducting electrolyte soaked between the two electrodes inside the battery. The ionic current is therefore separated from the electronic current, which can be easily controlled by a switch or a load in the external circuit.

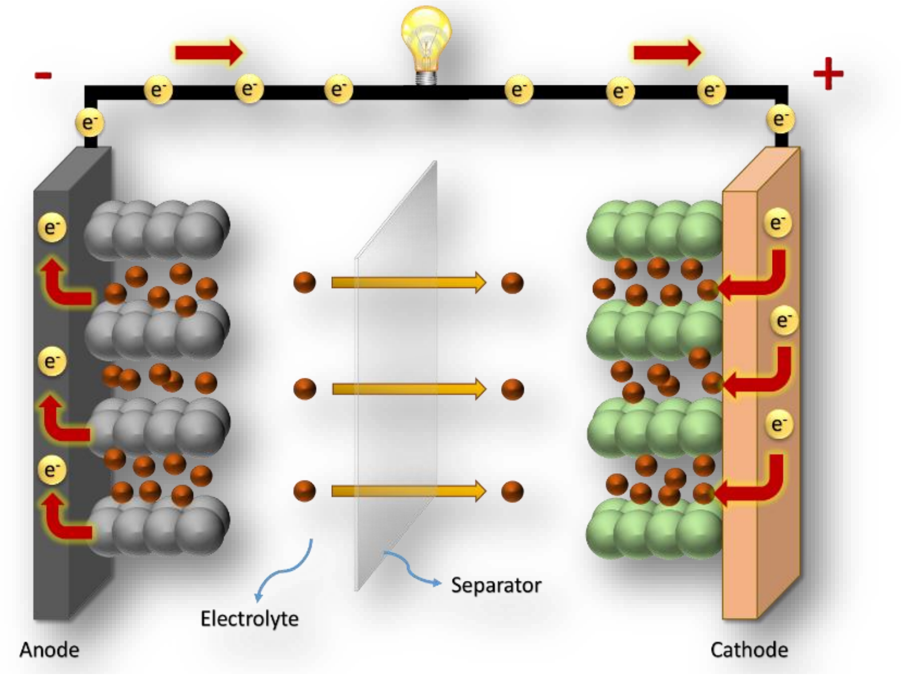

Figure 1.1: Schematic illustration of discharging process in a typical battery. The grey spheres represent the graphite anode and the green spheres represent the active material at the cathode. The electrolyte facilitates the transport of ions through a porous separator.

1.2 Important Characteristics of a Battery

The performance of batteries can be evaluated by a number of parameters, such as the specific energy, specific power, operating voltage range, lifetime, self-discharge, and safety. The specific energy, expressed in (Wh/g), measures the amount of energy that can be stored and released per unit mass of the battery. The higher the specific energy of a battery, the more energy it can store and the longer runtime it can provide. The house battery is an example of a high specific energy battery that is expected to deliver its energy over a long period of time — perhaps a few days use. The specific energy can be obtained by multiplying the specific capacity (Ah/g) with battery operating voltage (V). Specific capacity is a measure of how much charge a cell can reversibly provide per unit mass. The potential is related to the difference in the chemical potential between the cathode and the anode, and it is related to the Gibbs free energy of the chemical reaction in the cell:

$$\Delta G = -nF\Delta E \tag{1.1}$$

where ΔG is the Gibbs free energy (J), n is the number of electrons that participate in the redox reaction, F is the Faraday's constant (96485 C/mol), and ΔE is the redox potential difference between the anode and the cathode reactions. On the other hand, batteries made for power tools and electric powertrains provide high specific power. This is expressed in (W/g), and it measures how quickly a battery can deliver energy per unit mass. An analogy between specific energy and specific power can be made with a water bottle as shown in Figure 1.2. The size of the bottle represents the specific energy (capacity), while the spout pouring the water governs the specific power (loading). A large bottle can carry a lot of water, while a large opening can pour it quickly. The large container with a wide mouth is the best combination. The energy and power can be also expressed per unit volume, which refers to the energy density (Wh/g) and power density (W/l).

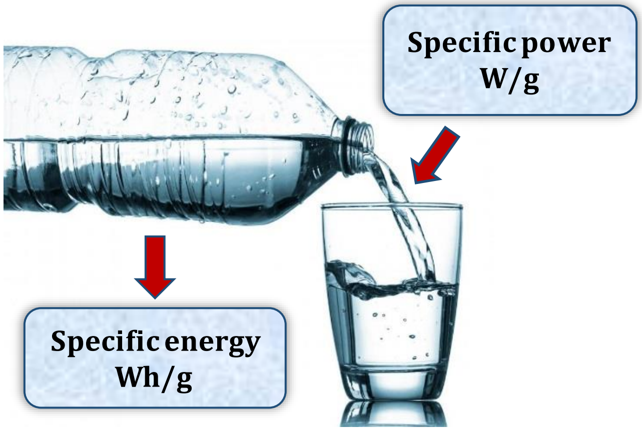

Figure 1.2: Relation between specific energy and specific power. The water in the bottle denotes the specific energy; the opening represents the specific power.

The coveted battery should also have a long lifetime, which determines the battery performance and the number of complete charging/discharging cycles that the battery is able to support until the end of useful life. Typically, battery health and longevity decline over time. Key factors affecting cycle life are the depth of discharge, charging level, temperature, and pressure. In general, battery life improves dramatically upon reducing deep discharging cycles and the charging cut-off voltage to avoid the battery reaching its maximum stress point. Similarly, avoiding high temperature and pressure is important to prevent premature failure of the cell. A further requirement is low self-discharge, which is a phenomenon that measures how quickly a battery will lose its stored energy while sitting on the shelf. This occurs due to internal chemical reactions in the battery, without any connections between the electrodes. Self-discharge is a battery characteristic rather than a manufacturing effect, and it tends to occur more quickly at higher temperatures. The energy loss is asymptotical, meaning that the amount of electrical self-discharge is highest immediately after charge and then tapers off. Another concern in batteries is safety. Batteries have the potential to be hazardous if they are abused or not carefully designed. This can result in an uncontrolled and dangerous failure of the cell including explosion, fire, and emission of toxic fumes.[6-7]

1.3 Classification of Batteries

Electrochemical batteries are generally classified into two different categories: primary and secondary batteries, or, in other words, non-rechargeable and rechargeable batteries. Primary batteries produce electricity until the supply of reactants is exhausted (same chemical potential on both electrodes) and the chemical energy cannot be readily restored once it has been converted to electrical energy. Examples on these disposable batteries are zinc–carbon, alkaline, lithium iron disulfide ($Li\text{-}FeS_2$), and lithium sulfur dioxide ($LiSO_2$) batteries. Primary batteries generally have high specific energy and can be used instantly even after long storage; they are also environmentally friendly when disposed.

Secondary batteries are designed so that they can restore their original composition by supplying electrical energy to the cell, which reverses the chemical reactions that occur during discharge/use. These batteries might cost more than disposable batteries; however, they can be inexpensively recharged several times before they require replacing. The most common rechargeable batteries that have reached the commercial market are Lead-Acid (Pb-acid), Nickel-Cadmium (NiCd), Nickel-Metal Hydride (NiMH) and Lithium-ion (Li-ion). A comparison of the energy density per unit of mass and volume for these batteries is plotted in Figure 1.3.

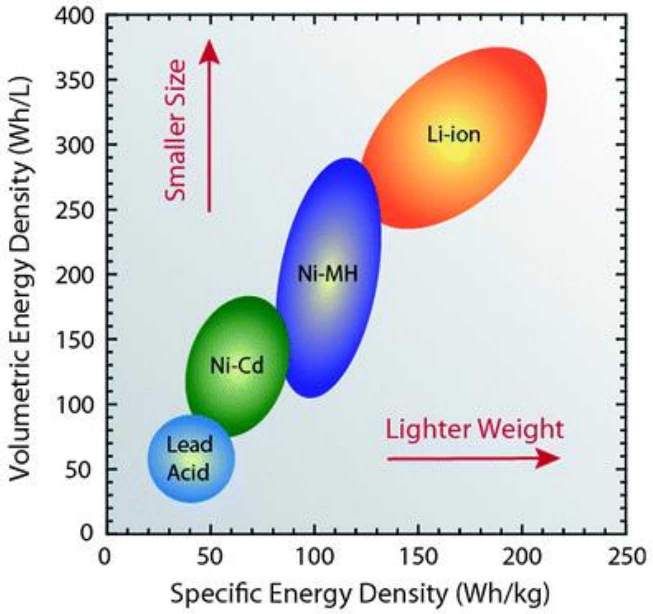

Figure 1.3: Comparison of rechargeable battery technologies as a function of volumetric and specific energy densities. The arrows indicate the direction of development to reduce battery size and weight. Figure is reproduced from Reference 8.

1.4 Rechargeable Batteries

Lead-Acid: This is the oldest rechargeable battery system for commercial use that was invented by the French physician Gaston Planté in 1859.[9] Despite its old age, the lead chemistry is still popular today. There are good reasons behind its widespread use; Pb-acid is rugged, forgiving if abused, cheap to purchase, and have low self-discharge (~5% per month). This makes the Pb-acid battery a good choice for hospital equipment, wheelchairs, emergency lighting and uninterruptible power supply (UPS) systems. However, Pb-acid batteries do not lend themselves to fast charging—typical charge time is between 8 to 16 hours. Pb-acid batteries also provide 200-300 charging/discharging cycles, which is relatively short. The main reason behind this limitation is the corrosion of the positive electrode,[10] depletion of the active material with time, and expansion of the positive plates. Moreover, among the modern rechargeable batteries, the Pb-acid family has the lowest specific energy (~30-50 Wh/Kg)[11] which makes it unsuitable for handheld devices that demand compact sizes. As for the environment, the high content of toxic lead and the acidic electrolyte (sulfuric acid) makes Pb-acid batteries environmentally unfriendly.

Nickel-Cadmium: It was invented by Waldemar Jungner in 1899 and offered several advantages over Pb-acid.[12] It is one of the most enduring batteries that allow ultra-fast charging[13] with minimal stress. NiCd batteries are used where long-life service, high discharge rate, and extreme temperatures are required; and when the economical price is important. Main applications are biomedical equipment, professional video cameras, and power tools. If properly maintained, NiCd provides a high number of charging/discharging cycles (~1500), and can be fully charged within 1 hour only. NiCd also offers low cost per cycle, which is the lowest among all other batteries. However, compared to newer systems, it has a relatively low specific energy (~45-80 Wh/Kg) and high self-discharge (~20%/month), which means that it needs recharging after storage. The NiCd contains toxic metals as well; therefore, some countries are limiting its usage and looking to replace it with other chemistries.

Nickel-Metal Hydride: Research on the NiMH system started in the 1970s in an attempt to replace the NiCd batteries, and in 1980 these batteries came onto the market.[14] Their constituents are less toxic to the environment, which encourages the customer to use NiMH rather than NiCd due to environmental concerns about careless disposal of the spent battery. The success of the NiMH has been also driven by its high specific energy that is about 40% higher than the standard NiCd. However, the cycle count for this type of batteries is moderate to low (~300-500), and their performance starts to deteriorate if repeatedly cycled. High self-discharge is another concern for NiMH users, as it exhibits about 30% reduction in its capacity per month.[15] NiMH batteries also generate more heat during charge and requires a longer charge time than NiCd.

Lithium-ion: Pioneering work with the lithium batteries began in 1912 under Gilbert Newton Lewis.[16] However, it was only in the 1970s that these batteries gained commercial importance. Lithium is the lightest of all metals and provides the largest energy density per weight. Moreover, it has a low redox potential $E^{\circ}(Li^{+}/Li) = -3.04$ V compared to SHE (Standard Hydrogen Electrode) so it can be easily reduced. Therefore, it is not surprising that lithium batteries offer the best prospects for developing high energy and high power batteries to satisfy the future needs. Nevertheless, batteries with metallic lithium electrodes displayed safety issues[17] as lithium is a very reactive element; it burns in the presence of oxygen and water and under normal atmospheric conditions. Besides, it was revealed in the 1980s that undesirable dendrites are produced at the anode during cycling; these penetrate the separator and cause a short circuit.[18] As a result, research shifted to develop batteries using lithium-ions. Though being slightly lower in specific energy than metallic lithium, the Li-ion is safer provided the currents and voltage limits are being respected during charging and discharging. In 1991, Sony Corporation introduced the first lithium-ion battery (LIB). Today, this chemistry has occupied a prime position in the market and used when high specific energy, light weight, and small dimensions is a prime concern. The capacity and operating voltage of LIB are 700 to 2400 mAh and ~3.6 V, respectively. Examples where LIBs have been increasingly used are electric vehicles,[19] space and aircraft power systems,[20] and even stationary power storage.[21] Other advantages for the LIBs include low self-discharge (less than half that of Ni-based systems), low maintenance battery, and the little harm they cause when disposed. Despite its overall advantages, LIB also has some drawbacks. It is subject to aging[22] whether the battery is in use or not, and some capacity deterioration is noticeable after one year. Storing the battery in a cool place (15 °C as recommended by manufacturers) and at 40% state-of-charge decreases this aging concern. LIBs are also expensive to manufacture — about 40% higher in cost than NiCd. Table 1.1 compares the characteristics of the four commonly used rechargeable batteries in terms of specific energy, cycle life, exercise requirements and cost, their environmental effect and applications.

Table 1.1: Characteristics of commonly used rechargeable batteries.

Properties	**Pb-acid**	**NiCd**	**NiMH**	**Li-ion**
Specific Energy (Wh/Kg)	30-50	45-80	60-120	420-640
Cycle Life	200-300	1500	300-500	500-1000
Charge Time	8-16 h	1 h	2-4 h	2-4 h
Self-Discharge/Month	5%	20%	30%	10%
Environmental Effect	Lead content makes it toxic	Contains toxic metals	Not toxic	Li-ions cause little harm when disposed
Applications	UPS systems	Biomedical equipment	Mobile phones	Notebook computers

1.5 Cathode Materials in Lithium-ion Batteries

Three main groups of cathode materials have been extensively studied for application in LIBs; these include spinel, layered, and olivine structures[23] of transition metal oxides $LiMO_2$ (where M could be Co, Ni, or Mn) and phosphates. The crystal structures of the three classes are represented in Figure 1.4, along with the dimensions of Li-ions mobility during charging/discharging reactions. Spinel oxides, for instance, offer 3D diffusion of Li-ions through their crystal lattice, whereas for the layered materials, Li-ions transport in 2D. Olivines on the other hand, offer a 1D transport of Li-ion along the channels of the orthorhombic structure (b-axis).

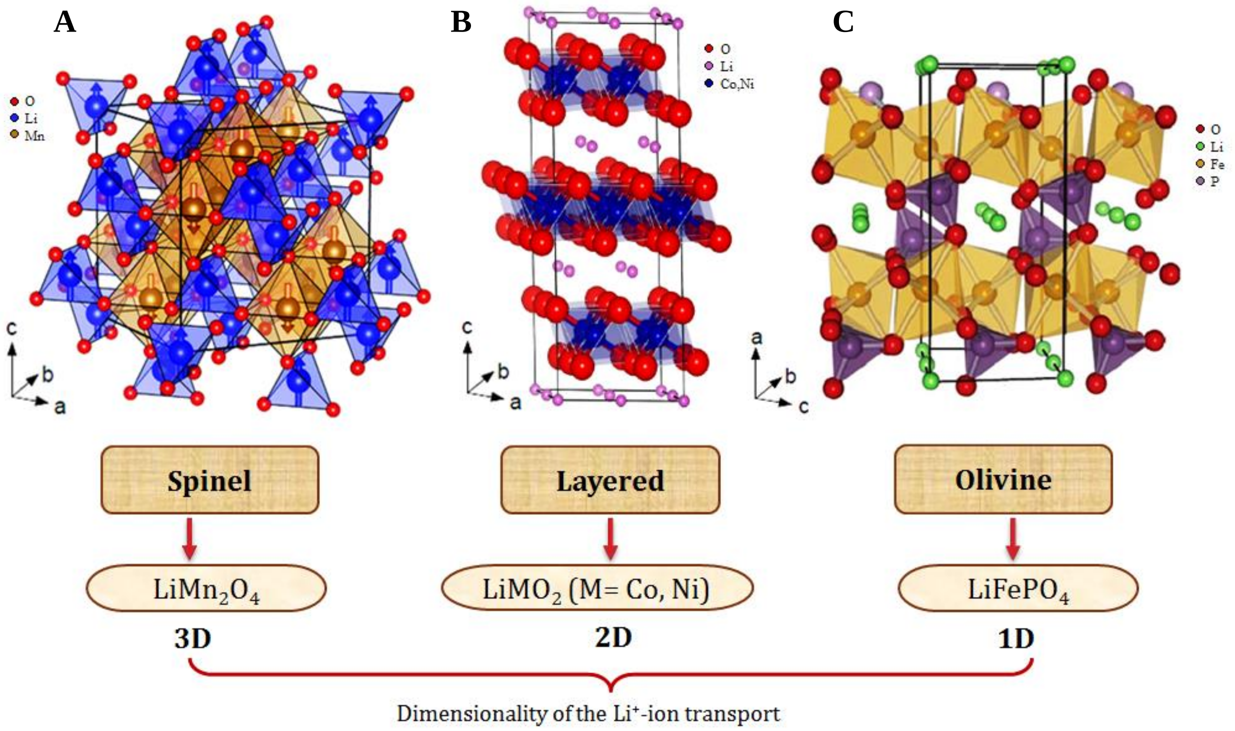

Figure 1.4: Crystal structure of the lithium-insertion compounds showing different frameworks for Li-ions mobility: (A) Spinel 3-D, (B) Layered 2-D, and (C) Olivine1-D.

Note that the two cathode materials $LiFePO_4$ (LFP) and $LiNi_{1/3}Mn_{1/3}Co_{1/3}O_2$ (NMC), discussed hereafter, will be the main focus of this thesis. LFP is studied in **Chapter 3** and **4**, and NMC is studied in **Chapter 5.**

1.5.1 Layered Compounds

1.5.1.1 Lithium Cobalt Oxide

$LiCoO_2$ is an example of layered structure; it consists of layers of lithium that lie between slabs of octahedra formed by cobalt and oxygen atoms. The octahedrons are edge-sharing, and tilted relative to the layered structure (see Figure 1.4B). In 1980, Goodenough and coworkers identified $LiCoO_2$ to act as positive electrode material of lithium batteries.[24] The high nominal voltage it provides (around 3.9V vs. Li/Li^+),[25] the long run-time it offers (500-1200 cycles),[26] and the great practical specific energy it can reach (546 Wh/Kg),[27] made this material attractive to be used as the first cathode material in commercial LIBs.

However, this widely used cobalt oxide LIB has drawbacks. It has relatively low specific power that leads to limited load capabilities. Therefore, electronic devices such as cameras, cell phones, laptops, and other low power draw applications all use cobalt-based LIBs. In fact, Li-cobalt can only be charged and discharged at a rate of about 1C. This means that a battery with a capacity of 2400 mAh, should not be charged or discharged at a current higher than 2.4 A. Forcing a faster charge or applying a load higher than 2.4 A would overheat the pack and its safety would be jeopardized. Li-cobalt also has low thermal stability; a full charge can promote thermal runaway that occurs around 150 °C.

A major limitation of $LiCoO_2$ batteries is the fact that its theoretical capacity is about 273 mAh/g[28] when all Li atoms are extracted from the material. In reality, however, the practical capacity achieves only 130–150 mAh/g,[29] indicating that only half of the Li atoms can be used during the charge/discharge process. When more than half of the Li atoms have been extracted, $LiCoO_2$ material has shown structural instability, degradation and fatigue that leads to poor cycling performance of the battery. $LiCoO_2$ is also prone to oxygen gas release at deep lithium extraction.[30] For $1.0 \geq x \geq 0.5$, the Li_xCoO_2 cathode is known to cycle well and there is no loss in oxygen occurring in the electrochemical cell. It has been shown by Laubach *et al.*[31] that for this range of x, the density of states (DOS) nearly does not change and the charge compensation with de-intercalation of Li leads to a removal of electrons from the Co: 3d derived states with the Fermi level moving downwards[32] (see Figure 1.5). For $x < 0.5$, a clear increase in hybridisation occurs between the Co: 3d orbitals and O: 2p orbitals associated with a reduction of the (CoO_6)-slab distances evidenced by the reduction of the c-axis lattice parameter.[33] As a consequence, the charge compensation of the delithiation leads to a removal of electrons from Co-O: d-p hybrid states, that translates to a partial oxidation of the O^{2-} ions. The loss of oxygen from the lattice in the $Li_{1-x}CoO_2$ system may be one of the reasons for the limited capacity. Moreover, the high cost of cobalt is a main drawback of $LiCoO_2$, which enticed battery manufacturers to partially substitute cobalt by other metals such as nickel[34-35] and manganese.[36]

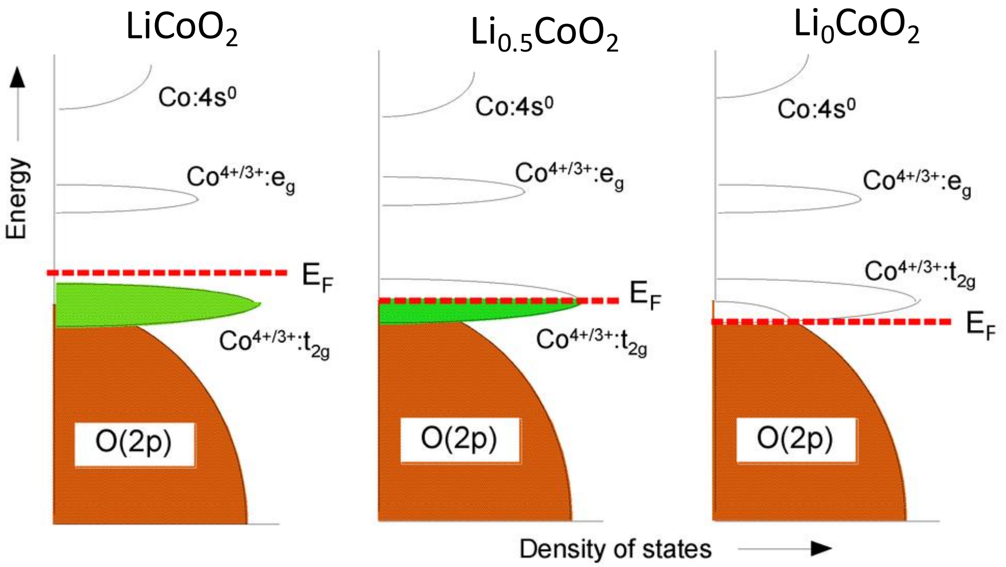

Figure 1.5: Change of the qualitative energy diagrams of Li_xCoO_2 as a function of the lithium content. From left to right: x = 1, x = 0.5, x = 0. Figure is reproduced from Reference 32.

1.5.1.2 Lithium Nickel Oxide

$LiNiO_2$ is isostructural with $LiCoO_2$ having alternating zigzag layers formed from the corner sharing between LiO_2 and NiO_6 octahedra (see Figure 1.4B). It provides a high cell voltage up to 4.0 V with a lower cost, reveals excellent cycle life, and shows higher reversible capacity (190 mAh/g)[37] than $LiCoO_2$ although they have the same theoretical capacity of about 274 mAh/g.

Despite the extensive research, $LiNiO_2$ is not commercialized in the pure state yet due to a few disadvantages. The first on the list is the difficulty in synthesizing $LiNiO_2$ with all the nickel ions in the Ni^{3+} oxidation state. This results in a deviation from the ideal stoichiometry due to the presence of Ni^{2+} ions at the Li^+ and Ni^{3+} sites as they all have similar ionic size.[38] The latter process, known as cation mixing, declines the compound electrochemical performance and makes it less acceptable as a cathode material in the power front mainly because the presence of the nickel cations within the lithium layer can inhibit lithium mobility.

Another drawback in the $LiNiO_2$ system is the inherent problem of the Jahn–Teller effect (tetragonal structural distortion) which may account for the instability of $LiNiO_2$ as a cathode material. In fact, the deintercalation of Li-ions during the charging process leads to the oxidation of nickel from Ni^{3+} to Ni^{4+}. The low-spin Ni^{3+} is well known as a d^7 Jahn–Teller ion with an electronic configuration of $t_{2g}{}^6e_g{}^1$. Ni^{4+} on the other hand, is a d^6 ion with $t_{2g}{}^6e_g{}^0$ state with no Jahn–Teller distortion. This is the first observation of a dynamic change in Jahn–Teller effect during the deintercalation process.[39]

Furthermore, at elevated temperatures, $LiNiO_2$ tend to undergo irreversible phase change from hexagonal to cubic.[40] The layered hexagonal phase is electrochemically active[41] while the cubic is not. Thus, if $LiNiO_2$ is sintered at a temperature higher than the phase transition temperature, it will contain certain amount of inactive cubic phase leading to a reduction in the electrochemical capacity ultimately.[37] $LiNiO_2$ also suffers from irreversible phase transition during the charge/discharge process (hexagonal to monoclinic). Remarkably, Li intercalation/deintercalation mechanism is totally different for $LiNiO_2$ and $LiCoO_2$. During the reduction step, the occurring structural transformation prevents the Li-ions to be full re-inserted into the $LiNiO_2$ crystal structure. After a few cycles, the reversible reaction can be described as follows:[42]

$$Li_{0.85}NiO_2 \rightarrow Li_{0.35}NiO_2 + 0.5Li^+ + 0.5e^- \tag{1.2}$$

The practical specific discharge capacity of $LiNiO_2$ is therefore decreased compared to the theoretical one. The addition of cobalt to nickel in small amounts results in a similar material combining the higher energy density of nickel material and the more ordered structure of the cobalt material.[23, 43]

1.5.1.3 Lithium Nickel Manganese Cobalt Oxide

Layered metal oxides with a combination of Ni-Mn-Co transition metals known as NMC, is a novel lithium insertion electrode material used in advanced LIBs. NMC consists of lithium layers lying between slabs of octahedra formed by the transition metals [Ni, Mn, and Co] and oxygen. This material has gained a considerable attention since 2008 as 4V-electrode materials to replace

$LiCoO_2$ in LIBs, owing to its high specific energy (610-650 Wh/Kg)[27], improved structural, chemical,[44] and thermal stability,[45] high reversible capacity (~215 mAh/g),[46] and excellent cycle life with a better stability even at elevated temperature. NMC can be tailored to serve as Energy Cells or Power Cells, as it can deliver a continuous discharge current of 20 A if optimized for specific power. This makes NMC a battery of choice for power tools, e-bikes, medical devices, and other electric powertrains.

The secret of NMC lies in combining the three transition metals cobalt, nickel and manganese in its crystal structure, thus forming a multi-metal oxide material to which lithium is added. Manganese on its own offers spinel structure to achieve low internal resistance but has a low specific energy; nickel is known for its high specific energy but poor stability. The combination of these metals enhances each other strengths and offers a unique blend with a lower cost of the raw material, as cobalt on its own is quite expensive. This makes NMC a promising candidate for the next-generation of large-scale LIBs.

The most commonly used NMC composition contains one-third nickel, one-third manganese, and one-third cobalt represented as $LiNi_{1/3}Mn_{1/3}Co_{1/3}O_2$ (NMC). The latter has been reported in 2001 by Ohzuku and Makimura as a positive electrode material[47] and now it is successfully commercialized. The oxidation states of Ni, Mn, and Co in this case are +2, +4, and +3, respectively.[48] The electrochemical reaction of lithium extraction takes place by the oxidation of Ni^{2+} to Ni^{3+}/Ni^{4+} ions and Co^{3+} to Co^{4+} ions depending on different cut-off voltages. Principle calculations suggest that the oxidation of nickel occurs during the extraction of the first two-thirds of the lithium, while the oxidation of cobalt arises at higher cell potentials, i.e. when the removal of the last one-third of lithium begins.[49] Manganese is electrochemically inactive, but provides the structural framework,[50] and reduces Mn dissolution and Jahn–Teller distortion.[51-52]

The capacity of NMC material can reach 160 mAh/g in the potential range of 2.5 to 4.3 V.[46] At higher cut-off voltage, a capacity of 200 mAh/g was recorded,[45] but in some cases there is marked capacity fade. Structural analysis of cycled NMC electrodes by high-resolution transmission electron microscopy and Raman spectroscopy indicated a transformation from layered to spinel phase when NMC material is cycled up to 4.6 V, which explains the pronounced capacity fading during prolonged cycling.[53] Various approaches including lattice doping,[54-55] structural optimization,[56-60] and surface coating[61-64] have been proposed to improve the cycling performance.[65-66] Moreover, research works confirmed that carbon[67-68] and graphene[69-70] coating enhance electron conductivity and improve the battery's high rate performance. Another main problem that still needs to be solved in NMC is the cation mixing between Ni^{2+} and Li^+ ions, since they have similar ionic radii (0.69 Å and 0.76 Å respectively). The partial occupation of Ni^{2+} lattice sites by Li^+ is known to deteriorate their electrochemical performance as it blocks the pathway of lithium diffusion.[71] It has been previously reported that the presence of Co inhibits Ni migration from the transition metal layers to the Li layers.[72] This means that Co can be used to stabilize the structure by reducing cation disorder, which is good for cycling. Some research is being devoted to adjust the lithium/transition-metal ratio during synthesis to minimize the cation mixing.[73]

1.5.2 Lithium Manganese Spinel

$LiMn_2O_4$ is an example of spinel structure. It consists of nearly ideal cubic close-packed (ccp) oxygen framework containing Li-ions located in the tetrahedral sites, and manganese ions located in half of the octahedral interstices; hence forming a three-dimensional framework of edge-sharing MnO_6 octahedra (see Figure 1.4A).

$LiMn_2O_4$ was originally proposed by Thackeray and coworkers as a positive electrode material in 1983.[74] However, it was only in 1996 that LIBs based on spinel-type $LiMn_2O_4$ cathodes were first commercialized by Moli Energy.[75] The special architecture of spinel structure offers a three-dimensional network of transport path which improves the mobility of ions between the electrodes. This results in lower internal resistance which enables fast charging and high-current discharging; it can actually be discharged at 20-30A with a moderate heat buildup. These characteristics of high thermal stability[76] and high specific power[77] make this material useful for power tools, medical devices and electric powertrains. Further advantages of the spinel material is its stable operating voltage, enhanced safety (thermal runaway at 250 °C, which is relatively high compared to the $LiCoO_2$), and the potential lower cost of Mn compared to Co and Ni, being more abundant in nature and having more friendly impact on the environment.

The spinel battery however, has its own weaknesses also. One of the most significant drawbacks is the lower capacity (~120 mAh/g)[78-79] compared to the cobalt-based system. $LiMn_2O_4$ also experiences a fast capacity fade with charge/discharge cycling and poor storage performance, which hinders its practical applications. Intensive research has particularly focused on the mechanism of capacity fading and has suggested numerous processes. The major one is the dissolution of manganese Mn^{3+} into the electrolyte during cycling.[80] Mn disproportionation results from some side reactions occurring at the interface between the electrode and the electrolyte during the charge/discharge process.[81] As the cathode electrode comes into a direct contact with the Li-based electrolyte, Mn dissolution proceeds through the following dismutation reaction:

$$2Mn^{3+}\ (solid) \rightarrow Mn^{4+}(solid) +\ Mn^{2+}\ (solution) \qquad (1.3)$$

This is induced by the presence of trace amounts of protons, most likely from hydrogen fluoride (HF), which originates with the hydrolysis of Li-based salt[82] and solvent oxidation.[83] Mn^{2+} ions leaches out from the positive electrode framework into the electrolyte and subsequently deposit on the graphite anode. This causes a loss of positive active material and blocking of pores in the negative electrode, which leads to a huge rise in impedance and severe capacity fade at elevated temperatures.

Another cause that was attributed to the capacity fading phenomena is the Jahn-Teller distortion of Mn^{3+} ions[35] around 3V. During discharging, the insertion of Li-ions results in an increase in the concentration of high-spin Mn^{3+}: d^4 $(t_{2g}^6 e_g^1)$ ions in the spinel lattice. This is accompanied by a severe Jahn-Teller distortion, which reduces the crystal symmetry from cubic to tetragonal symmetry that is detrimental to the electrochemical cycling.

Deviation from the stoichiometry of the spinel structure could be an alternative reason. It has been pointed out that during the process of lithium insertion, additional Li-ions could occupy the empty octahedral holes of the spinel framework, in addition to its tetrahedral sites. Since the octahedra share faces with the tetrahedra, electrostatic interactions between the Li-ions on these two sets of sites cause an immediate displacement of the tetrahedral-site Li-ions into neighboring vacant octahedral sites.[32] The reaction results in a transition to $Li_2Mn_2O_4$ inducing a huge volume change and severe capacity fade.

1.5.3 Olivine Lithium Iron Phosphate

$LiFePO_4$ (LFP) is a member of the olivine family crystallizing in an orthorhombic lattice structure. The oxygen ions form a distorted hexagonal close-packed (hcp) array, having Li and Fe occupying half of the octahedral sites and P ions occupying one-eighth of the tetrahedral sites. The cornershared FeO_6 octahedra and the edge-shared LiO_6 octahedra run parallel to the b-axis, and they are linked together by the PO_4 tetrahedra. The latter shares a common edge with one FeO_6 octahedra and two edges with LiO_6 octahedra (see Figure 1.4C).

In 1997, LFP has been characterized as a promising cathode material[84] exhibiting a redox potential of 3.6 V.[85] Its theoretical capacity reaches approximately 170 mAh/g, and it is more tolerant to full charge conditions (i.e. less stressed than other Li-ion systems if kept at high voltage for a prolonged time). Other key benefits are low material cost, better environmental compatibility compared to other cathode materials, excellent cycling performance, and good thermal stability.[86] Since the oxygen atoms are strongly bonded by both Fe and P atoms, the risk of oxygen release is reduced which also leads to enhanced safety of this material.

Unlike the other traditional cathode materials, the delithiation in LFP is not really a diffusional deintercalation process that yields a homogeneous material with varying lithium content. Instead, LFP undergoes a two-phase process ($LiFePO_4$ - $FePO_4$) during charge and discharge based on the following reaction:

$$LiFePO_4 \rightleftarrows (1-x)LiFePO_4 + xFePO_4 + xLi^+ + xe^- \tag{1.4}$$

The process left to right corresponding to charge (Li^+ deintercalation) is accompanied by the oxidation of Fe^{2+} ions to Fe^{3+} and the formation of a mixture of Li-rich phase and Li-poor phase. When all Li-ions are extracted from the host structure, all $LiFePO_4$ (known as triphylite) transforms into $FePO_4$ (known as heterosite). The reverse reaction takes place during discharge. The high reversibility of the charge/discharge processes can be explained by the high mobility of charge carriers (Li-ions and electrons) at the Li-rich/Li-poor phase boundary,[87-88] and the structural similarity between $LiFePO_4$ and $FePO_4$. Both phases are olivine-type orthorhombic structures, and the lattice volume differs by 6.77% only.[89]

On the other hand, LFP suffers from low specific energy (518-587 Wh/Kg)[27] limited by its tap density and operational voltage (3.6 V vs. Li/Li^+). This makes it inappropriate for applications that require high energy such as those directed to electrical vehicles. Moreover, a main obstacle for reaching the theoretical performances of LFP at ambient temperature is its high intrinsic resistance. This is caused by its low electronic conduction ($<10^{-9}$ S/cm), and the low diffusion coefficient of Li-ions (10^{-14}-10^{-16} cm^2/s at room temperature).[90-91] Both the electronic conductivity and the ionic diffusivity problems lead to a poor performance of LFP cathode in LIBs and result in capacity loss during high-rate discharge. To overcome the electronic transport limitations, research efforts have focused on doping LFP with metallic elements such as Cr, Mg, Ni, or Co.[92-94] Moreover, coating LFP by electronically conductive additive,[95-99] such as carbon, remarkably ameliorates the electrical conduction between particles.[95-96] However, uniform coating on LFP might be difficult to achieve sometimes,[100-101] which keeps the electrode performance limited in terms of rate capability and lifetime.

1.6 Surface Coating

In addition to the electrochemical properties of the active material, the performance of the cathode is strongly related to its crystal structure,[102-103] particle morphology,[104-105] grain size,[106-107] and surface area.[108] These factors critically depend on the preparation method and the optimization of synthetic conditions. Various synthetic routes, including coprecipitation,[109-112] sol–gel synthesis,[113-116] solid-state reaction,[117-119] hydrothermal synthesis,[120-122] microemulsion,[123-124] pyrolysis processes,[125-126] and mechanical milling[127-129] have been extensively exploited for the preparation of cathode materials.

One of the prospective solutions for enhancing the electrode performance is to use surface coating. Surface coating has proven to be an easy and effective way for improving the capacity retention, rate capability, and even thermal stability for a wide variety of cathode materials.[130-131] The positive effect of surface treatment include: (1) enhancing the electronic conductivity of the cathode material to facilitate the charge transfer at the surface and among the particles, (2) providing physical protection layer that reduces possible side reactions between cathode and electrolyte, and (3) suppressing phase transition and improving structural stability. Various coating materials including, carbon,[132-133] polymers,[134-135] metal oxides[63, 136] and phosphates[137] have been studied. For instance, coating $LiCoO_2$ with Al_2O_3 through sol-gel method showed improvement in the rate capability and negligible capacity loss even at the high-charge cut-off voltages (≥ 4.2 V).[138] This was attributed to the high concentration of Al atoms at the surface of the particles that enhanced structural stability of $LiCoO_2$ during cycling and prohibited the phase transition from a hexagonal to monoclinic phase. Moreover, ZrO_2 deposited on the surface of $LiMn_2O_4$ suppressed the dissolution of Mn^{3+} and scavenged the acidic HF species from the electrolyte solution, resulting in excellent capacity retention on cycling.[139] In another study, $AlPO_4$-coated $LiNi_{0.8}Co_{0.1}Mn_{0.1}O_2$ showed a superior cycling performance compared to the bare cathode, and noticeably reduced exothermic reaction of the cathode with the electrolyte.[140] High columbic efficiency and excellent rate discharge performance at a high current density was also reported for NMC cathode materials coated with MoO_3 via ball milling.[141] This was ascribed to MoO_3 coating that stabilized the active material structure and suppress the augmenter of the charge transfer resistance during cyclic process.

On the other hand, the addition of a conducting phase to improve the charge transfer has been widely investigated. Sputtered gold layer has been shown to enhance the performance of LFP,[142] but this involves high cost process and material. Silver is less expensive than gold and has been used to improve the performance of NMC,[143] $LiCoO_2$,[144] $LiMn_2O_4$[145] cathodes. Although these metals have been successfully applied, the most common addition for improving electrode conductivity is carbon. Previous studies revealed improved cycling performance and rate capability after carbon addition to many cathodes such as NMC,[146-147] $LiMn_2O_4$,[148] and mainly LFP,[149-150] which has relatively low electrical conductivity. The coating method, and the amount and the source of carbon used can significantly influence the effectiveness of the carbon coating. Controlling the carbon coating thickness is challenging in practical synthesis procedures. A low amount of carbon source cannot satisfy full coating and enough conductivity, while a too high content would block the diffusion of Li-ions. The study of R. Dominko showed that when the thickness of carbon coating increased form 1 to 10 nm, the reversible capacity of LFP/C composite decreased due to the increasingly hindered electrolyte transport.[151] Different carbon sources and coating methods have been also explored,[152-156] which determine the type and morphology of the carbon deposits obtained. For instance, carbon-coated $Li_3V_2(PO_4)_3$ cathode material was prepared by solid-state reaction process using four different organic precursors: citric acid, glucose, poly(vinylidene difluoride) (PVDF) and starch.[157] Among all tested samples, PVDF-sample displayed the best rate performance, owing to the continuous carbon network it formed with the nanosized active particles. The obtained morphology improved the electronic conductivity and lowered charge–transfer impedance significantly. It should be noted that the thermal decomposition of carbon sources (e.g. sugar and hydrocarbon) that is applied in an inert atmosphere to prevent carbon loss, generate a strong reductive environment like H_2, CO, or a combination of both.[130] Therefore, this method has been widely reported for phosphate-based materials,[157-158] but has limited application for lithium transition metal oxide, since the transition metals in the oxides can be further reduced and change the valence state of the elements and even the crystal structure of the oxide material. Continuous efforts are being devoted to develop a carbon-based coating technique that can be applied to lithium transition metal oxides without a significant negative impact on the substrate materials.[159-161]

In another study, *in situ* coating of carbon from the pyrolysis of polymer additives on the LFP particle surfaces was performed.[162] Various types of polymer additives were tested in order to study the influence of the structure of the polymer precursor on the behavior of materials. The obtained results indicated that polystyrene, having a large number of functionalized aromatic structures, caused the formation of more highly graphite-like carbon (higher sp^2/sp^3 peak ratio) during polymer pyrolysis and exhibited a better capacity. In addition to being used as precursors for carbon, polymers have been used as additives in cathodes.[163-164] The effect of poly(3,4-dioxyethylenethiophene) PEDOT coating on the electrochemical performance of NMC cathode was investigated at different annealing temperatures and coating amount.[61] The optimal conditions of the PEDOT coating layer was found to facilitate mass transfer at the interface of electrode and electrolyte, which alleviated the surface polarization and enhanced the rate capabilities of NMC. Furthermore, dry/wet mixing of carbon by ball milling has also proven to be convenient and cheap mechanical method for coating technology, and thus easy to scale up in commercial view. NMC/graphene composites obtained via ball milling delivered the highest discharge capacity at different C-rates when compared to NMC starting material.[69] The enhanced cycling performance and rate capability and of the NMC/graphene composite was attributed to an increase in the grain connectivity and high electronic conductivity. Nevertheless, the parameters used for the ball milling process are of particular importance, and must be considered in order to obtain improved performance materials. This is supported by a prior work on NMC cathode material,[165] which reported the effect of ball milling times, rotation speeds, and the size/number of balls on the material structure and properties. Using relatively mild milling conditions that produced an intermediate crystallite size, NMC cathodes with improved rate capabilities were obtained. However, high milling speeds and long milling times were determined to lower the electronic conductivity of NMC and increase the interfacial charge transfer resistance, which resulted in lowered electrochemical performance. Following a similar approach, **Chapter 5** of this thesis investigates the effect of ball milling of NMC with carbon black at different condition.

Another study conducted on LFP/C composites compared the effect of dry ball milling and wet ball milling in acetone on the electrode performance.[166] A higher discharge capacity and smaller ohmic resistance was obtained for the wet milled LFP. This was attributed to the round shaped particles resulting from the wet ball milling, which had higher current collecting efficiency than the smaller and irregular particles of LFP collected from the dry milling.

1.7 Dynamic Electrochemistry

Dynamic electrochemistry is generally referred to the study of charge transfer processes occurring at electrode surfaces driven at a non-equilibrium potential. The overall rate of an electrochemical reaction under study is controlled either by the rate of electron transfer at the surface of electrode (kinetics limitation, rate constant k_r), or by the rate at which electroactive species arrive to/move away from the electrode (mass transport limitation, rate constant k_t).[167] The two processes are displayed in Figure 1.6. When the electrode process is limited by mass transport ($k_t << k_r$), the process is said to be reversible. Whereas if the electrode process is kinetically limited by the surface electron transfer ($k_t >> k_r$), the process is said to being quasi-reversible or irreversible.

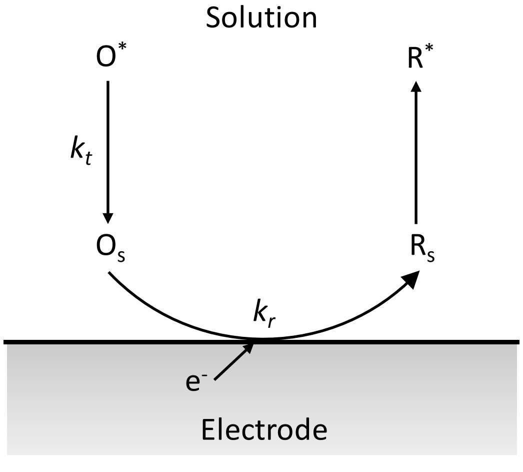

Figure 1.6: Dynamic electrochemistry with mass transport (k_t) and electron transfer for reduction reaction (k_r) processes presented. O is the oxidised form of species R.

Electrochemical reactions are performed using either two- or three-electrode electrochemical cell, depending on the current range measured. The two-electrode setup is adequate for small currents (less than 1 μA) with low ohmic drop. A varying potential is applied to a working electrode with respect to a second quasi-reference counter electrode (QRCE). QRCE is an electrode that plays the role of both the reference and counter electrodes. The electrolyte solution is placed between the two electrodes, and current is measured at the QRCE. For currents larger than 1 μA, a three-electrode setup is used. The current flows between the working and counter electrodes, while a reference electrode is used to accurately measure the applied potential relative to a stable reference reaction.

1.7.1 Electron Transfer at the Electrode

For the electrode process described by Equation 1.5, the heterogeneous electron transfer reaction is a function of the applied potential, where the rates of the reduction reaction k_f and oxidation reaction k_b are defined in Equations 1.6 and 1.7.

$$\mathrm{O} + e^- \underset{k_b}{\overset{k_f}{\rightleftharpoons}} \mathrm{R} \tag{1.5}$$

$$k_f = k^0 e^{-\alpha f(E-E^{0\prime})} \tag{1.6}$$

$$k_b = k^0 e^{(1-\alpha) f(E-E^{0\prime})} \tag{1.7}$$

k^0 is the standard rate constant (cm s^{-1}), α is the dimensionless electron transfer coefficient normally taken to be 0.5 in lithium batteries, $f = F/RT$ (R is the gas constant, T is the absolute temperature), E is electrode potential (V), and $E^{0'}$ is the formal electrode potential. (E-$E^{0'}$) is known as the overpotential, i.e. the additional potential beyond the thermodynamic requirement needed to drive the reaction at a certain rate.

The net current i flowing at the electrode as a function of overpotential is described by the *Butler-Volmer* kinetic expression given in Equation 1.8.

$$i = FAk^0\left[C_O(0,t)e^{-\alpha f(E-E^{0\prime})} - C_R(0,t)e^{(1-\alpha) f(E-E^{0\prime})}\right] \tag{1.8}$$

where A is the electrode area (cm^2), C_O and C_R (mol cm^{-3}) are the surface concentration of the oxidant species O and its reduced form R.

1.7.2 Mass Transport

Mass transport describes the method by which the electroactive species are transported between bulk solution and the electrode surface. It is characterized by three modes: diffusion, migration, and convection. The overall partial differential equation used to describe mass transport is the *Nernst-Planck* equation given as follows:

$$J_O = J_{O,d} + J_{O,m} + J_{O,c} = -D_O \nabla C_O - \frac{z_O F}{RT} D_O C_O \nabla \phi + C_O \upsilon \tag{1.9}$$

$J_{O,d}$, $J_{O,m}$, and $J_{O,c}$ denote the diffusional, migrational and convectional components of the flux of species O (mol s^{-1} cm^{-2}), D_O is the diffusion coefficient (cm^2 s^{-1}), C_O is the concentration (mol cm^{-3}), ∇C_O is the concentration gradient, z_O is the charge on the species, ϕ is the electric potential (V), $\nabla \phi$ is the potential gradient, and υ is the velocity of the solution (cm s^{-1}).

<u>Diffusion:</u> refers to the movement of species under the influence of a concentration gradient. The associated flux is described by Fick's first law:

$$J_{O,d} = -D_O \nabla C_O \tag{1.10}$$

Fick's second law describes the change in concentration of species O with time due to diffusion, and can be solved to predict the current and concentration profiles at the electrode:

$$\frac{\partial C_O}{\partial t} = D_O \nabla C_O \tag{1.11}$$

In batteries, Li-ions diffuse in electrolyte phase and in the solid phase, i.e. within the electrode active particles. Equation (1.11) can be used in spherical coordinates to describe the transport of Li-ions in the active particles, which can be modeled as spheres.

<u>Migration</u>: is movement of ions under the influence of an electric field (gradient in electrical potential). The migratory flux is described in Equation 1.12:

$$J_{O,m} = -\frac{z_O F}{RT} D_O C_O \nabla \phi \tag{1.12}$$

In LIBs, Li-ions are transported in the electrolyte solution by migration from the negative to the positive electrode, due to an ohmic potential difference over the electrolyte. Migration in the liquid phase can be described mathematically using the transference number, which represents the fraction of current carried by a specific ionic species due to migration (no concentration gradient exists).[168] Migration in the solid material is negligible in many cases.[169-170]

Convection: is the movement of species under the action of mechanical forces (e.g., stirring or vibrations). This is generally neglected for both solid and liquid phases in LIBs.

1.8 Experimental Electrochemistry

1.8.1 Cyclic Voltammetry

Cyclic voltammetry is a powerful electrochemical technique commonly used to investigate the oxidation and reduction processes of redox systems. It provides information about surface reaction mechanisms, as well as qualitative information about the number of oxidation states and their stability. Cyclic voltammetry is performed by cycling the potential of a working electrode in positive and negative directions, while measuring the resulting current. A typical cyclic voltammogram at a macro-electrode is given in Figure 1.7. Forward scan shows current due to an oxidation process, whereas the reverse scan shows current due to a reduction of the same species.

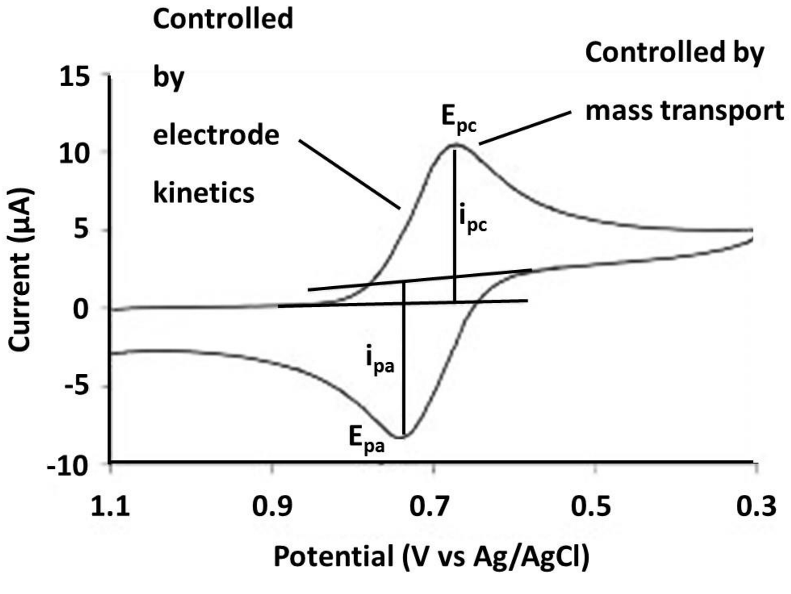

Figure 1.7: Initially the chemical reaction is governed by kinetics of the heterogeneous electron transfer across the electrode/solution interface. At the maximum, the current response is due to diffusion. Figure is reproduced from Reference 171.

The peaks in the cyclic voltammogram arise because mass transport cannot compete with electrode kinetics resulting in a depletion of the electroactive species. Cyclic voltammetry is usually carried out at certain scan rates, which control how fast the applied potential is scanned. For a given scan rate, the current of a cyclic voltammogram can be plotted vs. time. The resulting plot will look similar to the current vs. potential plot, since the potential is a linear function of time. The area under the peaks can then be integrated to evaluate the charge *(Q)*. Battery charge efficiency, also known as the coulombic efficiency, is the ratio (expressed as a percentage) between the amount of charge removed from a battery during reduction (discharging) and the amount of charge used during oxidation (charging) to restore the original capacity. In this thesis, cyclic voltammetry is used through out **Chapter 2, 3, 4, and 5** to collect different information related to the electrolyte stability and the electrochemical properties of the investigated cathode materials and other aspects.

1.8.2 Charge and Discharge Testing

The charge and discharge dynamics of batteries is characterized by measuring the voltage under constant charge and discharge current inputs. The rate of charging and discharging is governed by C-rates, which determines the speed at which a battery is cycled relative to its maximum capacity. A charge rate of 1C takes 1 hour to fully charge or discharge the cell, and a charge rate of 60C requires 1 minute. Constant-current load testing is performed to determine how much charging/discharging capacity can be input/output with varying current rates between two predefined voltage limits. The voltage limits depend on the operational voltage of the cathode and anode battery materials. A typical plot of a battery discharging at different C-rates is represented in Figure 1.8. As the current rate is constant, the voltage response is recorded vs. capacity. The discharge curves for the LIB show that the effective capacity of the cell is reduced when the cell is discharged at higher rates. This called the capacity offset, which is a common phenomena to most cell chemistries resulting from ohmic losses, mass transport limitations, and fast kinetics of the reaction between Li-ion and the active materials. The high rate discharge case indicates that the voltage drops quickly so that only a part of capacity can be used.

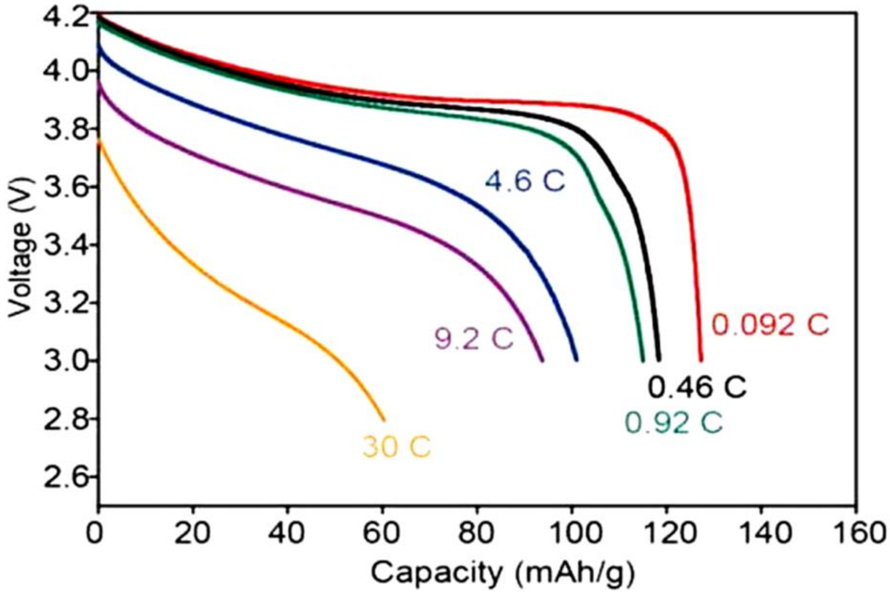

Figure 1.8: Discharge profiles of a $LiCoO_2$ cell measured at various C-rates. Figure is reproduced from Reference 172.

1.9 Scanning Probe Microscopy

LIBs are multi-component systems where various mechanisms and simultaneous processes take place. Advanced characterization techniques are therefore required to address and understand the complexity of battery processes, which enable technological improvements in their performance. A major difficulty when probing the reactions and intrinsic material properties of LIBs is the fact that the standard electrochemical techniques require porous composite films. These films are prepared by mixing the battery material of interest with electronically conductive filler and polymer binder. However, the use of additives results in complex electrode architectures, and have been reported to affect its charging/discharging properties.[173-174] Moreover, the porosity and the thickness of the electrode directly influence its electrochemical performance, due to the distributions of current density, electric potential, and the concentration of lithium within the porous electrode during charging/discharging.[168] These distributions are more pronounced at high cycling rates, and they prevent the electrochemical reactions from taking place uniformly across the electrode. As such, the electrochemical responses of the conventional composite electrodes represent the “apparent”, not the “intrinsic” properties of the active battery material, which make it difficult to detect the real performance of new active materials thoroughly. A truly fundamental understanding of these systems can only be gained from the development and implementation of microscopy techniques that can provide localized electrochemical measurements with high resolution. Recent studies have shown that LIB materials can be probed on the micron to nanometer scale using atomic force microscopy (AFM) and scanning tunneling microscopy (STM). These techniques provide accurate measurement of the morphological changes that occur during battery cycling such as exfoliation mechanisms[175-176] and solid electrolyte interphase (SEI) layer formation[177-178] on the anode, and surface roughness,[179] particle shape and size changes[180-182] on the cathode. More specialized scanning electrochemical probe microscopy techniques, which have proven powerful for dynamic mapping and local electrochemical measurements in LIBs, will be discussed in details herein given the focus of this thesis.

1.9.1 Scanning Electrochemical Microscopy (SECM)

Among electrochemical mapping techniques, scanning electrochemical microscopy (SECM)[183-184] was successfully employed in the field of LIBs for detecting various processes occurring at battery electrodes.[185-189] The operation of SECM is based on the use of ultramicroelectrode (UME) as a mobile tip, positioned near the substrate of interest to quantitatively probe interfacial physicochemical processes.[190] The tip is dipped in four-electrode electrochemical cell, together with the counter electrode, reference electrode and the sample, which often acts as a second working electrode. The tip can be accurately positioned in x,y,z-coordinates by step motors and/or piezoelectric elements (see Figure 1.9). Chemical changes in close proximity to the sample interface are detected by the SECM tip as it scans in x- and y-directions of the designated area, and a suitable electrochemical signal is recorded. This provides spatially resolved information about the electrochemical activity of the underlying surface.

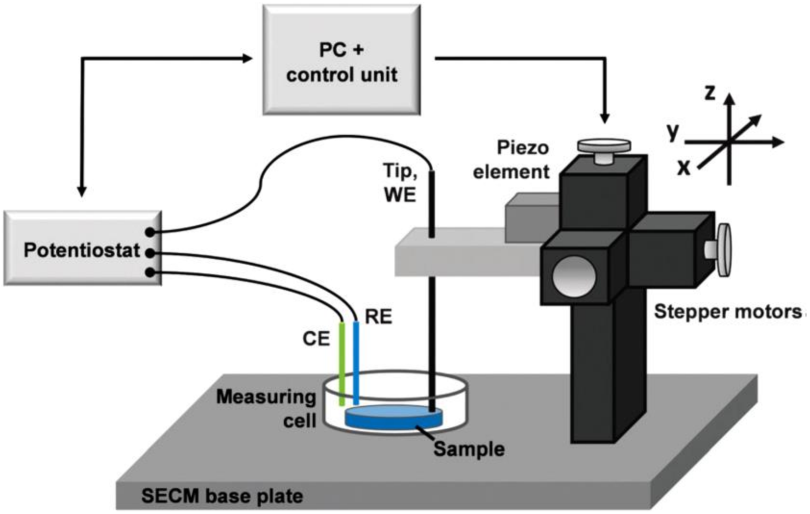

Figure 1.9: A scheme displaying a typical SECM set-up. The sample of interest is immersed in an electrolyte solution and a microelectrode tip is positioned in close proximity to the surface. The tip and substrate potential must often be simultaneously controlled and the Faradaic current flow is monitored during imaging. Hardware on the personal computer supplies control signals to the piezo-positioner and collects data from the tip and substrate. Figure is reproduced from Reference 191.

One of the main advantages of using small sized scanning probes in SECM is the formation of hemispherical diffusion field in small electrodes. This allows higher mass-transfer rates than that at macroscopic electrodes, and offers the ability to reach a steady state in seconds or milliseconds. Moreover, the current obtained during the electrochemical measurements is small enough that the resistive potential drop in solution and the double-layer charging current can be neglected. High spatial resolution is also achievable with these small tips, making it possible to perform electrochemical imaging on microscopic domains.[192]

Since SECM was first reported in the late 1980s,[193-194] numerous papers have been published on its methodology and diverse applications.[195-199] For instance, Jung *et al.* studied the transportation of Li-ions at the interface of a charging $LiCoO_2$ electrode using SECM. By scanning the probe at a constant distance from the substrate, heterogeneous electrochemical activity across the $LiCoO_2$ electrode was recorded, indicating non-uniform Li-ion transport throughout the sample.[185] Nevertheless, whether the probe is detecting the solvated Li-ions, or the products of the anodic decomposition of the electrolyte originating from the cathode, or Co species originating from dissolution of $LiCoO_2$ remained a matter of debate. Similarly, Snook *et al.* applied SECM to monitor dissolution of Co ions from $LiCoO_2$ battery material in ionic liquid. The reduction of Co^{3+}

to the unstable Co^+, and the evolution of solubilised oxygen from the cathode electrode during overcharging were found to have a considerable contribution to the loss of discharge capacity.[186] However, the tip was retained at a fixed position during the experiment, and no activity map was collected. Given the complications of overlapping processes, such as variation of Li-ion concentration, electrolyte decomposition, metal ions dissolution, and oxygen release from the crystal lattice of the metal oxide, many challenges were associated with the use of SECM for investigating cathode materials. Furthermore, SECM measurements require quite long time to perform while the entire sample is immersed in electrolyte solution. This might affect the surface properties of the sample due to adsorption or corrosion processes. The sample in SECM should also be flat and precisely aligned, as conventional SECM has no mechanism to maintain a constant tip-to-substrate separation. To address this issue, several methods have been proposed to incorporate positional feedback into SECM.[200-202] SECM also suffers from limited lateral resolution due to coupling between active sites on the substrate and the tip, and due the overlap of diffusion fields of neighboring active sites on the substrate.

1.9.2 Scanning Micropipette Contact Method (SMCM)

In an attempt to overcome many of the SECM limitations, pipette-based electrochemical techniques have been implemented to probe local dynamic electrochemical measurements of small areas of macroscopic electrode surfaces.[203-205] These pipette-based methods were originally used for corrosion studies, in which it was necessary to confine measurements to a small area of surface.[206-208] The scanning micropipette contact method (SMCM) advances these techniques by utilizing a mobile micropipette with a diameter aperture between 500 nm and 1000 µm. The pipette is filled with electrolyte solution containing electroactive species, and is brought down towards the electrode surface via piezoelectric positioners. A reference/counter electrode is housed within the pipette to form an electrochemical system when the substrate is a conductor, therefore making a two-electrode setup. When the pipette is in close proximity to substrate, a gentle meniscus of the liquid electrolyte protruding from the tip of the pipette wets the substrate. The area of the substrate, which acts as the working electrode, is defined by the meniscus contact area. This allows for highly localized electrochemical measurements without the need to immerse the substrate completely in solution. For visualization of redox activity, a bias voltage is applied between the substrate and the QRCE to induce the electron transfer process through the cell.

SMCM was used to visualize the electrochemical activity of LFP composite film at the nanoscale using an aqueous-based electrolyte.[209] The experimental setup is represented in Figure 1.10.

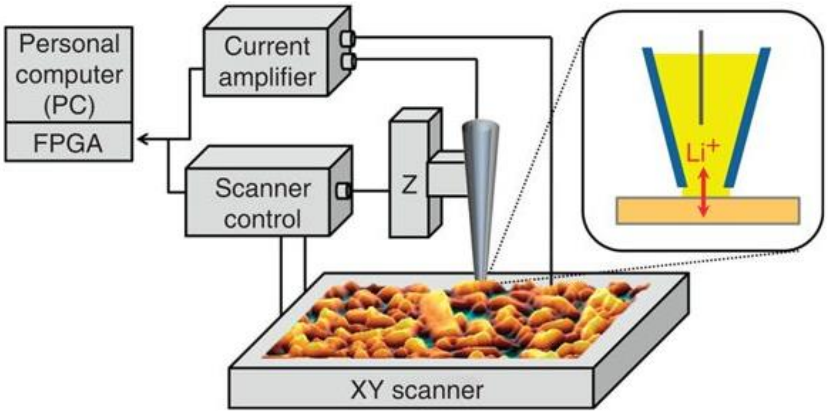

Figure 1.10: Schematic of the SMCM. Figure is reproduced from Reference 209.

Current activity maps of the electrode surface were derived simultaneously with local topography (see Figure 1.11), which makes this technique suitable for evaluating real battery electrodes that exhibit topographic variations. The obtained information was combined with complementary microscopic techniques (SEM and EXD) and surface potential measurements to allow chemical mapping (identification of LFP domains). The electrodes exhibited highly spatially heterogeneous electrochemistry at the nanoscale, both within secondary particles and at individual primary nanoparticles, which is highly dependent on the local composition. The correlation of electrochemical activity imaging with the underlying chemical composition of LFP composite surfaces highlights the considerable strength of multi-microscopy measurements in understanding the structure and function of complex materials at small scale. Nevertheless, the main limitation of this work was the use of aqueous electrolyte solution. LFP is known for its low cost, low toxicity, and abundant raw materials, but its cathodic operating potential is around 3.6 V vs. Li/Li$^+$. Accordingly, LFP operates within the electrochemical stability window of water. Yet, many of the active materials employed in LIBs such as $LiCoO_2$, $LiNi_{1/3}Mn_{1/3}Co_{1/3}O_2$, $LiNi_{0.5}Mn_{1.5}O_4$, graphite, silicon, or $Li_4Ti_5O_{12}$ do not operate within the water stability window. Moreover, substituting organic electrolyte solutions with aqueous electrolytes might result in dissolution of the materials. Therefore, the implementation of SMCM in an inert atmosphere using anhydrous battery electrolytes is of significant importance for this technique to reach its full potential, and this is actually the prime goal of this thesis. More details about SMCM technique and its development in an inert atmosphere are discussed in **Chapter 2.** In **Chapter 3, 4** and **5**, the use of SMCM to investigate LIB materials is reported.

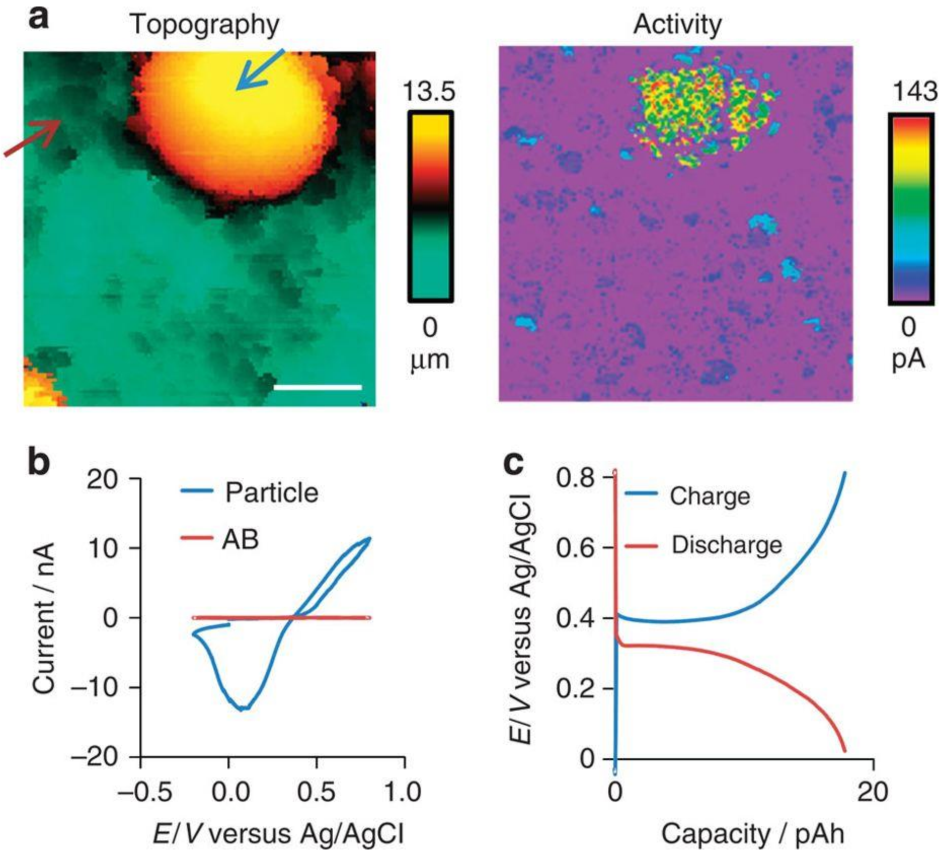

Figure 1.11: (a) Simultaneous SMCM topography (left) and current (right) images of a $LiFePO_4$ electrode. Scan ranges are 20 x 20 µm. The sample potential was +0.65 V versus Ag/AgCl QRCE (Li^+ deintercalation; scale bar, 5 µm). (b) CVs at different locations above a $LiFePO_4$ electrode surface corresponding to the blue and red arrow of (b). Particle and AB refers to $LiFePO_4$ and acetylene black (conductive additive), respectively. Scan rate is 0.1 V s^{-1}. (c) Local charge (deintercalation) and discharge (intercalation) characteristics applying current magnitudes of 200 pA in each case via SMCM. Figure is reproduced from Reference 209.

1.9.3 Scanning Ion Conductance Microscopy (SICM)

Following a similar approach, the scanning ion-conductance microscopy (SICM) has been also employed to investigate the redox activity of LIB electrodes. SICM employs a nanopipette filled with electrolyte as scanning probe. However, the pipette and the sample surface are both submerged in the electrolyte solution, thus exhibiting lower sensitivity and resolution compared to SMCM. The operation of SICM is based on ion current that flows between two biased reference/counter electrodes, one placed inside the pipette and another placed in the bathing solution. This direct (ion conductance) current (DC) is incredibly sensitive to the tip-substrate separation close to the substrate of interest. As the pipette probe comes into close proximity with the surface, the current starts to decrease because the surface obstructs the solution from entering to probe. A feedback mechanism then maintains the tip-sample separation constant, which allows the pipette to scan surface contours and generate topographic information. For more reliable feedback, the probe is oscillated in the Z direction. This makes the feedback more sensitive since the alternating current (AC) is more sensitive to tip-substrate distance than the DC, it is also less susceptible to bulk changes in the solution conductivity.

SICM was applied to tin negative electrode to measure spatially resolved Li^+ currents before and after lithiation.[210] Surface topography and local ion current maps were collected concurrently by applying an AC and DC currents respectively (see Figure 1.12). Importantly, organic electrolyte solutions were employed, which makes the study of any LIB material possible. The inhomogeneities obtained in the topographic and ionic current maps were ascribed to electrochemical processes such as lithiation and inhomogeneous SEI layer formation. The combination of both, topography and ion current, provides insight into the local electrochemical phenomena that govern the operation of LIBs.

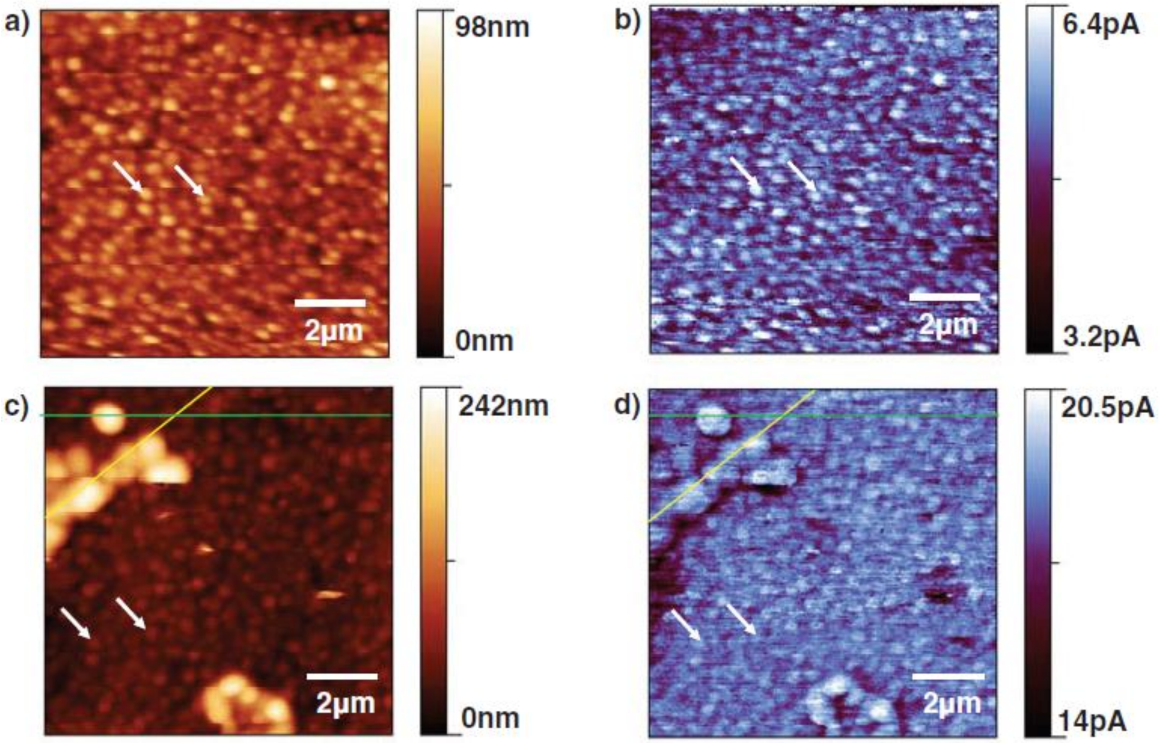

Figure 1.12: SICM (a,c) topography and (b,d) DC current images of a 60 nm thick tin thin film deposited on a 60 nm thick copper thin film on glass (a,b) before lithiation and (c,d) after 24 μAhcm^{-2} lithiation. Figure is reproduced from Reference 210.

1.10 Thesis Outline

The main objective of this thesis is to design a localized scanning probe technique to spatially resolve electrochemical features on LIBs cathode materials. The objective was achieved by developing the scanning micropipette contact method (SMCM) in a controlled atmosphere, where oxygen and water do not interfere with the oxidation and reduction reactions of the battery material. This provides the opportunity to probe the electrochemical activity of many active materials that do not operate within the water stability window. The proposed technique employs micropipette to probe small substrate areas (~10 μm in diameter) decorated with battery active material using lithium electrolyte solution. This forms a micron LIB, with the wetted area of the substrate acting as the cathode, the physical separation of the pipette barrel as a separator, and the reference/counter electrode as the anode. The investigation of dispersed particles of active material enables the determination of oxidation and reduction potentials, peak currents, charge capacity, and local heterogeneities of the material. Furthermore, when used in combination with scanning electron microscopy and atomic force microscopy, lateral translation of the sample electrochemical maps of the substrate is obtained.

Chapter 1 covers the fundamental properties of LIBs and compares briefly the performance characteristics of a few promising LIBs cathode materials and approaches for improving their performances. **Chapter 1** also highlights the working principles of the most commonly used scanning probe microscopy techniques that has been employed to study LIBs, including the SMCM technique, which is the main focus of this thesis.

Chapter 2 describes the systematic development of the SMCM to operate in an anaerobic environment. The optimization steps include stability tests to ensure a good performance of the technique on the length scale of the proposed electrochemical measurements. **Chapter 2** also discusses the principles and operation of the SMCM for investigating LIB cathode materials.

Chapter 3 presents localized electrochemical measurements performed on LFP active material using the combination of SMCM and SEM. The investigation of LFP isolated particles is performed on gold substrate using organic electrolyte solution. Data obtained by the micropipette method is compared to coin cell measurements to critically assess this technique for characterisation of active battery materials.

Chapter 4 reports the advancement of SMCM to use ionic liquid as a promising alternative to the conventional organic electrolytes. This allows the extension the electrochemical window of the electrolyte solution and enables the study of LIB materials with higher oxidation potential. Different stability tests are performed to ensure the ability of SMCM to operate at extended potentials with good efficiency. As a proof-of-concept, localized electrochemical measurements are performed on the conventional LFP active particles using the combination of SMCM and AFM.

Chapter 5 investigates the higher energy cathode material NMC by means of SMCM. Due to poor electronic conductivity between the active material and the glassy carbon substrate, ball milling is used to introduce carbon black as a conducting phase between the NMC particles. **Chapter 5** also presents the effect of different ball milling conditions on the electrochemical performance of NMC as examined via coin cells measurements.

Chapter 6 summarizes and concludes all findings presented in this thesis and discusses future directions.

1.11 References

1.Tulloch, G. E. *Journal of Photochemistry and Photobiology A: Chemistry* **2004,** 164, (1-3), 209-219.

2.Lewis, N. S.; Crabtree, G., Basic Research Needs for Solar Energy Utilization. US Department of Energy, Office of Basic Energy Science: 2005.

3.Crabtree, G. W.; Lewis, N. S. *Physics today* **2007,** 60, (3), 37-42.

4.Hill, J.; Nelson, E.; Tilman, D.; Polasky, S.; Tiffany, D. *Proceedings of the National Academy of sciences* **2006,** 103, (30), 11206-11210.

5.Scrosati, B.; Garche, J. *Journal of power sources* **2010,** 195, (9), 2419-2430.

6.Nedjalkov, A.; Meyer, J.; Köhring, M.; Doering, A.; Angelmahr, M.; Dahle, S.; Sander, A.; Fischer, A.; Schade, W. *Batteries* **2016,** 2, (1), 5.

7.Larsson, F.; Andersson, P.; Blomqvist, P.; Mellander, B.-E. *Scientific reports* **2017,** 7, (1), 10018.

8.Landi, B. J.; Ganter, M. J.; Cress, C. D.; DiLeo, R. A.; Raffaelle, R. P. *Energy & Environmental Science* **2009,** 2, (6), 638-654.

9.Kurzweil, P. *Journal of Power Sources* **2010,** 195, (14), 4424-4434.

10.Dell, R. *Solid State Ionics* **2000,** 134, (1), 139-158.

11.Palacin, M. R. *Chemical Society Reviews* **2009,** 38, (9), 2565-2575.

12.Bertin, F. C. H.; Espinosa, D. C. R.; Tenório, J. A. S. *Electronic Waste: Recycling Techniques* **2015**, 129.

13.Petchjatuporn, P.; Sirisuk, P.; Khaehintung, N.; Sunat, K.; Wicheanchote, P.; Kiranon, W. *Energy Conversion and Management* **2008,** 49, (2), 185-192.

14.Ruetschi, P.; Meli, F.; Desilvestro, J. *Journal of Power Sources* **1995,** 57, (1), 85-91.

15.Ikoma, M.; Hoshina, Y.; Matsumoto, I.; Iwakura, C. *Journal of the Electrochemical Society* **1996,** 143, (6), 1904-1907.

16.Davenport, D. A. *J. Chem. Ed* **1984,** 61, 2.

17.Wen, J.; Yu, Y.; Chen, C. *Materials express* **2012,** 2, (3), 197-212.

18.Bhattacharyya, R.; Key, B.; Chen, H.; Best, A. S.; Hollenkamp, A. F.; Grey, C. P. *Nature materials* **2010,** 9, (6), 504-510.

19.Fellner, C.; Newman, J. *Journal of Power Sources* **2000,** 85, (2), 229-236.

20.Bruce, G.; Mardikian, P.; Marcoux, L. *Journal of power sources* **1997,** 65, (1), 149-153.

21.Majima, M.; Ujiie, S.; Yagasaki, E.; Koyama, K.; Inazawa, S. *Journal of Power Sources* **2001,** 101, (1), 53-59.

22.Tröltzsch, U.; Kanoun, O.; Tränkler, H.-R. *Electrochimica Acta* **2006,** 51, (8), 1664-1672.

23.Fergus, J. W. *Journal of Power Sources* **2010,** 195, (4), 939-954.

24.Goodenough, J. B.; Mizuchima, K., Electrochemical cell with new fast ion conductors. Google Patents: 1981.

25.Ohzuku, T.; Brodd, R. J. *Journal of Power Sources* **2007,** 174, (2), 449-456.

26.Ozawa, K. *Solid State Ionics* **1994,** 69, (3-4), 212-221.

27.Brodd, R. J., *Batteries for sustainability: selected entries from the encyclopedia of sustainability science and technology*. Springer Science & Business Media: 2012.

28.Ohzuku, T.; Ueda, A. *Solid State Ionics* **1994,** 69, (3), 201-211.

29.Koksbang, R.; Barker, J.; Shi, H.; Saidi, M. *Solid state ionics* **1996,** 84, (1), 1-21.

30.Venkatraman, S.; Shin, Y.; Manthiram, A. *Electrochemical and solid-state letters* **2003,** 6, (1), A9-A12.

31.Laubach, S.; Laubach, S.; Schmidt, P. C.; Ensling, D.; Schmid, S.; Jaegermann, W.; Thißen, A.; Nikolowski, K.; Ehrenberg, H. *Physical Chemistry Chemical Physics* **2009,** 11, (17), 3278-3289.

32.Julien, C. M.; Mauger, A.; Zaghib, K.; Groult, H. *Inorganics* **2014,** 2, (1), 132-154.

33.Reimers, J. N.; Dahn, J. *Journal of The Electrochemical Society* **1992,** 139, (8), 2091-2097.

34.Delmas, C.; Saadoune, I. *Solid State Ionics* **1992,** 53, 370-375.

35.Gummow, R.; De Kock, A.; Thackeray, M. *Solid State Ionics* **1994,** 69, (1), 59-67.

36.Hu, M.; Tian, Y.; Wei, J.; Wang, D.; Zhou, Z. *Journal of Power Sources* **2014,** 247, 794-798.

37.Kalyani, P.; Kalaiselvi, N. *Science and Technology of Advanced Materials* **2005,** 6, (6), 689-703.

38.Li, W.; Reimers, J.; Dahn, J. *Physical Review B* **1992,** 46, (6), 3236.

39.Nakai, I.; Takahashi, K.; Shiraishi, Y.; Nakagome, T.; Nishikawa, F. *Journal of Solid State Chemistry* **1998,** 140, (1), 145-148.

40.Hewston, T.; Chamberland, B. *Journal of Physics and Chemistry of Solids* **1987,** 48, (2), 97-108.

41.Okada, M.; Takahashi, K.-i.; Mouri, T. *Journal of power sources* **1997,** 68, (2), 545-548.

42.Broussely, M.; Perton, F.; Labat, J.; Staniewicz, R.; Romero, A. *Journal of power Sources* **1993,** 43, (1-3), 209-216.

43.Whittingham, M. S. *Chemical Reviews* **2004,** 104, (10), 4271-4302.

44.Choi, J.; Manthiram, A. *Journal of The Electrochemical Society* **2005,** 152, (9), A1714-A1718.

45.Yabuuchi, N.; Ohzuku, T. *Journal of Power Sources* **2003,** 119, 171-174.

46.Shaju, K.; Rao, G. S.; Chowdari, B. *Electrochimica Acta* **2002,** 48, (2), 145-151.

47.Ohzuku, T.; Makimura, Y. *Chemistry Letters* **2001**, (7), 642-643.

48.Koyama, Y.; Tanaka, I.; Adachi, H.; Makimura, Y.; Ohzuku, T. *Journal of Power Sources* **2003,** 119, 644-648.

49.Hwang, B.; Tsai, Y.; Carlier, D.; Ceder, G. *Chemistry of Materials* **2003,** 15, (19), 3676-3682.

50.Yamada, A.; Tanaka, M.; Tanaka, K.; Sekai, K. *Journal of power sources* **1999,** 81, 73-78.

51.Labrini, M.; Saadoune, I.; Scheiba, F.; Almaggoussi, A.; Elhaskouri, J.; Amoros, P.; Ehrenberg, H.; Brötz, J. *Electrochimica Acta* **2013,** 111, 567-574.

52.Li, J.; Xiong, S.; Liu, Y.; Ju, Z.; Qian, Y. *Nano Energy* **2013,** 2, (6), 1249-1260.

53.Nayak, P. K.; Grinblat, J.; Levi, M.; Wu, Y.; Powell, B.; Aurbach, D. *Journal of Electroanalytical Chemistry* **2014,** 733, 6-19.

54.Gong, C.; Lv, W.; Qu, L.; Bankole, O. E.; Li, G.; Zhang, R.; Hu, M.; Lei, L. *Journal of Power Sources* **2014,** 247, 151-155.

55.Croguennec, L.; Bains, J.; Bréger, J.; Tessier, C.; Biensan, P.; Levasseur, S.; Delmas, C. *Journal of The Electrochemical Society* **2011,** 158, (6), A664-A670.

56.Sun, Y.-K.; Chen, Z.; Noh, H.-J.; Lee, D.-J.; Jung, H.-G.; Ren, Y.; Wang, S.; Yoon, C. S.; Myung, S.-T.; Amine, K. *Nature materials* **2012,** 11, (11), 942.

57.Zhang, L.; Li, N.; Wu, B.; Xu, H.; Wang, L.; Yang, X.-Q.; Wu, F. *Nano letters* **2014,** 15, (1), 656-661.

58.Cho, Y.; Oh, P.; Cho, J. *Nano letters* **2013,** 13, (3), 1145-1152.

59.Hou, P.; Wang, X.; Wang, D.; Song, D.; Shi, X.; Zhang, L.; Guo, J.; Zhang, J. *RSC Advances* **2014,** 4, (31), 15923-15929.

60.Hou, P.; Wang, X.; Song, D.; Shi, X.; Zhang, L.; Guo, J.; Zhang, J. *Journal of Power Sources* **2014,** 265, 174-181.

61.Liu, X.; Li, H.; Li, D.; Ishida, M.; Zhou, H. *Journal of Power Sources* **2013,** 243, 374-380.

62.Li, X.; He, W.; Chen, L.; Guo, W.; Chen, J.; Xiao, Z. *Ionics* **2014,** 20, (6), 833-840.

63.Li, J.; Zhang, Q.; Liu, C.; He, X. *Ionics* **2009,** 15, (4), 493-496.

64.Li, J.; Fan, M.; He, X.; Zhao, R.; Jiange, C.; Wan, C. *Ionics* **2006,** 12, (3), 215-218.

65.Xu, K. *Chemical reviews* **2014,** 114, (23), 11503-11618.

66.Fu, L.; Liu, H.; Li, C.; Wu, Y. P.; Rahm, E.; Holze, R.; Wu, H. *Solid State Sciences* **2006,** 8, (2), 113-128.

67.Sinha, N. N.; Munichandraiah, N. *ACS Applied Materials & Interfaces* **2009,** 1, (6), 1241-1249.

68.Kim, H.-S.; Kim, K.; Moon, S.-I.; Kim, I.-J.; Gu, H.-B. *Journal of Solid State Electrochemistry* **2008,** 12, (7-8), 867-872.

69.Venkateswara Rao, C.; Leela Mohana Reddy, A.; Ishikawa, Y.; Ajayan, P. M. *ACS Applied Materials & Interfaces* **2011,** 3, (8), 2966-2972.

70.Tsai, H.-L.; Hsieh, C.-T.; Li, J.; Gandomi, Y. A. *Electrochimica Acta* **2018,** 273, 200-207.

71.Hirano, A.; Kanno, R.; Kawamoto, Y.; Takeda, Y.; Yamaura, K.; Takano, M.; Ohyama, K.; Ohashi, M.; Yamaguchi, Y. *Solid State Ionics* **1995,** 78, (1-2), 123-131.

72.Graetz, J.; Ahn, C.; Yazami, R.; Fultz, B. *The Journal of Physical Chemistry B* **2003,** 107, (13), 2887-2891.

73.Zhang, X.; Jiang, W. J.; Mauger, A.; Qilu; Gendron, F.; Julien, C. M. *Journal of Power Sources* **2010,** 195, (5), 1292-1301.

74.Thackeray, M. M.; Goodenough, J. B., Solid state cell wherein an anode, solid electrolyte and cathode each comprise a cubic-close-packed framework structure. Google Patents: 1985.

75.Yamaki, J. *Encyclopedia of Electrochemical Power Sources* **2009,** 5, 183.

76.Dahn, J.; Fuller, E.; Obrovac, M.; Von Sacken, U. *Solid State Ionics* **1994,** 69, (3), 265-270.

77.Wei, C.; Deng, J.; Xi, L.; Zhou, H.; Wang, Z.; Chung, C. Y.; Yao, Q.; Rao, G. *Int J Electrochem Sci* **2013,** 8, 6775-6783.

78.Rao, M. *Journal of Optoelectronics and Biomedical Materials Vol* **2013,** 5, (1), 9-16.

79.Wagner, R.; Preschitschek, N.; Passerini, S.; Leker, J.; Winter, M. *Journal of Applied Electrochemistry* **2013,** 43, (5), 481-496.

80.Amatucci, G.; Schmutz, C.; Blyr, A.; Sigala, C.; Gozdz, A.; Larcher, D.; Tarascon, J. *Journal of power sources* **1997,** 69, (1), 11-25.

81.Arora, P.; White, R. E.; Doyle, M. *Journal of the Electrochemical Society* **1998,** 145, (10), 3647-3667.

82.Aurbach, D.; Zaban, A.; Schechter, A.; Ein-Eli, Y.; Zinigrad, E.; Markovsky, B. *Journal of The Electrochemical Society* **1995,** 142, (9), 2873-2882.

83.Jang, D. H.; Oh, S. M. *Journal of The Electrochemical Society* **1997,** 144, (10), 3342-3348.

84.Padhi, A. K.; Nanjundaswamy, K.; Goodenough, J. *Journal of the electrochemical society* **1997,** 144, (4), 1188-1194.

85.Padhi, A.; Nanjundaswamy, K.; Masquelier, C.; Okada, S.; Goodenough, J. *Journal of the Electrochemical Society* **1997,** 144, (5), 1609-1613.

86.Takahashi, M.; Tobishima, S.-i.; Takei, K.; Sakurai, Y. *Solid State Ionics* **2002,** 148, (3), 283-289.

87.Delmas, C.; Maccario, M.; Croguennec, L.; Le Cras, F.; Weill, F. *Nature Materials* **2008,** 7, 665.

88.Come, J.; Taberna, P.-L.; Hamelet, S.; Masquelier, C.; Simon, P. *Journal of The Electrochemical Society* **2011,** 158, (10), A1090-A1093.

89.Andersson, A. S.; Thomas, J. O. *Journal of Power Sources* **2001,** 97-98, 498-502.

90.Prosini, P. P.; Lisi, M.; Zane, D.; Pasquali, M. *Solid State Ionics* **2002,** 148, (1), 45-51.

91.Gao, F.; Tang, Z. *Electrochimica Acta* **2008,** 53, (15), 5071-5075.

92.Chung, S.-Y.; Bloking, J. T.; Chiang, Y.-M. *Nature materials* **2002,** 1, (2), 123-128.

93.Shi, S.; Liu, L.; Ouyang, C.; Wang, D.-s.; Wang, Z.; Chen, L.; Huang, X. *Physical Review B* **2003,** 68, (19), 195108.

94.Wang, D.; Li, H.; Shi, S.; Huang, X.; Chen, L. *Electrochimica Acta* **2005,** 50, (14), 2955-2958.

95.Wang, J.; Sun, X. *Energy & Environmental Science* **2012,** 5, (1), 5163-5185.

96.Wang, J.; Yang, J.; Tang, Y.; Li, R.; Liang, G.; Sham, T.-K.; Sun, X. *Journal of Materials Chemistry A* **2013,** 1, (5), 1579-1586.

97.Ravet, N.; Chouinard, Y.; Magnan, J.; Besner, S.; Gauthier, M.; Armand, M. *Journal of Power Sources* **2001,** 97, 503-507.

98.Huang, H.; Yin, S.-C.; Nazar, L. s. *Electrochemical and Solid-State Letters* **2001,** 4, (10), A170-A172.

99.Franger, S.; Le Cras, F.; Bourbon, C.; Rouault, H. *Electrochemical and Solid-State Letters* **2002,** 5, (10), A231-A233.

100.Wang, Y.; Wang, Y.; Hosono, E.; Wang, K.; Zhou, H. *Angewandte Chemie* **2008,** 120, (39), 7571-7575.

101.Hu, Y. S.; Guo, Y. G.; Dominko, R.; Gaberscek, M.; Jamnik, J.; Maier, J. *Advanced Materials* **2007,** 19, (15), 1963-1966.

102.Hwang, B. J.; Wu, Y. W.; Venkateswarlu, M.; Cheng, M. Y.; Santhanam, R. *Journal of Power Sources* **2009,** 193, (2), 828-833.

103.Zhi, X.; Liang, G.; Wang, L.; Ou, X.; Zhang, J.; Cui, J. *Journal of Power Sources* **2009,** 189, (1), 779-782.

104.Chang, Z.; Chen, Z.; Wu, F.; Tang, H.; Zhu, Z.; Yuan, X. Z.; Wang, H. *Solid State Ionics* **2008,** 179, (39), 2274-2277.

105.Zhu, H.-L.; Chen, Z.-Y.; Ji, S.; Linkov, V. *Solid State Ionics* **2008,** 179, (27-32), 1788-1793.

106.Xiao, L.; Guo, Y.; Qu, D.; Deng, B.; Liu, H.; Tang, D. *Journal of Power Sources* **2013,** 225, 286-292.

107.Drezen, T.; Kwon, N.-H.; Bowen, P.; Teerlinck, I.; Isono, M.; Exnar, I. *Journal of Power Sources* **2007,** 174, (2), 949-953.

108.Chen, H.; Grey, C. P. *Advanced Materials* **2008,** 20, (11), 2206-2210.

109.Lee, M.-H.; Kang, Y.-J.; Myung, S.-T.; Sun, Y.-K. *Electrochimica Acta* **2004,** 50, (4), 939-948.

110.Wang, J.; Yao, X.; Zhou, X.; Liu, Z. *Journal of Materials Chemistry* **2011,** 21, (8), 2544-2549.

111.Oh, S. W.; Bang, H. J.; Myung, S.-T.; Bae, Y. C.; Lee, S.-M.; Sun, Y.-K. *Journal of The Electrochemical Society* **2008,** 155, (6), A414-A420.

112.Chen, H.; Qiu, X.; Zhu, W.; Hagenmuller, P. *Electrochemistry communications* **2002,** 4, (6), 488-491.

113.Kızıltaş-Yavuz, N.; Herklotz, M.; Hashem, A. M.; Abuzeid, H. M.; Schwarz, B.; Ehrenberg, H.; Mauger, A.; Julien, C. M. *Electrochimica Acta* **2013,** 113, 313-321.

114.Huang, Z.-D.; Liu, X.-M.; Oh, S.-W.; Zhang, B.; Ma, P.-C.; Kim, J.-K. *Journal of Materials Chemistry* **2011,** 21, (29), 10777-10784.

115.Kim, M.-K.; Chung, H.-T.; Park, Y.-J.; Kim, J.-G.; Son, J.-T.; Park, K.-S.; Kim, H.-G. *Journal of power sources* **2001,** 99, (1-2), 34-40.

116.Hu, Y.; Doeff, M. M.; Kostecki, R.; Fiñones, R. *Journal of the Electrochemical Society* **2004,** 151, (8), A1279-A1285.

117.Zhang, S.; Allen, J.; Xu, K.; Jow, T. *Journal of Power Sources* **2005,** 147, (1-2), 234-240.

118.Prado, G.; Fournes, L.; Delmas, C. *Solid State Ionics* **2000,** 138, (1-2), 19-30.

119.He, Y.-S.; Ma, Z.-F.; Liao, X.-Z.; Jiang, Y. *Journal of Power Sources* **2007,** 163, (2), 1053-1058.

120.Xie, J.; Huang, X.; Zhu, Z.; Dai, J. *Ceramics International* **2010,** 36, (8), 2485-2487.

121.Ryu, W.-H.; Lim, S.-J.; Kim, W.-K.; Kwon, H. *Journal of Power Sources* **2014,** 257, 186-191.

122.Meligrana, G.; Gerbaldi, C.; Tuel, A.; Bodoardo, S.; Penazzi, N. *Journal of Power Sources* **2006,** 160, (1), 516-522.

123.Lu, C.-H.; Lin, Y.-K. *Journal of Power Sources* **2009,** 189, (1), 40-44.

124.Sinha, N. N.; Munichandraiah, N. *Journal of Solid State Electrochemistry* **2008,** 12, (12), 1619-1627.

125.Hong, Y. J.; Kim, J. H.; Kim, M. H.; Kang, Y. C. *Materials Research Bulletin* **2012,** 47, (8), 2022-2026.

126.Konarova, M.; Taniguchi, I. *Materials Research Bulletin* **2008,** 43, (12), 3305-3317.

127.Kim, S.-B.; Kim, S.-J.; Kim, C.-H.; Kim, W.-S.; Park, K.-W. *Materials Letters* **2011,** 65, (21-22), 3313-3316.

128.Fey, G. T.-K.; Chen, Y. G.; Kao, H.-M. *Journal of Power Sources* **2009,** 189, (1), 169-178.

129.Nakamura, K.; Hirano, H.; Nishioka, D.; Michihiro, Y.; Moriga, T. *Solid State Ionics* **2008,** 179, (27), 1806-1809.

130.Chen, Z.; Qin, Y.; Amine, K.; Sun, Y.-K. *Journal of Materials Chemistry* **2010,** 20, (36), 7606-7612.

131.Li, C.; Zhang, H. P.; Fu, L. J.; Liu, H.; Wu, Y. P.; Rahm, E.; Holze, R.; Wu, H. Q. *Electrochimica Acta* **2006,** 51, (19), 3872-3883.

132.Yang, C.; Zhang, X.; Huang, M.; Huang, J.; Fang, Z. *ACS Applied Materials & Interfaces* **2017,** 9, (14), 12408-12415.

133.Hsieh, C.-T.; Mo, C.-Y.; Chen, Y.-F.; Chung, Y.-J. *Electrochimica Acta* **2013,** 106, 525-533.

134.Huang, Y.-H.; Goodenough, J. B. *Chemistry of Materials* **2008,** 20, (23), 7237-7241.

135.Wu, C.; Fang, X.; Guo, X.; Mao, Y.; Ma, J.; Zhao, C.; Wang, Z.; Chen, L. *Journal of Power Sources* **2013,** 231, 44-49.

136.Kweon, H.-J.; Park, J.; Seo, J.; Kim, G.; Jung, B.; Lim, H. S. *Journal of power sources* **2004,** 126, (1-2), 156-162.

137.Wang, J.-H.; Wang, Y.; Guo, Y.-Z.; Ren, Z.-Y.; Liu, C.-W. *Journal of Materials Chemistry A* **2013,** 1, (15), 4879-4884.

138.Cho, J.; Kim, Y. J.; Park, B. *Chemistry of Materials* **2000,** 12, (12), 3788-3791.

139.Thackeray, M.; Johnson, C.; Kim, J.-S.; Lauzze, K.; Vaughey, J.; Dietz, N.; Abraham, D.; Hackney, S.; Zeltner, W.; Anderson, M. *Electrochemistry communications* **2003,** 5, (9), 752-758.

140.Cho, J.; Kim, T.-J.; Kim, J.; Noh, M.; Park, B. *Journal of The Electrochemical Society* **2004,** 151, (11), A1899-A1904.

141.Huang, J.; Fang, X.; Wu, Y.; Zhou, L.; Wang, Y.; Jin, Y.; Dang, W.; Wu, L.; Rong, Z.; Chen, X. *Journal of Electroanalytical Chemistry* **2018**.

142.Morales, J.; Trócoli, R.; Rodríguez-Castellón, E.; Franger, S.; Santos-Peña, J. *Journal of Electroanalytical Chemistry* **2009,** 631, (1), 29-35.

143.Guo, R.; Shi, P.; Cheng, X.; Ma, Y.; Tan, Z. *Journal of Power Sources* **2009,** 189, (1), 2-8.

144.Ghosh, P.; Mahanty, S.; Basu, R. N. *Materials Chemistry and Physics* **2008,** 110, (2), 406-410.

145.Wen, Z.; Huang, S.; Yang, X.; Lin, B. *Solid State Ionics* **2008,** 179, (27), 1800-1805.

146.Marcinek, M. L.; Wilcox, J. W.; Doeff, M. M.; Kostecki, R. M. *Journal of The Electrochemical Society* **2009,** 156, (1), A48-A51.

147.Lin, B.; Wen, Z.; Han, J.; Wu, X. *Solid State Ionics* **2008,** 179, (27-32), 1750-1753.

148.Patey, T. J.; Büchel, R.; Ng, S.; Krumeich, F.; Pratsinis, S. E.; Novák, P. *Journal of power sources* **2009,** 189, (1), 149-154.

149.Lu, C.-Z.; Fey, G. T.-K.; Kao, H.-M. *Journal of power sources* **2009,** 189, (1), 155-162.

150.Joachin, H.; Kaun, T. D.; Zaghib, K.; Prakash, J. *Journal of the Electrochemical Society* **2009,** 156, (6), A401-A406.

151.Dominko, R.; Bele, M.; Gaberscek, M.; Remskar, M.; Hanzel, D.; Pejovnik, S.; Jamnik, J. *Journal of the Electrochemical Society* **2005,** 152, (3), A607-A610.

152.Chen, Z.-y.; Zhu, H.-l.; Ji, S.; Fakir, R.; Linkov, V. *Solid State Ionics* **2008,** 179, (27), 1810-1815.

153.Yan, X.; Yang, G.; Liu, J.; Ge, Y.; Xie, H.; Pan, X.; Wang, R. *Electrochimica Acta* **2009,** 54, (24), 5770-5774.

154.Ong, C.-W.; Lin, Y.-K.; Chen, J.-S. *Journal of The Electrochemical Society* **2007,** 154, (6), A527-A533.

155.Shin, H. C.; Cho, W. I.; Jang, H. *Electrochimica Acta* **2006,** 52, (4), 1472-1476.

156.Li, H.; Zhou, H. *Chemical Communications* **2012,** 48, (9), 1201-1217.

157.Rui, X. H.; Li, C.; Chen, C. H. *Electrochimica Acta* **2009,** 54, (12), 3374-3380.

158.Chen, Z.; Dahn, J. *Journal of the Electrochemical Society* **2002,** 149, (9), A1184-A1189.

159.Cao, Q.; Zhang, H. P.; Wang, G. J.; Xia, Q.; Wu, Y. P.; Wu, H. Q. *Electrochemistry Communications* **2007,** 9, (5), 1228-1232.

160.Kim, J.; Kim, B.; Lee, J.-G.; Cho, J.; Park, B. *Journal of Power Sources* **2005,** 139, (1), 289-294.

161.Kim, H.-S.; Kong, M.; Kim, K.; Kim, I.-J.; Gu, H.-B. *Journal of Power Sources* **2007,** 171, (2), 917-921.

162.Nien, Y.-H.; Carey, J. R.; Chen, J.-S. *Journal of Power Sources* **2009,** 193, (2), 822-827.

163.Yang, X.; Bao, C.; Xie, L.; Zhu, L.; Cao, X. *Ceramics International* **2019**.

164.Zhang, P.; Zhang, L.; Ren, X.; Yuan, Q.; Liu, J.; Zhang, Q. *Synthetic Metals* **2011,** 161, (11), 1092-1097.

165.Stein, M.; Chen, C.-F.; Mullings, M.; Jaime, D.; Zaleski, A.; Mukherjee, P. P.; Rhodes, C. P. *Journal of Electrochemical Energy Conversion and Storage* **2016,** 13, (3), 031001.

166.Zhang, D.; Cai, R.; Zhou, Y.; Shao, Z.; Liao, X.-Z.; Ma, Z.-F. *Electrochimica Acta* **2010,** 55, (8), 2653-2661.

167.Bard, A. J.; Faulkner, L. R.; Leddy, J.; Zoski, C. G., *Electrochemical methods: fundamentals and applications*. wiley New York: 1980; Vol. 2.

168.Newman, J.; Thomas-Alyea, K. E., *Electrochemical systems*. John Wiley & Sons: 2012.

169.Thomas, K. E.; Newman, J.; Darling, R. M., Mathematical modeling of lithium batteries. In *Advances in lithium-ion batteries,* Springer: 2002; pp 345-392.

170.Jiang, F.; Peng, P. *Scientific reports* **2016,** 6, 32639.

171.Fisher, A. C., *Electrode Dynamics*. Oxford University Press 1996.

172.Choi, D. I.; Han, G.-B.; Lee, D. J.; Park, J.-K.; Choi, J. W. *Journal of The Electrochemical Society* **2011,** 158, (10), A1150-A1154.

173.Dominko, R.; Gaberscek, M.; Drofenik, J.; Bele, M.; Pejovnik, S.; Jamnik, J. *Journal of Power Sources* **2003,** 119, 770-773.

174.Dominko, R.; Gaberšček, M.; Drofenik, J.; Bele, M.; Pejovnik, S. *Electrochemical and Solid-State Letters* **2001,** 4, (11), A187-A190.

175.Inaba, M.; Siroma, Z.; Funabiki, A.; Ogumi, Z.; Abe, T.; Mizutani, Y.; Asano, M. *Langmuir* **1996,** 12, (6), 1535-1540.

176.Seidl, L.; Martens, S.; Ma, J.; Stimming, U.; Schneider, O. *Nanoscale* **2016,** 8, (29), 14004-14014.

177.Tokranov, A.; Sheldon, B. W.; Li, C.; Minne, S.; Xiao, X. *ACS Applied Materials & Interfaces* **2014,** 6, (9), 6672-6686.

178.Wang, L.; Deng, D.; Lev, L. C.; Ng, S. *Journal of Power Sources* **2014,** 265, 140-148.

179.Zhu, J.; Zeng, K.; Lu, L. *Electrochimica Acta* **2012,** 68, 52-59.

180.Ramdon, S.; Bhushan, B.; Nagpure, S. C. *Journal of Power Sources* **2014,** 249, 373-384.

181.Demirocak, D. E.; Bhushan, B. *Journal of Colloid and Interface Science* **2014,** 423, 151-157.

182.Inaba, M.; Doi, T.; Iriyama, Y.; Abe, T.; Ogumi, Z. *Journal of Power Sources* **1999,** 81-82, 554-557.

183.Microscopy, S. E., Bard, AJ, Mirkin, MV, Eds. Marcel Dekker: New York: 2001.

184.Amemiya, S.; Bard, A. J.; Fan, F.-R. F.; Mirkin, M. V.; Unwin, P. R. *Annu. Rev. Anal. Chem.* **2008,** 1, 95-131.

185.Xu, F.; Beak, B.; Jung, C. *Journal of Solid State Electrochemistry* **2012,** 16, (1), 305-311.

186.Snook, G. A.; Huynh, T. D.; Hollenkamp, A. F.; Best, A. S. *Journal of Electroanalytical Chemistry* **2012,** 687, 30-34.

187.Barton, Z. J.; Rodríguez-López, J. n. *Analytical chemistry* **2014,** 86, (21), 10660-10667.

188.Zampardi, G.; Ventosa, E.; La Mantia, F.; Schuhmann, W. *Electroanalysis* **2015,** 27, (4), 1017-1025.

189.Bülter, H.; Peters, F.; Schwenzel, J.; Wittstock, G. *Angewandte Chemie International Edition* **2014,** 53, (39), 10531-10535.

190.Mirkin, M. V.; Horrocks, B. R. *Analytica Chimica Acta* **2000,** 406, (2), 119-146.

191.Ventosa, E.; Schuhmann, W. *Physical Chemistry Chemical Physics* **2015,** 17, (43), 28441-28450.

192.Bard, A. J.; Mirkin, M. V.; Unwin, P. R.; Wipf, D. O. *The Journal of Physical Chemistry* **1992,** 96, (4), 1861-1868.

193.Bard, A. J.; Fan, F. R. F.; Kwak, J.; Lev, O. *Analytical Chemistry* **1989,** 61, (2), 132-138.

194.Kwak, J.; Bard, A. J. *Analytical Chemistry* **1989,** 61, (17), 1794-1799.

195.Wittstock, G.; Burchardt, M.; Pust, S. E.; Shen, Y.; Zhao, C. *Angewandte Chemie International Edition* **2007,** 46, (10), 1584-1617.

196.Sun, P.; Laforge, F. O.; Mirkin, M. V. *Physical Chemistry Chemical Physics* **2007,** 9, (7), 802-823.

197.Mirkin, M. V.; Nogala, W.; Velmurugan, J.; Wang, Y. *Physical Chemistry Chemical Physics* **2011,** 13, (48), 21196-21212.

198.Lee, J.; Ye, H.; Pan, S.; Bard, A. J. *Analytical Chemistry* **2008,** 80, (19), 7445-7450.

199.Ye, H.; Lee, J.; Jang, J. S.; Bard, A. J. *The Journal of Physical Chemistry C* **2010,** 114, (31), 13322-13328.

200.McKelvey, K.; Edwards, M. A.; Unwin, P. R. *Analytical Chemistry* **2010,** 82, (15), 6334-6337.

201.Kim, J.; Shen, M.; Nioradze, N.; Amemiya, S. *Analytical chemistry* **2012,** 84, (8), 3489-3492.

202.Hengstenberg, A.; Kranz, C.; Schuhmann, W. *Chemistry–A European Journal* **2000,** 6, (9), 1547-1554.

203.Ebejer, N.; Schnippering, M.; Colburn, A. W.; Edwards, M. A.; Unwin, P. R. *Analytical chemistry* **2010,** 82, (22), 9141-9145.

204.Lai, S. C.; Patel, A. N.; McKelvey, K.; Unwin, P. R. *Angewandte Chemie International Edition* **2012,** 51, (22), 5405-5408.

205.Lai, S. C. S.; Dudin, P. V.; Macpherson, J. V.; Unwin, P. R. *Journal of the American Chemical Society* **2011,** 133, (28), 10744-10747.

206.Suter, T.; Böhni, H. *Electrochimica Acta* **1997,** 42, (20), 3275-3280.

207.Böhni, H.; Suter, T.; Schreyer, A. *Electrochimica Acta* **1995,** 40, (10), 1361-1368.

208.Eng, L.; Wirth, E.; Suter, T.; Böhni, H. *Electrochimica Acta* **1998,** 43, (19), 3029-3033.

209.Takahashi, Y.; Kumatani, A.; Munakata, H.; Inomata, H.; Ito, K.; Ino, K.; Shiku, H.; Unwin, P. R.; Korchev, Y. E.; Kanamura, K. *Nature communications* **2014,** 5, 5450.

210.Lipson, A. L.; Ginder, R. S.; Hersam, M. C. *Advanced Materials* **2011,** 23, (47), 5613-5617.

Chapter 2

Development of Scanning Micropipette Contact Method and its Application to Investigate Cathode Battery Materials

LIBs are commercially successful method for portable electrical energy, demonstrated by their use in portable electronics and the recent application as an alternative automotive power source to the internal combustion engine. However, for LIBs to be a competitive alternative to fossil fuels in the automotive industry, electrode materials with improved capacity and charge/discharge rates are required. As new anode and cathode materials are developed, they are typically screened for advantageous properties by assembly into a working battery. This involves the fabrication of a film from a mixture of conductive material, polymer binder, and the active material of interest. However, the use of these additives influence the electrochemical performance of the electrode. Moreover, the conventional composite electrodes convolute the responses from all active material particles in the film. This makes it difficult to detect the main source of limitation when the performance of the battery is below the theoretical level. Therefore, more localized measurement techniques are needed for fundamental studies of intrinsic material properties.

Chapter 2 proposes the application of the scanning micropipette contact method (SMCM) to investigate electrochemical information on LIB materials. A practical guide for developing and optimizing the SMCM technique in anaerobic environment is provided. The designed technique enables localized electrochemical measurements with micron scale resolution, and it allows the assessment of active battery materials without the need to prepare coin cells. SMCM employs a micropipette probe to deliver solution to the working electrode that is decorated with the active material of interest. Once the micropipette wets the surface, a complete electrical circuit between the working electrode and the QRCE is formed through the electrolyte within the pipette, and then local electrochemical responses can be probed. Chapter 2 explores the approaches used for designing the SMCM technique based on the cathode material to be investigated. These include the identification of the suitable electrolyte and working electrode surface, the calibration of pipettes, the fabrication and the stability testing of the AlLi QRCE, as well as the stability testing of the droplet.

2.1 Introduction

Scanning electrochemical probe microscopy techniques have proven highly valuable for the study of electrochemical processes in energy-related systems, owing to their ability to provide spatially resolved information about redox activities. These techniques have been widely applied in corrosion,[1-2] photocatalysis,[3-4] electrocatalysis,[5-8] semiconductors,[9] and in interpreting charge transfer kinetics and mechanisms.[10] Recently, the scanning probe methods have been successfully employed in the field of lithium-ion batteries (LIBs) as a powerful tool for monitoring the local electrochemical phenomena that govern the operation of battery electrodes.[11-17]

The scanning micropipette contact method (SMCM)[18-19] is a recent addition to a large family of scanning electrochemical probe microscopy methods, implemented to probe the electrochemical properties of small areas of macroscopic electrode surfaces.[20-22] SMCM employs a mobile pipette, typically between 500 nm and 1000 µm diameter, filled with an electrolyte solution along with a quasi-reference counter electrode (QRCE). The probe is localized in space by a x,y,z-positioning system, and is brought into contact with the substrate by applying a potential difference between the QRCE and the substrate. The liquid meniscus of the electrolyte solution formed at the pipette tip is held across the substrate by surface tension, while the wetted area along the substrate defines the working electrode. After performing the local electrochemical measurements required, the probe is retracted and moved to a new landing site, where a new approach is made.

SMCM has been used to address different energy-related issues. For example, SMCM was employed to elucidate the electrodeposition mechanism of Au,[23] Pd,[24] and Pt[24] nanoparticles on networks of pristine single walled carbon nanotubes (SWNT). SMCM enabled multiple measurements to be made on the same pristine sample by simply moving the position of the microcapillary across the network, thus negating the need for lengthy lithographic procedures normally used. By combination of the resulting current−time curves with atomic force microscopy (AFM) and scanning electron microscopy (SEM) analysis, the effect of electrode potential and deposition time on the nanoparticle formation process were investigated, and the parameters controlling nanoparticle number density, distribution, and size were identified. SMCM has been also used to probe the localized electrochemical activity of heterogeneous electrode surfaces. For instance, measurements on basal plane highly oriented pyrolytic graphite (HOPG),[19] with a step spacing significantly larger than the pipette diameter, revealed higher electron transfer activity than recently reported. In the same study, variations in the redox activity of chemically heterogeneous aluminum alloys were also detected. The high spatial resolution that SMCM technique provides reduced the possibility for side reactions such as corrosion, since the surface imaged was only in contact with solution for a short period of time.

Visualization of redox activity at LIBs electrodes was also achieved using SMCM. Takahashi and co-workers introduced SMCM as a technique to map spatial heterogeneities in the electrochemistry of lithium iron phosphate (LFP) electrodes at the nano-scale, and to track the electrode topography.[14] Although their method was successfully applied, the use of aqueous electrolyte solution remained a key limitation, since the operation of many cathode materials used in LIBs is outside the water stability window. SMCM was then promoted by Mauzeroll and co-workers to be used in anaerobic environment with organic electrolytes[25] and ionic liquids,[26] therefore extending the investigation of isolated particles of LIB materials to high energy active materials. As a proof-of-concept, a low density dispersion of LFP active material was examined on gold substrate using propylene carbonate (PC). The correlation between SMCM electrochemical responses and the complementary electron microscopy images for the scanned area revealed variations in particle electrochemical performances, which demonstrated that SMCM can electrochemically identify heterogeneities among the particles.[25] On the other hand, the use of ionic liquid for investigating LFP particles on glassy carbon substrate resulted in enhanced coulombic efficiency (higher than 90%).[26]

This chapter discusses the different steps associated with the optimization of SMCM to be used as a technique for investigating LIB cathode materials under anaerobic conditions. These include selection of the suitable electrolytes and the working substrates, calibration of pipettes, testing the droplet stability, as well as the fabrication of the AlLi QRCE. The optimization steps involved either electrochemical measurements or SEM imaging, and in some cases a combination of both. The main goal of these optimizations is to serve as practical guide for beginners in this field to accurately design their experiments based on the active battery material being tested.

2.2 Experimental Section

In analogy to coin cells, the operation of SMCM requires the presence of: (1) Li conducting electrolyte to promote the movement of ions during the oxidation/reduction reactions, (2) conducting substrate to support the electroactive material, and (3) QRCE that performs the same role as lithium metal in a coin cell. The optimization of this experimental setup for the most suitable electrolyte and conducting substrate, and the fabrication of the pipettes and the QRCE are represented herein.

The potential window of several electrolyte solutions and the stability of different macro-electrodes were examined using a three-electrode cell. The working electrode was placed into 10 ml of electrolyte solution along with two metallic Li strips (99.9% Alfa Aesar) used as reference and counter electrodes. Cyclic voltammetry measurements were performed at a scan rate of 50 mV s^{-1} on an ElPro Scan 3 (HEKA Electronics, Germany) instrument. Three different organic electrolytes were tested using a solution of 0.25 M of $LiClO_4$ (99.9% Sigma Aldrich). These include the ethyl methyl carbonate (EMC 99.92% BASF), diethyl carbonate (DEC 99.92% BASF), and propylene carbonate (PC 99.7% Sigma Aldrich). The ionic liquid 1-ethyl-3-methylimidazolium bis(trifluoromethylsulfonyl)imide (EMI TFSI 99.5% Iolitech) was similarly tested in a solution of 0.1 M of LiTFSI (99.9% Sigma Aldrich). The same EMI TFSI solution was also used to study three different macro-electrodes: gold (Au), platinum-disk (Pt), and glassy carbon (GC).

For the pipettes preparation, quartz capillaries with 0.3 mm inner diameter and 1.0 mm outer diameter were used (Sutter Instruments). These capillaries were then pulled down to micrometer scale diameter aperture using the laser-based micropipette puller (Model P-2000 Sutter Instruments). Scanning electron microscopy (SEM, with a Hitachi SU3500 VPSEM instrument) was used to observe the tip size of the pulled pipettes. The stability of these pipettes was then tested using 1 mM of the redox mediator 10-methylphenothiazine (MPT 98 % Alfa Aesar).

The fabrication of the $Al_{1-x}Li_x$ QRCE was conducted inside the glovebox (MBraun, water and oxygen content <1 ppm) using a three-electrode cell. An aluminum wire (Al 125 µm diameter, 99.5%, Goodfellow) was placed into a 0.25 M $LiClO_4$ solution in propylene carbonate (PC 99.7% Sigma Aldrich) served as the working electrode, and two Li metal strips (99.9% Alfa Aesar) served as reference and counter electrodes. The $Al_{1-x}Li_x$ alloy was formed galvanostatically by applying a constant current of -300 µA per 2 cm submersion of the Al wire for an hour. The stability of the QRCE was then tested by measuring the open circuit potential (OCP) for one hour upon fabrication.

2.3 Results and Discussion

2.3.1 Identifying the Optimal Electrolyte

During LIBs operation, all Faradaic processes are expected to take place at the electrodes, while the electrolyte should undergo no net chemical changes. Generally, an ideal electrolyte is inert to electrode substrates, and should have a wide electrochemical window to avoid electrolyte degradation from occurring within the potential range used during the experiment. The electrolyte has to be also a good ionic conductor and electronic insulator, to allow facile ion transport without self-discharging. Depending on the application of interest, a variety of electrolytes have been utilized in SMCM measurements, ranging from aqueous solutions,[15, 19, 27-28] to organic electrolytes,[25, 29-30] inorganic electrolytes,[31-32] ionic liquids,[26, 33-35] and in some cases, acid-based solutions.[36-37] For the investigation of LIB materials, the most commonly used electrolytes are carbonates or carbonate blends consisting of one or more of the following: PC, DEC, EMC, DMC (dimethyl carbonate) and ethylene carbonate (EC). Although these organic liquids are good for dissolving Li salts,[38] and have a relatively low viscosity required for Li-ion conductivity, they are flammable and volatile, and their use induces serious safety risks.[39-42] On the other hand, ionic liquids have been recently considered as alternative electrolytes for LIBs,[43-45] as they offer unique advantages over carbonate-based electrolytes, such as high oxidation potential, low vapor pressure, and high Li-salt solubility. Despite they are known to have high viscosities that reduce the activation energy for Li-ion diffusion, ionic liquids with imidazolium-based cations are considered promising candidates[46-49] for LIBs due to their lower viscosity and higher ionic conductivities compared to other ionic liquids.

Figure 2.1 represents the electrochemical responses of the three organic solvents that were tested: EMC, DEC, and PC, and the ionic liquid EMI TFSI.

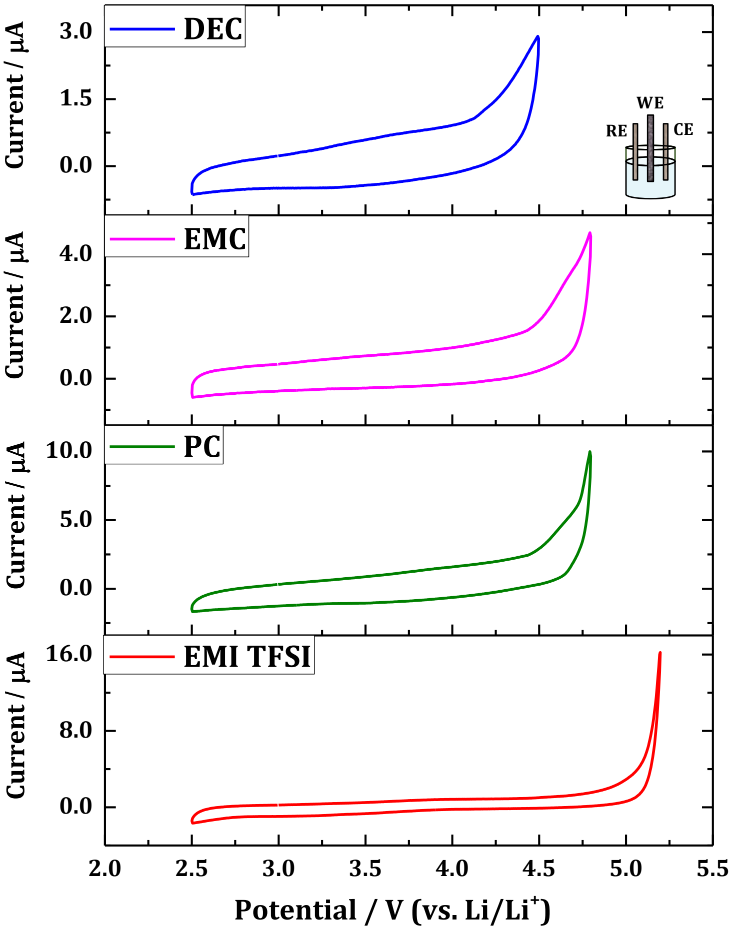

Figure 2.1: Cyclic voltammograms showing the potential window of 0.25 M $LiClO_4$ in DEC, EMC and PC organic electrolytes, and of 0.1 M LiTFSI in EMI TFSI ionic liquid. A three-electrode cell was used, where glassy carbon electrode served as the working electrode, and Li strips served as the reference and counter electrodes. The measurements were collected by sweeping the potential between 2.5 V and 5.2 V at a scan rate of 50 mV s^{-1}.

The measurements were performed in macroscopic three-electrode cell, where Li strips served as reference and counter electrodes, and glassy carbon as the working electrode. The three electrodes were immersed into $LiClO_4$ solution prepared by dissolving $LiClO_4$ salt in each of these organic electrolytes, and in LiTFSI solution in EMI TFSI ionic liquid. The cyclic voltammograms were recorded by sweeping the potential between 2.5 V and 5.2 V at a scan rate of 50 mV s^{-1}. The electrolyte potential window defines the potential range over which an electrolyte can be used for voltammetric/amperometric detection of electroactive species without undergoing significant chemical changes. A detectable change from the background current was obtained around 4.3 V vs. Li/Li^+ for DEC, compared to 4.6 V vs. Li/Li^+ for both EMC and PC, indicating that the respective electrolyte solutions are not stable beyond the stated potentials. As for ionic liquid, the oxidation limit was recorded at 5.1 V vs. Li/Li^+.

The choice of the electrolyte for the SMCM measurements depends on the oxidation and reduction potential limits of the active battery material being detected. For instance, in the case of LFP active material, the charging/discharging process of the Fe^{3+}/Fe^{2+} redox couple occurs at 3.7 V and 3.1 V vs. Li/Li^+ respectively,[50-52] which indicates that PC electrolyte is a good choice for the investigation of LFP. In contrast, for the lithium nickel manganese cobalt oxide (NMC) active material, the oxidation/reduction peaks of nickel appear at 3.99 and 3.58 V vs. Li/Li^+ and for cobalt at 4.71 and 4.54 V vs. Li/Li^+.[53] This indicates that the study of NMC requires electrolytes with extended potential window such as ionic liquids. Note that SMCM can be also implemented with more volatile solvents, since the high pressure inside the glove box makes the evaporation of solvent at the pipette/substrate interface less pronounced.

2.3.2 Identifying the Optimal Working Electrode

In the SMCM experimental setup, the substrate serves as the working electrode, and it has to be conductive in order to allow the redox reaction of the electroactive species to take place. Moreover, it has to be chemically stable in the electrolyte and within the range of the working potentials to avoid any side reactions. Different conducting substrates have been employed in SMCM for LIB applications, including gold,[25, 35, 54] Pt,[14, 31] glassy carbon,[26, 55] and in some cases battery composite films coated on aluminum current collector.[14-15] As for applications other than LIBs, HOPG,[19, 56-57] aluminum alloys,[19] indium tin oxide (ITO),[29, 58] and polycrystalline boron-doped diamond (pBDD)[27, 59] have been used.

In order to identify the suitable substrate for the SMCM measurements, the potential window of the selected electrolyte was tested using different working electrodes. Figure 2.2 represents the cyclic voltammetry measurements performed with 0.1 M LiTFSI in EMI TFSI using three-electrode cell, with Li strips serving as reference and counter electrodes, while gold, platinum or glassy carbon electrodes serving as the working electrode. The measurements on Au electrode showed an oxidation and a reduction peak occurring around 4.3 V vs. Li/Li$^+$, which was attributed to gold oxidation or stripping, followed by gold deposition during the reduction step. Examining the Pt electrode displayed an oxidation peak around 4.5 V, referred to formation of platinum oxide in the presence of a small amount of trace water.[60-61] On the other hand, measurements performed on glassy carbon substrate yields cyclic voltammetry with well-defined oxidation limit for the EMI TFSI ionic liquid around 5.1 V vs. Li/Li$^+$. The obtained results indicated that gold and platinum are suitable working substrates for testing low energy active material such as LFP, whereas the glassy carbon is a better choice for testing higher energy active material such as NMC.

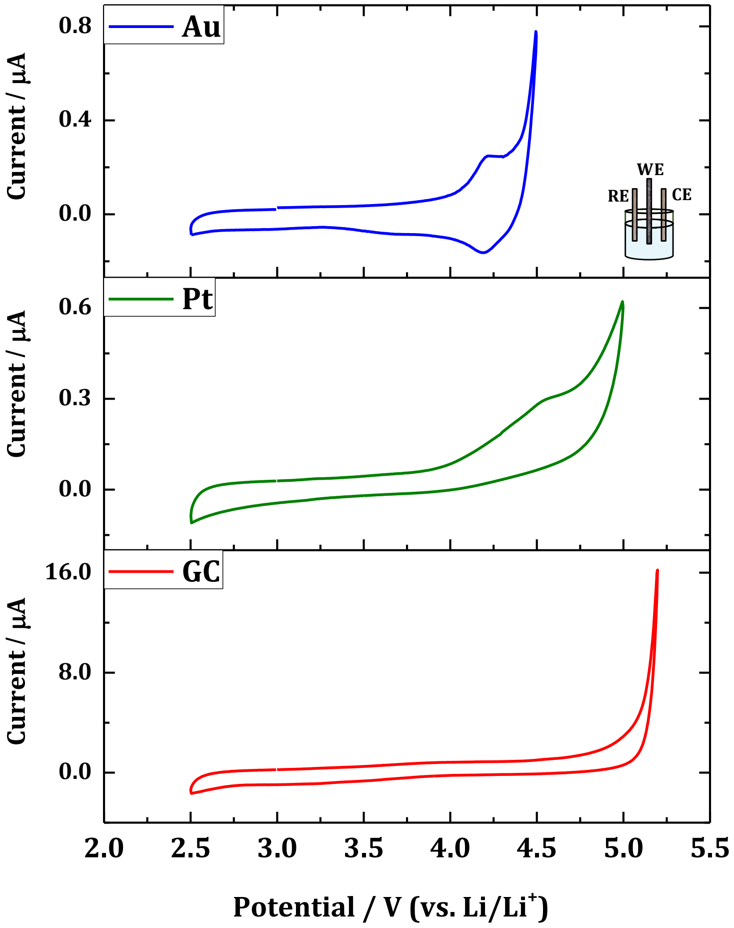

Figure 2.2: Cyclic voltammograms showing the potential window of 0.1 M LiTFSI in EMI TFSI solution using gold, platinum, and glassy carbon as working electrodes. A three-electrode cell was used, with Li strips serving as the reference and counter electrodes. The measurements were collected by sweeping the potential between 2.5 V and 5.2 V at a scan rate of 50 mV s^{-1}.

2.3.3 Calibration of Pipettes

Micropipettes were pulled from quartz capillaries using a laser-based puller, whereby a laser beam is focused on the glass capillary, thus heating it. When hot enough, quartz glass lights up and then separates quickly upon applying a certain pulling force. This results in two pipettes, with tiny and uniform tips. Importantly, the opening size of the pipette governs how big the electrolyte droplet on the surface will be. Therefore, it is essential to select the appropriate parameters that can control the geometry of the micropipette being fabricated. These include the heat, filament, velocity, delay and pulling force applied. The heat setting specifies the output power of the laser. Generally, higher heat settings tend to give longer and finer tips. The filament on the other hand specifies the scanning pattern of the laser beam that is used to supply heat to the glass, and it can also affect the time it takes to pull an electrode. Narrower filament means applying more power to the section of the glass being heated. The velocity value determines the point at which the heat is turned off, and reflects the speed at which the puller bar must be moving before the hard pull is executed. The delay parameter controls the time between when the heat turns off and the hard pull is activated. The longer the delay is, the cooler the glass will be when the hard pull occurs. Therefore, increasing the delay results in increased tip diameter and decreased taper length. The pulling force determines the strength of the hard pull, which is turned on after the programmed delay has elapsed. The higher the pull, the smaller the tip's diameter and the longer the taper.

For the SMCM measurements, the size of the pipette tip has to be adjusted based on the size of the particles of the active material being tested. Figure 2.3 represents the SEM images for the dispersion of the NMC and LFP active materials on glassy carbon substrate. The images clearly show that the size of LFP particles is smaller than that of NMC. The latter is forming kind of aggregates that are about 10 μm in diameter, compared to 1 μm particles in the case of LFP. This indicates that for the investigation of NMC, large pipettes with a diameter aperture of about 10 μm is required, whereas smaller pipettes (~1 μm tip diameter) would be suitable to study LFP.

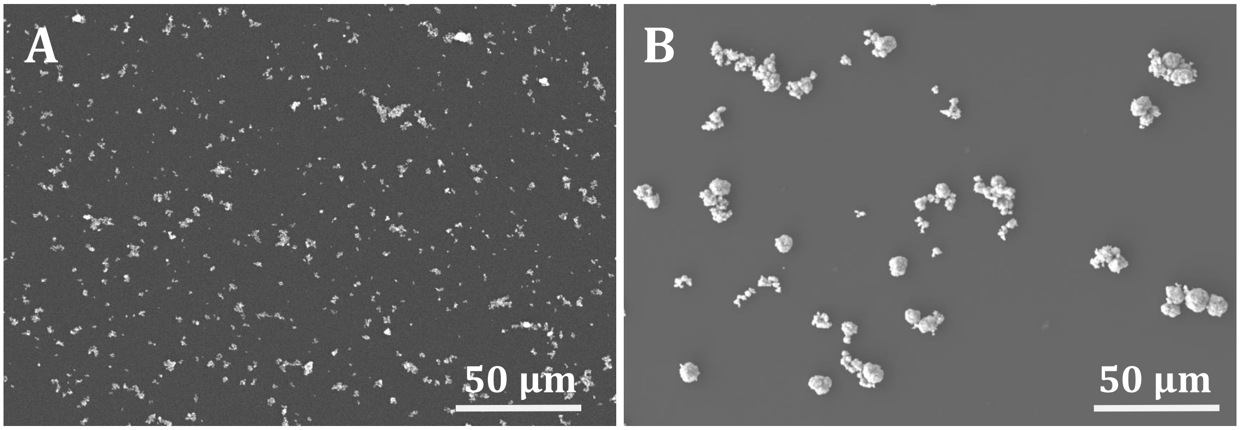

Figure 2.3: SEM images showing the dispersion of LFP (A) and NMC (B) active material obtained by drop casting an isopropanol suspension of particles (5 mg/mL) on a glassy carbon substrate.

After several trials, the final set of parameters that were selected to obtain pipettes of 1 µm and 10 µm tip diameter are reported in Table 2.1.

Table 2.1: The programmable parameters used on P-2000 laser-based micropipette puller to obtain small and large pipettes.

Parameters	**Heat**	**Filament**	**Velocity**	**Delay**	**Pull**
1 µm	585	2	30	130	50
10 µm	650	4	10	130	5

SEM imaging showing a horizontal and bottom view of the pulled pipettes with the two different sets of parameters is represented in Figure 2.4. The real tip diameter for the small and large pipettes is calculated from the SEM images to be 1.1 µm and 10.0 µm respectively.

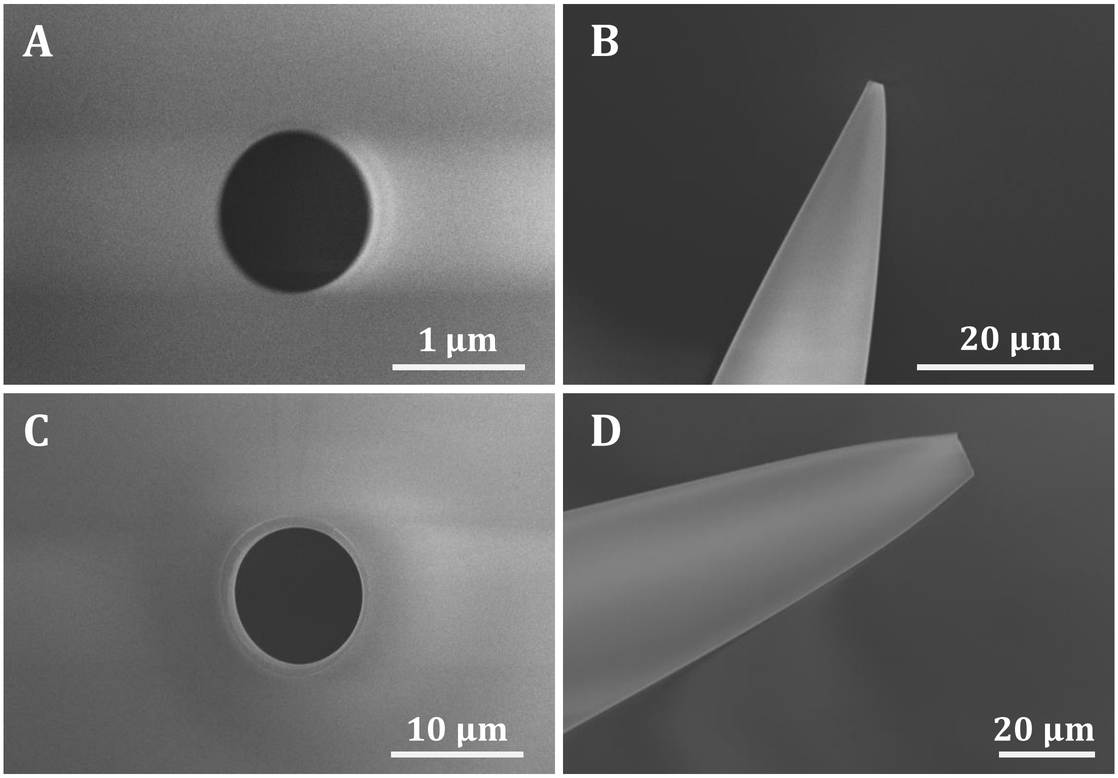

Figure 2.4: SEM bottom view images of the tip defining the aperture diameter of 1 µm pipette (A) and 10 µm pipette (C). SEM side view images of 1 µm pipette (B) and 10 µm pipette (D).

2.3.4 Droplet Stability

Maintaining a stable droplet during the SMCM measurements is very important to ensure reproducible contact area as the pipette moves across the substrate and to retain a constant tip to substrate distance . The droplet stability was confirmed using the redox mediator of MPT dissolved in the organic electrolyte PC. The diffusion coefficient of MPT was first determined using three-electrode cell with 1 mm diameter Au working electrode, and Li strips as reference and counter electrodes. Figure 2.5A shows the cyclic voltammetry measurements performed with 1 mM MPT in PC at different scan rates ranging between 500 mV s^{-1} to 5 mV s^{-1}. The redox potential was obtained around 3.6 V vs. Li/Li^+.

The peak currents, i_p, during anodic scans at different sweep rates were used to extract the diffusion coefficient, D, of MPT using the Randles-Sevcik equation:

$$i_p = 0.4463 \left(\frac{F^3}{RT}\right)^{1/2} n^{3/2}\, A D^{1/2} C \upsilon^{1/2} \tag{2.1}$$

where F is Faraday's constant, R the gas constant, T the absolute temperature, A the electrode area (cm^2), n the number of electrons involved in the redox process (1 in this case), C the bulk concentration of redox species (mol cm^{-3}), υ the potential scan rate (V s^{-1}), i_p in units of amperes and D is in units of cm^2 s^{-1}.

Figure 2.5B represents in set 1 the linear Randles–Sevcik plot (i_p *vs.* $\upsilon^{1/2}$) obtained from the cyclic voltammograms of Figure 2.5A. The measurements were then confirmed by another trial and the obtained results are shown in set 2. The diffusion coefficient of MPT was determined to be 1.3 x 10^{-6} cm^2 s^{-1}, which is similar to what has been previously reported.[62-63]

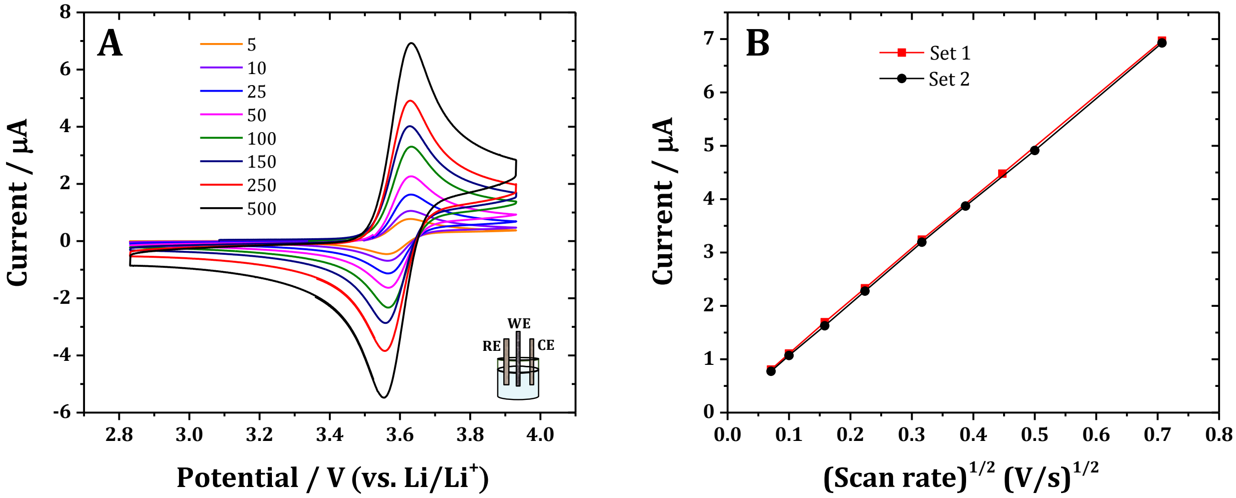

Figure 2.5: (A) Cyclic voltammograms showing the oxidation/reduction reaction of 1 mM MPT redox mediator in PC. A three-electrode cell was used, where gold electrode served as the working electrode, and Li strips served as the reference and counter electrodes. The measurements were collected by sweeping the potential between 2.8 V and 3.9 V at different scan rates. The legend corresponds to scan rate in mV s^{-1}. (B) Randles–Sevcik plot of peak current as a function of the square root of the scan rate for the cyclic voltammograms obtained in A (set 1) and for another trial (set 2).

Prior to use, the outer wall of the pipette was silanized to ensure a reasonable confinement of the protruding meniscus to the very end of the pipette.[64] In order to protect the internal walls of the capillary from coating, nitrogen gas was flushed through the pipette aperture during silanization. Figure 2.6 represents a horizontal and bottom view under SEM for silanized pipettes with 1 and 10 µm tip diameter. The outer wall of the pipette tip appears to be coated with silane, though not in a completely uniform manner. Appendix A (Figures A1-A4) compares the energy dispersive X-ray analysis (EDX) for 1 µm pipettes before and after silanization.

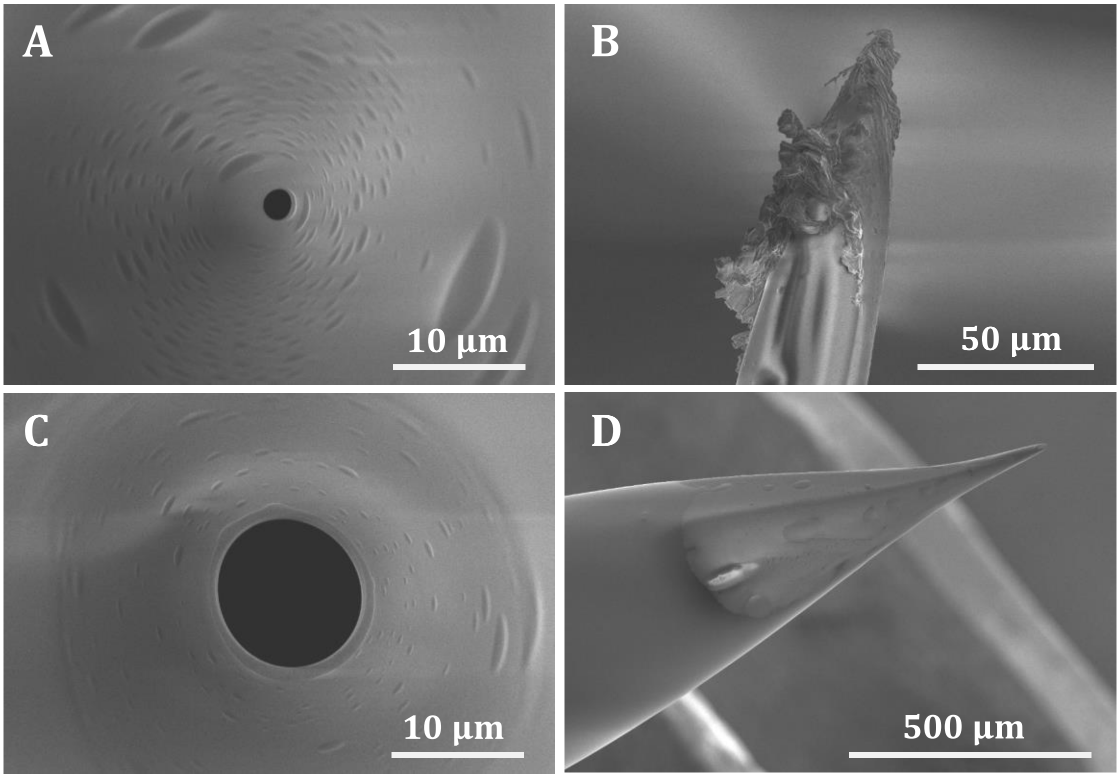

Figure 2.6: SEM bottom view images of the tip of 1 µm pipette (A) and 10 µm pipette (C) after silanization. SEM side view images of 1 µm pipette (B) and 10 µm pipette (D) after silanization.

To select the best silane for the SMCM experiments, cyclic voltammetry measurements were carried out using pipettes that were treated with different salinization agents: trichloro(methyl) silane (CH_3Cl_3Si), trichloro(hexyl) silane ($CH_3(CH_2)_5SiCl_3$), and trichloro(perfluorooctyl)silane ($(CF_3(CF_2)_5CH_2CH_2SiCl_3$. Measurements were performed at scan rate of 50 mV s^{-1} using 1 mM MPT solution in PC, with $Al_{1-x}Li_x$ serving as QRCE and gold serving as the working substrate. The electrochemical responses for MPT oxidation/reduction reaction obtained with pipettes before and after silanization are compared in Figure 2.7.

When the pipette was not silanized, the recorded anodic peak current was in the range of 200 pA. This corresponds to a contact area of ~20 µm in diameter, defined by the area of the droplet that is wetting the surface of the substrate. The contact area was estimated from the Randles-Sevcik equation using the diffusion coefficient of MPT calculated earlier. In contrast, upon silanizing the pipettes, a significant decrease in the current range was obtained for all the tested silanization agents, indicating a decrease in the wetting area. This confirms the importance of silanization to obtain a well-defined contact area. The lowest current was recorded for the trichloro(perfluorooctyl)silane, attributed to the hydrophobic characteristic of the alkyl fluorinated chain. The estimated contact area in this case was ~10 µm in diameter, which is the smallest among all other tested agents. Therefore, trichloro(perfluorooctyl)silane was selected for treating the pipettes before the SMCM measurements.

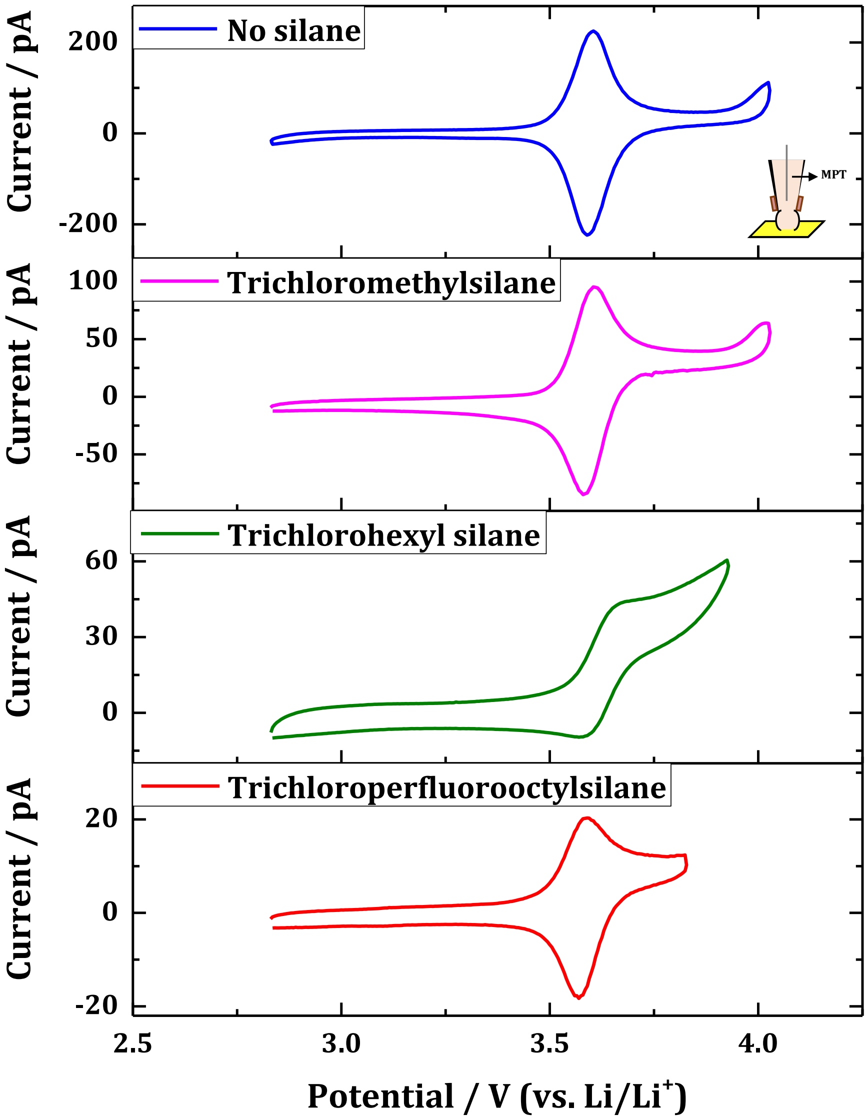

Figure 2.7: Cyclic voltammograms showing the oxidation/reduction reaction of 1 mM MPT redox mediator in PC using 1 µm micropipette silanized with different silanization agents. The measurements were collected on a gold substrate at a scan rate of 50 mV s^{-1}.

To examine the stability of the droplet in the micropipette technique, MPT was dissolved in the electrolyte being used in the SMCM measurements (PC or ionic liquid) and then introduced into a 1 μm silanized pipette. Several cyclic voltammograms were then performed on different points across the selected substrate. An example on the oxidation/reduction reaction of 10 mM of MPT solution prepared in the ionic liquid EMI TFSI is depicted in Figure 2.8. The measurements were repeated on three different landing points on a glassy carbon substrate (no active cathode material deposited onto the surface). The obtained data showed consistent cyclic voltammetry responses and a similar current range on different areas. The current was recovered when the droplet was retracted and placed in a different position. This demonstrates that for each measuring point a stable and reproducible contact area was created, which confirms electrochemical stability. Similar measurements performed in PC on gold substrate are reported in Appendix A (see Figure A5).

2.3.5 Fabrication of $Al_{1-x}Li_x$ QRCE

In SMCM, the pipette and the substrate constitute a microscopic electrochemical cell, where the working electrode is balanced by a single QRCE. This is considered reasonable as the generated current is very small (fA to nA), and significant polarization of the reference potential is negligible. In the case of higher currents, where ohmic effects or polarization of the QRCE are more likely to occur, a three-electrode SMCM setup can be used.[65] Typically, silver-chloride coated silver wire (Ag/AgCl),[14-15, 66] and palladium-hydrogen (Pd-H_2) electrode[27, 31, 67] are the most common QRCE employed in SMCM. For LIB applications, AlLi electrodes have gained a special interest.[65, 68-69] They are considered attractive alternatives to pure Li metals that cause dendritic deposition and corrosion,[70-72] which appears to be an adverse phenomenon encountered in the development of organic solvent-based rechargeable batteries. AlLi alloying works because:[73] (i) the alloy has more anodic potential which lessens the driving force for solution reduction; (ii) the lithium deposit is dissolved into the alloying substrate, thus making it less possible to undercut the deposit by reaction with the solution. The formation of AlLi alloy passes through two different phases, the α-phase containing ~7 atomic percent (a/o) of Li, and the β-phase with higher Li content in the range of 47 to 56 a/o Li. At room temperature, the potential of β-AlLi is in the range of 330-386 mV vs. Li.[74] Recently, AlLi electrode has been engaged in SMCM for the investigation of LFP active material using PC organic electrolyte[25] and EMI TFSI ionic liquid.[26] With the prolonged measurements of SMCM, a major consequence is the stability of the defined reference potential

(QRCE potential) in order to ensure the reliability of the collected data. As such, stability tests for Ag/AgCl[75] and AlLi electrodes have been reported.[26]

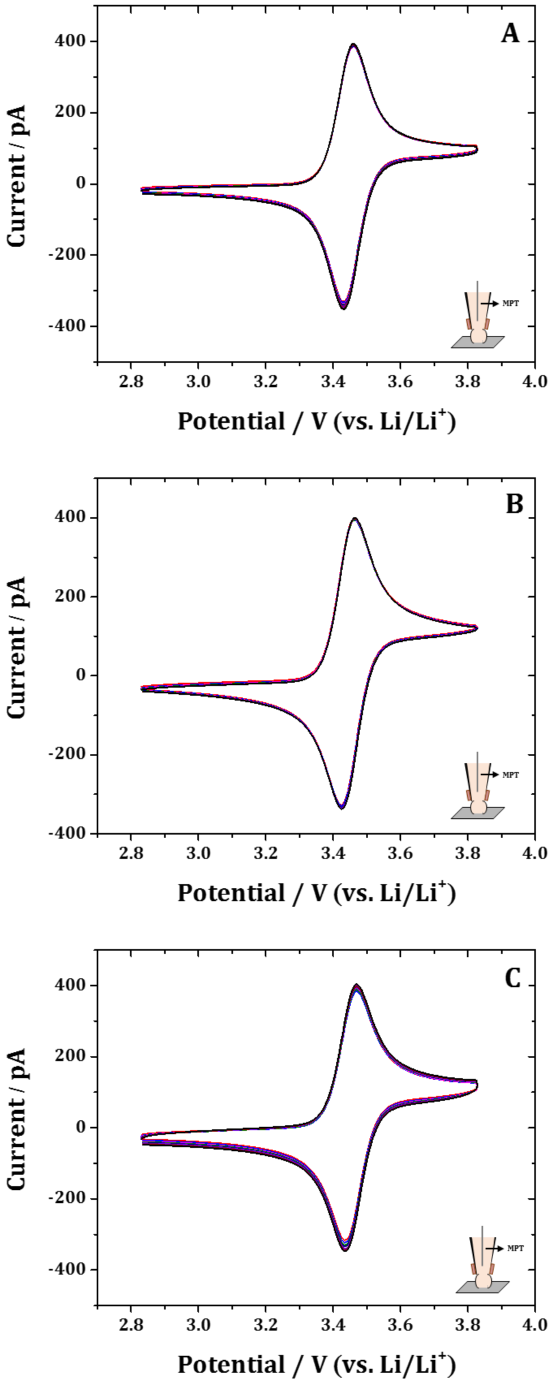

Figure 2.8: Cyclic voltammograms of the oxidation/reduction reaction of the 10 mM MPT redox mediator in EMI TFSI using the micropipette technique (first 5 cycles are shown). Measurement were recorded at three different locations across a glassy carbon substrate at a scan rate of 50 mV s^{-1}.

Herein, the fabrication of $Al_{1-x}Li_x$ QRCE was performed in a three-electrode cell using $LiClO_4$ solution in PC. A constant current was applied between the working electrode (Al wire) and the counter electrode (Li strip) for about one hour. A typical potential against time curve for the fabrication of the $Al_{1-x}Li_x$ QRCE is displayed in Figure 2.9A. Two stages during the reduction process may be distinguished. First, there is a rapid decrease in the potential; this is attributed to the charging of the double layer, and probably, reduction of the passivating layer on the Al electrode.[74] The following slow increase in the potential is connected to the nucleation process taking place to nucleate the new AlLi alloy phase in the Al electrode. The potential was 0.3 V during oxidation against Li/Li^+. The QRCE was then tested for stability by OCP measurements before carrying out electrochemical measurements (see Figure 2.9B). The potential of the $Al_{1-x}Li_x$ QRCE was recorded to be 0.33 V vs. Li/Li^+.

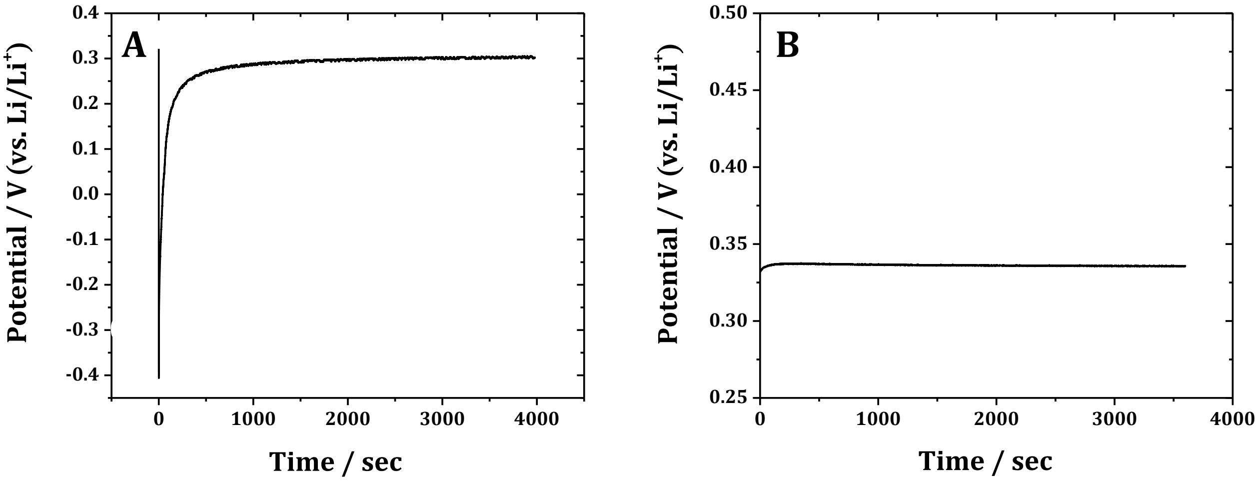

Figure 2.9: Potential against time transients at constant current for the electrode process $Al + Li^+ + 1e^- \rightleftarrows Li(Al)$ at an aluminum electrode in 0.25 M $LiClO_4$ solution in PC. The electrode potential was 0.3 V during oxidation vs. Li/Li^+ reference electrode in the same system (A). Open circuit potential of $Al_{1-x}Li_x$ QRCE measured in PC solution upon fabrication (B).

The $Al_{1-x}Li_x$ QRCE was further visualized on a micron scale using SEM. SEM images of the Al wire were taken before and after the fabrication of the QRCE electrode (see Figure 2.10). The thickness of the Al wire was shown to increase by about 10 μm as a result of the uniform Li deposition taking place. Importantly, the electrode maintained the same thickness even after using it for electrochemical measurements, as illustrated by the SEM images in Figure 2.10C, which were taken for the same QRCE after several hours of usage. However, the morphology of the electrode seems to be slightly altered, whereby a few patches are formed in some areas of the electrode. This might be attributed to the oxidation of Li taking place along the QRCE during the electrochemical measurements.

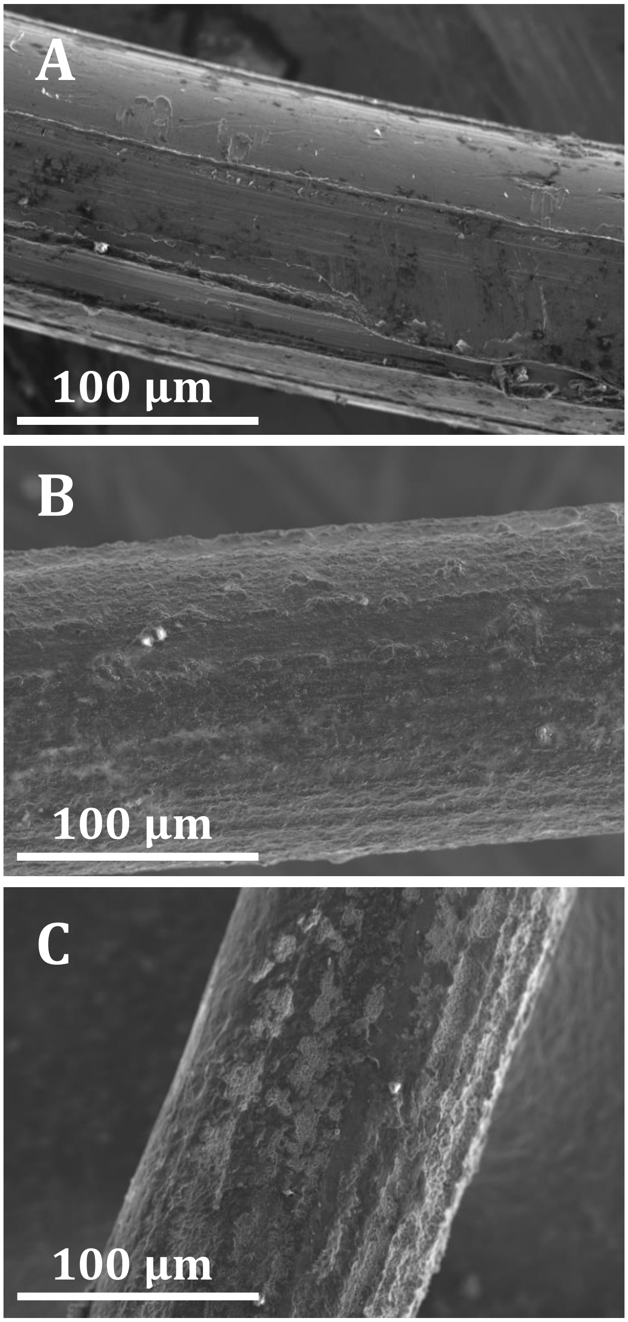

Figure 2.10: SEM imaging of Al wire with 125 µm diameter (A), $Al_{1-x}Li_x$ QRCE after the formation of Al-Li alloy galvanostatically (B), $Al_{1-x}Li_x$ QRCE after being used for electrochemical measurements (C).

To check if this slight change in the electrode morphology affect the stability of the $Al_{1-x}Li_x$ QRCE after being used for electrochemical measurements, the OCP measurements were repeated again for the same QRCE in two different electrolytes, PC and the ionic liquid EMI TFSI, after 24 hours of continuous usage. In both cases, a very small potential shift was obtained (less than 0.05 V), illustrating that the $Al_{1-x}Li_x$ QRCE had the stability needed for electrochemical SMCM measurements regardless of the electrolyte medium. The electrochemical responses for the OCP measurements are represented in Figure 4.2B of Chapter 4 in the thesis.

2.4 Conclusions

SMCM has proven to be a valuable technique for mapping the redox activity at LIB cathodes. The small dimensions of the micropipette used has the benefit of using lower volumes of electrolyte and smaller amounts of the active material studied, as compared to the conventional electrochemical cells. Besides, the possibility of addressing small areas using SMCM allows the electrochemical measurements to be performed on a micro to nanoscale, thereby achieving high spatial resolution imaging of the electroactive surface. By selecting the appropriate electrolyte and working electrode, choosing the suitable size of the pipette, and ensuring the stability of the QRCE in the utilized electrolyte and within the range of the working potential, the localized investigation of many LIB materials is possible. Importantly, applying SMCM in anaerobic conditions opens the possibility for investigating various active materials employed in LIBs, even if they do not operate within the water stability window. In addition, replacing the conventional organic electrolytes by ionic liquids extends the use of SMCM to higher oxidation potentials, which enables the investigation of higher energy active materials.

2.5 References

1.Paik, C.; White, H.; Alkire, R. *Journal of the electrochemical society* **2000,** 147, (11), 4120-4124.

2.Niu, L.; Yin, Y.; Guo, W.; Lu, M.; Qin, R.; Chen, S. *Journal of Materials Science* **2009,** 44, (17), 4511-4521.

3.Lee, J.; Ye, H.; Pan, S.; Bard, A. J. *Analytical Chemistry* **2008,** 80, (19), 7445-7450.

4.Ye, H.; Lee, J.; Jang, J. S.; Bard, A. J. *The Journal of Physical Chemistry C* **2010,** 114, (31), 13322-13328.

5.Eckhard, K.; Chen, X.; Turcu, F.; Schuhmann, W. *physical chemistry chemical physics* **2006,** 8, (45), 5359-5365.

6.Fernández, J. L.; Walsh, D. A.; Bard, A. J. *Journal of the American Chemical Society* **2005,** 127, (1), 357-365.

7.Zeradjanin, A. R.; Ventosa, E.; Bondarenko, A. S.; Schuhmann, W. *ChemSusChem* **2012,** 5, (10), 1905-1911.

8.Bertoncello, P. *Energy & Environmental Science* **2010,** 3, (11), 1620-1633.

9.Neufeld, A. K.; O'Mullane, A. P.; Bond, A. M. *Journal of the American Chemical Society* **2005,** 127, (40), 13846-13853.

10.Mirkin, M. V.; Horrocks, B. R. *Analytica Chimica Acta* **2000,** 406, (2), 119-146.

11.Xu, F.; Beak, B.; Jung, C. *Journal of Solid State Electrochemistry* **2012,** 16, (1), 305-311.

12.Snook, G. A.; Huynh, T. D.; Hollenkamp, A. F.; Best, A. S. *Journal of Electroanalytical Chemistry* **2012,** 687, 30-34.

13.Barton, Z. J.; Rodríguez-López, J. n. *Analytical chemistry* **2014,** 86, (21), 10660-10667.

14.Takahashi, Y.; Kumatani, A.; Munakata, H.; Inomata, H.; Ito, K.; Ino, K.; Shiku, H.; Unwin, P. R.; Korchev, Y. E.; Kanamura, K. *Nature communications* **2014,** 5, 5450.

15.Kumatani, A.; Takahashi, Y.; Miura, C.; Ida, H.; Inomata, H.; Shiku, H.; Munakata, H.; Kanamura, K.; Matsue, T. *Surface and Interface Analysis* **2019,** 51, (1), 27-30.

16.Lipson, A. L.; Ginder, R. S.; Hersam, M. C. *Advanced Materials* **2011,** 23, (47), 5613-5617.

17.Zampardi, G.; La Mantia, F.; Schuhmann, W. *RSC Advances* **2015,** 5, (39), 31166-31171.

18.Yang, D.; Han, L.; Yang, Y.; Zhao, L. B.; Zong, C.; Huang, Y. F.; Zhan, D.; Tian, Z. Q. *Angewandte Chemie* **2011,** 123, (37), 8838-8841.

19.Williams, C. G.; Edwards, M. A.; Colley, A. L.; Macpherson, J. V.; Unwin, P. R. *Analytical chemistry* **2009,** 81, (7), 2486-2495.

20.Assi, F.; Böhni, H. *Wear* **1999,** 233, 505-514.

21.Hassel, A.; Lohrengel, M. *Electrochimica Acta* **1997,** 42, (20-22), 3327-3333.

22.Lohrengel, M.; Moehring, A.; Pilaski, M. *Electrochimica Acta* **2001,** 47, (1-2), 137-141.

23.Dudin, P. V.; Unwin, P. R.; Macpherson, J. V. *The Journal of Physical Chemistry C* **2010,** 114, (31), 13241-13248.

24.Day, T. M.; Unwin, P. R.; Macpherson, J. V. *Nano Letters* **2007,** 7, (1), 51-57.

25.Snowden, M. E.; Dayeh, M.; Payne, N. A.; Gervais, S.; Mauzeroll, J.; Schougaard, S. B. *Journal of Power Sources* **2016,** 325, 682-689.

26.Dayeh, M.; Ghavidel, M. Z.; Mauzeroll, J.; Schougaard, S. B. *ChemElectroChem* **2019,** 6, (1), 195-201.

27.Patten, H. V.; Lai, S. C.; Macpherson, J. V.; Unwin, P. R. *Analytical chemistry* **2012,** 84, (12), 5427-5432.

28.Liu, D. Q.; Chen, C. H.; Perry, D.; West, G.; Cobb, S. J.; Macpherson, J. V.; Unwin, P. R. *ChemElectroChem* **2018,** 5, (20), 3028-3035.

29.Gasiorowski, J.; Mardare, A. I.; Sariciftci, N. S.; Hassel, A. W. *Journal of Electroanalytical Chemistry* **2013,** 691, 77-82.

30.Kollender, J. P.; Gasiorowski, J.; Sariciftci, N. S.; Mardare, A. I.; Hassel, A. W. *The Journal of Physical Chemistry C* **2014,** 118, (30), 16919-16926.

31.Chen, C.-H.; Jacobse, L.; McKelvey, K.; Lai, S. C. S.; Koper, M. T. M.; Unwin, P. R. *Analytical Chemistry* **2015,** 87, (11), 5782-5789.

32.Sharel, P.; Kim, Y.-R.; Perry, D.; Bentley, C. L.; Unwin, P. R. *ACS applied materials & interfaces* **2016,** 8, (44), 30458-30466.

33.Aaronson, B. D.; Lai, S. C.; Unwin, P. R. *Langmuir* **2014,** 30, (7), 1915-1919.

34.Aaronson, B. D.; Byers, J. C.; Colburn, A. W.; McKelvey, K.; Unwin, P. R. *Analytical chemistry* **2015,** 87, (8), 4129-4133.

35.Aaronson, B. D.; Garoz-Ruiz, J.; Byers, J. C.; Colina, A.; Unwin, P. R. *Langmuir* **2015,** 31, (46), 12814-12822.

36.Parker, A. S.; Patel, A. N.; Al Botros, R.; Snowden, M. E.; McKelvey, K.; Unwin, P. R.; Ashcroft, A. T.; Carvell, M.; Joiner, A.; Peruffo, M. *Journal of dentistry* **2014,** 42, S21-S29.

37.Parker, A. S.; Al Botros, R.; Kinnear, S. L.; Snowden, M. E.; McKelvey, K.; Ashcroft, A. T.; Carvell, M.; Joiner, A.; Peruffo, M.; Philpotts, C. *Journal of colloid and interface science* **2016,** 476, 94-102.

38.Xu, K. *Chemical reviews* **2004,** 104, (10), 4303-4418.

39.Ribière, P.; Grugeon, S.; Morcrette, M.; Boyanov, S.; Laruelle, S.; Marlair, G. *Energy & Environmental Science* **2012,** 5, (1), 5271-5280.

40.Chen, M.; Yuen, R.; Wang, J. *Journal of Thermal Analysis and Calorimetry* **2017,** 129, (1), 181-188.

41.Chen, M.; Zhou, D.; Chen, X.; Zhang, W.; Liu, J.; Yuen, R.; Wang, J. *Journal of Thermal Analysis and Calorimetry* **2015,** 122, (2), 755-763.

42.Liu, X.; Wu, Z.; Stoliarov, S. I.; Denlinger, M.; Masias, A.; Snyder, K. *Fire Safety Journal* **2016,** 85, 10-22.

43.Ohno, H., *Electrochemical aspects of ionic liquids*. John Wiley & Sons: 2005.

44.Lewandowski, A.; Świderska-Mocek, A. *Journal of Power Sources* **2009,** 194, (2), 601-609.

45.Balducci, A.; Jeong, S.; Kim, G.; Passerini, S.; Winter, M.; Schmuck, M.; Appetecchi, G.; Marcilla, R.; Mecerreyes, D.; Barsukov, V. *Journal of power sources* **2011,** 196, (22), 9719-9730.

46.Garcia, B.; Lavallée, S.; Perron, G.; Michot, C.; Armand, M. *Electrochimica Acta* **2004,** 49, (26), 4583-4588.

47.Seki, S.; Kobayashi, Y.; Miyashiro, H.; Ohno, Y.; Usami, A.; Mita, Y.; Kihira, N.; Watanabe, M.; Terada, N. *The Journal of Physical Chemistry B* **2006,** 110, (21), 10228-10230.

48.Ferrari, S.; Quartarone, E.; Tomasi, C.; Ravelli, D.; Protti, S.; Fagnoni, M.; Mustarelli, P. *Journal of Power Sources* **2013,** 235, 142-147.

49.Swiderska-Mocek, A. *Electrochimica Acta* **2014,** 132, 504-511.

50.Tang, K.; Yu, X.; Sun, J.; Li, H.; Huang, X. *Electrochimica Acta* **2011,** 56, (13), 4869-4875.

51.Huang, Y. H.; Wang, F. M.; Huang, T. T.; Chen, J. M.; Hwang, B. J.; Rick, J. *International Journal of Electrochemical Science* **2012,** 7, (2), 1205-1213.

52.Mi, C. H.; Zhang, X. G.; Li, H. L. *Journal of Electroanalytical Chemistry* **2007,** 602, (2), 245-254.

53.Wu, F.; Wang, M.; Su, Y.; Bao, L.; Chen, S. *Journal of Power Sources* **2010,** 195, (8), 2362-2367.

54.Ebejer, N.; Schnippering, M.; Colburn, A. W.; Edwards, M. A.; Unwin, P. R. *Analytical chemistry* **2010,** 82, (22), 9141-9145.

55.Bentley, C. L.; Unwin, P. R. *Faraday discussions* **2018,** 210, 365-379.

56.Snowden, M. E.; Güell, A. G.; Lai, S. C. S.; McKelvey, K.; Ebejer, N.; O'Connell, M. A.; Colburn, A. W.; Unwin, P. R. *Analytical Chemistry* **2012,** 84, (5), 2483-2491.

57.Lai, S. C.; Patel, A. N.; McKelvey, K.; Unwin, P. R. *Angewandte Chemie International Edition* **2012,** 51, (22), 5405-5408.

58.Zhan, D.; Yang, D.; Zhu, Y.; Wu, X.; Tian, Z.-Q. *chemical communications* **2012,** 48, (93), 11449-11451.

59.Wu, S.-L.; Zhang, W.; Song, X.; Shukla, A. K.; Liu, G.; Battaglia, V.; Srinivasan, V. *Journal of The Electrochemical Society* **2012,** 159, (4), A438-A444.

60.Silvester, D. S.; Aldous, L.; Hardacre, C.; Compton, R. G. *The Journal of Physical Chemistry B* **2007,** 111, (18), 5000-5007.

61.Chi, X.; Tang, Y.; Zeng, X. *Electrochimica Acta* **2016,** 216, 171-180.

62.Moshurchak, L. M.; Buhrmester, C.; Wang, R. L.; Dahn, J. R. *Electrochimica Acta* **2007,** 52, (11), 3779-3784.

63.Buhrmester, C.; Moshurchak, L.; Wang, R. L.; Dahn, J. *Journal of The Electrochemical Society* **2006,** 153, (2), A288-A294.

64.Shao, Y.; Mirkin, M. V. *Analytical Chemistry* **1998,** 70, (15), 3155-3161.

65.Mariano, R. G.; McKelvey, K.; White, H. S.; Kanan, M. W. *Science* **2017,** 358, (6367), 1187-1192.

66.Chen, C.-H.; Ravenhill, E. R.; Momotenko, D.; Kim, Y.-R.; Lai, S. C. S.; Unwin, P. R. *Langmuir* **2015,** 31, (43), 11932-11942.

67.Lai, S. C. S.; Dudin, P. V.; Macpherson, J. V.; Unwin, P. R. *Journal of the American Chemical Society* **2011,** 133, (28), 10744-10747.

68.Besenhard, J. O.; Hess, M.; Komenda, P. *Solid State Ionics* **1990,** 40-41, 525-529.

69.Rao, B. M. L.; Francis, R. W.; Christopher, H. A. *Journal of The Electrochemical Society* **1977,** 124, (10), 1490-1492.

70.Besenhard, J. O.; Eichinger, G. *Journal of Electroanalytical Chemistry and Interfacial Electrochemistry* **1976,** 68, (1), 1-18.

71.Orsini, F.; du Pasquier, A.; Beaudouin, B.; Tarascon, J. M.; Trentin, M.; Langenhuizen, N.; de Beer, E.; Notten, P. *Journal of Power Sources* **1999,** 81-82, 918-921.

72.Dollé, M.; Sannier, L.; Beaudoin, B.; Trentin, M.; Tarascon, J.-M. *Electrochemical and Solid-State Letters* **2002,** 5, (12), A286-A289.

73.Hughes, M.; Hampson, N. A.; Karunathilaka, S. A. G. R. *Journal of Power Sources* **1984,** 12, (2), 83-144.

74.Baranski, A. S.; Fawcett, W. R. *Journal of The Electrochemical Society* **1982,** 129, (5), 901-907.

75.Bentley, C. L.; Perry, D.; Unwin, P. R. *Analytical Chemistry* **2018,** 90, (12), 7700-7707.

Chapter 3

Measurement on Isolated Lithium Iron Phosphate Particles Reveals Heterogeneity in Material Properties Distribution

Chapter 2 focused on the development of scanning droplet technique for localized measurement of battery active materials in an inert atmosphere. The proposed technique employs micron probes to investigate key properties of battery material such as capacity, efficiency, and local heterogeneities. Chapter 3 demonstrates the first successful measurements on isolated LFP active material using the SMCM technique. Localized galvanostatic and potentiodynamic measurements were performed on a small substrate areas (~10 µm diameter) using a carbonate solution. Complementary scanning electron microscopy images compared the quantity and the size of the particles present in the scanned area to the electrochemical responses. Under favorable conditions, individual nano-particles were successfully examined, which validates the ability of this technique to determine the properties of air-sensitive active battery material down to the single particle level, without the additional complications arising from the presence of binders and electronically conductive fillers. Results collected by SMCM were compared to results from coin cell measurements in order to assess the similarities between individual particle responses and bulk electrode. This comparison also determines the applicability of SMCM as a tool for investigating individual active material particles for LIB positive electrodes. The obtained results revealed heterogeneous electrochemical responses for isolated primary particles and agglomerates, showing that not all active particles within a batch have uniform properties. The ability to analyze the active material with complementary experimental techniques at a small scale is of significant benefit for fundamental studies and for the quality control during the manufacture of active materials.

The work presented in this chapter was previously published and is reproduced from:

Snowden, M. E.; Dayeh, M.; Payne, N. A.; Gervais, S.; Mauzeroll, J.; Schougaard, S. B., *Journal of Power Sources* **2016,** *325*, 682-689.

3.1 Introduction

Lithium-ion batteries (LIBs) are a commercial success, providing reusable energy storage for portable electronics. Recently, automobiles using LIBs as an alternative to the internal combustion engine or as a hybrid system are commercially available. Research into how to increase the energy capacity, decrease recharge times, and increase the lifetime of a battery are areas of academic and industrial importance.[1]

Among the various cathode materials available for LIBs, lithium iron phosphate (LFP) has been intensively studied due to its stable potential profile during charge and discharge, high reversibility, and reasonable theoretical capacity (170 mA h g^{-1}).[2-3] However, there is a large debate on the fundamental electrochemical and physical mechanisms underlying the operation of LFP, with several proposed reaction pathways.[4-6] A major difficulty when probing the reactions and intrinsic properties of LIB active materials are heterogeneities within the porous cathode thick film (10-100 μm). Typically, the cathode is cast from a slurry, or ink, which contains 85-95 wt% active material (e.g. LFP, $LiCoO_2$, etc. for positive electrodes, and graphite, silicon, etc. for negative electrodes), and the balance of 5-15 wt% is a mixture of electronically conductive filler (most often carbon) and a polymeric binder (e.g. polyvinylidene fluoride) to mechanically stabilize the film.[7-9] However, data from these techniques convolute the responses from all active material particles in the electrode, thus providing information about their average properties. Moreover, the way the film is cast and dried, the ratio of the individual components within the film, and the final assembly of the coin cell can significantly alter the performance of the battery. For instance, a relatively high resistance of the electrolyte-filled pores in the film, and the finite thickness cause electrochemical potential gradients across the composite film.[10-11] Also mass transport within the porous film is hindered, and coating on the surface of active particles considerably affect the overall cell performance as well.[12-13] Therefore, deriving fundamental properties requires the deconvolution of contributions caused by conductivity within the film and mass transport in the electrolyte and within the active particles. Given these complications, it is unsurprising that intrinsic properties, such as the diffusion coefficient of Li-ions within an LFP particle has been reported with widely varying values of 10^{-18} to 10^{-12} cm^2 s^{-1}.[14]

Experimental studies to probe the LFP reaction mechanism have been performed using simultaneous spectroscopic and electrochemical measurements. *Ex-situ* spectroscopy techniques including; X-Ray diffraction (XRD),[15-16] Raman spectrometry,[17] and transmission scanning electron microscopy,[18] as well as *in-situ* studies using XRD,[19-21] or neutron powder diffraction[22] have been used to investigate crystal structure transformations during the charge and discharge of LFP. However, these techniques are typically performed on composite electrodes, which have non-uniform lithium distribution due to inhomogeneous reaction environment. Therefore, they cannot easily isolate the mass transport, reactivity and conduction contributions. One approach to study the reaction properties of LFP while ensuring that the surface of all particles in the sample experiences the same chemical potential was to perform chemical oxidation and reduction, where the driving chemical force was delivered to the particle surface by reactive solution species.[23-24] Data from these tests, however, represent the total response from all active material particles in the electrode and can only provide average properties for the active material particles. As such, the development of localized electrochemical probes to investigate the fundamental properties of active battery materials in battery relevant environments is required.

Recently, high-resolution electrochemical microscopy techniques have been utilized in screening localized properties and reactivity of a wide variety of electrode surfaces. The influence of forming the SEI layer upon the surface of a graphite electrode, and how this reduced the rate of lithium (de)intercalation reactions was probed by scanning electrochemical microscope (SECM).[25] The variation in the local reactivity of Li-ions at a gold surface was also investigated using mercury capped microelectrodes for stripping voltammetry.[26] In another study, a scanning micropipette technique was employed to probe LFP using an aqueous electrolyte,[27] demonstrating localized electrochemistry on films and particles. However, the oxidation of LFP was obscured by the aqueous solvent window.[28] For commercial applications, one critical feature of an active material is the charge per volume of particles, and the behavior of isolated particles compared to clusters, which has not been addressed previously with a scanning electrochemical techniques.

We present herein a methodology for examining the electrochemical behavior of isolated active material particles, down to the single particle level. As a proof-of-concept experiment, LFP particles were dispersed on gold substrate and investigated electrochemically by means of the scanning micropipette contact method (SMCM).[29] When positioned in a close proximity to the substrate, a micropipette with 1 um tip diameter delivered a solution of $LiClO_4$ in propylene carbonate (PC) to wet both the particles and the substrate. The area of the working electrode was defined by the area of the substrate wetted by the electrolyte. $Al_{1-x}Li_x$ quasi-reference counter electrode (QRCE) was inserted into the barrel of the capillary to complete the electrochemical circuit. Localized galvanostatic and potentiodynamic measurements were performed on a micron-scale level. Scanning electron microscopy was then employed to characterize the particles within the tested area. This complementary measurement technique allowed the quantity and the volume of particles to be correlated to the electrochemical responses. In order to demonstrate the viability of this technique for interpreting electrochemical properties, the obtained results were compared to coin cell measurements in an attempt to evaluate the similarities between individual particle responses and bulk electrode. Our study revealed heterogeneous electrochemical responses for isolated primary particles and agglomerates, showing that not all particles within a batch are created equally. This technique provides significant interest for fundamental characterization and investigations of electrochemical properties for air-sensitive active battery material, as well as a quality testing of film composition, casting methodologies, developing synthetic procedures and for quality control during the manufacture of active materials.

3.2 Experimental Section

3.2.1 Coin Cells Measurements

The electrochemical performance of the commercial LFP (carbon coated) was determined with CR2032-type coin cells assembled in an Argon atmosphere using metallic lithium (Alfa Aesar 99.9%) as the anode. The positive electrode was prepared by coating a suspension of 85 wt % LFP, 10 wt % acetylene black (Super C5, TimCal) and 5 wt % polyvinylidene fluoride (Kynar) in N-methyl-2-pyrrolidone (99% Sigma Aldrich) on Al current collector (Exopack). The slurry was subsequently dried at 60 °C under reduced pressure overnight to yield a thickness of 25 μm. 1 M $LiPF_6$ in 1:1 ethylene carbonate/dimethyl carbonate (EC:DMC, Novalyte Technologies) electrolyte and Celgard 2500 separator were used (Figure 3.1A). Electrochemical testing was performed by galvanostatic cycling with a Bio-Logic VMP3 potentiostat.

3.2.2 SMCM Measurements

The schematic of the SMCM experimental setup is represented in Figure 3.1B. Micropipettes with a 1 µm tip diameter were pulled from quartz capillaries (0.3 mm inner diameter and 1.0 mm outer diameter (Sutter Instruments)), using a laser puller (Model P-2000 Sutter Instruments). The tips were made hydrophobic using perfloro-octyl silane (Sigma Aldrich). The $Al_{1-x}Li_x$ QRCE was fabricated galvanostatically in 0.1 M $LiClO_4$ solution in propylene carbonate (PC 99.7% Sigma Aldrich) using a three-electrode cell; an Al wire (250 µm diameter, Goodfellow) served as the working electrode, and two Li metal strips as counter and reference electrodes. The stability of the $Al_{1\_x}Li_x$ QRCE was tested by open circuit potential measurements (E = 0.330 V vs. Li/Li^+). Gold substrates were fabricated by evaporating 10 nm of Cr as an adhesion layer followed by a 200 nm of Au layer onto a borosilicate slide. LFP particles were drop-cast onto the gold substrate from an acetonitrile solution (0.1 mg/mL) and then allowed to dry at room temperature.

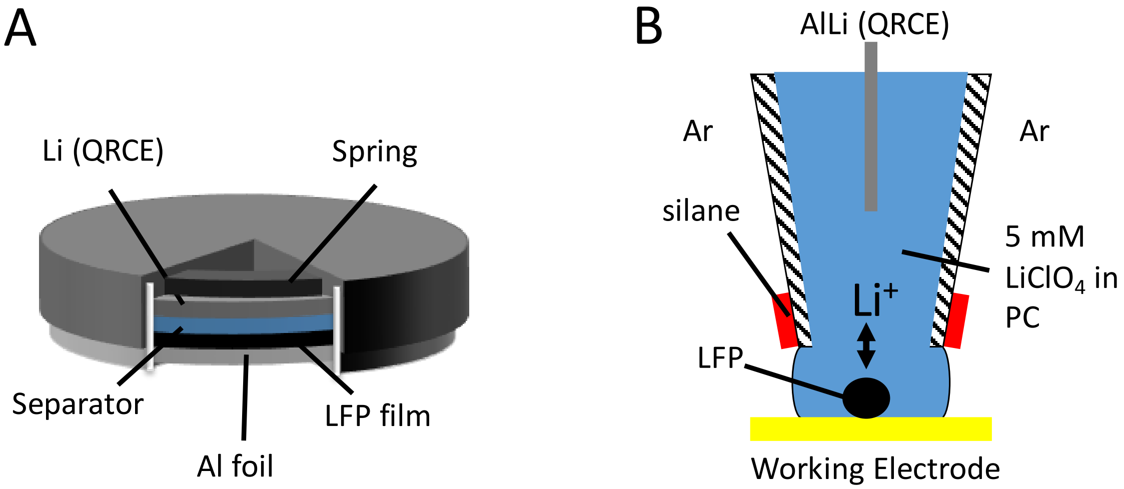

Figure 3.1: Schematics of (A) a coin cell and (B) the micropipette cell. Neither to scale.

SMCM measurements were performed on an ElPro Scan 3 (HEKA Electronics, Germany) inside an Argon filled glovebox (MBraun, USA) with a water and oxygen content of less than 1 ppm. The ElPro Scan 3 offers a galvanostatic current accuracy of ±6 fA confirmed using a commercial dummy cell provided by the manufacturer. The gold substrate was decorated with LFP particles and used as the working electrode. The pipette was filled with 5 mM $LiClO_4$ solution in PC, and the $Al_{1-x}Li_x$ QRCE was then inserted into the barrel of the pipette. Using piezo controls of ElPro Scan 3 instrument, the pipette was lowered towards the gold substrate at a 1 µm s^{-1} approach rate while a potential of 2.5 V was applied. When the lower meniscus of the droplet protruding out of the pipette wetted the surface, an electrical circuit between the working electrode and the QRCE was created. This resulted in current spike that was used as a signal to halt the descent of the pipette. This ensured that the pipette did not directly contact the substrate surface or any active material particle dispersed on it. Galvanostatic and potentiometric measurements were performed at different scan rates, before retracting the pipette 100 µm from the substrate surface. Note that the potential scale was reported with respect to Li/Li^+ within this article, for the ease of comparison to existing LFP literature. After a series of electrochemical measurements over the same landing point, the pipette was translated to a new location measurements to form a 6x6 point scan, with 20 µm spacing in both the *x* and *y* directions. When the scans were completed, the tip was deliberately crashed on the substrate in a predefined pattern to facilitate alignment in subsequent analysis. The scanned area was then visualized by scanning electron microscopy (Hitachi SU3500 VP-SEM). Montage images were captured using the AZtec software package (Oxford), and particle areas were measured using the ImageJ software.

3.3 Results and Discussion

3.3.1 Galvanostatic Measurements

Figure 3.1 represents the similarities and the differences between the coin cell and SMCM setups. In the case of the coin cell, active battery material was drop-cast onto an Al current collector to from a 25 µm thick working electrode, whereas for the case of SMCM, gold current collector was decorated with a sub monolayer of active material dispersed onto the surface. The main difference between both electrochemical experimental setups is the capability of the SMCM technique to measure isolated particles in the absence of any polymeric binder or electronically conductive carbon filler, which are essential for the proper functioning of the electrode in the coin cell. The area of the working electrode was defined by the stable droplet wetting the surface (~10 µm in diameter), as opposed to the whole composite film being probed in the coin cell. In both electrochemical cells, the same role was performed by the QRCEs. In the micropipette technique however, an $Al_{1-x}Li_x$ alloy with a potential of 0.330 V vs. Li/Li$^+$ was utilized as the QRCE, compared to the Li metal in the coin cell. A polymer membrane was used to physically separate the working electrode from the QRCE in the case of the coin cell, whereas in the SMCM, this separation was maintained by the distance of the $Al_{1-x}Li_x$ QRCE from the pipette tip and tip-to substrate distance (~0.5 μm). Hence, both techniques provide similar electrochemical environments for the investigation of LFP oxidation/reduction process (Equation (3.1)):

$$FePO_4 + Li^+ + e^- \rightleftarrows LiFePO_4 \tag{3.1}$$

Figure 3.2 compares galvanostatic measurements obtained by SMCM and by coin cell. The SMCM cyclic data were collected using PC solution containing 5 mM $LiClO_4$, along with an $Al_{1-x}Li_x$ QRCE, and a constant current of 1 pA and -1 pA for LFP oxidation and reduction respectively. During oxidation, the potential vs. time response (Figure 3.2A) revealed a sharp rise in potential for $t < 1$ s, peaking at $t = 2.8$ s, then slightly decreasing until $t = 20$ s. Importantly, a similar trend was observed in the coin cell measurements (Figure 3.2B) at 5C rate and higher. There are several theories for the occurrence of the peak at the beginning of the charge cycle including phase separation of sites saturated with lithium and without lithium, and transport limitations in the particle or in the solution.[4-6] For times 20 s < t < 50 s, a gradual increase in potential was recorded, suggesting an increase in required energy to remove lithium from the LFP particle as the lithium content decreases. For times $t > 50$ s, a rapid increase in the potential was obtained, indicating that it is not possible to remove Li-ions from the material during this galvanostatic cycle anymore.

Figure 3.2B represents the charge/discharge curves recorded at different rates in a coin cell. A charge rate of C took 1 hour to fully charge or discharge the cell, and 60C was performed at a rate that required 1 minute. It is noticeable that as the rate of charge and discharge increases, the capacity of the coin cell tends to decrease, in addition, the splitting of the potential for charge and discharge becomes more significant due to resistance within the battery and higher applied currents. SEM images of the area measured by the micropipette technique (Figure 3.2C) and a typical area of a cast battery film (Figure 3.2D) show the structure of the two surfaces. For the SMCM measurement, a small agglomerate of battery active material particles, dispersed on Au surface, was present within the area wetted by the droplet. Note here that Au was stable within the potential range measured without supporting the oxidation and reduction of Li-ions. In contrary, the battery film was a mixture of LFP active particles, carbon conductor and polymer binder.

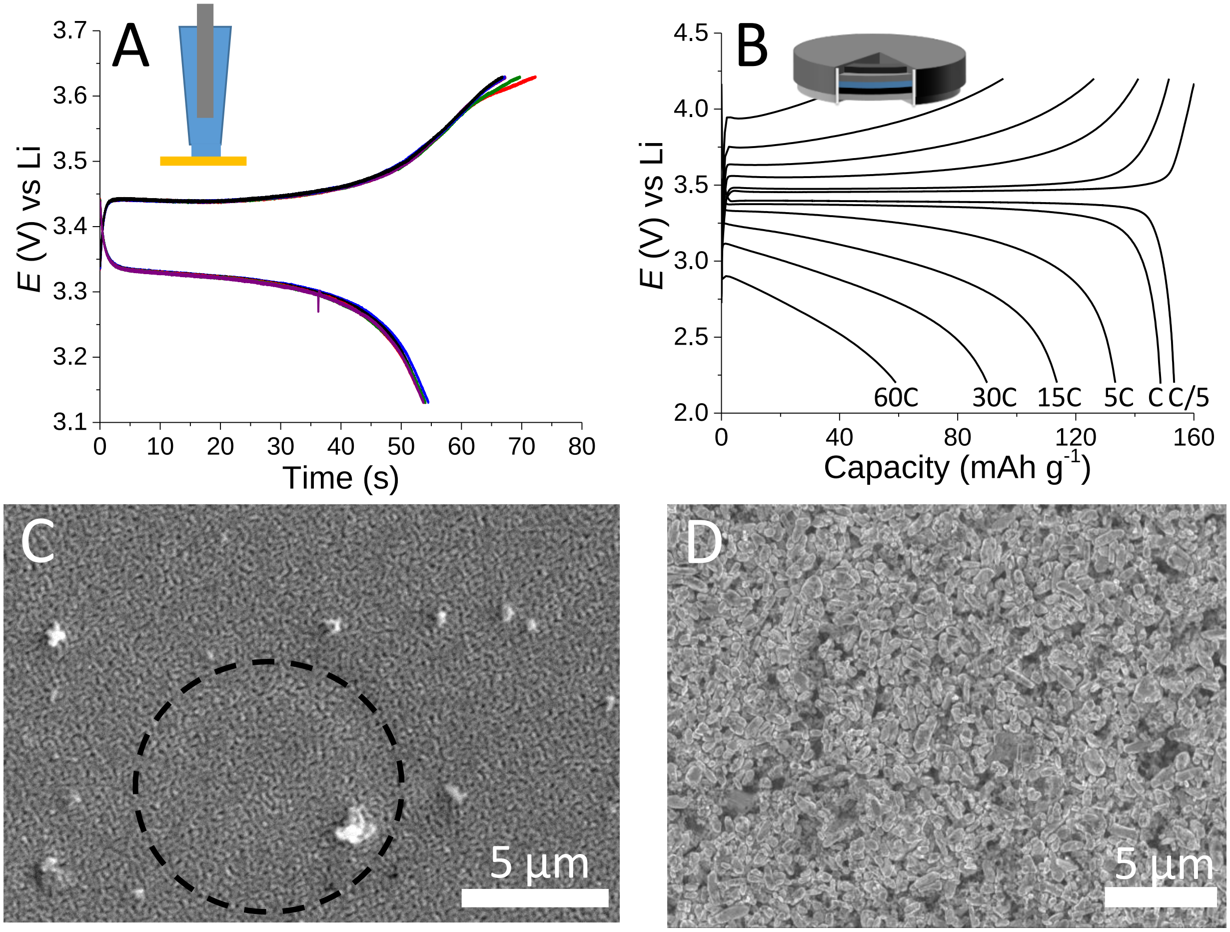

Figure 3.2: Galvanostatic charging and discharging measurements for (A) a micropipette containing 5 mM $LiClO_4$ at 1 pA current, and (B) a coin cell containing 1M $LiPF_6$ in EC:DMC (1:1 v/v), at 60C, 30C, 15C, 5C, C, and C/5 rates. (C) SEM image of the LFP sample measured in Figure 3.2A, with the area probed by the micropipette delimited by the black dashed circle. (D) Typical SEM image of a cast film used in the coin cell measurements.

The active particles almost had a cylindrical shape with a diameter of 100 nm. Using a density of $FePO_4$ of 3.6 g cm^{-3} and a capacity of 170 mA h g^{-1}, the theoretical capacity of these particles was calculated to be 2.97 x 10^{-10} mAh (supposing that the area observed by SEM refers to particles that settle flat on the substrate). The galvanostatic measurements performed by SMCM at currents of 1 pA, revealed a charging capacity of 1.67 x 10^{-11} mA h within 60 s (~60C rate), which corresponds to 56% of the theoretical value. Figure 3.2B shows that the coin cell measurements at 60C and 30C discharge rates provides, respectively, 35% and 53% of the theoretical capacity for the film, showing a good correlation between the high discharge rate and the decrease in the performance of both the coin cell and SMCM. Moreover, a smaller separation between the charge and discharge potentials was observed in the SMCM measurements, indicating that there was a much lower ohmic drop within the system due to the low current applied in SMCM. Remarkably, the electrochemical measurements for both systems provided qualitatively similar potential-time responses and almost same mid-point between the charging and discharging operating potentials, therefore, the SMCM approach can be used to investigate the active materials for LIB as individual particles dispersed upon a substrate.

3.3.2 Cyclic Voltammetry at Different Scan Rates

Figure 3.3A shows the cyclic voltammetry responses performed at scan rates of 50, 20, 10, 5, and 1 mV s^{-1}. For each scan rate, the 5th consecutive wave was reported, with the exception of 1 mV s^{-1}, where the 3rd wave was reported. The anodic and cathodic peaks corresponding to lithium deintercalation and intercalation from and into the LFP particles occurred at ~3.65 V and 3.15 V vs. Li/Li^+ respectively. These findings were in good agreement with the previously reported cyclic voltammetry measurements on coin cells, where the oxidation/reduction peaks of LFP appear at 3.7 and 3.1 V vs. Li/Li^+ respectively.[28, 30-31] As the scan rate increased from 1 to 50 mV s^{-1}, the width of the oxidation and reduction peaks and the peak-to-peak separation increased symmetrically. Similarly, the magnitude of the peak currents increased linearly with the scan rate as it increased (Figure 3.3C). This behavior was similar to a thin layer of adsorbed species,[32] considering a thin layer cell/depletion behavior within the particle. When the scan rate was greater than 50 mV s^{-1}, the cyclic voltammogram waves were not reproducible anymore. For scan rates of 20 mV s^{-1} or less, the oxidation peak of the cyclic voltammogram returned back to a base line current value, and the charge integration for the oxidation and reduction curves at 5 and 10 mV s^{-1} gave 170 pC (4.7 x 10^{-11} mAh). This signifies complete lithium intercalation/deintercalation processes at those scan rates. Besides, the magnitude of the currents for the reduction were lower than that for the oxidation. This observation of a slower rate of discharge for LFP agrees with chemical lithiation/delithiation reactions.[23-24]

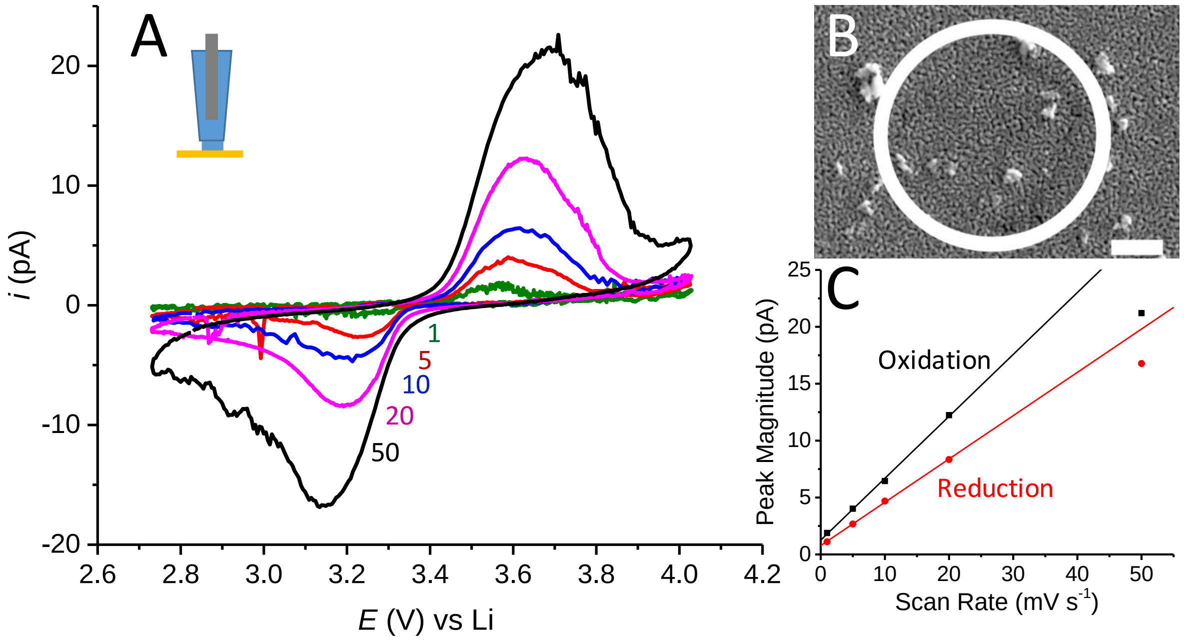

Figure 3.3: (A) Cyclic voltammograms performed at scan rates of 1, 5, 10, 20, and 50 mV s^{-1} using the micropipette method with 5 mM $LiClO_4$ solution in PC on a LFP dispersion. The legend corresponds to scan rate in mV s^{-1}; (B) SEM image of the area of the LFP dispersion probed in (A). The scale bar is 2 µm. (C) Plot of peak heights vs. scan rate, for the oxidation and reduction of LFP.

3.3.3 Cyclic Voltammetry Maps

To provide information about the charge capacity of individual particles, cyclic voltammetry measurements were performed at multiple points upon LFP particles drop cast onto a gold substrate. 36 measurement points were laid out in a 6 by 6 grid. The points were spaced by 20 µm in both the *x* and *y* directions to ensure complete separation of the areas wet by the meniscus. Based upon the different sweep rate experiments, a cyclic voltammogram of 5 mV s^{-1} scan rate was chosen to promote complete oxidation and reduction of the LFP particles (Figure 3.3A), with 5 cycles recorded at each measurement point. The area measured by the SMCM technique was then visualized by SEM to determine the area of the active particles lying on the substrate at each location probed by the pipette.

Figures 3.4A and B represent the forward peak current (i_{pf}) and forward peak potential (E_{pf}) extracted from the 5th cyclic voltammogram cycle at 5 mV s^{-1} scan rate, with respect to their *x* and *y* coordinates upon the substrate surface. The current responses for the majority of the points were greater than 0 pA ($i_{pf} > 0$), and a forward peak potential between 3.62 and 3.68 V vs. Li/Li$^+$ was recorded ($3.62 < E_{pf} < 3.68$). A similar response was observed in the reduction wave for backward peak currents lower than 0 pA ($i_{pb} < 0$), providing a backward peak potential between 3.09 and 3.19 V vs. Li/Li$^+$ (see Figure B1 in Appendix B).

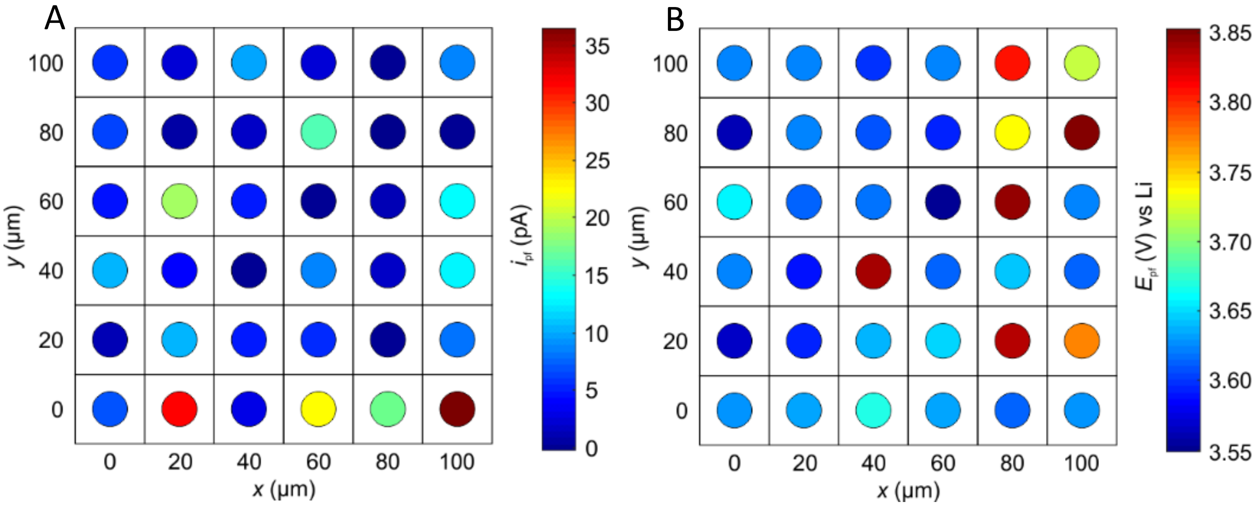

Figure 3.4: The map of (A) the forward peak current and (B) the forward peak potential for the grid of electrochemical measurements for the LFP dispersion on the gold substrate. The micropipette contained a 5 mM $LiClO_4$ solution in PC. The electrochemical data was obtained from the 5th cyclic voltammetry wave, at a potential scan rate of 5 mV s^{-1}.

Figure 3.5A displays a montage of 6000x magnified SEM images stitched together, providing a high-resolution microscopic map of the substrate area where the electrochemical measurements were performed. The image shows that the dispersion for the active material on the surface of the substrate is a combination of individual particles and particle agglomerates. The colored circles represent the wetting area of the meniscus upon the substrate, while the color of the outline represents the magnitude of the forward peak current (see Figure 3.4A). Figure 3.5B compares the area of the particles obtained from SEM montage image to the forward peak current and the corresponding integrated charge. A higher peak current response and measured charge are typically correlated to a larger surface area of particles within the wetting area. For clarity, the measurement points with no LFP signal were not plotted. Considering a capacity of 170 mAh g^{-1} and a density of 3.6 g cm^{-3} for LFP, the theoretical charge was plotted for two limiting cases: a sphere with diameter determined by the cross sectional area, and a cylindrical particle with 100 nm diameter lying flat on the surface of the substrate. The majority of areas probed had a capacity below the predicted maximum for a 100 nm thick particle, with the remaining areas were close to the theoretical value for a sphere. For the outliers below the theoretical capacity for a cylinder, there is a linear trend with the visible area of the particle, however, the data has a wide spread. This deviation has been previously reported for pipette measurements in aqueous media,[27] and could be attributed to particles near the perimeter of the marked area being wet by the meniscus due to the high wettability of the particles to PC, or variation in reactivity of the active material. The latter might result from variations in the surface coating[13, 33] or crystal properties such as morphology[34] and phase[35] for primary and secondary particles.[36] To confirm the stability of the particles during the SMCM measurements, control measurements were also performed and displayed in Appendix B (see Figure B2).

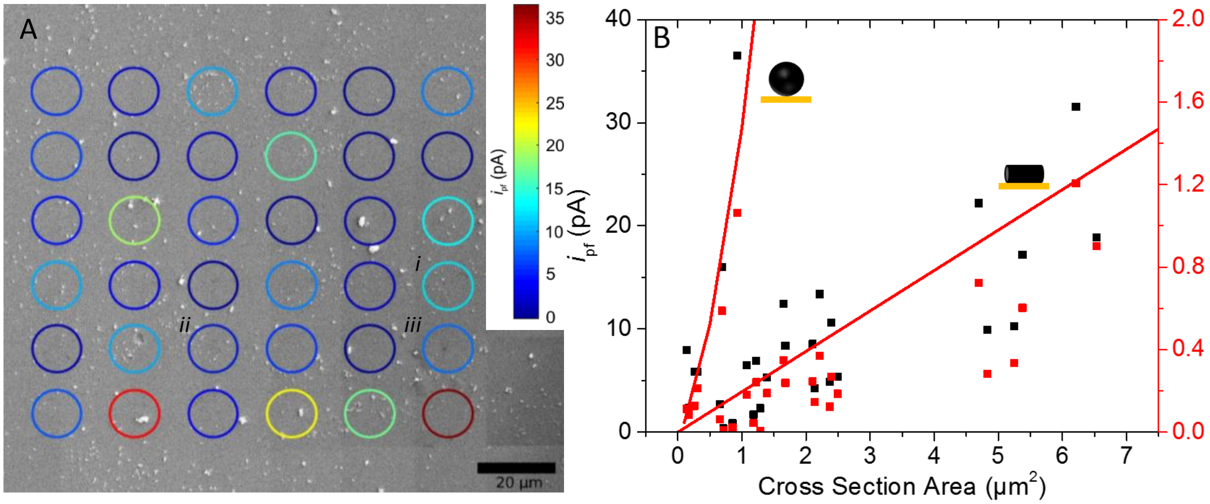

Figure 3.5: (A) Montage SEM micrographs of the SMCM scan area (also displayed in Figure 3.4). The circles represent the area wetted by the pipette during the scan, with the colors corresponding to the forward peak height. Points i, ii and iii correspond to the data from Figure 3.6B The peak current (black) and total charge (red) calculated from the oxidation wave plotted against the estimated area of particles observed by SEM. For comparative purposes, solid lines indicate theoretical capacity prediction for idealized spherical and cylindrical particles where the projected dimensions are assumed equal to the SEM area. See text for details.

SMCM measurements performed on different locations among the sample revealed heterogeneous electrochemical performance between the particles. For instance, at some tested points, complexed cyclic voltammetry responses with more than a single peak were observed (Figure 3.6A). When no LFP particles were present within the wetted area, a background signal was collected (blue line, Figure 3.6A). In contrast, in the presence of active LFP particles, cyclic voltammetry response displayed a single peak for 67% of the measurements (green line, Figure 3.6A and corresponding

SEM image Figure 3.6B). In other areas where LFP particles were also present, 27% of the cyclic voltammograms showed a double peak or a shoulder in the oxidation and the reduction peaks (red line Figure 3.6A and corresponding SEM image in Figure 3.6D).

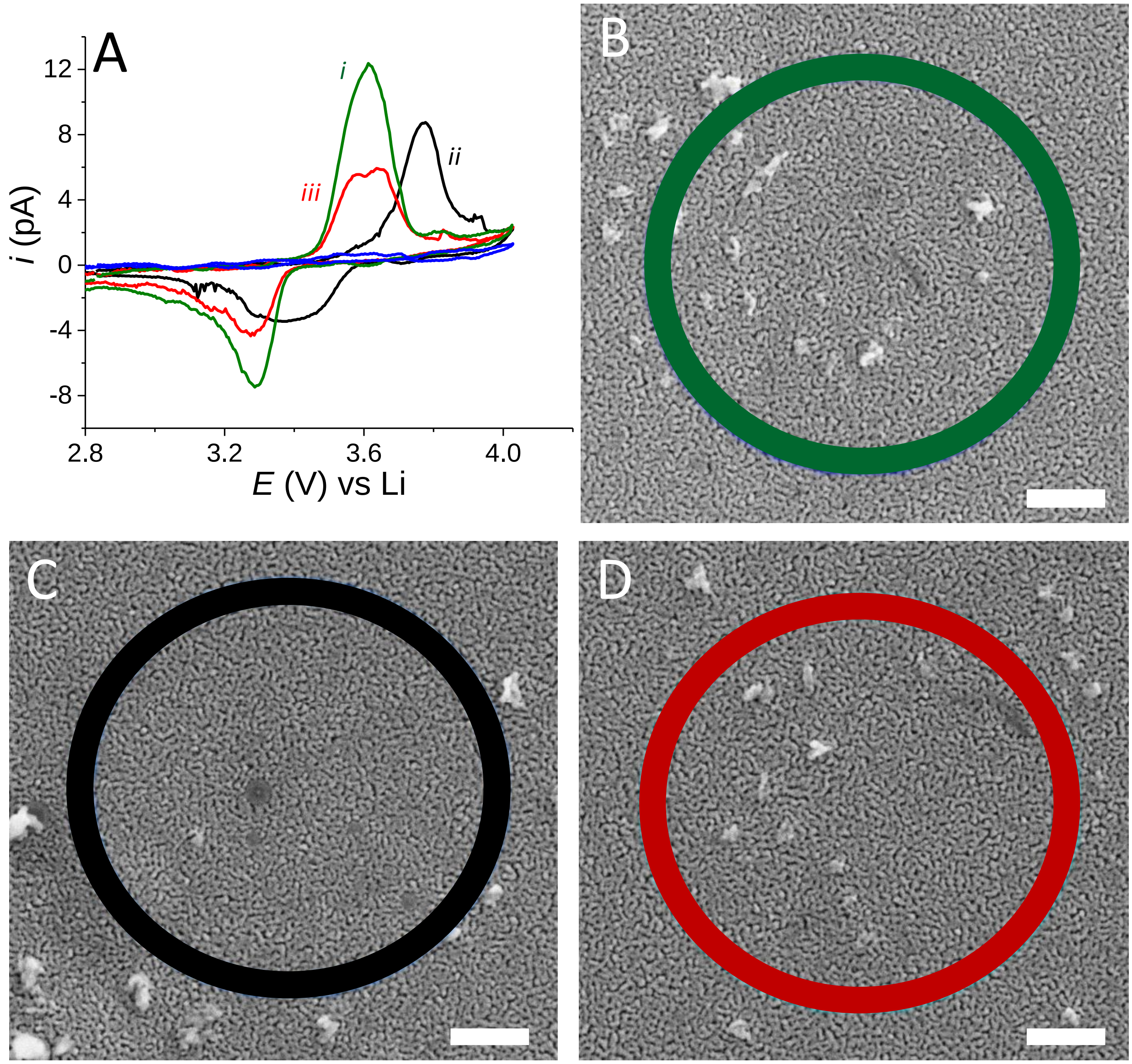

Figure 3.6: (A) The 5th cyclic voltammetry wave recorded at four grid locations. The blue line is the (background) capacitive response from the gold substrate, while waves i, ii and iii, were recorded at the grid locations marked with the same Roman numerals in Figure 3.5(A). SEM images of the areas displaying non-background cyclic voltammetry are shown panels (B), (C) and (D) and correspond to areas i, ii, and iii, respectively. The scale bar in (B), (C) and (D) corresponds to 2 μm.

Another local feature observed on some points was a large shift (+150 mV) in the oxidation and reduction peak potentials (black line Figure 3.6A). For these cases however, the reduction peak was much broader, indicating that the discharging process of the particles in that area is slower than normal. The corresponding SEM image (Figure 3.6C) shows several particles on the perimeter of the wetted area. In general, an increase in the peak separation is a result of different factors that are either technique based, such as poor wetting or resistive contact, or particle based due to variations in the carbon coating of the particle.[33, 37-38] Another factor for the shift in the peak potentials could be mass transport within the solid solution being more, or less, hindered due to particle geometry, or defects in the lattice structures,[39-40] while the origin of a change in the average oxidation-reduction potential could be chemical impurities,[41] structural defects[42] or a combination of the two. Although there are several reasons that could be attributed to the difference in the responses, electrochemistry on isolated particles allows qualities that would have been hidden in a composite electrode to be observed. The combination of SEM measurements and electrochemical observation of isolated particles by SMCM technique yields a new methodology by which the quality in the electrochemical performance of a material can be addressed down to the single particle level.

3.4 Conclusions

Localized electrochemical measurements were performed on isolated LFP active particles in a battery relevant environment, and then probed by SEM. To determine the lithiation/delithiation properties of the active material, galvanostatic and potentiodynamic experiments were carried out. The obtained peak potentials in both cases were in good agreement with the reported values for macroscopic films measured in LFP coin cells.

Cyclic voltammetry measurements performed at scan rates of 20 mV s^{-1} or more proved that the capacity of LFP particles being charged and discharged was dependent upon the scan rate. For sweeps less than 10 mV s^{-1}, no change in capacity was observed. Additionally, a higher peak current was obtained for the oxidation wave compared to the corresponding reduction wave, indicating that the charge reaction is faster than the discharge. This was in agreement with previously reported cyclic voltammetry data in the literature.[28, 30-31]

For the majority of probed areas from the SMCM map, cyclic voltammetry responses obtained at 5 mV s^{-1} revealed a single oxidation and reduction peak at ~3.65 V and ~3.15 V vs. Li/Li^+

respectively. However, differences in electrochemical performance between particles can be observed as a shift in the oxidation and reduction potentials. This demonstrates that SMCM can electrochemically identify heterogeneities among isolated primary particles and agglomerates, showing that not all particles within a batch have uniform properties. Furthermore, scanning electron microscopy is used to characterize particles after electrochemical measurements are performed. These complimentary measurement techniques allow the quantity and volume of particles to be compared to the electrochemical response. This is of significant interest for fundamental investigations of electrochemical properties of air sensitive materials, and for battery material characterization.

3.5 References

1.Ellis, B. L.; Lee, K. T.; Nazar, L. F. *Chemistry of Materials* **2010,** 22, (3), 691-714.

2.Yuan, L.-X.; Wang, Z.-H.; Zhang, W.-X.; Hu, X.-L.; Chen, J.-T.; Huang, Y.-H.; Goodenough, J. B. *Energy & Environmental Science* **2011,** 4, (2), 269-284.

3.Takahashi, M.; Tobishima, S.-i.; Takei, K.; Sakurai, Y. *Solid State Ionics* **2002,** 148, (3), 283-289.

4.Delmas, C.; Maccario, M.; Croguennec, L.; Le Cras, F.; Weill, F. *Nat Mater* **2008,** 7, (8), 665-671.

5.Delacourt, C.; Safari, M. *Electrochimica Acta* **2011,** 56, (14), 5222-5229.

6.Malik, R.; Abdellahi, A.; Ceder, G. *Journal of the electrochemical society* **2013,** 160, (5), A3179-A3197.

7.Zaghib, K.; Shim, J.; Guerfi, A.; Charest, P.; Striebel, K. *Electrochemical and Solid-State Letters* **2005,** 8, (4), A207-A210.

8.Jin, E. M.; Jin, B.; Jun, D.-K.; Park, K.-H.; Gu, H.-B.; Kim, K.-W. *Journal of Power Sources* **2008,** 178, (2), 801-806.

9.Lu, C.-Z.; Fey, G. T.-K.; Kao, H.-M. *Journal of power sources* **2009,** 189, (1), 155-162.

10.Thorat, I. V.; Stephenson, D. E.; Zacharias, N. A.; Zaghib, K.; Harb, J. N.; Wheeler, D. R. *Journal of Power Sources* **2009,** 188, (2), 592-600.

11.Stephenson, D. E.; Walker, B. C.; Skelton, C. B.; Gorzkowski, E. P.; Rowenhorst, D. J.; Wheeler, D. R. *Journal of The Electrochemical Society* **2011,** 158, (7), A781-A789.

12.Jiang, Z.; Jiang, Z.-j. *Journal of Alloys and Compounds* **2012,** 537, 308-317.

13.Doeff, M. M.; Hu, Y.; McLarnon, F.; Kostecki, R. *Electrochemical and solid-state letters* **2003,** 6, (10), A207-A209.

14.Park, M.; Zhang, X.; Chung, M.; Less, G. B.; Sastry, A. M. *Journal of Power Sources* **2010,** 195, (24), 7904-7929.

15.Andersson, A. S.; Kalska, B.; Häggström, L.; Thomas, J. O. *Solid State Ionics* **2000,** 130, (1), 41-52.

16.Liu, H.; Strobridge, F. C.; Borkiewicz, O. J.; Wiaderek, K. M.; Chapman, K. W.; Chupas, P. J.; Grey, C. P. *Science* **2014,** 344, (6191), 1252817.

17.Maccario, M.; Croguennec, L.; Desbat, B.; Couzi, M.; Le Cras, F.; Servant, L. *Journal of the Electrochemical Society* **2008,** 155, (12), A879-A886.

18.Gu, L.; Zhu, C.; Li, H.; Yu, Y.; Li, C.; Tsukimoto, S.; Maier, J.; Ikuhara, Y. *Journal of the American Chemical Society* **2011,** 133, (13), 4661-4663.

19.Kao, Y.-H.; Tang, M.; Meethong, N.; Bai, J.; Carter, W. C.; Chiang, Y.-M. *Chemistry of Materials* **2010,** 22, (21), 5845-5855.

20.Orikasa, Y.; Maeda, T.; Koyama, Y.; Murayama, H.; Fukuda, K.; Tanida, H.; Arai, H.; Matsubara, E.; Uchimoto, Y.; Ogumi, Z. *Chemistry of Materials* **2013,** 25, (7), 1032-1039.

21.Orikasa, Y.; Maeda, T.; Koyama, Y.; Murayama, H.; Fukuda, K.; Tanida, H.; Arai, H.; Matsubara, E.; Uchimoto, Y.; Ogumi, Z. *Journal of the American Chemical Society* **2013,** 135, (15), 5497-5500.

22.Sharma, N.; Guo, X.; Du, G.; Guo, Z.; Wang, J.; Wang, Z.; Peterson, V. K. *Journal of the American Chemical Society* **2012,** 134, (18), 7867-7873.

23.Lepage, D.; Sobh, F.; Kuss, C.; Liang, G.; Schougaard, S. B. *Journal of Power Sources* **2014,** 256, 61-65.

24.Kuss, C.; Carmant-Dérival, M.; Trinh, N. D.; Liang, G.; Schougaard, S. B. *The Journal of Physical Chemistry C* **2014,** 118, (34), 19524-19528.

25.Bülter, H.; Peters, F.; Schwenzel, J.; Wittstock, G. *Angewandte Chemie International Edition* **2014,** 53, (39), 10531-10535.

26.Barton, Z. J.; Rodríguez-López, J. *Analytical Chemistry* **2014,** 86, (21), 10660-10667.

27.Takahashi, Y.; Kumatani, A.; Munakata, H.; Inomata, H.; Ito, K.; Ino, K.; Shiku, H.; Unwin, P. R.; Korchev, Y. E.; Kanamura, K. *Nature communications* **2014,** 5.

28.Mi, C. H.; Zhang, X. G.; Li, H. L. *Journal of Electroanalytical Chemistry* **2007,** 602, (2), 245-254.

29.Williams, C. G.; Edwards, M. A.; Colley, A. L.; Macpherson, J. V.; Unwin, P. R. *Analytical Chemistry* **2009,** 81, (7), 2486-2495.

30.Tang, K.; Yu, X.; Sun, J.; Li, H.; Huang, X. *Electrochimica Acta* **2011,** 56, (13), 4869-4875.

31.Huang, Y. H.; Wang, F. M.; Huang, T. T.; Chen, J. M.; Hwang, B. J.; Rick, J. *International Journal of Electrochemical Science* **2012,** 7, (2), 1205-1213.

32.Wopschall, R. H.; Shain, I. *Analytical Chemistry* **1967,** 39, (13), 1514-1527.

33.Hong, S.-A.; Kim, S. J.; Kim, J.; Lee, B. G.; Chung, K. Y.; Lee, Y.-W. *Chemical Engineering Journal* **2012,** 198-199, 318-326.

34.Fisher, C. A. J.; Islam, M. S. *Journal of Materials Chemistry* **2008,** 18, (11), 1209-1215.

35.Cogswell, D. A.; Bazant, M. Z. *Nano Letters* **2013,** 13, (7), 3036-3041.

36.Zhang, W.-J. *Journal of Power Sources* **2011,** 196, (6), 2962-2970.

37.Shin, H. C.; Cho, W. I.; Jang, H. *Electrochimica Acta* **2006,** 52, (4), 1472-1476.

38.Wang, J.; Sun, X. *Energy & Environmental Science* **2012,** 5, (1), 5163-5185.

39.Dokko, K.; Koizumi, S.; Nakano, H.; Kanamura, K. *Journal of Materials Chemistry* **2007,** 17, (45), 4803-4810.

40.Malik, R.; Burch, D.; Bazant, M.; Ceder, G. *Nano letters* **2010,** 10, (10), 4123-4127.

41.Kobayashi, G.; Yamada, A.; Nishimura, S.-i.; Kanno, R.; Kobayashi, Y.; Seki, S.; Ohno, Y.; Miyashiro, H. *Journal of Power Sources* **2009,** 189, (1), 397-401.

42.Amisse, R.; Sougrati, M. T.; Stievano, L.; Davoisne, C.; Dražič, G.; Budič, B.; Dominko, R.; Masquelier, C. *Chemistry of Materials* **2015,** 27, (12), 4261-4273.

Chapter 4

Micropipette Contact Method to Investigate High-Energy Cathode Materials by using an Ionic Liquid

In Chapter 3, the SMCM technique was used to probe the electrochemical properties of the cathode battery material LFP. The successful results obtained proved that the SMCM is highly relevant for probing intrinsic properties of battery materials, and it is also capable of identifying variations in particle consistency. Therefore, the use of SMCM to probe higher energy active material was set as a second goal. As presented in the previous chapter, the investigation of LFP was performed on a gold substrate using the organic carbonate solvent PC with lithium salt. Since LFP is known to operate within a small potential range, the use of organic electrolyte was a good choice. Nevertheless, studying higher energy battery materials require electrolytes with wider potential window. This entailed extending the SMCM to ionic liquids, which are know to have large window of electrochemical stability.

Chapter 4 describes the evolution of the SMCM technique to include ionic liquid as an alternative electrolyte solution to the conventional organic electrolytes. In particular, the ionic liquid EMI TFSI containing 0.1 M LiTFSI salt was introduced into the micropipette for SMCM measurements. Localized electrochemical measurements were performed on LFP particles that were drop-cast onto a glassy carbon substrate. Investigation of the active materials occurred on a small scale (~10 µm diameter), defined by the area of meniscus contact between the electrolyte solution in the micropipette and the substrate. Complementary atomic force microscopy images of the scanned area gave an estimation to the volumes of the probed particles, which were used to calculate their corresponding experimental capacity. The study showed that the SMCM probe is stable and can be used to analyze high energy LIB materials in the range of 2.5 to 5.1 V vs. Li/Li^+. To confirm the feasibility of using this system for high energy materials, three-electrode cell measurements were also carried out on conventional composite films of LFP and the higher energy cathode material NMC using the ionic liquid EMI TFSI. The obtained results illustrated that SMCM could be successfully used in the presence of the ionic liquid to study conventional active material such as LFP, and it could be extended to study higher energy particles such as NMC.

The work presented in this chapter was previously published and is reproduced from:

Dayeh, M.; Ghavidel, M. Z.; Mauzeroll, J.; Schougaard, S. B., *ChemElectroChem* **2019,** *6* (1), 195-201.

4.1 Introduction

The conventional electrochemical techniques used to investigate the intrinsic material properties of lithium-ion batteries (LIBs) cause complications due to the heterogeneity of electrode composite films. Multi-component composite thick films have been studied by electrochemical impedance spectroscopy,[1] potentiostatic and galvanostatic intermittent titration techniques,[2] and cyclic voltammetry.[3] The electrochemical response is thus a convolution of the active materials properties and the effect of the electrode structure, like electronic conductivity and mass transport limitations, which make analysis difficult.[4] Moreover, due to the large number of particles being studied, only average properties can be found, making it impossible to study localized electrochemical properties of the active material.

To overcome this challenge, the development of localized electrochemical probes is required. For instance, Lim *et al.* have used high-resolution X-ray absorption spectroscopy to derive the local current within particles resulting from the imposed potential.[5] Similarly, in-situ electrochemical transmission electron microscopy has been used.[6] Additionally, high-resolution electrochemical microscopy techniques have screened the localized properties and reactivity of a wide variety of electrode surfaces. In-situ studies have been performed by scanning electrochemical microscopy (SECM) in order to investigate the transport of Li^+ ions in active materials[7] and the formation of the SEI layer.[8] Scanning electrochemical cell microscopy (SECCM) has been used to evaluate the local redox activity of a lithium iron phosphate (LFP) electrode.[9] Scanning ion-conductance microscopy (SICM) has been also applied to silicon and tin negative electrodes to measure spatially resolved Li^+ currents.[10] Recently, our group has conducted localized galvanostatic and potentiodynamic measurements on LFP particles using scanning micropipette contact method (SMCM).[11] In this study we determined the single particle properties in an anaerobic environment without the additional complications arising from the presence of binders and electronically conductive fillers.[12] Moreover, we showed that the galvanostatic response of particle aggregates resembled closely that of standard coin cell measurement based on industrially relevant composite electrodes. In addition, the SMCM technique has the added benefit that it is able to monitor particle to particle variation.

In line with current LIB research that seeks to improve the energy density through the use of higher redox potential cathode material, such as lithium nickel manganese cobalt oxide (NMC), SMCM should be extended to ionic liquids, which are considered promising alternatives to conventional molecular solvents.[13-14] They possess unique physicochemical properties,[15] such as negligible vapor pressure, non-flammability, and a wide electrochemical stability window. In particular, ionic liquids based on the imidazolium cation,[16-18] such as 1-ethyl-3-methylimidazolium (EMI),[19-20] are of high interest because of their low viscosities and high ionic conductivities, which is why they were chosen for the present study.

The use of ionic liquids has indeed been reported in SECCM, in an attempt to improve the efficiency of dye-sensitized solar cells,[21-22] but never for investigating LIB materials. Herein, we benchmark the use of ionic liquids in SMCM using LFP. LFP has a reasonable theoretical capacity (170 mAh g^{-1})[23-25] but low specific energy (518–587 $Whkg^{-1}$)[26] that is limited by its tap density and operational voltage (3.4 V vs. Li/Li^+). Although it is not an ideal candidate for applications requiring high energy density such as electrical vehicles, it is an ideal reference material to benchmark the use of ionic liquids in SMCM. LFP is commercially available, and its moderate operational voltage ensures that a large overpotential can be imposed within the electrochemical window of the electrolyte solution to drive reactions. Moreover, the two-phase reaction mechanism, ensures that lithiation/delithiation potential is fixed over a large Li concentration range.

In this study, the SMCM technique was extended to higher oxidation potentials, using the ionic liquid 1-ethyl-3-methylimidazolium bis(trifluoromethylsulfonyl)imide (EMI TFSI). For SMCM measurements, the LFP particles were dispersed on a glassy carbon (GC) substrate. In addition, the conventional composite films of LFP and NMC-111 were also prepared and tested in a three-electrode cell using EMI TFSI and propylene carbonate (PC) in order to confirm the feasibility of using this system for high power materials. To further optimize the system, the electrochemical stability of EMI TFSI was measured and compared to the commonly used PC electrolyte. Stability tests for the quasi-reference counter electrode (QRCE) $Al_{1-x}Li_x$ and the droplet were also performed using the ionic liquid. Finally, the coulombic efficiency and electrochemical response of dispersed LFP particles were obtained using SMCM measurement in EMI TFSI.

4.2 Experimental Section

4.2.1 Three-Electrode Measurements

The electrochemical performance of LFP and NMC-111 active materials were first examined using a three-electrode cell. A composite film was prepared by casting a slurry containing 80 wt% active material (LFP or NMC), 10 wt% acetylene black (Super C5, TimCal), and 10 wt% polyvinylidene fluoride (PVDF, Kynar) in N-methyl-2-pyrrolidone (NMP), 99% Sigma Aldrich) on aluminium foil current collector. PVDF was dissolved in NMP prior to adding active material. For every gram of active material, 3.5 ml of NMP was used. The coating was then dried overnight at 60 °C under vacuum, to yield a thickness of 25 μm. This working electrode was immersed into 10 ml of the electrolyte solution, and metallic Li strips (99.9 % Alfa Aesar) were used as counter and reference electrodes. The composite films were tested by cyclic voltammetry at a scan rate of 0.5 mV s^{-1} using an ElPro Scan 3 (HEKA Electronics, Germany) instrument. Measurements were performed using two different electrolytes, 0.5 M $LiPF_6$ (99.9 % STREM chemicals) solution in ethyl methyl carbonate (EMC 99.92 % BASF), and 0.1 M LiTFSI (99.9 % Sigma Aldrich) in the ionic liquid 1-ethyl-3-methylimidazolium bis(trifluoromethylsulfonyl)imide (EMI TFSI 99.5 % Iolitech).

4.2.2 SMCM Measurements

The SMCM setup (Figure 4.1) consists of a glassy carbon working electrode, onto which LIB active material is dispersed by drop-casting an isopropanol suspension of particles (3 mg/mL), and the SMCM probe which is localized in space by a x,y,z-positioning system. It should be noted here that SMCM was used to probe the electrochemical properties of active material particles in the absence of a polymer binder and an electronically carbon black filler.

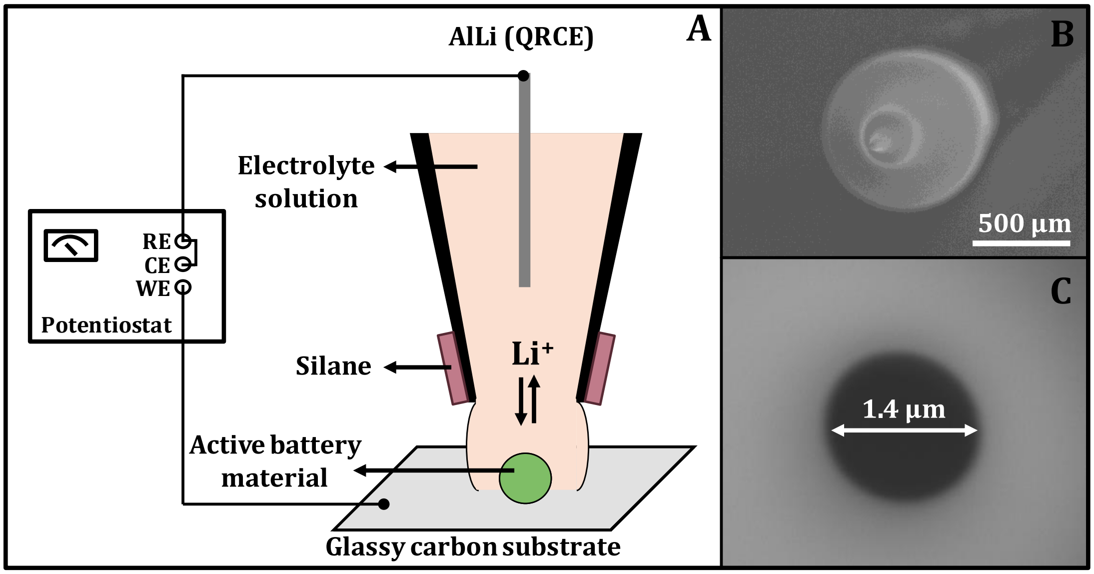

Figure 4.1: (A) Schematic illustration of the SMCM probe setup within the glove box. The active material was drop-cast onto a glassy carbon surface without any binder. The electrodes were connected through BNC cables to the potentiostat placed outside the glovebox. (B) SEM images of micropipette used for the SMCM measurements showing the uniform tip and (C) a bottom view of the tip defining the aperture diameter.

Scanning electron microscopy (SEM, with a Hitachi SU3500 VPSEM instrument) was used to observe the as-deposited dispersion of the active material on the glassy carbon surface. Micropipettes were pulled from quartz capillaries (0.3 mm inner diameter and 1.0 mm outer diameter (Sutter Instruments)), using a laser puller (Model P-2000 Sutter Instruments). SEM imaging of the pulled pipettes showed that the diameter aperture was 1.4 µm. The tip was rendered hydrophobic by dipping it into trichloro perfluoro-octylsilane (Sigma Aldrich), while nitrogen gas was passed through the aperture to ensure that the internal surface of the capillary was uncoated. The $Al_{1-x}Li_x$ QRCE was fabricated galvanostatically[12] in 0.25 M $LiClO_4$ solution in PC (99.7 % Sigma Aldrich). An aluminum wire (125 µm diameter, 99.5 %, Goodfellow) served as working electrode, and two Li metal strips as counter and reference electrodes. Li deposition was maintained for 30 minutes at a constant current of -100 µA. The stability of the $Al_{1-x}Li_x$ electrode was examined vs. the Li electrode in PC solution and in the ionic liquid EMI TFSI by measuring the open circuit potential (OCP) for 5 minutes before carrying out electrochemical measurements, and after 24 hours of continuous cyclic voltammetry measurements. The SMCM probe was prepared by filling the pipette with a 0.1 M LiTFSI salt solution in EMI TFSI, and inserting the $Al_{1-x}Li_x$ QRCE into the opening of the capillary. SMCM measurements were performed inside an argon filled glovebox (MBraun, water and oxygen content <1 ppm). Using the piezo-electric controls of the ElPro Scan 3 instrument, the micropipette approached the glassy carbon substrate at a speed of 1 µm s^{-1}, while applying a potential of 2.5 V vs. the substrate. Upon contact of the micropipette solution meniscus, the drop wetted the glassy carbon substrate and the electrochemical circuit was completed, thus producing a spike in the measured current. This spike was used to halt the pipette approach, thus ensuring that the pipette tip did not come into direct contact with the surface of the substrate or the active material particles. Cyclic voltammetry measurements were then performed at different scan rates (ranging from 1 to 50 mV s^{-1}) using the same potentiostat, without displacing the probe on the surface. The area of the working electrode is defined by the area of the droplet that is wetting the surface of the substrate (in the present case ~10 µm). The same probe may be reused by retracting it from the surface and displacing it to another area of the substrate loaded with active material particles before repeating the approach. For ease of comparison with the literature, the potential scale was reported with respect to Li/Li^+ throughout this article, by adding 0.330 V to the potential measured vs. $Al_{1-x}Li_x$ QRCE. The Coulombic efficiency was determined by evaluating the area under the oxidation/reduction peaks, after subtraction of the interpolated baseline response. The experimental capacity of the deposited material was also calculated by estimating the volume of the particles within the landing area using atomic force microscopy (AFM) measurements combined with SEM images. All AFM measurements were acquired on an MFP3D microscope equipped with a molecular force probe controller (Asylum Research-an Oxford Instruments Company, Santa Barbara, CA) in alternating contact (AC) mode in air. The cantilevers used for imaging were model ACTA (AppNano, Mountain View, CA).

4.3 Results and Discussion

4.3.1 Primary Tests on PC and EMI TFSI

The stability and potential window for electrolyte solutions based on two different solvents (PC and EMI TFSI) were investigated using cyclic voltammetry. Measurements were performed with 0.25 M $LiClO_4$ solution in PC and 0.1 M LiTFSI in EMI TFSI using the SMCM technique, with glassy carbon serving as working electrode and $Al_{1-x}Li_x$ as QRCE. The cyclic voltammograms (Figure 4.2A) were recorded by sweeping the potential between 1.8 V and 5.2 V at a scan rate of 50 mV s^{-1}. A significant nonlinear increase in current was observed for the forward scan at 4.6 V for PC and 5.1 V for the EMI TFSI, indicating that the respective electrolyte solutions were not stable beyond the stated potentials. Although the stability of the electrolyte solution is improved only by 0.5 V by the ionic liquid, an oxidation potential greater than 4.6 V was essential for completely charging active materials such as NMC. Therefore, EMI TFSI based electrolyte is a better candidate than PC.

The $Al_{1-x}Li_x$ QRCE was fabricated previously in our laboratory and tested in PC electrolyte[12] but not in EMI TFSI ionic liquid. Therefore, the stability of the fabricated QRCE was tested by measuring OCP of $Al_{1-x}Li_x$ vs. Li reference electrode upon fabrication in PC, as well as before and after completion of the SMCM measurements in EMI TFSI (Figure 4.2B). The potential shift was lower than 0.05 V over a period of 24 h, which is well within the limits needed for the QRCE in the SMCM measurements.

Another parameter that strongly affects the reproducibility of the SMCM measurements is droplet stability. This was tested using the redox mediator 10-methylphenothiazine (MPT 98% Alfa Aesar). An electrolyte solution of 10 mM MPT in EMI TFSI was introduced into the micropipette, and cyclic voltammetry was employed to measure the stability of the MPT redox reaction on bare glassy carbon surface (Figure 4.2C). The redox potential of 3.5 V vs. Li/Li^+ was obtained over 100 cycles, illustrating that the droplet had the stability needed for electrochemical SMCM measurements (~10%/h current decrease). The MPT test and the stability of $Al_{1-x}Li_x$ indicate that the SMCM probe using ionic liquid is appropriate for investigating active material with wide range of charging/discharging potentials up to ~5.1 V vs. Li/Li^+.

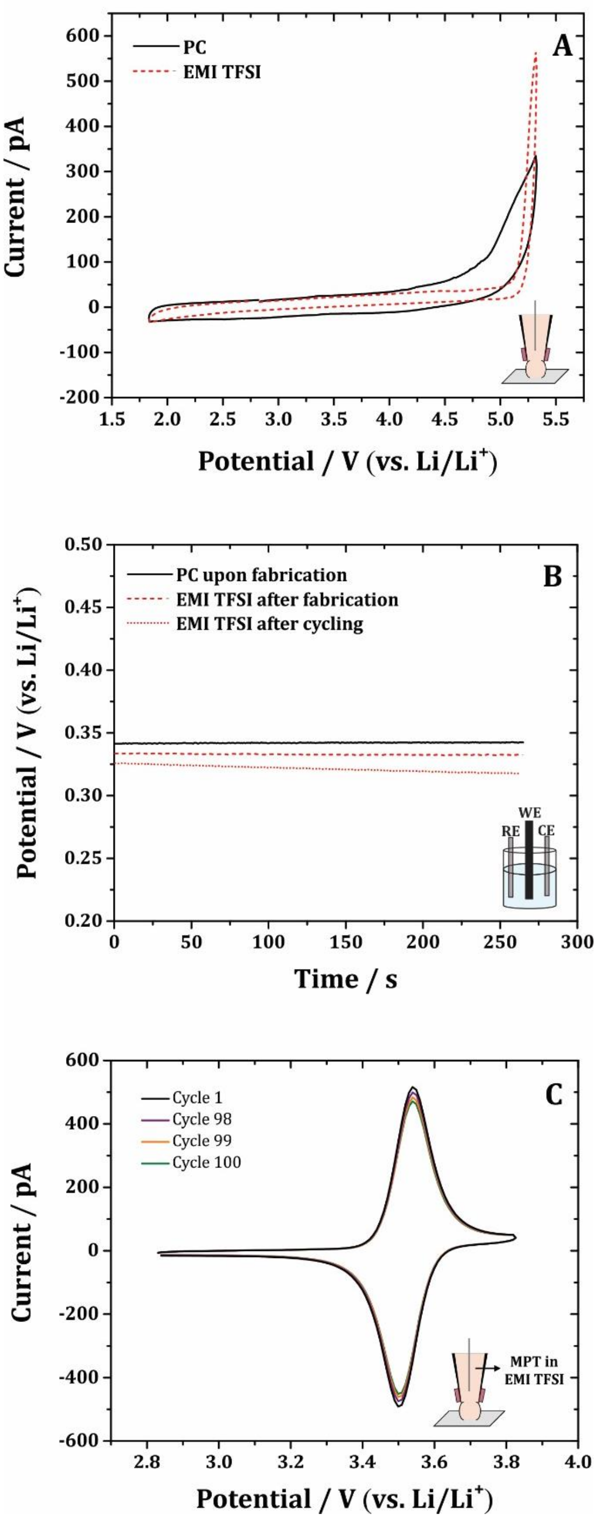

Figure 4.2: (A) Cyclic voltammograms showing the potential window of 0.25 M $LiClO_4$ in PC and 0.1 M LiTFSI in EMI TFSI solutions (scan rate=50 mV s^{-1}). (B) Open circuit potential of $Al_{1-x}Li_x$ QRCE measured in PC upon fabrication, and in EMI TFSI ionic liquid before and after the electrochemical cycling. (C) Cyclic voltammograms of the oxidation/reduction reaction of the 10 mM MPT redox mediator in EMI TFSI using micropipette.

4.3.2 Composite Films of LFP and NMC

In order to study the effects of changing the electrolyte from carbonate base to ionic liquid electrolyte, and to compare the electrochemical activity of the commercial LFP and NMC-111 active materials, cyclic voltammetry for composite films was performed in macroscopic three-electrode cells using $LiPF_6$ in EMC and LiTFSI in EMI TFSI electrolytes. Five consecutive voltammograms were recorded at a scan rate of 0.5 mV s^{-1}. The last wave for each measurement is shown in Figure 4.3. For the LFP film in $LiPF_6$/EMC, a pair of well-defined peaks corresponding to the charging/discharging process of the Fe^{3+}/Fe^{2+} redox couple were obtained at 3.95 and 2.90 V vs. Li/Li^+, with an average value of 3.43 V (Figure 4.3A). The peak-to-peak splitting is dependent on many factors including transport limitations related to the composite electrodes,[27-30] charge transfer resistance at the particle surface,[25] and transport limitations within the active material particles.[25, 31] Li intercalation and deintercalation peaks for the LFP composite electrode in EMI TFSI electrolyte appear at 4.10 and 2.80 V vs. Li/Li^+ (Figure 4.3C). The calculated average of 3.45 V is comparable to that obtained in EMC, but with larger peak separation. This increase in peak-to-peak splitting is consistent with the fact that Li^+ diffusion in EMI TFSI is slower than in the carbonate electrolyte solution as a result of viscosity changes. The viscosity of the ionic liquid is ~40 cP, i.e. 56 times greater than that of EMC (~0.7 cP). It was shown that the diffusion coefficient of Li^+ correlates to the viscosity rather than the specific conductivity.[32] Although EMI TFSI has high viscosity, it can still be used as an electrolyte solution for electrochemical measurements. This was shown in Figure 4.3, where the results obtained in the ionic liquid are comparable to those collected in an organic carbonate electrolyte solution. Note that the results in Figures 4.2 and 4.3 are not directly comparable given fact that potential drop due to electrolyte resistance (IR drop), are different.

For the NMC composite film in the carbonate electrolyte, two anodic peaks and two cathodic peaks are readily visible (Figure 4.3B). The first sharp and intense anodic peak centered at 4.10 V vs. Li/Li^+ corresponds to the oxidation of Ni^{2+}/Ni^{4+}, whereas the second low-intensity peak at 4.70 V vs. Li/Li^+ corresponds to the oxidation of Co^{3+}/Co^{4+}. The cathodic peaks at 4.40 and 3.50 V vs. Li/Li^+ are related to Co^{4+}/Co^{3+} and Ni^{4+}/Ni^{2+} reduction, respectively. These potential values are in good agreement with those from previously reported studies, where the oxidation/reduction peaks of nickel appear at 3.99 and 3.58 V vs. Li/Li^+ and for cobalt at 4.71 and 4.54 V vs. Li/Li^+.[33]

Examining the NMC composite electrode in the LiTFSI/EMI TFSI electrolyte solution yields cyclic voltammograms with peaks less well-defined and at higher overpotentials (Figure 4.3D). This is probably due to ionic liquid not wetting the electrode as efficiently as the carbonate electrolyte or due to the previously mentioned decrease in Li diffusivity in a viscous medium.[34] Combining the three-electrode measurements using composite films illustrated that the commercial samples of LFP and NMC were electrochemically active and their electrochemical responses are comparable to recently reported studies.[33, 35]

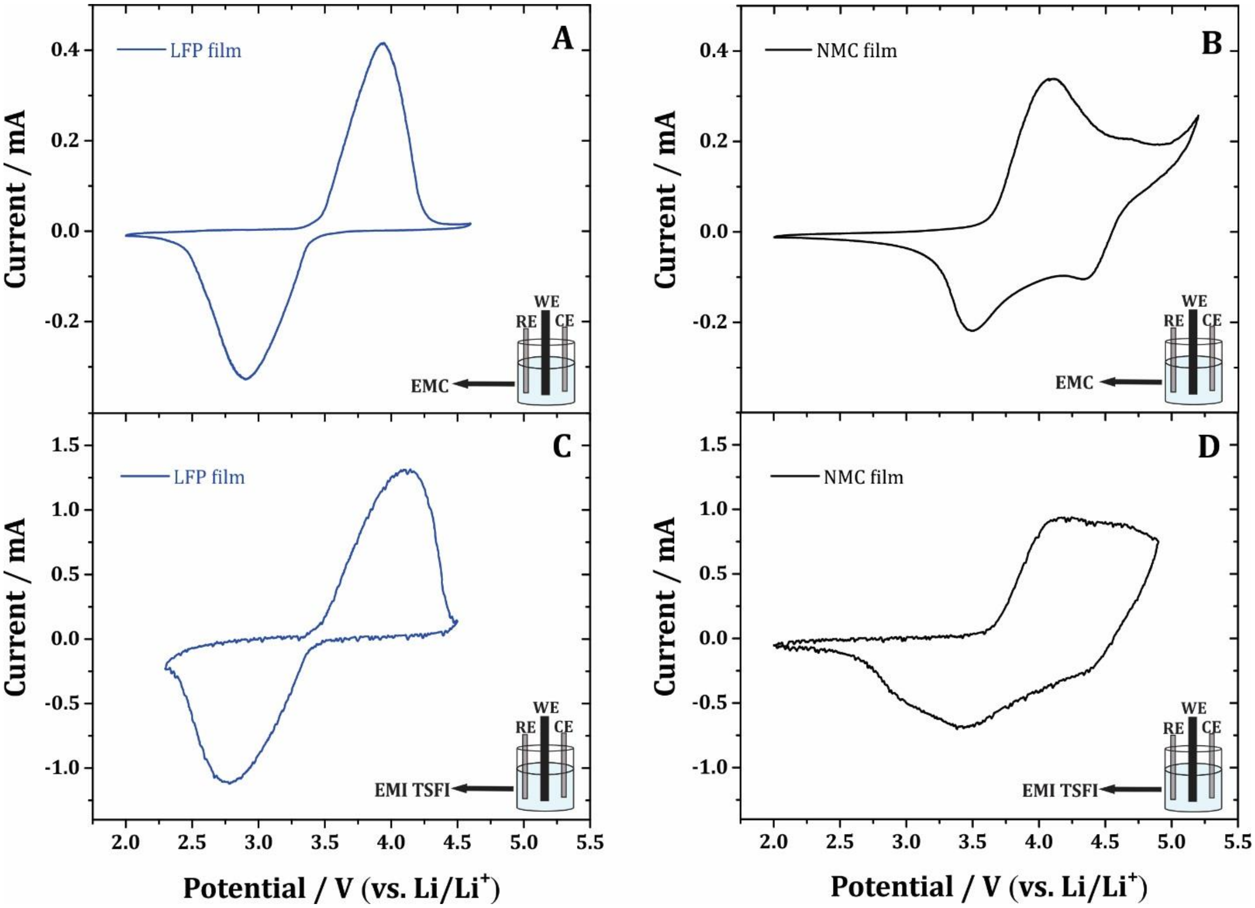

Figure 4.3: Cyclic voltammograms for the composite films of LFP (A, C) and NMC (B, D) using a three-electrode cell. The measurements were done in 0.5 M $LiPF_6$ in EMC (A, B) and 0.1 M LiTFSI in EMI TFSI (C, D) using Li metal strips as reference and counter electrodes, while the composite films were working electrodes (scan rate=0.5 mV s^{-1}). The 5th cycle is plotted for each measurement.

4.3.3 SMCM Measurements on LFP Particles using a LiTFSI Solution in EMI TFSI

Cyclic voltammetry scan for the charging/discharging of LFP was performed with 0.1 M LiTFSI in EMI TFSI solution at scan rates of 1, 5, 10, 20, and 50 mV s^{-1} using the SMCM technique (Figure 4.4A). The SEM image in Figure 4.4B represents the actual landing area with the LFP particles from which the electrochemical measurements shown in Figure 4.4A were collected. Several particles were sampled, but only data for one sample is shown in Figure 4.4B (for more sampled particles, please refer to Figure C2 in Appendix C). For each scan rate, 5 consecutive voltammograms were recorded with the exception for 1 mV s^{-1}, where only 3 cycles were recorded. The last wave for each scan rate is displayed in Figure 4.4A. At 50 mV s^{-1}, the oxidation peak of Li extraction from the LFP particles was recorded at 3.70 V vs. Li/Li^+ and the reduction peak (Li insertion) was recorded at 3.0 V vs. Li/Li^+. The potential difference between the oxidation and reduction peaks decreased with decreasing scan rate. Similarly, the width of the oxidation/reduction peaks and the magnitude of the peak currents decreased as the scan rate decreased from 50 to 1 mV s^{-1}.

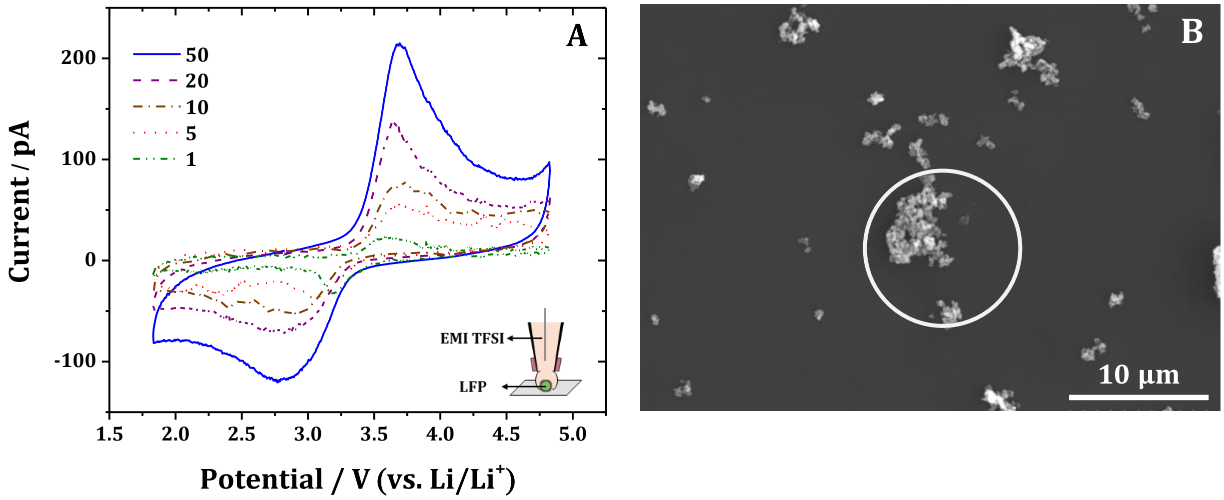

Figure 4.4: (A) Cyclic voltammograms obtained at different scan rates using SMCM with 0.1 M LiTFSI in EMI TFSI on LFP particles dispersed on a glassy carbon electrode. The legend corresponds to scan rate in mV s^{-1}. The 5th consecutive wave is reported for each scan rate, except for 1 mV s^{-1} where the 3rd wave is reported. (B) The SEM image shows the dispersed LFP active material on a glassy carbon substrate. The white circle depicts the landing area from where the cyclic voltammogram in (A) were collected.

It should be noted that the peak-to-peak separation was greater than previously reported values[12] for voltammetry scans performed at the same rate. This could be attributed to resistive contact between the solely dispersed active particles and the glassy carbon substrate, or poor wetting of the electrode surface, as well as particle to particle reaction kinetics variations. The micropipette technique is governed by delicate balance between the wettability of the ionic liquid to the internal and external walls of the glass pipette, as well as its wettability to the cathode material and glassy carbon substrate. To optimize the location of the ionic liquid droplet, several different silanization agents were examined, the aperture of the glass micropipette was adjusted as well as the nature of the conductive substrate. These issues are more pronounced in the micropipette technique than in bulk measurements, where the active material is mixed with polymer binder and conducting agent before it is cast onto a current collector, and the whole electrode is in contact with the electrolyte solution during the electrochemical measurements.

The charge integration for the oxidation/reduction peaks was performed for the 5th cycle at each scan rate, with the exception of 1 mV s^{-1}, where the 3rd cycle was used. Upon running more cycles, the peaks become less defined (after 70 cycles) and salt precipitation on the glassy carbon substrate was observed. Appendix C (Figure C5) displays a typical SEM image that was taken for a landing point after long-term cycling (about 16 hours), in addition to the detailed energy dispersive X-ray analysis (EDX) used for chemical characterization. A coulombic efficiency higher than 90% was obtained in ionic liquid based electrolyte solution (Table C1 in Appendix C). This is significant progress from the previous study of LFP on gold substrate using PC,[12] where the maximum coulombic efficiency was 79%. This suggests that the combination of replacing the gold substrate with the glassy carbon electrode and changing the electrolyte solution suppresses some of the parasitic reactions that affected earlier SMCM analysis of LIB materials.

In order to estimate the capacity of the active particles within the actual landing area, AFM measurements were conducted in approximation of the landing sites. Several AFM images were taken, covering in total about 100 LFP particle agglomerates. A typical AFM image showing the dispersion of the particles on the substrate surface is depicted in Figure 4.5A. The histograms represented in Appendix C (Figure C4) show the distribution of the particles' size in terms of height, area, and volume, with the highest frequency lying between 0.2 to 0.9 µm, 1 to 4 μm^2, and 1 to 2 μm^3 respectively. This distribution is reasonable, because the LFP particles used in this experiment were agglomerates of small individual particles whose size ranges from 0.08 to 1.15 µm (average of 0.3 µm). The AFM results reveal that there is a linear relation between 2D area and 3D volume of the LFP agglomerates. From the estimated area of the agglomerates within the landing sites (using SEM images and ImageJ software), one can evaluate their volume and consequently calculate the experimental capacity with reasonable accuracy. A plot of the particles' volume vs. their area is shown in Figure 4.5B. The black squares denote the correlation of area to volume of the particles collected from AFM images, while the red circles represent the area calculated from different landing sites using ImageJ. The expected volume of these actual particles was then calculated based on the volume-area linear relation. It must be noted here that the height and volume estimation of the particles using SEM was not possible even upon tilting the sample, due to the very small particle sizes and the size of the glassy carbon electrode.

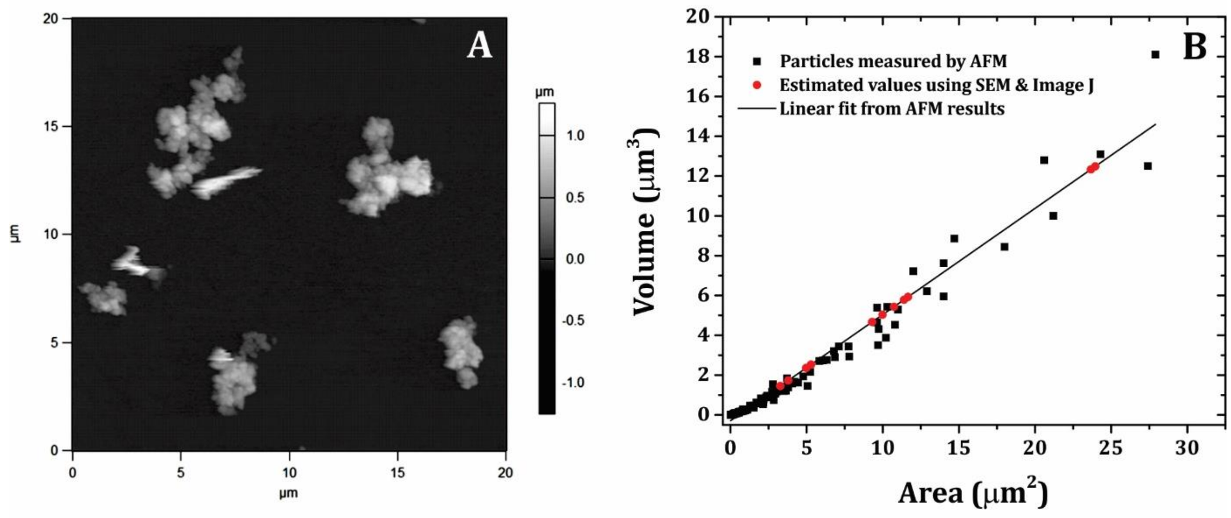

Figure 4.5: (A) Typical AFM image of the dispersed LFP active material on a glassy carbon substrate. (B) A plot correlating (black) the area of 100 particles after taking several AFM images to their corresponding volume, (red) the actual area of the active particles within the landing zone and their corresponding volume.

Using SMCM, the experimental capacity of the active particles within the landing area was calculated at 11 different landing sites. An average of 19 mAh g^{-1} was obtained at the scan rate of 50 mV s^{-1}, which increases to 39 mAh g^{-1} at the scan rate of 5 mV s^{-1} (using LFP density of 3.6 g cm^{-3} and a theoretical capacity of 170 mAh g^{-1}). This corresponds to almost 11% and 23% of the theoretical values respectively. Guerfi *et al.* showed that the rate performance of LFP in ionic liquids is strongly dependent on the viscosity and ionic conductivity of the electrolyte.[36] The high viscosity of EMI TFSI can make the lithium extraction from LFP structure more difficult even at low rates. Moreover, the electrolyte viscosity makes the wettability of the carbon layer on the surface of the LFP active particles more difficult. High viscosity can also mitigate the uniform wettability of the active particles, which could also contribute to the lower performance of LFP in ionic liquid. Upon reducing the scan rate (reducing the current intensity), the capacity of charging was improved. This agrees with the measurements in regular batteries. Note that coin cells measurements were also performed in our lab on LFP using the ionic liquid EMI TFSI, however low capacitites were obtained at different C-rates and the capacity was fading with time (see Figure C6 in Appendix C). This was attributed to the decomposition of the imidazolium-based ionic liquid when it is in contact with lithium metal used as the anode, which resulted in color change as represented in Appendix C (see Figure C7). The chemical instability of this ionic liquid in contact with lithium metal has been reported previously in the literature.[37]

In order to check if the SMCM is feasible to be used at low scan rates where the electrode material is limiting, the peak currents were extrapolated down to 0.05 mV/s scan rate, and the recorded values were in the range of 0.85 to 1.4 pA. These values are within the precision stability window of the instrument which can reach down to 500 fA. Although theoretically possible, performing the SMCM measurements at low scan rates is difficult. This is attributed to the salt precipitation obtained on the glassy carbon substrate, which blocks the electrochemical measurements that require long time (see Figure C5 Appendix C). Therefore, it is more likely to reach small scan rates by performing the SMCM measurements with lower salt concentration.

It is also important to consider that for the SMCM measurements, since we are not limited by ionic and electronic transport in the porous electrode, we can reliably enter into high-speed kinetics. This can be used to test theoretical dynamic models of lithium transport, in a dynamic range not attainable within a normal electrode.[38] Cyclic voltammetry or other potentiodynamic techniques may be initialized from any concentration of Li within the particle, as such, dynamic parameters like apparent diffusion coefficients may be obtained. Moreover, Overall, the ability to probe small aggregate of battery materials under anaerobic conditions and using emerging electrolyte creates new opportunities for fundamental studies of intrinsic material properties.

4.4 Conclusions

A new protocol was developed to probe the electrochemical activity of LIB materials using SMCM. In order to identify the optimum electrolyte, the stability and potential window for two different electrolytes (PC and EMI TFSI) were investigated using cyclic voltammetry. The voltammograms indicated that EMI TFSI was suitable to examine high energy materials as it was stable until 5.10 V vs. Li/Li$^+$. Open circuit potential measurements showed $Al_{1-x}Li_x$ to be sufficiently stable in EMI TFSI to be used as QRCE electrode. In addition, the EMI TFSI droplet stability was confirmed using MPT as a redox mediator.

Localized electrochemical measurements using SMCM and EMI TFSI electrolyte were performed on the LFP particles drop cast on a glassy carbon substrate. Comparing the localized and three-electrode cell measurements in the EMI TFSI electrolyte illustrated that SMCM in the presence of EMI TFSI can be successfully used to study conventional particles such as LFP and could be extended to study high energy particles such as NMC.

Our study showed that the glassy carbon is a better substrate compared to gold for the study of LIB active materials by SMCM. In addition, using ionic liquid in the newly developed SMCM probes improved the measured coulombic efficiency of the lithiation/delithiation. These results also indicated that the viscosity and wettability of ionic liquid and the particle to particle variations could have an effect on the peak resolution and peak splitting potential of Li intercalation/deintercalation.

4.5 Acknowledgements

This work is supported by Natural Sciences and Engineering Research Council of Canada (NSERC) and General Motors Company (Grant: NSERC/McMaster/APCPJ 412488-11) as well as NSERC (Grant: CRDPJ 494074-16). Authors would like to thank F. Wang, C. Heinemann, I. C. Halalay, and M. Jiang for scientific discussions and a critical reading of the manuscript. Microscopy and Imaging Lab (MILab) supported by the Quebec Center of Advanced Materials (QCAM) is also acknowledged for the technical assistance with AFM images.

4.6 References

1.Shi, Y.-L.; Shen, M.-F.; Xu, S.-D.; Qiu, X.-Y.; Jiang, L.; Qiang, Y.-H.; Zhuang, Q.-C.; Sun, S.-G. *Int. J. Electrochem. Sci* **2011,** 6, 3399-3415.

2.Levi, M. D.; Aurbach, D. *Characterization of Materials* **2002**, 1-21.

3.Fonseca, C. P.; Neves, S. *Journal of power sources* **2004,** 135, (1-2), 249-254.

4.Cornut, R.; Lepage, D.; Schougaard, S. B. *Electrochimica Acta* **2015,** 162, 271-274.

5.Lim, J.; Li, Y.; Alsem, D. H.; So, H.; Lee, S. C.; Bai, P.; Cogswell, D. A.; Liu, X.; Jin, N.; Yu, Y.-s. *Science* **2016,** 353, (6299), 566-571.

6.Gu, L.; Zhu, C.; Li, H.; Yu, Y.; Li, C.; Tsukimoto, S.; Maier, J.; Ikuhara, Y. *Journal of the American Chemical Society* **2011,** 133, (13), 4661-4663.

7.Xu, F.; Beak, B.; Jung, C. *Journal of Solid State Electrochemistry* **2012,** 16, (1), 305-311.

8.Zampardi, G.; La Mantia, F.; Schuhmann, W. *RSC Advances* **2015,** 5, (39), 31166-31171.

9.Takahashi, Y.; Kumatani, A.; Munakata, H.; Inomata, H.; Ito, K.; Ino, K.; Shiku, H.; Unwin, P. R.; Korchev, Y. E.; Kanamura, K. *Nature communications* **2014,** 5, 5450.

10.Lipson, A. L.; Ginder, R. S.; Hersam, M. C. *Advanced Materials* **2011,** 23, (47), 5613-5617.

11.Williams, C. G.; Edwards, M. A.; Colley, A. L.; Macpherson, J. V.; Unwin, P. R. *Analytical chemistry* **2009,** 81, (7), 2486-2495.

12.Snowden, M. E.; Dayeh, M.; Payne, N. A.; Gervais, S.; Mauzeroll, J.; Schougaard, S. B. *Journal of Power Sources* **2016,** 325, 682-689.

13.Lewandowski, A.; Świderska-Mocek, A. *Journal of Power Sources* **2009,** 194, (2), 601-609.

14.Balducci, A.; Jeong, S.; Kim, G.; Passerini, S.; Winter, M.; Schmuck, M.; Appetecchi, G.; Marcilla, R.; Mecerreyes, D.; Barsukov, V. *Journal of power sources* **2011,** 196, (22), 9719-9730.

15.Ohno, H., *Electrochemical aspects of ionic liquids*. John Wiley & Sons: 2005.

16.Ferrari, S.; Quartarone, E.; Tomasi, C.; Ravelli, D.; Protti, S.; Fagnoni, M.; Mustarelli, P. *Journal of Power Sources* **2013,** 235, 142-147.

17.Li, M.; Wang, L.; Du, T. *Journal of Applied Polymer Science* **2014,** 131, (20).

18.Swiderska-Mocek, A. *Electrochimica Acta* **2014,** 132, 504-511.

19.Garcia, B.; Lavallée, S.; Perron, G.; Michot, C.; Armand, M. *Electrochimica Acta* **2004,** 49, (26), 4583-4588.

20.Seki, S.; Kobayashi, Y.; Miyashiro, H.; Ohno, Y.; Usami, A.; Mita, Y.; Kihira, N.; Watanabe, M.; Terada, N. *The Journal of Physical Chemistry B* **2006,** 110, (21), 10228-10230.

21.Aaronson, B. D.; Lai, S. C.; Unwin, P. R. *Langmuir* **2014,** 30, (7), 1915-1919.

22.Aaronson, B. D.; Garoz-Ruiz, J.; Byers, J. C.; Colina, A.; Unwin, P. R. *Langmuir* **2015,** 31, (46), 12814-12822.

23.Ellis, B. L.; Lee, K. T.; Nazar, L. F. *Chemistry of Materials* **2010,** 22, (3), 691-714.

24.Yuan, L.-X.; Wang, Z.-H.; Zhang, W.-X.; Hu, X.-L.; Chen, J.-T.; Huang, Y.-H.; Goodenough, J. B. *Energy & Environmental Science* **2011,** 4, (2), 269-284.

25.Takahashi, M.; Tobishima, S.-i.; Takei, K.; Sakurai, Y. *Solid State Ionics* **2002,** 148, (3), 283-289.

26.Brodd, R. J., *Batteries for sustainability: selected entries from the encyclopedia of sustainability science and technology*. Springer Science & Business Media: 2012.

27.Wang, J.; Polleux, J.; Lim, J.; Dunn, B. *The Journal of Physical Chemistry C* **2007,** 111, (40), 14925-14931.

28.Levi, M. D.; Aurbach, D. *Journal of Electroanalytical Chemistry* **1997,** 421, (1-2), 79-88.

29.Gomadam, P. M.; Weidner, J. W.; Dougal, R. A.; White, R. E. *Journal of power sources* **2002,** 110, (2), 267-284.

30.Zhang, D.; Haran, B.; Durairajan, A.; White, R. E.; Podrazhansky, Y.; Popov, B. N. *Journal of Power Sources* **2000,** 91, (2), 122-129.

31.Augustyn, V.; Come, J.; Lowe, M. A.; Kim, J. W.; Taberna, P.-L.; Tolbert, S. H.; Abruña, H. D.; Simon, P.; Dunn, B. *Nature materials* **2013,** 12, (6), 518.

32.Shamsipur, M.; Beigi, A. A. M.; Teymouri, M.; Pourmortazavi, S. M.; Irandoust, M. *Journal of Molecular Liquids* **2010,** 157, (1), 43-50.

33.Wu, F.; Wang, M.; Su, Y.; Bao, L.; Chen, S. *Journal of Power Sources* **2010,** 195, (8), 2362-2367.

34.Wu, T.-Y.; Hao, L.; Chen, P.-R.; Liao, J.-W. **2013**.

35.Mi, C. H.; Zhang, X. G.; Li, H. L. *Journal of Electroanalytical Chemistry* **2007,** 602, (2), 245-254.

36.Guerfi, A.; Duchesne, S.; Kobayashi, Y.; Vijh, A.; Zaghib, K. *Journal of Power Sources* **2008,** 175, (2), 866-873.

37.Schmitz, P.; Jakelski, R.; Pyschik, M.; Jalkanen, K.; Nowak, S.; Winter, M.; Bieker, P. *ChemSusChem* **2017,** 10, (5), 876-883.

38.Kuss, C.; Trinh, N. D.; Andjelic, S.; Saulnier, M.; Dufresne, E. M.; Liang, G.; Schougaard, S. B. *The journal of physical chemistry letters* **2017,** 8, (24), 6160-6164.

Chapter 5

Probing the Effect of Ball Milling on the Structure and Properties of $LiNi_{1/3}Mn_{1/3}Co_{1/3}O_2$ Cathode Material

During the past decade, the market of LIBs has expanded from consumer electronics to more challenging applications such as spacecraft and vehicle electrification. Hence, considerable efforts have been devoted to developing rechargeable batteries with superior performances in order to meet the increasing energy demands. These batteries require higher energy density than currently available, but this remains a challenge for battery scientists given the limited choices of cathode materials existing. Recently, layered lithium metal oxides have been regarded as prospective cathode materials for LIBs, owing to their unique performance characteristics as well as for cost and availability considerations. In particular, $LiNi_{1/3}Mn_{1/3}Co_{1/3}O_2$ (NMC) has proven to be a promising candidate of active element of positive electrode for high energy LIBs, as it seems to integrate the features of $LiCoO_2$, $LiNiO_2$ and $LiMnO_2$. NMC also exhibits impressive stability upon cycling, high rate capability, and good safety features. In this viewpoint, it would be interesting to perform localized electrochemical measurements on NMC to probe the intrinsic material properties.

In Chapter 4, the application of SMCM technique was optimized to higher oxidation potentials, indicating the possibility to use it for investigating high energy LIBs materials. Chapter 5 presents the first attempt to visualize the electrochemical properties of the high energy cathode material NMC using SMCM. Localized cyclic voltammetry measurements were performed on the micron scale using the ionic liquid EMI TFSI in an inert atmosphere. In order to improve electronic conductivity of NMC particles and facilitate the localized electrochemical measurements, carbon black was introduced as a conductive additive between the NMC particles. Both chemical and mechanical methods were examined for the carbon addition process. The chemical coating was performed under argon atmosphere via thermal decomposition of sucrose, which was used as the carbon source. On the other hand, the mechanical approach was accomplished via ball milling of NMC with carbon black. Different ball milling parameters were explored, including the time and the number of balls used, as well as milling with and without carbon in dry and wet conditions. TGA analysis was used to estimate the exact carbon content of the ball-milled samples. The influence of ball milling conditions on the crystal structure and the crystallite size of NMC was also determined with XRD. SEM imaging was used to determine changes in microstructure from the ball milling process, and TEM imaging was used to visualize the carbon layer and measure its thickness. The electrochemical performance of the NMC samples before and after ball milling was examined by coin cells measurements. The discharge capacity was recorded at different rates to compare the electrochemical behavior of NMC samples at different milling conditions, and in the presence and absence of carbon.

5.1 Introduction

In the past decade, rechargeable lithium-ion batteries (LIBs) have emerged as the dominant power source for portable electronic devices such as cellular phones, digital cameras, and laptop computers.[1-2] Owing to their unique advantages such as high energy density and cyclability,[3-4] the use of LIBs has been expanded. Currently, LIBs are applied in robotic technology,[5] aerospace industry,[6-7] as well as in powering emission-free vehicles.[8-9] Cathode materials play a significant role in determining the performance of LIBs. Recently, the layered-structured active material with a composition of Li–Ni–Mn–Co–O has been proposed as a possible alternative to the commonly used $LiCoO_2$ in LIBs, taking advantage of the lower cost and toxicity of Ni and Mn compared to Co. Among many investigated compositions, the ternary transition metal oxide $LiNi_{1/3}Mn_{1/3}Co_{1/3}O_2$ (abbreviated as NMC), has been reported one of the most promising candidates in high energy rechargeable LIBs.[10] This material exhibits good cycle life,[11-12] and it possesses sufficiently high structural[13] and thermal stability[14-17] to phase transition and oxygen loss. NMC also delivers a reversible capacity of 160 mAh/g in the voltage range of 2.8–4.3 V.[18-19] When charged up to 4.6 V or higher, capacities more than 200 mAh/g has been achieved,[20-21] although this comes at the expense of capacity retention.[22-23] Efforts to improve the performance of NMC cathodes have included optimization of the material structure,[24] variation of the material composition,[12] and addition of dopants such as Na and Al.[25-26] Previous reports have also demonstrated that conductive polymers, when used as a coating layer, can facilitate the electron transport in NMC and restrain the electrode directly connected with the electrolyte during the charge/discharge processes.[27-30] Moreover, modification of the NMC surface by coating with electrically conductive material, such as carbon[31-35] and exfoliated graphene,[36-38] has been directed to enhance its electronic conductivity.

LIB cathodes that can be rapidly oxidized and reduced while retaining high capacities are strongly desired for electric vehicles.[39] However, conventional NMC cathodes showed a significant decay in the capacity at high discharge rates.[40] Multiple transport phenomena are involved in electrochemical charge storage process, which influence the overall electrode performance. These include interfacial charge transfer, electrode–current collector contact resistance, electronic conductivity of the electrode particles, interparticle contact, solid-phase diffusivity (Li-ion diffusion within the electrode particle), and electrolyte diffusivity (Li-ion diffusion in the electrolyte within the cathode). Among these, the diffusion of Li-ions within the electrode particles has been verified as the rate-determining step for the discharge process at high rates.[40]

Therefore, evolution to nanostructured materials that provide high surface area have been extensively explored in an attempt to enhance the kinetic properties.[12, 41-44] It is expected that the production of nanostructures may result in the reduction of the diffusion length of the Li-ions within the host lattice, and hence, in the improvement of the electrode charge/discharge rates. Ball milling has been demonstrated to be an effective mechanical process for reducing particle size for a wide range of energy related materials,[45] such as $LiFePO_4$,[46-47] $LiMnPO_4$,[48] and $LiMn_2O_4$.[49-50] Other studies have also focused on ball-milled NMC[51-53] and similar transition metal oxide materials for a better electrode performance.[54-55] However, the choice of the ball-milling parameters (such as milling time, speed, and number of balls used) can significantly affect the structural and electrical properties of NMC, as supported by prior work.[56] Aggressive milling conditions induced smaller NMC crystallite sizes but also diminished the electrochemical performance, while mild milling conditions provided intermediate NMC crystallites with higher capacities and improved rate capabilities.

Rational improvement of battery technologies requires fundamental studies of the intrinsic material properties. Although standard electrochemical techniques have been used to study the structural transformations and the physicochemical processes in battery materials,[57-59] the heterogeneity of the electrode composite film leads to difficulties in data interpretation. To address this issue, scanning electrochemical probe microscopes have been developed. These techniques have proven powerful to visualize localized electrochemical properties of many electrode surfaces, as exemplified by the scanning electrochemical microscopy (SECM)[60] and related techniques.[61-64] In Chapter 3 and 4, we have shown that the scanning micropipette contact method (SMCM) can be applied in an inert atmosphere to probe particle-to-particle variation of properties of $LiFePO_4$ active material. Measurements were first performed using organic electrolyte[65] and later with ionic liquid.[66]

In this chapter, the SMCM technique was applied to investigate NMC cathode material using the ionic liquid 1-ethyl-3-methylimidazolium bis(trifluoromethylsulfonyl)imide (EMI TFSI). In order to reduce the electronic resistance between the active material and the glassy carbon working substrate, the conductive additive carbon black was introduced between the NMC particles. This was achieved either by mixing the NMC with carbon via ball milling at different conditions, or by chemically coating the active particles with carbon via sucrose carbonization. The discharging capacity of the NMC starting material and the ball-milled samples were also tested and compared by coin cells measurements. Different ball milling parameters were explored, including the time and the number of balls used, as well as milling with and without carbon in dry and wet conditions. The obtained samples were analysed by thermogravimetric analysis (TGA) in order to calculate the exact carbon content achieved after ball milling. X-ray diffraction (XRD) was used to determine the crystallinity of the samples and monitor the changes of the crystallite sizes after ball milling. The samples were further characterized by scanning electron microscopy (SEM) and transmission electron microscopy (TEM) to explore the morphological changes of the particles from the ball milling process and to estimate the carbon layer thickness. To allow differentiation between the notations of particles used throughout the text, it is worth to clarify here that crystallites are observed from the XRD analysis, whereas secondary particles are observed from SEM images. The secondary particles are aggregates of smaller particles. After ball milling, the secondary particles break up and form aggregate structures that are composed of smaller particles compared to the unmilled NMC sample.

5.2 Experimental Section

5.2.1 Samples Preparation

Ball milling: The mechanical reaction of the NMC samples was carried out in an FTS MM400 shaker mill using 30 mL stainless steel milling jars containing either NMC starting material, or 80% NMC and 20% carbon black (Timcal graphite and carbon Super P conductive carbon black). The ball milling was performed at a speed of 1770 rpm for different durations and using either 1 or 2 stainless steel milling balls according to details described in Table 5.1. Before ball milling, the stainless steel jars were loaded with 300 mg batches within an argon-filled glovebox (MBraun, O_2 and H_2O levels $\leqslant$1 ppm). The jars were sealed under vacuum to prevent oxygen exposure during the milling process. After ball milling, the samples were removed from the milling jars and stored in the argon-filled glovebox. In the case of wet ball milling, the starting materials were mixed in a planetary ball mill with isopropanol (ratio of 1.6 g/30 mL) using 80 mL milling jars and 100 balls per container. The mill was operated at a speed of 250 rpm.

Table 5.1: Sample identification (ID) and ball milling conditions utilized for NMC samples.

Sample ID	Milling time	Number of balls	Ball size	Milled with carbon
NMC starting material	—	—	—	—
NMC-20-1	20 min	1	1 cm	No
NMC-20-2	20 min	2	1 cm	No
NMC-45-1	45 min	1	1 cm	No
NMC-45-2	45 min	2	1 cm	No
NMC-CC-20-1	20 min	1	1 cm	Yes
NMC-CC-20-2	20 min	2	1 cm	Yes
NMC-CC-45-1	45 min	1	1 cm	Yes
NMC-CC-45-2	45 min	2	1 cm	Yes
NMC-wet	3 hours	100	3 mm	No
NMC-CC-wet	3 hours	100	3 mm	Yes

Chemical coating: The as-received NMC was mixed with 30 wt% sucrose powder (99.5% Sigma Aldrich) in water. The resulting wet precipitate was dried in the oven overnight at 90 °C. The sample was then calcined at 650 °C for 6 h in a tubular furnace flowing under argon gas to achieve the carbon coating.

5.2.2 Material Characterization

The crystal structure of each sample was characterized by power X-ray diffraction (XRD) on a Bruker D8 advance diffractometer (Bruker AXS, Madison, WI) using Ni-filtered Cu-Kα radiation (λ=0.15406 nm). The source was operated at 40 kV and 40 mA. The 2θ angular scan was explored from 10° to 90° (only 10° to 70° data are presented here) with an integration time of 1 second. For all the XRD measurement, the resolution in the scans was kept at 0.02°. The X-ray diffraction patterns were interpreted using the Crystallographic crystal study database (CCSD). Crystallite size for the pristine and ball-milled samples was estimated using the Scherrer equation:

$$L = K.\lambda/\beta.cos\theta \qquad (5.1)$$

where L is the crystallite size, K is the Scherrer constant used as 1.0 for the analysis herein, λ is the wavelength of the X-ray, β is the full width at half maximum (FWHM) in radians, and θ is the Bragg angle. Note that the calculation of the crystallite size in this case has not been corrected for machine broadening, and therefore the reported numbers in Table 5.2 might not be very accurate. This is just meant as an estimation in order to get an idea about the trend of the crystallite size obtained after ball milling and upon changing the ball milling parameters.

Thermogravimetric analysis (TGA) for the NMC starting material and the ball-milled samples was performed using a Mettler-Toledo TGA/DSC 1 Star System thermobalance to monitor the weight loss/gain processes. For this purpose, samples were loaded in alumina crucibles and the data were collected at a heating rate of 10 °C/min between 30 and 800 °C under dynamic atmosphere of nitrogen and air. The flow rates of the purge gas and sample gas were set at 50 mL/min and 50 mL/min respectively. The morphology and microstructure of the NMC particles were examined on a field emission scanning electron microscope (FEI Inspect F50 FE-SEM) with an accelerating voltage of 10.0 kV. In order to avoid charge accumulation during observation, a 4-nm-thick layer of platinum was deposited by cathodic sputtering on the surface of the materials. The thickness of the surface carbon layer on NMC particles was determined by transmission electron microscopy (Philips CM200 TEM) operating at 200 kV. Powder samples were collected on a micro-grid supported on a carbon-coated copper grid.

5.2.3 Electrochemical Measurements

5.2.3.1 Coin Cells Measurements

The NMC starting material used in this study is commercial and has no carbon coating. To prepare lithium coin cells (CR-2032), electrodes were fabricated by mixing 80% NMC (either as-received or ball-milled), 10% carbon black (Super C5, Timcal), 10% polyvinylidene difluoride (PVDF, Kynar), in N-methyl-2-pyrrolidone (NMP, 99% Sigma Aldrich). PVDF was dissolved in NMP prior to adding active material. For every gram of active material, 3.5 ml of NMP was used. The mixed slurry was cast onto a carbon coated aluminum foil (Exopack) current collector. The resulting electrode films were then dried, first in air at 60 °C for 4 h, and then under vacuum at 100 °C overnight. The cast electrode sheets were punched into disks of 15 mm diameter that is ~20 μm thick and having a mass loading of ~5 mg/cm^2 in total (active material,binder and conductive additive). Electrochemical cells were assembled in an argon-filled glovebox (with O_2 and H_2O levels maintained below 1 ppm) using the prepared NMC disks as the cathode and lithium metal (99.9% Alfa Aesar) as the anode, separated by microporous separator (Celgard 2500). The electrolyte solution was 1 M $LiPF_6$ in a mixture of ethylene carbonate (EC) and dimethyl carbonate (DMC) (1:1 volume ratio, Novolyte). Electrochemical cells were cycled in a galvanostatic mode at different scan rates with a potential window between 2.5–4.3 V. The cycling of the cells was performed at room temperature with a Bio-Logic VMP3 potentiostat.

5.2.3.2 SMCM Measurements

The experimental setup of the SMCM technique represented in Figure 5.1 is composed of two parts: (1) a micropipette, which acts as both a scanning tip and a micro-electrochemical cell containing the electrolyte, and (2) a conductive substrate, which acts as the working electrode. Micropipettes of 1 μm tip diameter were pulled from standard quartz capillaries (Sutter Instruments) of dimensions 1.0 × 0.3 mm (o.d. × i.d.), using a laser puller (P-2000, Sutter Instruments, U.S.A.). The outer wall of the tip was silanized with perfluoro-octyl silane (Sigma

Aldrich), rendering it hydrophobic, in order to confine the electrolyte meniscus to the apex of the tip. An $Al_{1-x}Li_x$ quasi-reference counter electrode (QRCE) was inserted at the unpulled end of the micropipette serving as both counter electrode and reference electrode. The fabrication of the $Al_{1-x}Li_x$ QRCE was carried out using a three-electrode setup.[65] An Al wire (125 µm diameter, Good Fellows) serving as the working electrode, and 2 Li metal strips as counter and reference electrodes were immersed into 0.25 M $LiClO_4$ propylene carbonate (PC 99.7% Sigma Aldrich) solution. Li deposition was performed galvanostatically (constant current of -300 mA) for 30 minutes. The stability of the QRCE was then verified by measuring the open circuit potential (E = 0.330 V vs. Li/Li^+) in the ionic liquid 1-ethyl-3-methylimidazolium bis(trifluoromethylsulfonyl)imide (EMI TFSI 99.5% Iolitech) before and after electrochemical measurements.[66]

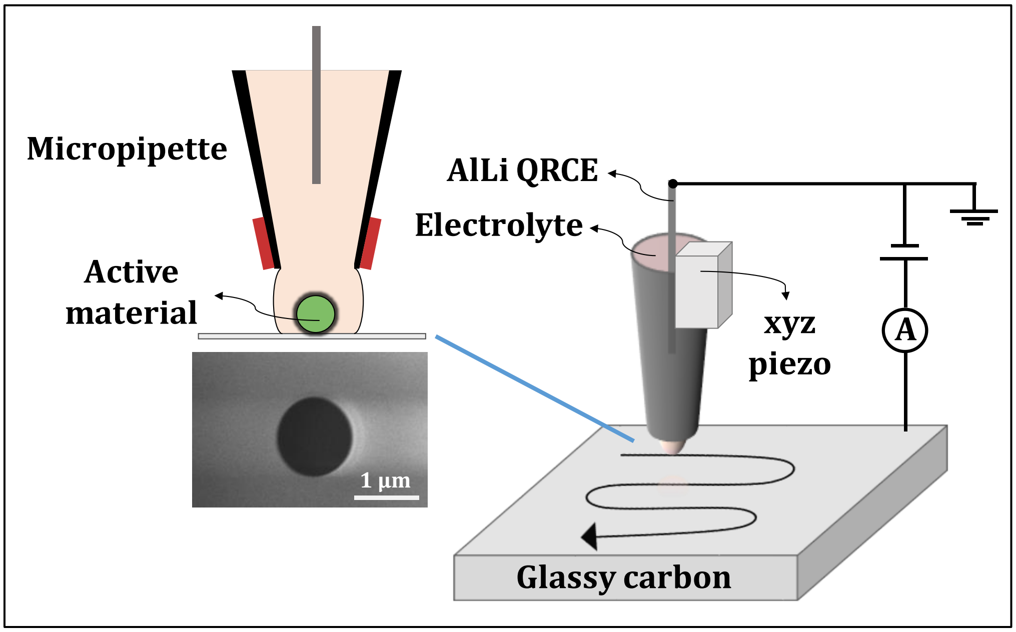

Figure 5.1: Schematic diagram of SMCM system with pipette of 1 µm tip diameter (inserted SEM image).

It should be noted that the potential scale is reported with respect to Li/Li^+ throughout this chapter for ease of comparison with the existing battery literature. The principles and operation of the technique are similar to those reported previously in Chapter 3 and 4,[65-66] but the cathode material NMC is being tested herein. To prepare the NMC substrate for SMCM measurements, a suspension of NMC particles (either as-received or ball-milled) was prepared in isopropanol (3 mg/ml) and drop-cast on the conductive glassy carbon (GC) support. The micropipette, that was filled with electrolyte solution (0.1 M LiTFSI salt solution in EMI TFSI ionic liquid) and housing the $Al_{1-x}Li_x$ QRCE, was connected to the piezo-electric controls (*x*, *y*, *z* arrangement) of the ElPro Scan 3 instrument (HEKA Electronics, Germany). The probe was lowered towards the surface of the glassy carbon substrate (at 1 μm s^{-1} rate), using the *z*-micropositioner until it made contact with the substrate. Upon wetting of the substrate, the electrochemical circuit was completed between the QRCE and the working electrode. This entailed a spike in the measured current that was used to trigger the approach curve ending, therefore ensuring that no direct contact was made between the micropipette and the substrate surface decorated with NMC active material. Cyclic voltammetry measurements were then performed at different scan rates (ranging between 200 to 5 mV s^{-1}) using the same potentiostat, before retracting the pipette. Following electrochemical measurements, the micropipette was moved to new locations for subsequent measurements.

5.3 Results and Discussion

5.3.1 SMCM Measurements on NMC Before Ball Milling

The SMCM measurements were implemented using 1 μm pipette filled with 0.1 M LiTFSI in EMI TFSI. The micropipette landed on the pristine NMC cathode material dispersed on glassy carbon substrate. The working electrode/electrolyte interface was created at locations defined by the area of the droplet wetting the surface (in the present case ~10 μm). The stability of the droplet formed by the ionic liquid EMI TFSI was previously confirmed using the redox mediator MPT.[66] The cyclic voltammogram for the charging/discharging of the NMC starting material displayed in Figure 5.2 did not show any significant electrochemical response. Only a background signal of the glassy carbon substrate was collected. Since NMC starting material proved to be active in the coin cells measurements (see section 5.3.5.1), the poor electrochemical bahavior in SMCM suggests high electronic resistance existing between the NMC particles and the glassy carbon substrate. To enhance the conductivity, carbon black was introduced between the NMC particles to enable the investigation of NMC by SMCM (see section 5.3.5.2).

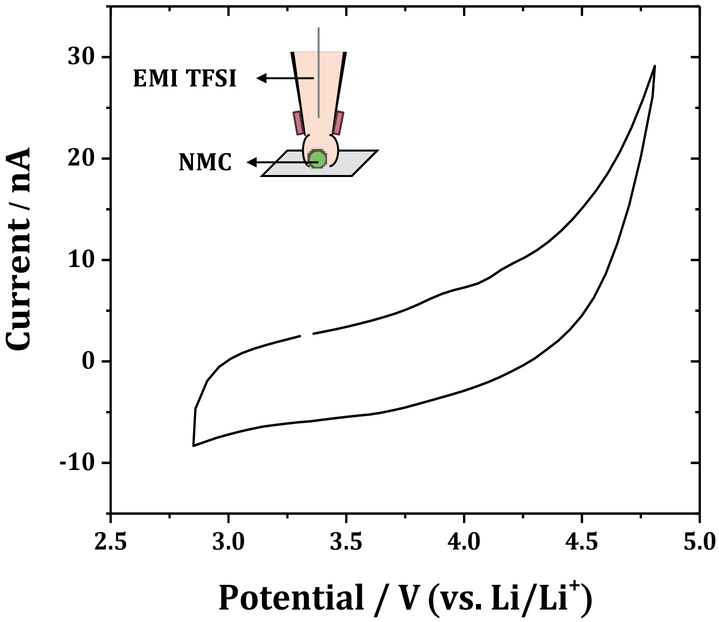

Figure 5.2: Cyclic voltammograms obtained at 50 mV s^{-1} using SMCM with 0.1 M LiTFSI in EMI TFSI on pristine NMC cathode material dispersed on a glassy carbon electrode.

5.3.2 Effect of Ball Milling on the Structure of NMC

To explore the effect of ball milling and carbon mixing on the crystalline structure of NMC cathode material, XRD tests were carried out and the results are shown in Figure 5.3. All milled samples (b-k) showed similar diffraction patterns that are typical of the layered hexagonal α-$NaFeO_2$ crystal structure with crystallographic space group $R\bar{3}m$ (space group no. 166). The structure consists of layers of edge sharing MO_6 octahedra (M = Ni, Co, Mn) and Li-ions arranged between them in the octahedral interstitial sites.[12, 18, 43, 67] The similarity in peak positions obtained between the unmilled sample (a) and all milled samples (b-k) clearly indicates that the ball milling did not change the crystal structure of the material. However, the peak intensities and peak widths were significantly changed. The sharp peaks of the diffraction pattern reveal high crystallinity of the NMC powder, whereas the increase in the peaks width suggest a decrease in the crystallite size.

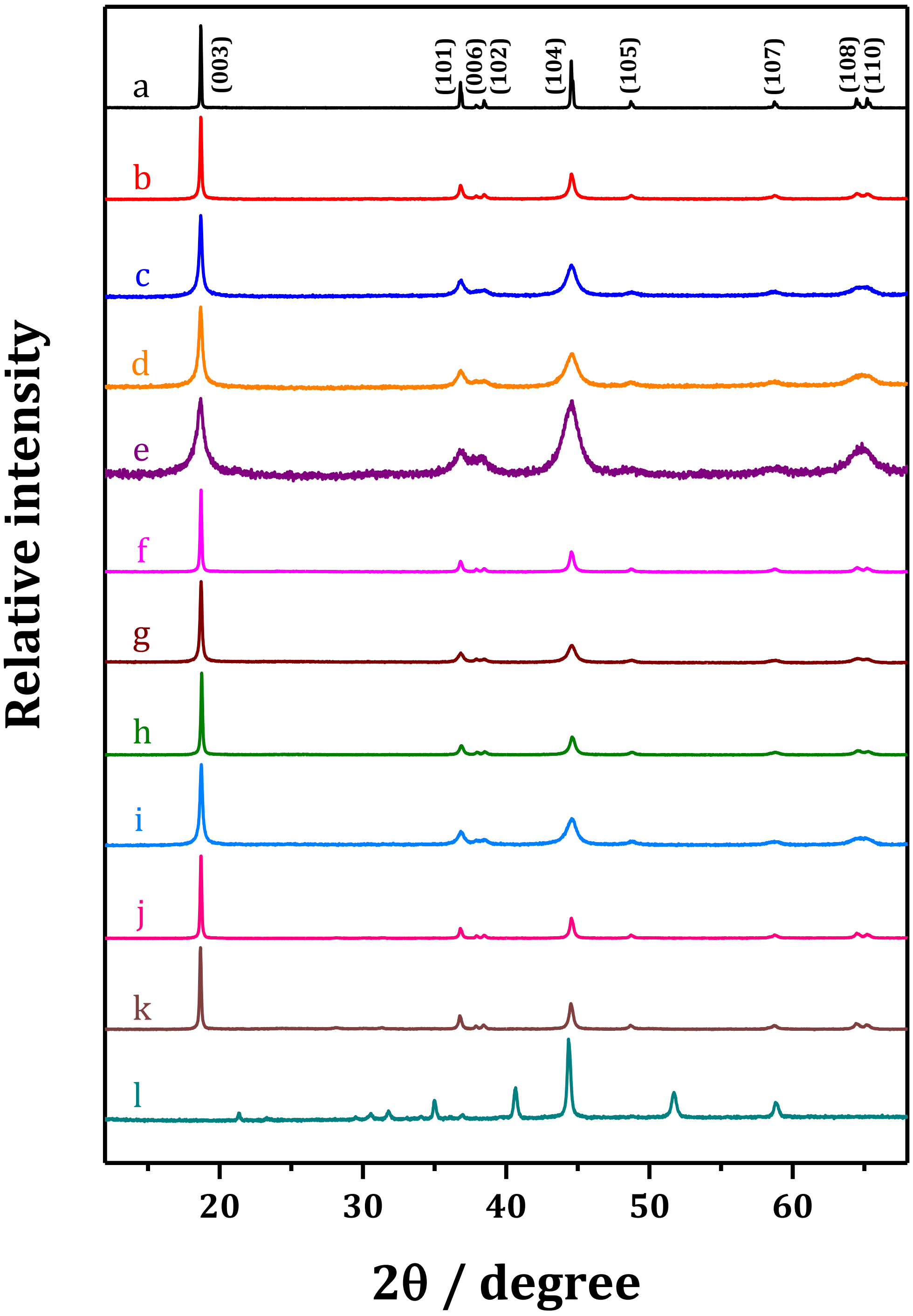

Figure 5.3: Comparison of powder X-ray diffraction (XRD) patterns of NMC pristine sample (a), NMC samples ball-milled at different conditions: NMC-20-1 (b), NMC-20-2 (c), NMC-45-1 (d), NMC-45-2 (e), NMC-CC-20-1 (f), NMC-CC-20-2 (g), NMC-CC-45-1 (h), NMC-CC-45-2 (i), NMC-wet (j), NMC-CC-wet (k), and the chemically carbon coated sample NMC-sucrose (l). Miller indexes of main reflections are indicated.

From the limited number of conditions evaluated in this study, substantial changes in the crystallinity of the samples and their corresponding crystallite size were obtained upon performing the ball milling, and upon changing the milling conditions. Compared to the as-received NMC material, the ball milling was determined to lower the crystallinity of the samples and resulted in smaller crystallites under all the tested conditions. This observation was more pronounced when the number of balls and milling time were increased. The increasing peak width is displayed in the exploded view of the (003) peak in Figure 5.4 for the ball-milled samples without carbon. Nevertheless, mixing with carbon in dry conditions (while keeping all other milling conditions constant) maintained larger crystallites when compared to the milled samples with no carbon (see Table 5.2). This is opposite to the results obtained in wet milling, where the size of the crystallites decreased upon mixing with carbon as compared to NMC-wet with no carbon.

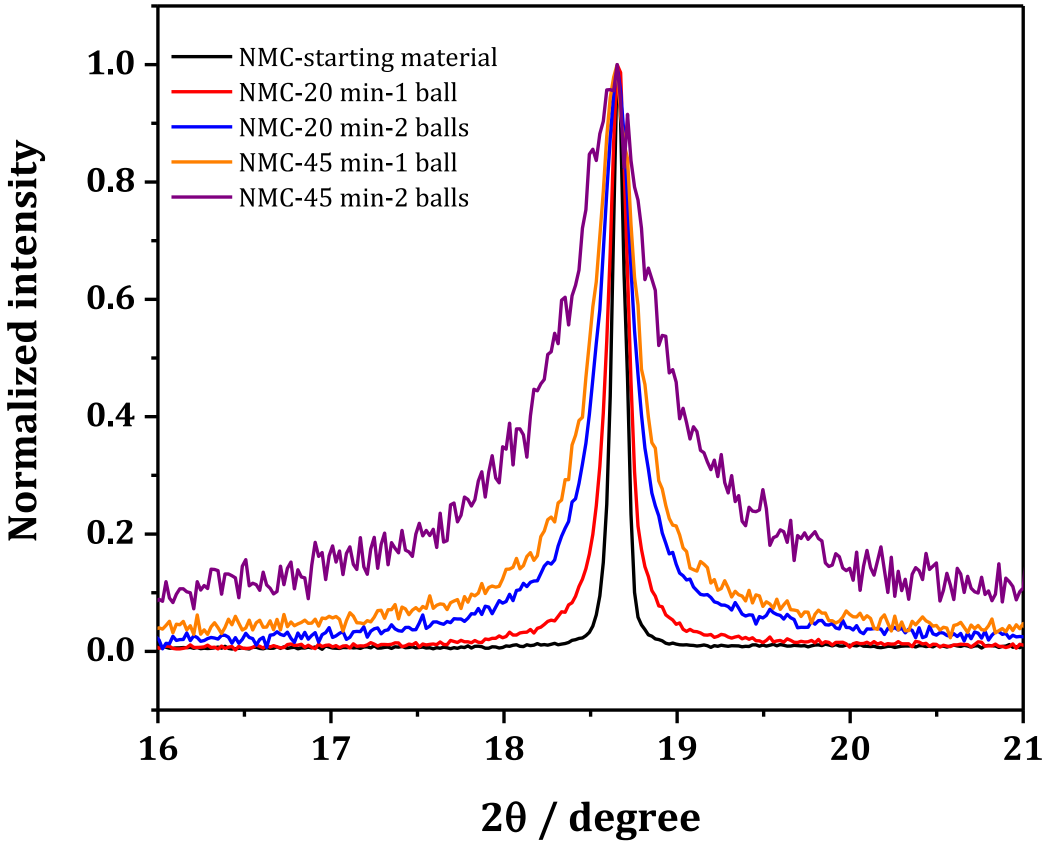

Figure 5.4: Expanded range of XRD patterns for 2θ between 16 and 21 degrees showing the change in the peak width for the ball-milled samples as a function of the milling conditions (different times and different number of balls).

As shown in Figure 5.3, the highly resolved splitting of (006)/(102) and (108)/(110) peaks of the NMC starting material (a) provides evidence of a characteristic well-ordered layered structure.[68-70] The splitting of these doublets however became less noticeable upon milling for a longer time as the case of sample (d), and it completely disappeared upon using 2 balls (samples c and e) where the peaks merged. This indicates that the ball milling is distorting the ordering of NMC. However, when NMC is ball milled with carbon, the (006)/(102) and (108)/(110) doublets split again as shown in Figure 5.3. Yet, the splitting became less resolved in the case of samples (g) and (i) where 2 balls were used. This suggests that carbon formed kind of a protective layer that was preventing the complete destruction of the NMC crystalline structure during ball milling, but it was less effective upon using 2 balls. Moreover, the ratios of the integrated intensities of the (003) and the (104) peaks $I_{(003)}/I_{(104)}$ in the XRD patterns has been considered as one of the indicators of the degree of cation mixing.[69, 71-72] This cation mixing is known to be one of the sources of deterioration of the electrochemical performance of NMC.[14, 73] Generally, it is believed that the materials have a smaller degree of cationic disorder when the value of $I_{(003)}/I_{(104)}$ is beyond 1.2. The ratios of the intensities of the main (003) and (104) XRD peaks, and the crystallites size calculated from Scherrer's equation are summarized in Table 5.2.

Table 5.2: Listing of ratios of the XRD peaks intensities for the pristine and ball-milled NMC samples at different conditions. Crystallite size of samples was determined via Scherrer analysis of X-ray diffraction.

Sample ID	Crystallite size (nm)	$I_{(003)}/I_{(104)}$
NMC starting material	85.7	1.24
NMC-20-1	64.2	1.20
NMC-20-2	37.9	1.02
NMC-45-1	30.1	1.10
NMC-45-2	15.2	0.67
NMC-CC-20-1	70.5	1.63
NMC-CC-20-2	51.8	1.06
NMC-CC-45-1	66.2	1.53
NMC-CC-45-2	40.5	1.01
NMC-wet	68.6	1.9
NMC-CC-wet	64.7	1.35

A high degree of cation ordering of lithium and transition metal ions in the NMC crystal lattice was inherent in the pristine and ball-milled NMC samples with 1 ball, as indicated by high integral intensity ratios. However, lower ratios were obtained for samples milled with 2 balls, which suggests that the cation mixing was more pronounced in these cases, and thereby the electrochemical activity of these cathode materials is expected to be diminished as will be discussed later. This interpretation is consistent with the previous results, where the use of 2 balls also resulted in distorted structure. In the case of wet milling, the ordered layered structure of NMC was retained with and without carbon mixing as reflected by the doublet splitting and the high integral intensities of the (003) and the (104) peaks (calculated values are reported in Table 5.2). Note that annealing the distorted NMC samples obtained after the ball milling step (at 800 °C for 6 hours) resulted in sharper and stronger diffraction peaks of the material as represented in Appendix D (see Figure D3). In addition, the ratio of intensities of the (003) and (104) peaks increased, and the two pairs of doublets (006)/(102) and (108)/(110) became well resolved. This indicates that annealing allows crystallites to grow and defects to heal which could enhance the electrochemical activity.

On the other hand, the diffraction peaks of the NMC-sucrose (l) were significantly different from the pristine NMC material (a). The peaks could not be indexed based on the $R\bar{3}m$ structure indicating chemical modifications. The thermal decomposition of sucrose in an inert atmosphere generates a strong reductive environment like H_2 and CO, which could have easily reduced the transition metals in NMC and changed their valence state and the crystal structure of the oxide material.[74]

5.3.3 TGA Analysis of NMC before and after Ball Milling

Figure 5.5A represents the TGA curve of the pristine NMC cathode material. The gradual heating of the sample up to 800 °C did not lead to significant weight loss (~0.3% only). This indicated that the NMC starting material has a good thermal stability in the tested range of temperatures. In contrast, ball milling of NMC for 20 minutes using 1 ball showed 5.9% of weight loss (Figure 5.5C). The weight loss gradually increased with increased milling time and the number of balls used and it reached 10.2% in the case of NMC-45-2. This weight loss was attributed to the small amounts of oxygen release occurring during heating.[15-17] The TGA curve of carbon black represented in Figure 5.5B revealed that the complete oxidization and decomposition of carbon happened after 750 °C. Mixing of NMC with carbon during ball milling resulted in higher weight loss (~20.1%) as Figure 5.5D displays. Similar results were obtained with all NMC samples ball-milled with carbon at different conditions, where the weight loss ranged between 22.6 and 24.5%. The weight loss in the NMC-CC samples between 0–450 °C is assigned to the evolution of carbon dioxide gas resulting from the combustion of carbon. The obtained TGA results were then used to calculate the exact percentage of carbon resulting from ball milling, compared to the theoretical 20% amount added. By subtracting the weight loss of the ball-milled sample before and after carbon addition, the carbon content was found to be ~15% for the dry milled samples and ~20% for the wet milled samples. This 5% loss in the percentage of carbon obtained in the dry milling might be due to the residues of carbon left on the walls of the milling jars and the milling balls.

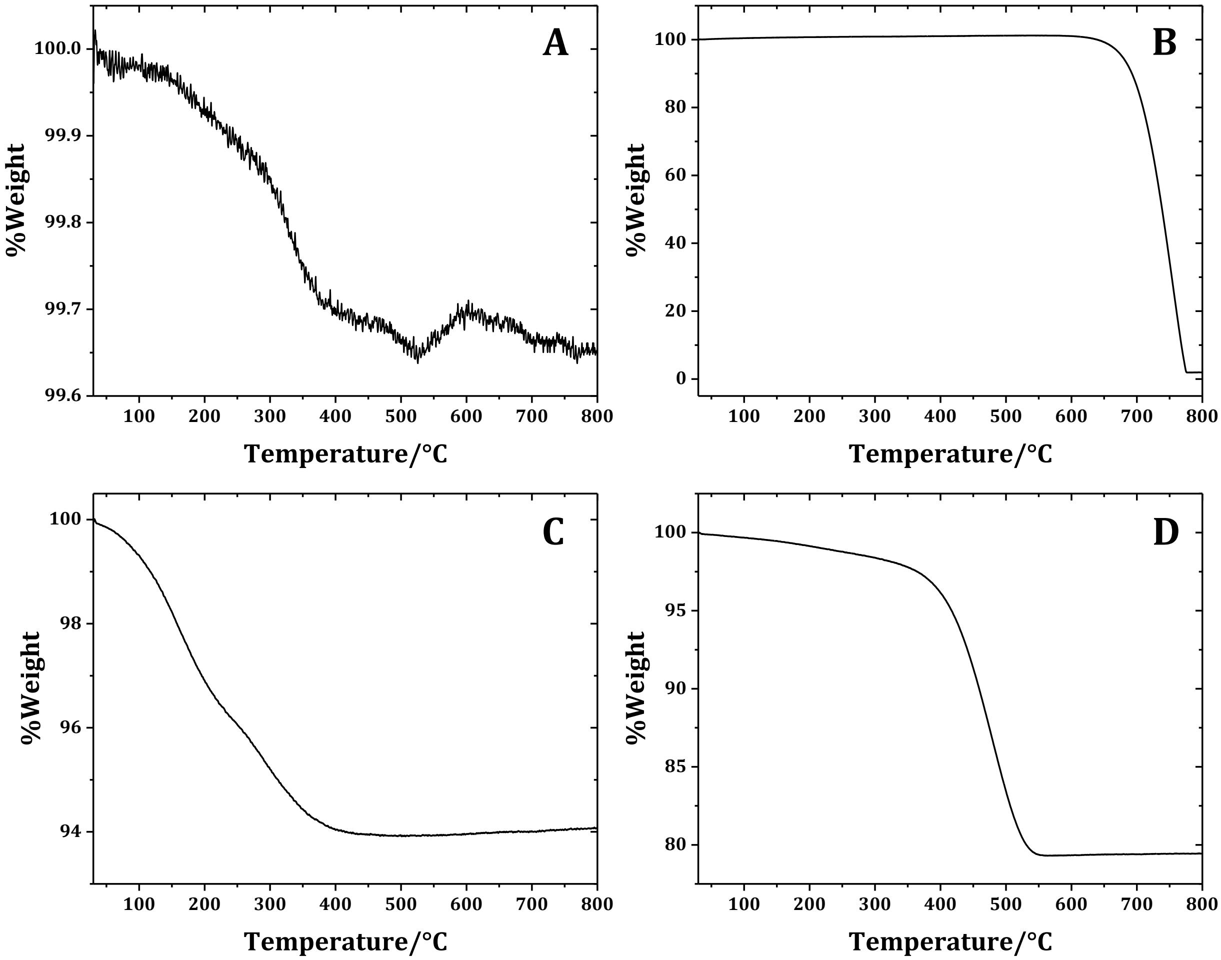

Figure 5.5: Thermogravimetric analysis profiles for NMC starting material (A), carbon black (B), NMC-20-1 (C), and NMC-CC-20-1 (D).

5.3.4 Morphological Characterization of NMC

Typical SEM micrographs of the pristine and ball-milled NMC samples are displayed in Figure 5.6. As Figure 5.6A shows, the pristine NMC material consists of well-developed regular small particles with diameters in the range of 0.3–1.9 μm and an average of 0.71 μm. It should be noted that the dimensions of these small particles are about one order of magnitude larger than the crystallite size (~86 nm) estimated from the XRD pattern, so that these small particles should not be confused with the crystallites. The small particles aggregate to form larger secondary particles with a broad diameter range [6.5–21 μm] (see Figure D1 in Appendix D). After ball milling, the morphology of the NMC evolved from individual small particles for the pristine material, to more sintered and therefore smaller particles for the NMC-20-1 (Figure 5.6B). The particles obtained for 20 minutes milling with 1 ball have nanometer dimensions with an average of 227 nm. Increasing the milling time and the number of balls resulted in similar morphologies but smaller particles with an average of 145 nm, 132 nm and 97 nm for the NMC-45-1, NMC-20-2, and NMC-45-2 respectively. In the case of wet milling, the small particles appeared with irregular shapes that have plate-like morphology (Figure 5.6D). These particles have an average size of 0.72 μm, which is comparable to the average size calculated for the pristine sample. The small particles size trend with milling conditions agreed with the crystallite sizes estimated from the XRD patterns. SEM imaging at a low magnification showed that the variation in ball milling conditions influenced the relative concentration of the secondary particles. From Figure D1 two distinct trends emerge: (1) break-up of the secondary particles and (2) formation of aggregate structures. The extent to which these occur depends on the milling intensity. The sample with the most aggressive milling conditions (NMC-45-2) showed a significant reduction of secondary particles and a higher degree of aggregates formation compared to the NMC-20-1 milled at lower intensity conditions. From the SEM images for dry (Figure 5.6C) and wet (Figure 5.6E) milling of NMC mixed with carbon, the particle morphology was similar to that observed prior to carbon addition (Figures 5.5B and D, sintered particles in dry milling and plate-like particles in wet milling). Given that the carbon particles are spherical in shape (see the inset of Figure 5.6C), it was easier to distinguish between the carbon and NMC particles in the case of wet milling compared to dry milling. Yet, the surface of the NMC material during dry milling showed higher roughness than the ball-milled sample without carbon. This provides evidence for the presence of carbon on the surface and in between the NMC particles in the dry milled sample. Figure 5.6F represents the SEM micrograph of the chemically carbon coated NMC sample using sucrose. In this case, NMC presents non-homogeneous particle morphology with some spherical carbon particles existing on the NMC particle surface.

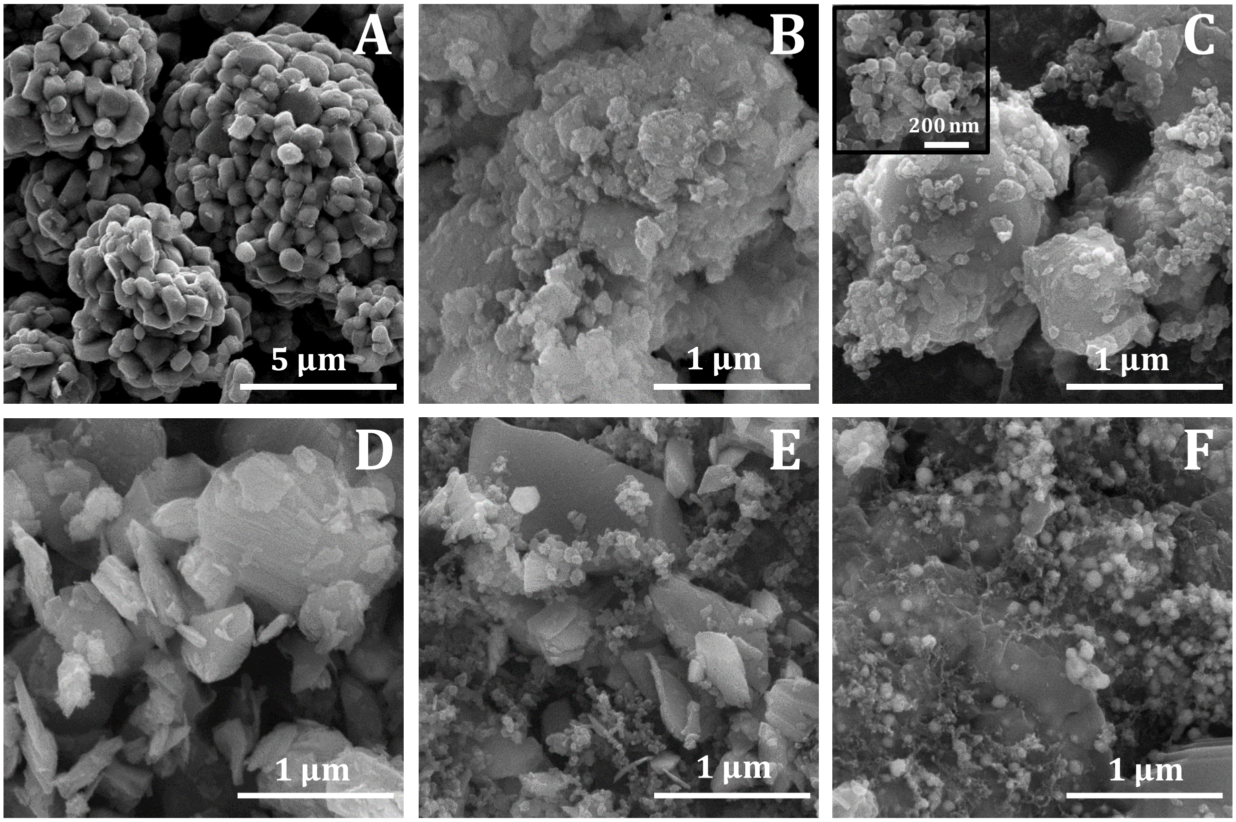

Figure 5.6: SEM images of the pristine NMC material (A), ball-milled NMC samples at different conditions: NMC-20-1 (B), NMC-CC-20-1 (C), NMC-wet (D), NMC-CC-wet (E), and the chemically carbon coated sample NMC-sucrose (F). The inset in (C) represents the SEM image of the carbon black used during ball milling.

From TEM imaging (Figure 5.7), the morphology of the pristine NMC particles was smooth across the edge and showed facetted surface as indicated in Figure 5.7A. These well-resolved lattice fringes designate the crystallinity of the sample. At a smaller scale, the measurement of the fringe spacing was found to be around 0.47 nm (see Figure 5.7B). This corresponds to the spacing between the (003) planes of the hexagonal layered materials, which is in agreement with the XRD results. Figure 5.7C represents the TEM image of NMC after ball milling with carbon in dry conditions. The micrograph clearly shows that after ball milling, the morphology of the spherical NMC particles changed (compared to Figure 5.7A) and the size decreased as well. Moreover, the carbon forms a nonhomogeneous layer around the NMC particles with a thickness of 42 nm to 178 nm. A closer image showing the NMC-carbon layer formed after ball milling is displayed in Figure 5.7D. Similar results were obtained in the case of wet milling (Figure 5.7E), where the thickness of the irregular carbon layer ranges between 62 to 185 nm. In contrast, the use of sucrose to coat the NMC with carbon chemically resulted in a uniform carbon coating surrounding the NMC particles as shown in Figure 5.7F. The thickness of this carbon coating varied between 2.4 to 8.5 nm, which is about two orders of magnitude thinner than the carbon layer obtained in the case of dry and wet ball milling.

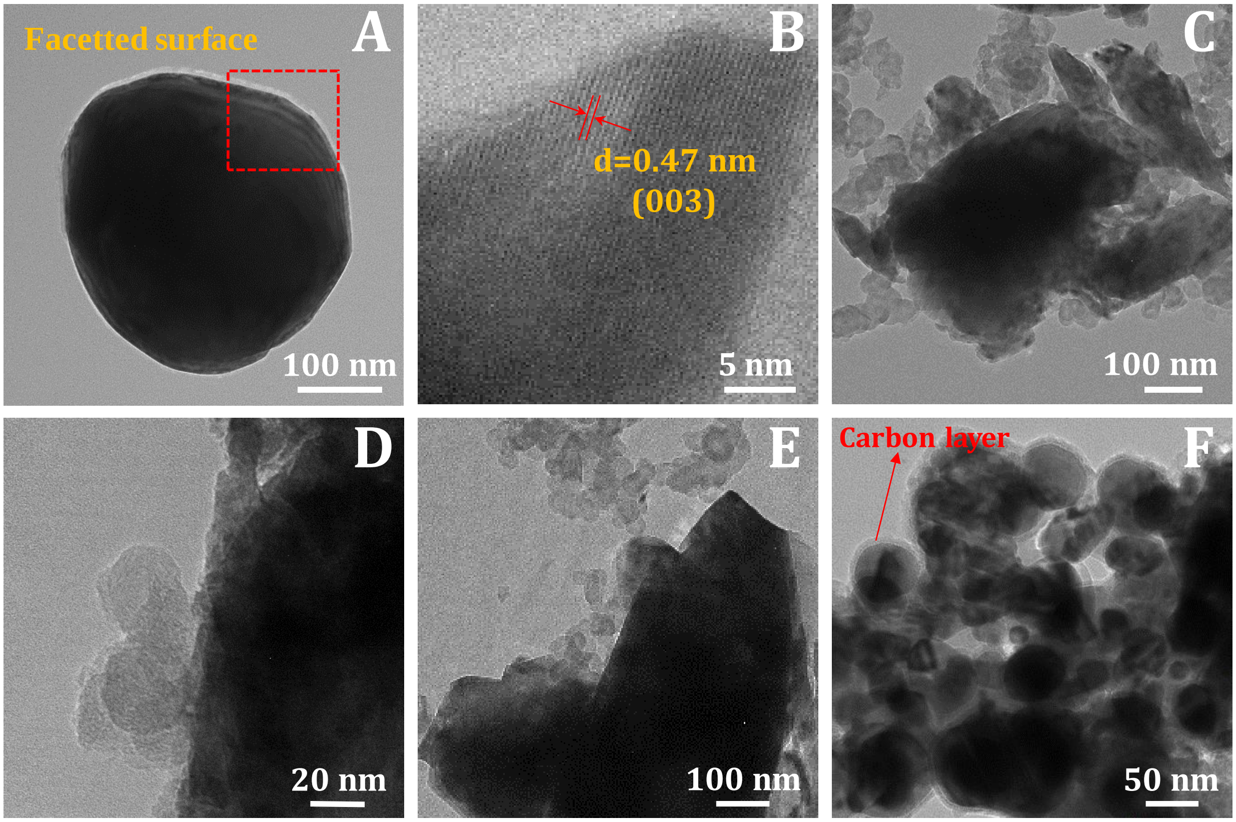

Figure 5.7: TEM images of the pristine NMC material showing the spherical morphology in (A) and the lattice fringes at a smaller scale (B). TEM images of the ball-milled NMC samples with carbon: Dry NMC-CC-20-1 (C and D) and the wet milled NMC (E). TEM image of the chemically carbon coated sample NMC-sucrose (F).

5.3.5 Effect of Ball Milling on the Electrochemical Performance of NMC

5.3.5.1 Coin Cells Measurements

The cathode material NMC undergoes the following reversible redox reaction upon charging/discharging:

$$LiNi_{1/3}Mn_{1/3}Co_{1/3}O_2 \rightleftarrows Li_{(1-x)}Ni_{1/3}Mn_{1/3}Co_{1/3}O_2 + xLi^+ + xe^- \qquad (5.2)$$

During the charging process, Li-ions and electrons are deintercalated from the structure and the voltage increases. During the discharging process, Li-ions and electrons are intercalated back into the structure, and the voltage decreases. Different NMC electrodes were fabricated and tested to determine the effect of ball milling conditions on the electrochemical performance. Figure 5.8 compares the discharge curves of NMC cathodes for the starting material vs. the ball-milled samples before and after carbon mixing. Cycling was performed at scan rates C/10, C/5, C and 2C in the potential range of 2.3-4.5V. For simplicity, only the samples milled for 20 minutes at a rate of C/10 are represented.

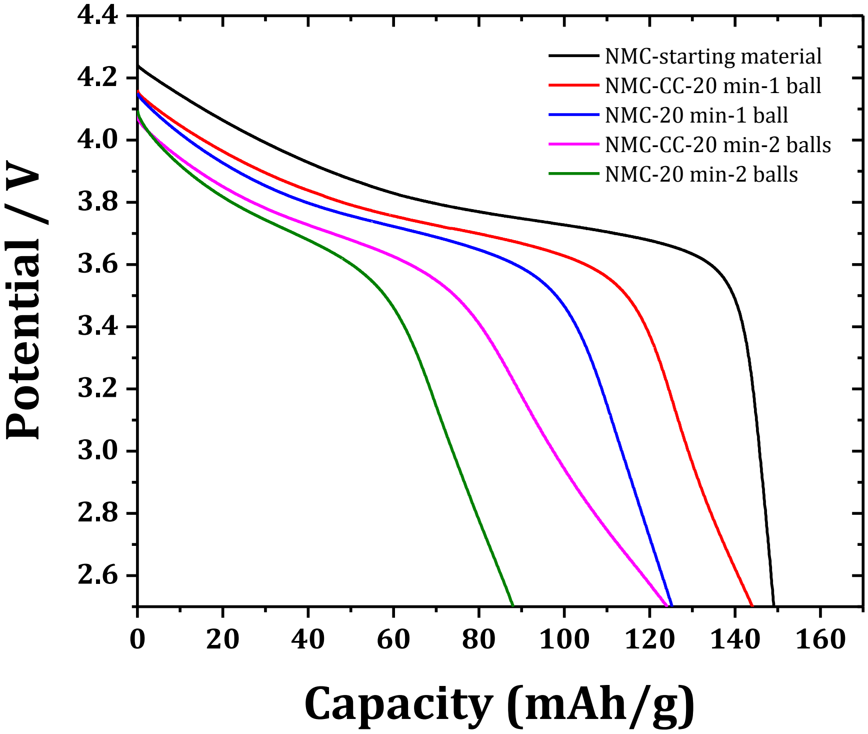

Figure 5.8: The discharge curves measured between 2.5-4.3 V at C/10 rate for the NMC electrodes before and after ball milling/carbon mixing.

The discharge capacities of other rates are shown in Table 5.3 for all milled samples. Despite the smaller particle sizes as determined from SEM and XRD analysis, the electrochemical charge and discharge of ball-milled samples displayed lower capacities and lower voltages for all milling conditions compared with the pristine NMC material. The galvanostatic data in Figure 5.8 also showed that NMC sample with the least aggressive milling conditions (20 minutes-1ball) performed the best of the milled materials, with enhanced performance for the samples mixed with carbon.

Table 5.3: Average discharge capacities for the NMC starting material and ball-milled NMC cathodes at rates of C/10, C/5, C, and 2C.

Sample ID	Average C/10 specific discharge capacity (mAh/g)	Average C/5 specific discharge capacity (mAh/g)	Average C specific discharge capacity (mAh/g)	Average 2C specific discharge capacity (mAh/g)
NMC starting material	145	142	131	121
NMC-20-1	130	125	105	92
NMC-20-2	90	73	38	25
NMC-45-1	93	75	42	30
NMC-45-2	67	45	14	7
NMC-CC-20-1	144	139	120	98
NMC-CC-20-2	126	112	77	58
NMC-CC-45-1	139	135	116	96
NMC-CC-45-2	120	105	75	50

To interpret the obtained results, it is important to identify the factors that influence the electrode capacity, voltage, and rate capabilities such as the charge transfer reaction at the interface between the electrode and electrolyte, the electronic conductivity of the electrode particles, and interparticle contact. It has been previously reported that the electrode-electrolyte interface has a significant effect on the battery performance.[75] Interfacial charge transfer resistance measured by electrochemical impedance spectroscopy (EIS) was found to be higher for ball-milled samples compared to the pristine NMC material,[56] which correlates with the lower voltages and capacities obtained from the galvanostatic discharge results in Figure 5.8. The higher interfacial resistance obtained after ball milling was attributed to the formation of aggregates as depicted in the SEM micrographs (see Figure D1). These new aggregates were presumed to have an amorphous phase at the surface and consequently different surface structure that would not be detected with XRD. However, the diffraction peaks for the ball-milled materials showed lower intensities compared with the pristine sample, which provide evidence on the lower degree of crystallinity obtained after milling. As lithium intercalation and deintercalation occur along specific crystallographic planes and directions, lower crystallinity deteriorates the electrode performance.[76] Moreover, the distorted layered structure and the high degree of cation mixing obtained from XRD analysis upon using 2 balls can be the reason behind the lower performance of the samples ball-milled with 2 balls compared to the samples with 1 ball. More analysis is required to specify the nature of the higher interfacial resistance for the ball-milled samples.

To further understand the low electrochemical activity of ball-milled NMC materials, the electrical conductivity of the cathode samples was considered. Previous studies have shown that the electronic conductivity of NMC decreases after ball milling,[56] which again may be related to the active material aggregation under aggressive milling conditions as observed from SEM data (Figure D1). The interconnections between particles were proved to significantly affect the electrical properties of the material,[77] and hence, the aggregate structures are said to have higher resistances compared to the original particles. The interparticle resistance within the formed aggregates can be controlled by introducing conductive elements, such as carbon black, between the particles. This resulted in improved electronic properties and consequently enhanced performance for the ball-milled materials with carbon compared to the ones with no carbon as obtained from the galvanostatic data in Figure 5.8. The discharge curves comparing the effect of time on the electrochemical performance of the cathodes are represented in Appendix D (Figure D2). The obtained data in Figure D2A clearly indicates that ball milling for 45 minutes lowered the electrode performance compared to the samples milled at 20 minutes (using the same number of balls). Similar results were obtained even after carbon addition (see Figure D2B). This can be attributed to the formation of more and more aggregates when ball milling was carried out for longer time, which leads to higher interfacial and electronic resistances as discussed earlier.

5.3.5.2 Localized Electrochemical Measurements by SMCM

Figure 5.9 displays the curves of the cyclic voltammograms for the charging/discharging of NMC material, after ball milling with carbon, using SMCM technique. The NMC-CC-20-1 sample was selected because it showed the highest capacity among other ball-milled samples in the coin cells measurements. Although this sample had the least changes after ball milling, the main purpose of ball milling of NMC in this study was to introduce carbon black as a conductive additive between the NMC particles. Therefore, it is reasonable to choose the material that showed the least change, because this material will have similar properties to the NMC starting material which was the core of this study.

The SMCM measurements were performed between 1.8 and 5.1 V vs. Li/Li$^+$ at scan rates of 5, 10, 20, and 50 mV s^{-1}, with 5 cycles recorded for each. Only the last cycle is displayed in Figure 5.9. The obtained results showed a remarkable improvement compared to Figure 5.2 before ball milling with carbon. Therefore, the existence of electronically conductive additive such as carbon between the NMC particles decreased the electronic resistance and served in the investigation of NMC by SMCM. The oxidation and reduction peaks for lithium extraction and insertion at 50 mV s^{-1} occurred at potentials of 4.64 and 2.98 V vs. Li/Li$^+$ respectively. The oxidation/reduction potentials as well as the magnitude of the peak currents decreased as the scan rate decreased from 50 to 5 mV s^{-1}. At scan rates of 5 and 10 mV s^{-1}, the oxidation peak of the cyclic voltammograms almost returned to a background current value, indicating a complete reaction. The charge integration for the oxidation waves was 2.78 μC (7.7 x 10^{-7} mAh) for 10 mV s^{-1}, and 3.18 μC (8.8 x 10^{-7} mAh) for 5 mV s^{-1}.

Cyclic voltammetry measurements on NMC composite films were previously carried out in our lab using a three-electrode cell.[66] The obtained results in organic electrolyte EMC revealed two anodic peaks and two cathodic peaks corresponding to the respective oxidation and reduction reactions of Ni^{2+}/Ni^{4+} and Co^{3+}/Co^{4+}. However, these peaks were less defined when the three-electrode measurements were carried out in the ionic liquid EMI TFSI at higher overpotentials. As such, the appearance of only one pair of anodic/cathodic peaks in the case of the SMCM measurements herein suggests that the double peaks could not be resolved upon using ionic liquid. Previous studies have shown that the major oxidation peaks for Ni and Co are expected to be around 3.99 and 4.71 V, and the reduction peaks around 4.54 and 3.58 V respectively.[78-79] In contrast, the oxidation/reduction potentials were significantly shifted in the present study, consequently causing a larger redox peak separation. The major differences in the cyclic voltammograms obtained (peaks convolution and potential shift) could be attributed to the high viscosity of the ionic liquid used, which resulted in a sluggish diffusion for Li-ions and poor wetting of the electrode surface.[80-81] Additionally, the changes in the particles morphology (shape, particle size and specific surface area), and the increase in the interfacial/electronic resistances obtained after ball milling are known to have a great impact on the electrochemical performances of the material,[70, 82-84] which could further justify the collected results. More efforts are still required in order to improve the resolution of the SMCM and make it feasible for investigating newly synthesized or modified NMC particles.

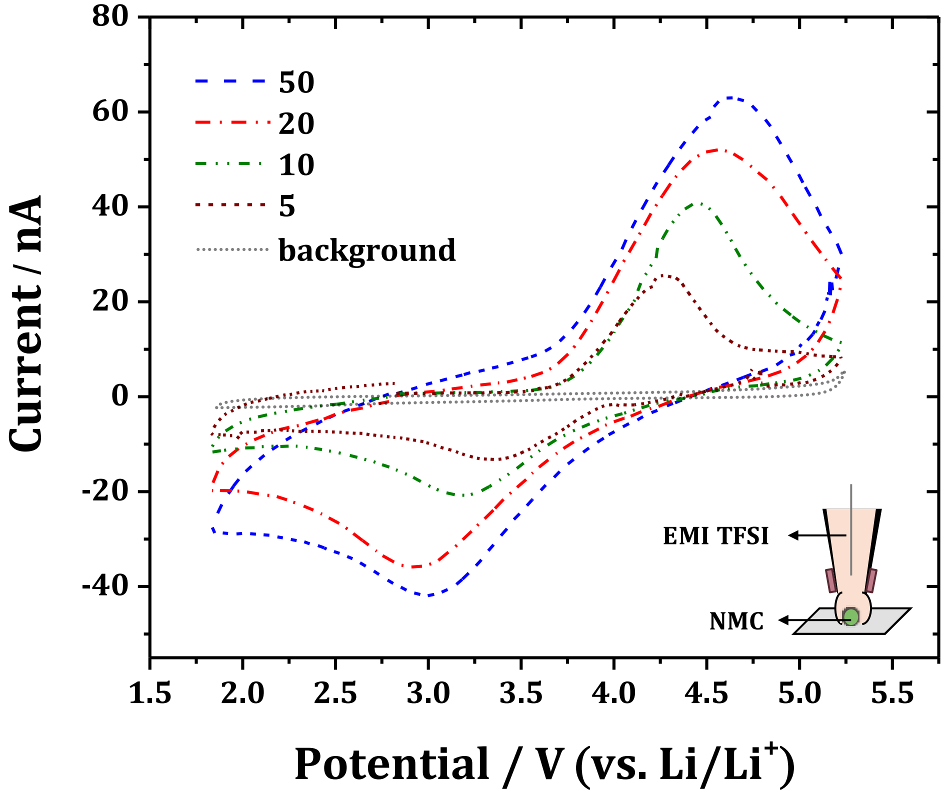

Figure 5.9: Cyclic voltammograms obtained at different scan rates using SMCM with 0.1 M LiTFSI in EMI TFSI on NMC particles dispersed on a glassy carbon electrode. The legend corresponds to scan rate in mV s^{-1}. The background current represents the micropipette landing on the glassy carbon substrate where no active material is present.

5.4 Conclusions

In this study, the scope of SMCM technique was extended to visualize the current response of the high energy cathode material NMC. Investigation of the active material was performed on a micron scale using the ionic liquid EMI TFSI. The electronic resistance between the active material and the working substrate was controlled by introducing carbon black between the NMC particles. This was achieved either by ball milling the NMC with carbon, or by chemically coating the active particles with carbon via sucrose carbonization. The latter route appeared to be effective in terms of coating as the TEM imaging showed, yet the change in the NMC phase at high temperatures rendered the material inactive. The effect of dry and wet milling, as well as the effect of ball milling time and the number of balls used was also studied by XRD, SEM, and TEM. Ball milling was determined to decrease the crystallite sizes and the small particles size as the intensity of the ball milling increases. However, coin cells measurements showed that the milled NMC samples have lower capacity and lower voltages compared to the pristine material. This was attributed to the formation of aggregate structures as detected by SEM imaging, which are known to have high interfacial and electronic resistances. Therefore, ball milling appeared to influence multiple material properties beyond the crystallite size. More control experiments are still required to optimize the milling conditions and understand their effect on the electrochemical performance of NMC.

5.5 References

1.Wakihara, M.; Yamamoto, O., *Lithium ion batteries: fundamentals and performance*. John Wiley & Sons: 2008.

2.Van Schalkwijk, W.; Scrosati, B., Advances in lithium ion batteries introduction. In *Advances in Lithium-Ion Batteries*, Springer: 2002; pp 1-5.

3.Ellis, B. L.; Lee, K. T.; Nazar, L. F. *Chemistry of Materials* **2010,** 22, (3), 691-714.

4.Whittingham, M. S. *Chemical Reviews* **2004,** 104, (10), 4271-4302.

5.Chang, M.-H.; Huang, H.-P.; Chang, S.-W. *Energies* **2013,** 6, (4), 2007-2030.

6.Marsh, R. A.; Vukson, S.; Surampudi, S.; Ratnakumar, B. V.; Smart, M. C.; Manzo, M.; Dalton, P. J. *Journal of Power Sources* **2001,** 97-98, 25-27.

7.Ratnakumar, B.; Smart, M.; Kindler, A.; Frank, H.; Ewell, R.; Surampudi, S. *Journal of power sources* **2003,** 119, 906-910.

8.Goodenough, J. B.; Kim, Y. *Chemistry of Materials* **2010,** 22, (3), 587-603.

9.Rahimi-Eichi, H.; Ojha, U.; Baronti, F.; Chow, M.-Y. *IEEE Industrial Electronics Magazine* **2013,** 7, (2), 4-16.

10.Majima, M.; Ujiie, S.; Yagasaki, E.; Koyama, K.; Inazawa, S. *Journal of Power Sources* **2001,** 101, (1), 53-59.

11.Martha, S. K.; Markevich, E.; Burgel, V.; Salitra, G.; Zinigrad, E.; Markovsky, B.; Sclar, H.; Pramovich, Z.; Heik, O.; Aurbach, D.; Exnar, I.; Buqa, H.; Drezen, T.; Semrau, G.; Schmidt, M.; Kovacheva, D.; Saliyski, N. *Journal of Power Sources* **2009,** 189, (1), 288-296.

12.Martha, S. K.; Sclar, H.; Szmuk Framowitz, Z.; Kovacheva, D.; Saliyski, N.; Gofer, Y.; Sharon, P.; Golik, E.; Markovsky, B.; Aurbach, D. *Journal of Power Sources* **2009,** 189, (1), 248-255.

13.Choi, J.; Manthiram, A. *Journal of The Electrochemical Society* **2005,** 152, (9), A1714-A1718.

14.Yabuuchi, N.; Ohzuku, T. *Journal of Power Sources* **2003,** 119, 171-174.

15.Noh, H.-J.; Youn, S.; Yoon, C. S.; Sun, Y.-K. *Journal of power sources* **2013,** 233, 121-130.

16.Bak, S.-M.; Hu, E.; Zhou, Y.; Yu, X.; Senanayake, S. D.; Cho, S.-J.; Kim, K.-B.; Chung, K. Y.; Yang, X.-Q.; Nam, K.-W. *ACS applied materials & interfaces* **2014,** 6, (24), 22594-22601.

17.Tian, C.; Lin, F.; Doeff, M. M. *Accounts of chemical research* **2017,** 51, (1), 89-96.

18.Fujii, Y.; Miura, H.; Suzuki, N.; Shoji, T.; Nakayama, N. *Journal of Power Sources* **2007,** 171, (2), 894-903.

19.Xu, J.; Lin, F.; Doeff, M. M.; Tong, W. *Journal of Materials Chemistry A* **2017,** 5, (3), 874-901.

20.Shaju, K.; Rao, G. S.; Chowdari, B. *Electrochimica Acta* **2002,** 48, (2), 145-151.

21.Belharouak, I.; Sun, Y.-K.; Liu, J.; Amine, K. *Journal of Power Sources* **2003,** 123, (2), 247-252.

22.Yabuuchi, N.; Makimura, Y.; Ohzuku, T. *Journal of The Electrochemical Society* **2007,** 154, (4), A314-A321.

23.Wu, S.-L.; Zhang, W.; Song, X.; Shukla, A. K.; Liu, G.; Battaglia, V.; Srinivasan, V. *Journal of The Electrochemical Society* **2012,** 159, (4), A438-A444.

24.Hou, P.; Wang, X.; Song, D.; Shi, X.; Zhang, L.; Guo, J.; Zhang, J. *Journal of Power Sources* **2014,** 265, 174-181.

25.Gong, C.; Lv, W.; Qu, L.; Bankole, O. E.; Li, G.; Zhang, R.; Hu, M.; Lei, L. *Journal of Power Sources* **2014,** 247, 151-155.

26.Croguennec, L.; Bains, J.; Bréger, J.; Tessier, C.; Biensan, P.; Levasseur, S.; Delmas, C. *Journal of The Electrochemical Society* **2011,** 158, (6), A664-A670.

27.Liu, X.; Li, H.; Li, D.; Ishida, M.; Zhou, H. *Journal of Power Sources* **2013,** 243, 374-380.

28.Yang, X.; Bao, C.; Xie, L.; Zhu, L.; Cao, X. *Ceramics International* **2019**.

29.Lee, Y.-S.; Lee, K.-S.; Sun, Y.-K.; Lee, Y. M.; Kim, D.-W. *Journal of Power Sources* **2011,** 196, (16), 6997-7001.

30.Zhang, P.; Zhang, L.; Ren, X.; Yuan, Q.; Liu, J.; Zhang, Q. *Synthetic Metals* **2011,** 161, (11), 1092-1097.

31.Sinha, N. N.; Munichandraiah, N. *ACS Applied Materials & Interfaces* **2009,** 1, (6), 1241-1249.

32.Guo, R.; Shi, P.; Cheng, X.; Du, C. *Journal of Alloys and Compounds* **2009,** 473, (1-2), 53-59.

33.Kim, H.-S.; Kim, K.; Moon, S.-I.; Kim, I.-J.; Gu, H.-B. *Journal of Solid State Electrochemistry* **2008,** 12, (7-8), 867-872.

34.Marcinek, M. L.; Wilcox, J. W.; Doeff, M. M.; Kostecki, R. M. *Journal of The Electrochemical Society* **2009,** 156, (1), A48-A51.

35.Lin, B.; Wen, Z.; Han, J.; Wu, X. *Solid State Ionics* **2008,** 179, (27-32), 1750-1753.

36.Tsai, H.-L.; Hsieh, C.-T.; Li, J.; Gandomi, Y. A. *Electrochimica Acta* **2018,** 273, 200-207.

37.Venkateswara Rao, C.; Leela Mohana Reddy, A.; Ishikawa, Y.; Ajayan, P. M. *ACS Applied Materials & Interfaces* **2011,** 3, (8), 2966-2972.

38.Jan, S. S.; Nurgul, S.; Shi, X.; Xia, H.; Pang, H. *Electrochimica Acta* **2014,** 149, 86-93.

39.Fergus, J. W. *Journal of Power Sources* **2010,** 195, (4), 939-954.

40.Zheng, H.; Li, J.; Song, X.; Liu, G.; Battaglia, V. S. *Electrochimica Acta* **2012,** 71, 258-265.

41.Lu, C.-H.; Wu, T.-Y.; Wu, H.-C.; Yang, M.-H.; Guo, Z.-Z.; Taniguchi, I. *Materials Chemistry and Physics* **2008,** 112, (1), 115-119.

42.Pohjalainen, E.; Rauhala, T.; Valkeapää, M.; Kallioinen, J.; Kallio, T. *The Journal of Physical Chemistry C* **2015,** 119, (5), 2277-2283.

43.Sclar, H.; Kovacheva, D.; Zhecheva, E.; Stoyanova, R.; Lavi, R.; Kimmel, G.; Grinblat, J.; Girshevitz, O.; Amalraj, F.; Haik, O. *Journal of The Electrochemical Society* **2009,** 156, (11), A938-A948.

44.Zheng, J. P.; Crain, D. J.; Roy, D. *Solid State Ionics* **2011,** 196, (1), 48-58.

45.Ning, L.; Wu, Y.; Fang, S.; Rahm, E.; Holze, R. *Journal of power sources* **2004,** 133, (2), 229-242.

46.Franger, S.; Le Cras, F.; Bourbon, C.; Rouault, H. *Journal of power Sources* **2003,** 119, 252-257.

47.Zhang, D.; Cai, R.; Zhou, Y.; Shao, Z.; Liao, X.-Z.; Ma, Z.-F. *Electrochimica Acta* **2010,** 55, (8), 2653-2661.

48.Ni, J.; Kawabe, Y.; Morishita, M.; Watada, M.; Sakai, T. *Journal of Power Sources* **2011,** 196, (19), 8104-8109.

49.Liu, Z.; Yu, A.; Lee, J. *Journal of power sources* **1998,** 74, (2), 228-233.

50.Zhang, H.; Xu, Y.; Liu, D. *RSC Advances* **2015,** 5, (15), 11091-11095.

51.Voronov, V.; Shvetsov, A.; Gubin, S.; Cheglakov, A.; Kornilov, D. Y.; Karaseva, A.; Krasnova, E.; Tkachev, S. *Russian Journal of Inorganic Chemistry* **2016,** 61, (9), 1153-1159.

52.Nelson, G. J.; Ausderau, L. J.; Shin, S.; Buckley, J. R.; Mistry, A.; Mukherjee, P. P.; De Andrade, V. *Journal of The Electrochemical Society* **2017,** 164, (7), A1412-A1424.

53.Jiang, X.; Sha, Y.; Cai, R.; Shao, Z. *Journal of Materials Chemistry A* **2015,** 3, (19), 10536-10544.

54.Kim, S.-B.; Kim, S.-J.; Kim, C.-H.; Kim, W.-S.; Park, K.-W. *Materials Letters* **2011,** 65, (21-22), 3313-3316.

55.Sun, Y.-K.; Kang, S.-H.; Amine, K. *Materials research bulletin* **2004,** 39, (6), 819-825.

56.Stein, M.; Chen, C.-F.; Mullings, M.; Jaime, D.; Zaleski, A.; Mukherjee, P. P.; Rhodes, C. P. *Journal of Electrochemical Energy Conversion and Storage* **2016,** 13, (3), 031001.

57.Huang, R.; Ikuhara, Y. *Current Opinion in Solid State and Materials Science* **2012,** 16, (1), 31-38.

58.Baddour-Hadjean, R.; Pereira-Ramos, J.-P. *Chemical reviews* **2009,** 110, (3), 1278-1319.

59.Lim, J.; Li, Y.; Alsem, D. H.; So, H.; Lee, S. C.; Bai, P.; Cogswell, D. A.; Liu, X.; Jin, N.; Yu, Y.-s. *Science* **2016,** 353, (6299), 566-571.

60.Xu, F.; Beak, B.; Jung, C. *Journal of Solid State Electrochemistry* **2012,** 16, (1), 305-311.

61.Williams, C. G.; Edwards, M. A.; Colley, A. L.; Macpherson, J. V.; Unwin, P. R. *Analytical Chemistry* **2009,** 81, (7), 2486-2495.

62.Takahashi, Y.; Kumatani, A.; Munakata, H.; Inomata, H.; Ito, K.; Ino, K.; Shiku, H.; Unwin, P. R.; Korchev, Y. E.; Kanamura, K. *Nature communications* **2014,** 5, 5450.

63.Kumatani, A.; Takahashi, Y.; Miura, C.; Ida, H.; Inomata, H.; Shiku, H.; Munakata, H.; Kanamura, K.; Matsue, T. *Surface and Interface Analysis* **2019,** 51, (1), 27-30.

64.Lipson, A. L.; Ginder, R. S.; Hersam, M. C. *Advanced Materials* **2011,** 23, (47), 5613-5617.

65.Snowden, M. E.; Dayeh, M.; Payne, N. A.; Gervais, S.; Mauzeroll, J.; Schougaard, S. B. *Journal of Power Sources* **2016,** 325, 682-689.

66.Dayeh, M.; Ghavidel, M. Z.; Mauzeroll, J.; Schougaard, S. B. *ChemElectroChem* **2019,** 6, (1), 195-201.

67.Mohanty, D.; Gabrisch, H. *Journal of Power Sources* **2012,** 220, 405-412.

68.Dahn, J.; von Sacken, U.; Michal, C. *Solid State Ionics* **1990,** 44, (1-2), 87-97.

69.Ohzuku, T.; Ueda, A.; Nagayama, M. *Journal of The Electrochemical Society* **1993,** 140, (7), 1862-1870.

70.Cho, T. H.; Park, S. M.; Yoshio, M.; Hirai, T.; Hideshima, Y. *Journal of Power Sources* **2005,** 142, (1), 306-312.

71.Makimura, Y.; Ohzuku, T. *Journal of Power Sources* **2003,** 119, 156-160.

72.Gopukumar, S.; Chung, K. Y.; Kim, K. B. *Electrochimica Acta* **2004,** 49, (5), 803-810.

73.Chen, Z.; Wang, J.; Chao, D.; Baikie, T.; Bai, L.; Chen, S.; Zhao, Y.; Sum, T. C.; Lin, J.; Shen, Z. *Scientific Reports* **2016,** 6, 25771.

74.Chen, Z.; Qin, Y.; Amine, K.; Sun, Y.-K. *Journal of Materials Chemistry* **2010,** 20, (36), 7606-7612.

75.Xu, K. *Chemical reviews* **2014,** 114, (23), 11503-11618.

76.Hwang, B. J.; Wu, Y. W.; Venkateswarlu, M.; Cheng, M. Y.; Santhanam, R. *Journal of Power Sources* **2009,** 193, (2), 828-833.

77.Doescher, M. S.; Pietron, J. J.; Dening, B. M.; Long, J. W.; Rhodes, C. P.; Edmondson, C. A.; Rolison, D. R. *Analytical Chemistry* **2005,** 77, (24), 7924-7932.

78.Wu, F.; Wang, M.; Su, Y.; Bao, L.; Chen, S. *Journal of Power Sources* **2010,** 195, (8), 2362-2367.

79.Johnson, C. S.; Li, N.; Lefief, C.; Vaughey, J. T.; Thackeray, M. M. *Chemistry of Materials* **2008,** 20, (19), 6095-6106.

80.Wu, T.-Y.; Hao, L.; Chen, P.-R.; Liao, J.-W. **2013**.

81.Shamsipur, M.; Beigi, A. A. M.; Teymouri, M.; Pourmortazavi, S. M.; Irandoust, M. *Journal of Molecular Liquids* **2010,** 157, (1), 43-50.

82.Li, D.-C.; Muta, T.; Zhang, L.-Q.; Yoshio, M.; Noguchi, H. *Journal of Power Sources* **2004,** 132, (1), 150-155.

83.Martin, M. A.; Chen, C.-F.; Mukherjee, P. P.; Pannala, S.; Dietiker, J.-F.; Turner, J. A.; Ranjan, D. *Journal of The Electrochemical Society* **2015,** 162, (6), A991-A1002.

84.Cabelguen, P.-E.; Peralta, D.; Cugnet, M.; Maillet, P. *Journal of Power Sources* **2017,** 346, 13-23.

Chapter 6

Conclusions and Future Work

The overreaching theme of this thesis was the development of an analytical technique, namely the SMCM, for investigating active material particles for LIB positive electrodes. Micron scale probes were utilized for spatially resolved detection of ion fluxes at the surface of the battery active material. This aim was demonstrated in an anaerobic environment on two cathode materials, LFP and the higher energy NMC, without the additional complications arising from the presence of binders and electronically conductive fillers. Extrapolating the obtained peak currents to low scan scan rates also showed that the SMCM is a useful investigating technique even when electrode material is limiting, but more efforts are still required to make this experimentally possible. Complementary scanning electron microscopy and atomic force microscopy images of the scanned area were established for correlating the collected electrochemical signals to the number and volume of the probed particles. The following chapter summarizes the work presented in the previous chapters of this thesis and proposes future directions for each chapter.

6.1 Summary and Contributions to Original Knowledge

Chapter 1 introduced the principles and the theory of LIBs, and highlighted briefly the structure and performance characteristics of some widely studied positive electrode materials and their applications. These include transition metal oxides and phosphates based intercalation materials with layered, spinel and olivine structures. Chapter 1 also reviewed the most commonly used scanning electrochemical probe techniques, such as SECM, SMCM, and SICM, which have been utilized for the investigation of several processes occurring at battery electrodes. These techniques provide the opportunity to probe electrochemical processes on a micro- or nanoscale, thus providing insights that cannot be attained by classical voltammetry methods. The scanning probe techniques have been successfully applied in the field of LIBs, such as studying the transportation of Li-ions, imaging the topography and local Li-ion currents, and tracking the topography and interfacial current activity at battery electrode materials. However, the use of aqueous electrolyte solution remained a key limitation, since many cathode materials used in LIBs have higher cathodic operating potential, and therefore do not operate within the electrochemical stability window of water. This limitation addresses the evolving need for characterization of LIBs in anaerobic environment using a true battery electrolyte, which is the main motivation for this thesis.

Chapter 2 provided a practical guide to SMCM. It presented the approaches used in designing and optimizing the SMCM technique to be applied in an inert atmosphere. The principles and operation of the SMCM for investigating LIB cathode materials were also discussed. The technique used a moveable silanized micropipette probe containing electrolyte solution and an $Al_{1-x}Li_x$ QRCE. The pipette was brought into close contact with a sample electrode surface (working electrode) that was decorated with the active cathode material of interest, while applying a constant potential with respect to the QRCE. The electrochemical processes were measured when the liquid meniscus at the pipette end came into contact with the surface; that being detected by a small current flow. A standard procedure for the fabrication of AlLi QRCE was created, and its stability has been tested. This provided a reliable potential reference that is essential for electrochemical measurements. Additionally, the identification of the suitable electrolyte and working electrode surface, the selection of the suitable pipette size and the best silanizing agent, as well as the detection of the droplet stability were all explored in this chapter based on the cathode material to be investigated. For instance, probing LFP active material that has short potential range and small particle size could be achieved using gold substrate and 1 µm pipette filled with organic electrolyte. In contrast, the detection of the higher energy NMC with lager active particles could be accomplished on a glassy carbon substrate with 10 µm pipette containing an ionic liquid. The $Al_{1-x}Li_x$ QRCE can be commonly used in both cases, because the stability test showed positive results in organic electrolyte and in the ionic liquid EMI TFSI before and after electrochemical measurements. Similarly, the droplet stability examined using the redox mediator MPT in both PC and EMI TFSI solution showed almost a constant wetting area when the hopping probe was moved across the substrate.

Chapter 3 reported the first successful measurements on battery electrode material using the SMCM technique in an argon atmosphere. Localized galvanostatic and potentiodynamic measurements were performed on isolated nano particles and agglomerates of LFP cathode material. Investigation of the active material occurred on a small scale (~10 μm diameter), defined by the area of meniscus contact between a solution of $LiClO_4$ in PC filling the micropipette and gold substrate decorated with the LFP particles. After performing the electrochemical measurements, SEM was used to characterize the active particles within the scanned area. The combination of these two techniques allowed the quantity and the size of the active particles to be compared to the electrochemical responses. Data collected with the micropipette method were also compared to conventional coin cells measurements. The charge observed by integration of the forward peak of the cyclic voltammogram was in reasonable agreement with that expected from the theoretical capacity of the same volume of LFP observed in by SEM. The obtained similarities between individual particle responses and bulk electrode indicated the applicability of SMCM as a tool for elucidating key electrochemical properties of battery materials. The study also revealed heterogeneous electrochemical responses for isolated primary particles and agglomerates, showing that not all particles within a batch have uniform properties. This is of significant interest for fundamental investigations of electrochemical properties of air sensitive materials, and for battery material characterization.

Chapter 4 described the evolution of the SMCM technique to include ionic liquid as an alternative electrolyte solution to the conventional organic electrolytes. Although SMCM has proven a powerful methodology for probing the electrochemical properties of small numbers of active material particles as presented in Chapter 3, there were great limitations to the use of this method for studying higher energy cathode materials that require higher oxidation potentials. This entailed the use of electrolytes with a larger stability window such as ionic liquids. In particular, the ionic liquid EMI TFSI containing 0.1 M LiTFSI salt was introduced into the micropipette for SMCM measurements. Moreover, the gold substrate used in the previous study was not stable at potential higher than 4.3 V vs. Li/Li^+. Consequently, it was replaced by a glassy carbon substrate as it has a higher oxidation limit. Stability tests for the $Al_{1-x}Li_x$ QRCE and the droplet were also carried out using the ionic liquid. The obtained results showed that the new SMCM probe was stable and could be used to analyse high energy active materials in the range of 2.5 to 5.1 V vs. Li/Li^+. As a proof-of-concept, localized electrochemical measurements were performed on the conventional LFP active particles. A coulombic efficiency higher than 90% was obtained in ionic liquid at all tested points. This was a marked improvement from the previous study of LFP on gold substrate using

PC. The results also indicated that the viscosity and wettability of ionic liquid and the particle to particle variations could have an effect on the peak resolution and peak splitting potential of Li intercalation/deintercalation. AFM imaging for the scanned area was carried out to compare the experimental and theoretical capacities of the examined active particles. Three-electrode cell measurements with LFP composite film were also performed in EMI TFSI electrolyte and compared to the SMCM data. The obtained results illustrated that SMCM, in the presence of the ionic liquid, could be successfully used to study conventional active material such as LFP and could be extended to study higher energy particles such as NMC.

Chapter 5 presented the first attempt to visualize the electrochemical properties of the higher energy cathode material NMC using the SMCM technique. Investigations of the active material was performed on a glassy carbon surface using the ionic liquid EMI TFSI. However, collecting a significant electrochemical response was not possible due to the electronic resistance existing between the particles and the substrate. To enhance the conductivity, carbon black was introduced between the NMC particles via ball milling, which turned to be effective. The localized cyclic voltammetry measurements collected by SMCM showed convoluted and shifted anodic and cathodic peaks corresponding to the oxidation and reduction of the transition metals Ni and Co. This was attributed to the viscosity of the ionic liquid that slower the diffusion of Li-ions. Chapter 5 also sought the effect of ball milling and the used parameters on the structure and performance of the cathode material NMC. The explored conditions included the time and the number of balls used, as well as milling with and without carbon in dry and wet conditions. SEM imaging of the NMC ball-milled samples revealed significant morphological changes as compared to the NMC starting material in addition to aggregate structures formation as the time and the number of balls used increased. Moreover, XRD analysis showed a decrease in the crystallite size at higher ball milling intensity. However, a lower degree of crystallinity and a higher degree of cation mixing and distorted structure was obtained. This had a significant influence on the electrochemical performance of the active material. Coin cells measurements performed on NMC before and after ball milling showed that the milled NMC samples had lower discharging capacity and lower voltages compared to the pristine NMC material, with enhanced performance for the samples mixed with carbon. This was attributed to the formation of aggregate structures as detected by SEM imaging, which are known to have lower electrical conductivity and higher interfacial charge transfer resistance. Therefore, ball milling with carbon additive using relatively mild conditions provided intermediate NMC crystallites with higher capacities and improved rate capabilities.

6.2 Future Directions

Chapter 2 described the systematic development of the SMCM technique in a controlled environment for the investigation of LIB materials on a micron scale. The work can be further extended to probe the electrochemical properties of the cathode materials at a higher resolution (down to a single particle level). This can be achieved through the calibration of nanosized pipettes for localized electrochemical measurements at smaller scales. Since the current used to trigger the approach curve ending is around 2 pA, a pipette with 200 nm diameter aperture (wetting surface ~2 um in diameter) would be the ultimate size of pipets to be used. Moreover, a better evidence about the droplet stability can be attained by using a redox mediator other than MPT. An example in that regard could be the redox mediator TEMPO, which is known to be stable at high oxidation potentials compared to MPT.[1] This will give a better evidence about the droplet stability when the electrochemical measurements are extended to higher over potentials. Examining other electrolytes for SMCM measurements is another suggestion. For example, it would be interesting to test sulfones that are known to have wide potential stability window, or to test other ionic liquids that have less viscosity than the EMI TFSI used in this thesis. This might play a significant role in enhancing the diffusion of Li-ions. SMCM can be also extended to investigate anode materials which gets oxidized and reduced at lower potentials compared to cathodes. Therefore, a redox mediator that is active within a lower potential range is required for testing the droplet stability. A good example is the cobaltocene [$Co(Cp)_2$] and bis(pentamethylcyclopentadienyl)cobalt [$Co(Cp^*)_2$].[2-3] Other modifications related to the size of the pipette would depend on the size of the anode particles.

Chapter 3 demonstrated the use of SMCM technique to map spatial heterogeneities in the electrochemistry of isolated LFP active particles. To take the work a step further, localized topographical images could be also acquired and linked to the current and potential maps of LFP that were collected. This can be attained by recording the tip height position after each landing point during imaging, thus enabling the topography of the surface to be tracked. The collected microscale topography allows distinct features of the sample to be used for co-location of the different microscopy techniques (SEM or AFM for example). This will provide the opportunity to link the surface component (active material or substrate surface) and the charge/discharge maps via a multi-microscopy approach in which SMCM is a central technique. The presented work can be further extended to explore the diffusion coefficient of Li-ions at agglomerate and single particle level. This can be achieved by measuring the current vs. time (chronoamperometry measurements) to detect the steady state current at different locations along the substrate.

Chapter 4 presented the ability to estimate the volume of the active particles that were tested by SMCM. This was done by establishing a correlation between AFM images and SEM images of the landing areas. However, the AFM images in this study were randomly collected in proximity to the area scanned by SMCM because the exact landing locations were hard to visualize by AFM. Therefore, the calculated volume of the actual active particles that were examined by SMCM was just an approximation. The most obvious suggestion to solve this issue is to create a certain pattern on the glassy carbon substrate in a way that enables precise detection of the landing area under AFM. This could be achieved by etching the glassy carbon substrate to create an ordered pattern labeled with numbers. These numbers will be easy to detect by SEM and AFM and will facilitate the imaging process for the landing sites. By finding the real active particles under AFM, the exact volume of the particles will be measured, and hence, their exact experimental capacity will be calculated and compared to theoretical values. The obtained experimental capacity of the active particles at different scan rates can be further compared to the rate performance of LFP in coin cells using ionic liquid. This was not possible to perform due to the chemical instability of the imidazolium-based ionic liquid (EMI TFSI) in contact with lithium metal. Alternatively, the use of graphite anode for running the rate tests in EMI TFSI in coin cells would be an important step to try.

Chapter 5 presented the use of ball milling to introduce carbon black between the NMC active particles in an attempt to reduce the electronic resistance between the active material and the working electrode during SMCM measurements. As an alternative approach, it is possible to ball mill NMC with graphene, which is known for its high electronic conductivity and large surface area. This has been previously tested with NMC,[4] and results have shown improved rate capability and cycling performance of the NMC–graphene composite, attributed to an increase in the grain connectivity and high electronic conductivity. Another approach that can be applied in that regard is the use of conductive polymers as a coating layer instead of carbon. For instance, PEDOT coating layer was found to facilitate the electron transport in NMC and restrain the electrode directly connected with the electrolyte during the charge/discharge processes resulting in enhanced the rate capabilities of NMC.[5] Moreover, the lower performance of the ball-milled NMC samples compared to the pristine material was attributed to higher interfacial and electronic resistances obtained after ball milling as reported previously in the literature. To confirm these assumptions, it will be important to run EIS and electronic conductivity experiments to measure the interfacial charge transfer resistance and detect the electrical conductivity of the formed NMC aggregates after ball milling respectively. On the other hand, previous studies have shown that reducing the electrode thickness reduces the Li-ion diffusion distance in the liquid phase within the electrode pores and results in improved cell performance. Therefore, it is worth to prepare thinner electrodes for coin cells measurements and check their effect on the capacity of ball-milled NMC cathodes. Future directions of the work presented in this chapter also include exploring other parameters and performing more control experiments to optimize the milling conditions and understand their effect on the electrochemical performance of NMC.

6.3 References

1.Moshurchak, L. M.; Buhrmester, C.; Wang, R. L.; Dahn, J. R. *Electrochimica Acta* **2007,** 52, (11), 3779-3784.

2.Jia, C.; Pan, F.; Zhu, Y. G.; Huang, Q.; Lu, L.; Wang, Q. *Science advances* **2015,** 1, (10), e1500886.

3.Pan, F.; Yang, J.; Huang, Q.; Wang, X.; Huang, H.; Wang, Q. *Advanced Energy Materials* **2014,** 4, (15), 1400567.

4.Venkateswara Rao, C.; Leela Mohana Reddy, A.; Ishikawa, Y.; Ajayan, P. M. *ACS Applied Materials & Interfaces* **2011,** 3, (8), 2966-2972.

5.Liu, X.; Li, H.; Li, D.; Ishida, M.; Zhou, H. *Journal of Power Sources* **2013,** 243, 374-380.

Appendix A

Supporting Information for Chapter 2

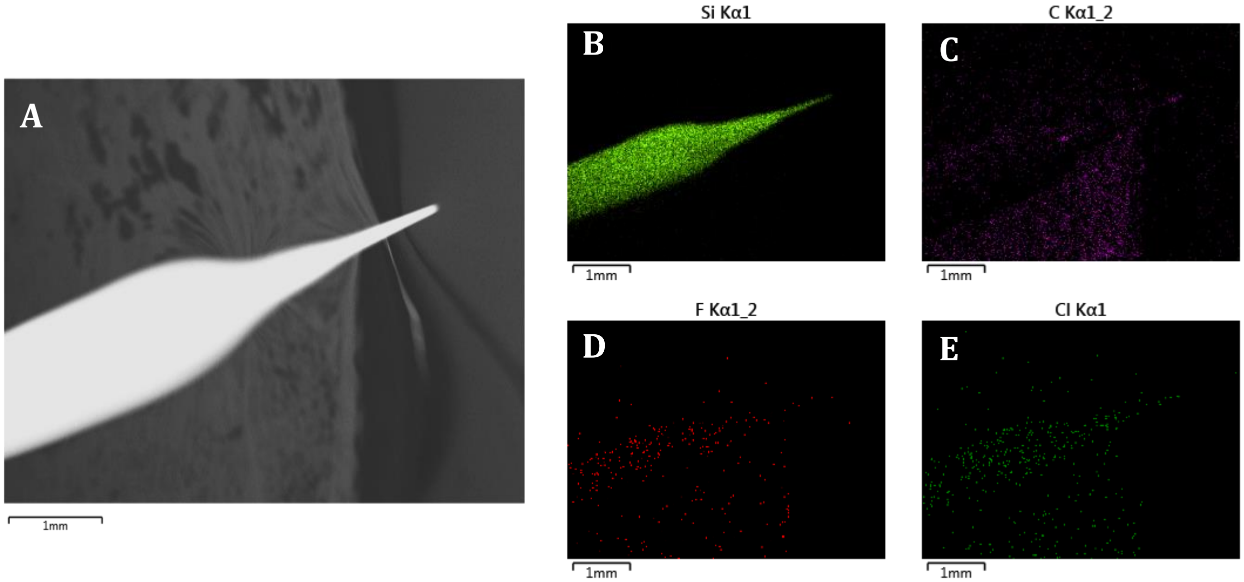

Figure A1: SEM side view image of 1 µm pipette (A) and the corresponding EDX map analysis (B-E) of the pipette before silanization.

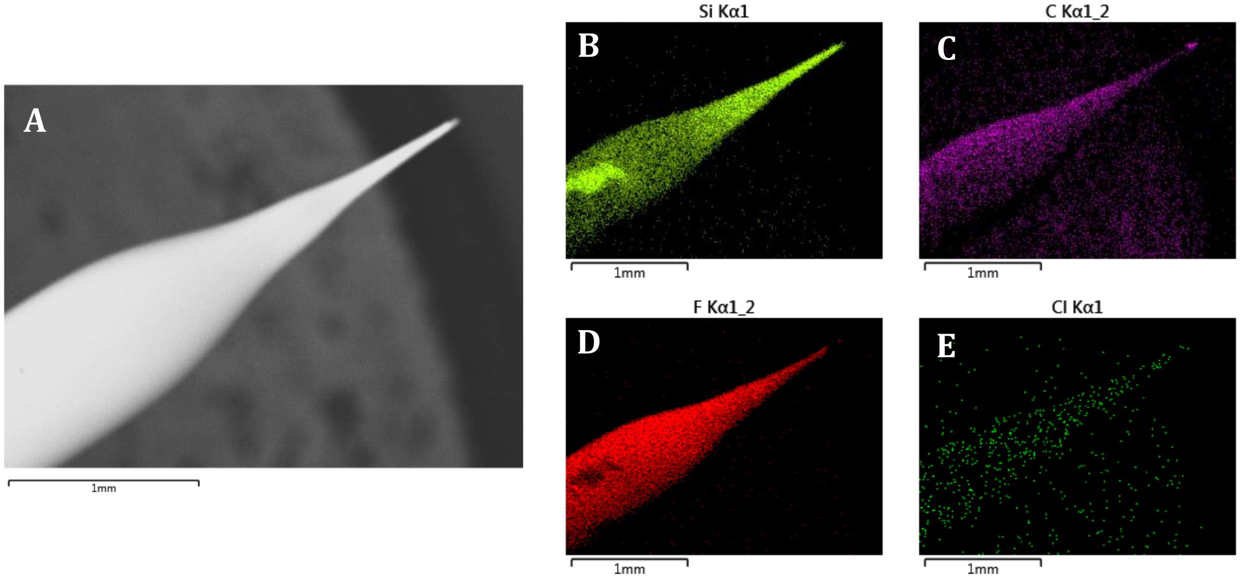

Figure A2: SEM side view image of silanized 1 µm pipette (A) and the corresponding EDX map analysis (B-E) of the pipette after using trichloro perfluoro-octyl silane ($CF_3(CF_2)_5CH_2CH_2SiCl_3$). Results reveal a significant increase in the F, C, and Cl signal.

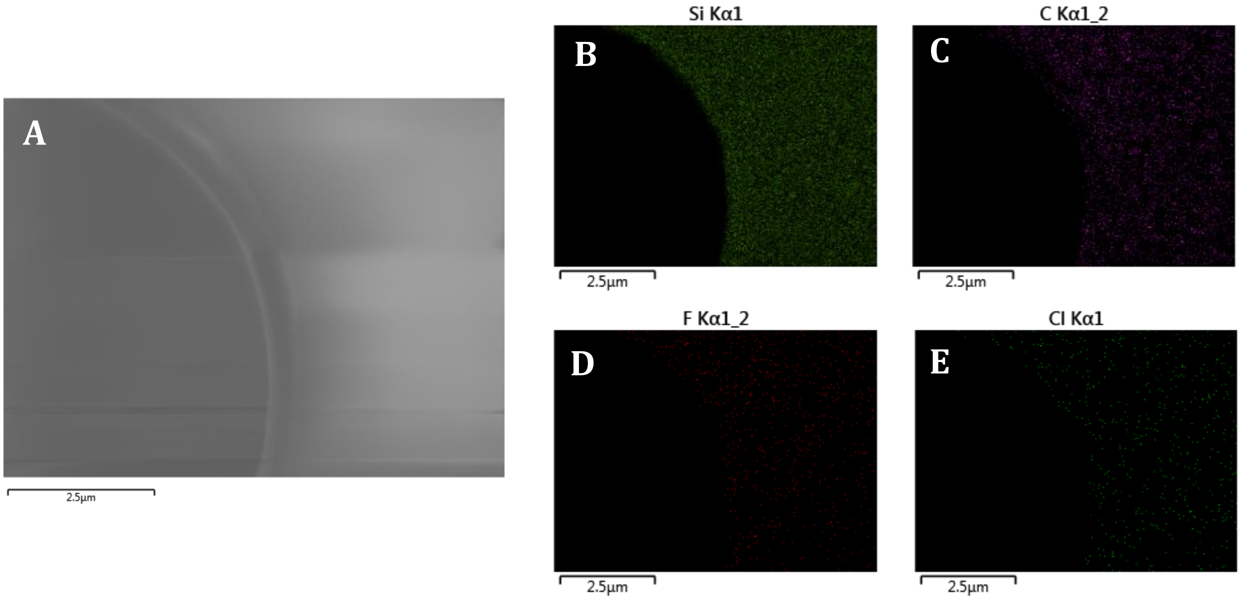

Figure A3: SEM botom view image of 1 µm pipette (A) and the corresponding EDX map analysis (B-E) of the pipette before silanization.

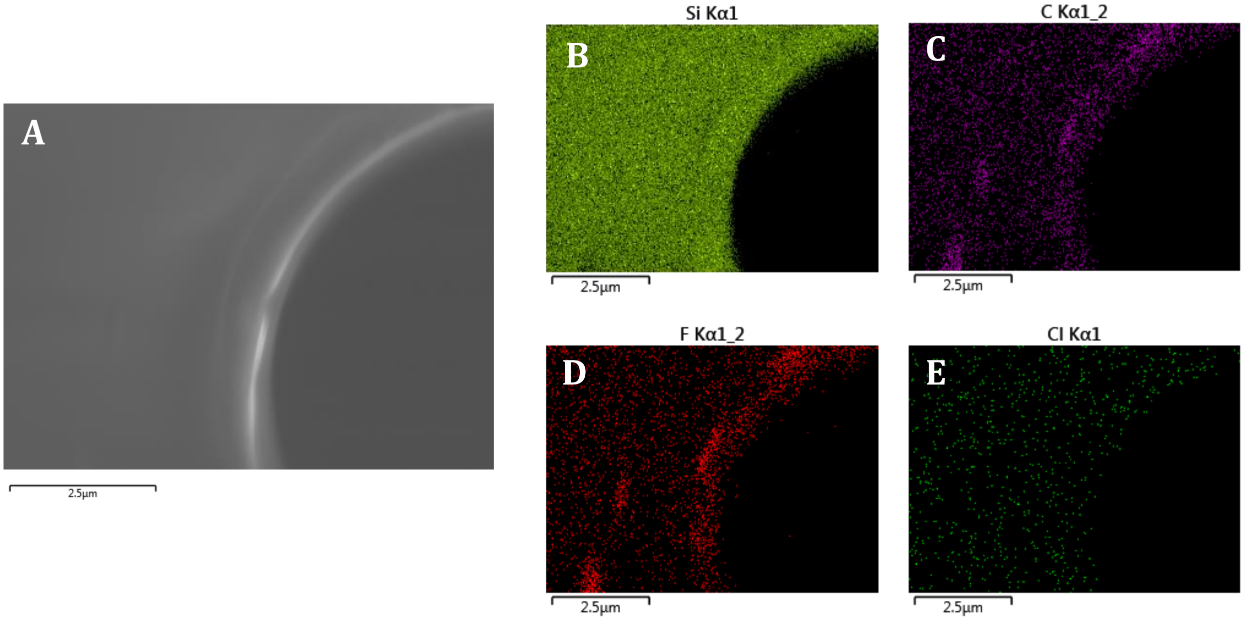

Figure A4: SEM botom view image of 1 µm pipette (A) and the corresponding EDX map analysis (B-E) of the pipette after using trichloro perfluoro-octyl silane ($CF_3(CF_2)_5CH_2CH_2SiCl_3$). Results reveal a significant increase in the F, C, and Cl signal.

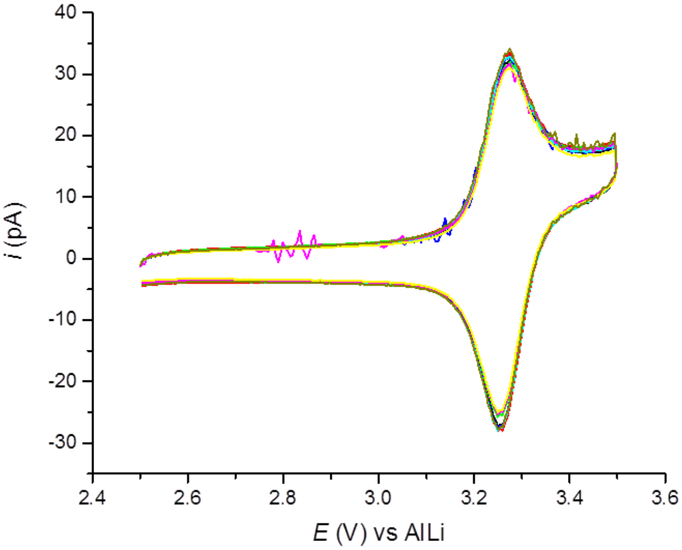

Figure A5: Cyclic voltammograms recorded at eight different measurement points on a gold substrate, using a 1 μm pipette containing MPT solution in PC. The superimposable cycles reflect the droplet stability.

Appendix B

Supporting Information for Chapter 3

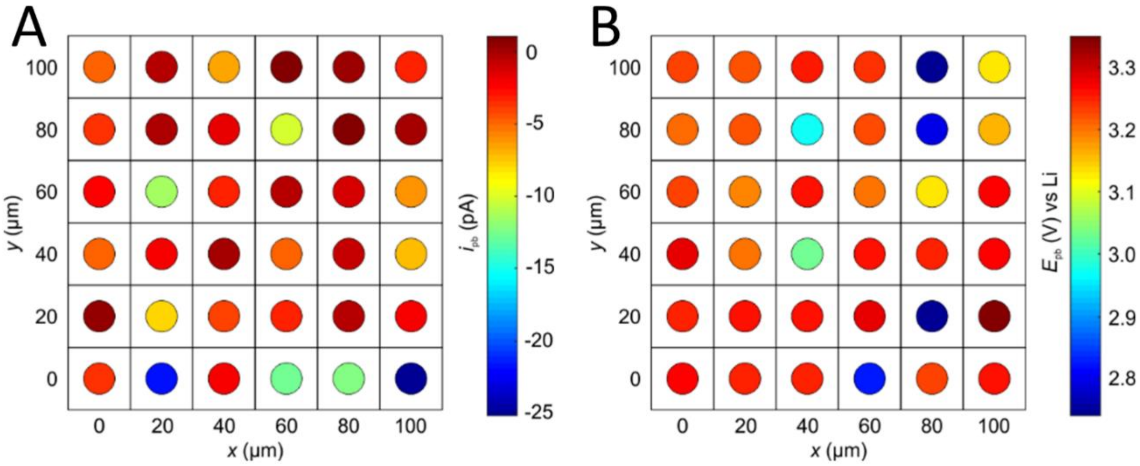

Figure B1: Electrochemical maps of the current (A) and the peak potential (B) for the reduction of LFP on gold substrate. These data were obtained at a scan rate of 5 mV s^{-1} from the same location on the substrate as reported in Figure 3.4 of Chapter 3.

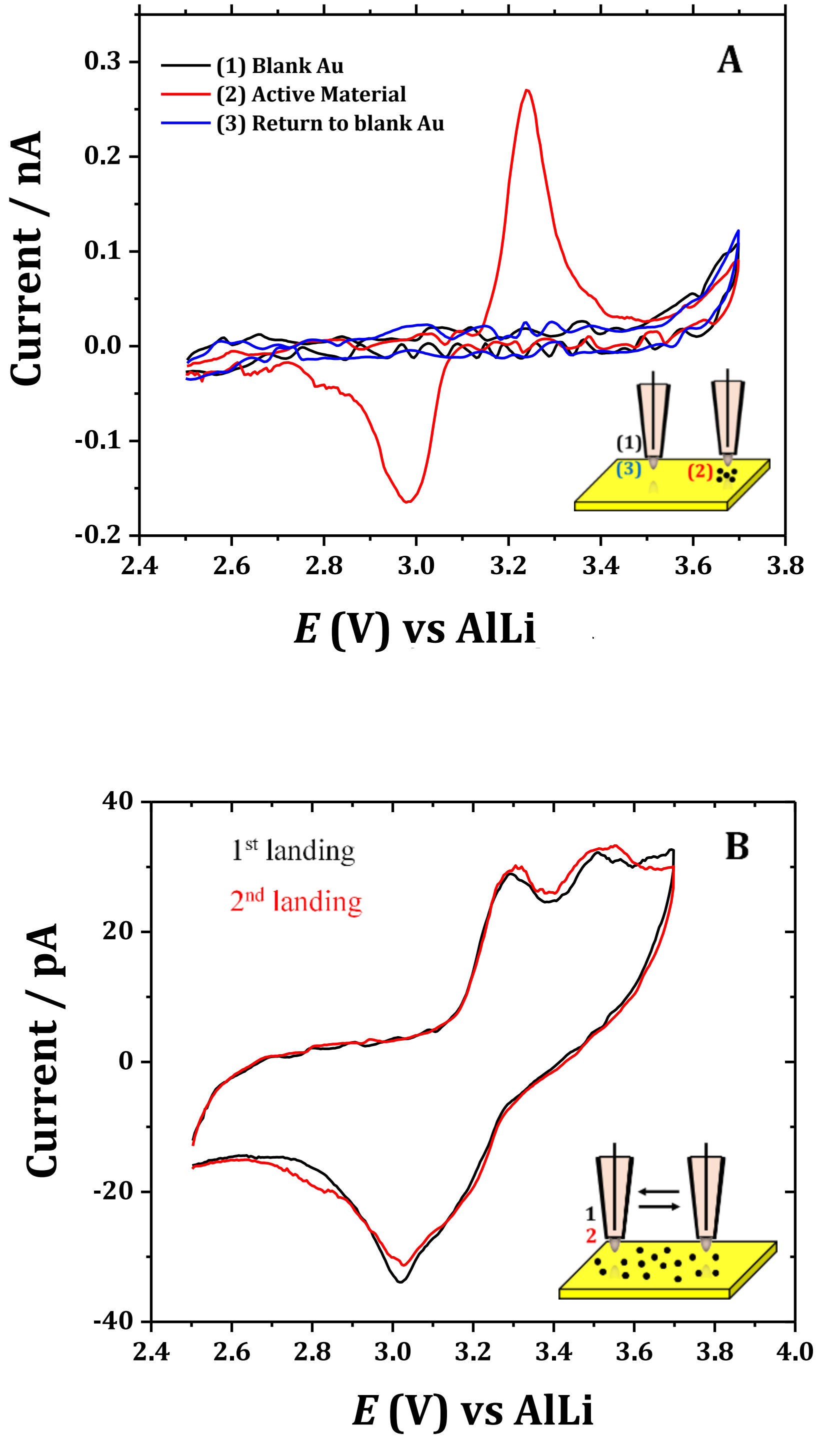

Figure B2: (A) Cyclic voltammetry waves performed at 5 mV s^{-1} by SMCM over a section of the gold substrate without LFP deposition (1–black line), the pipette was positioned over an area containing LFP (2–red line), and was returned back to the original area without LFP (3–blue line). (B) Repeated area measurements on a line scan.

In B2 (A), the cyclic voltammetry measurements collected before and after landing on LFP displayed a background signal of the gold substrate. This indicated that the LFP particles are stable on the gold substrate and are not repositioned between measurement sites.

In B2 (B), a cyclic voltammogram response was collected upon landing on LFP (1st landing). The pipette was retracted and relocated over a new area of LFP, then return to the original measurement point for the repeat cyclic voltammogram (2nd landing). The reproducible cyclic voltammograms confirm that particles are not being removed from the substrate surface, due to the interaction of the pipette.

Appendix C

Supporting Information for Chapter 4

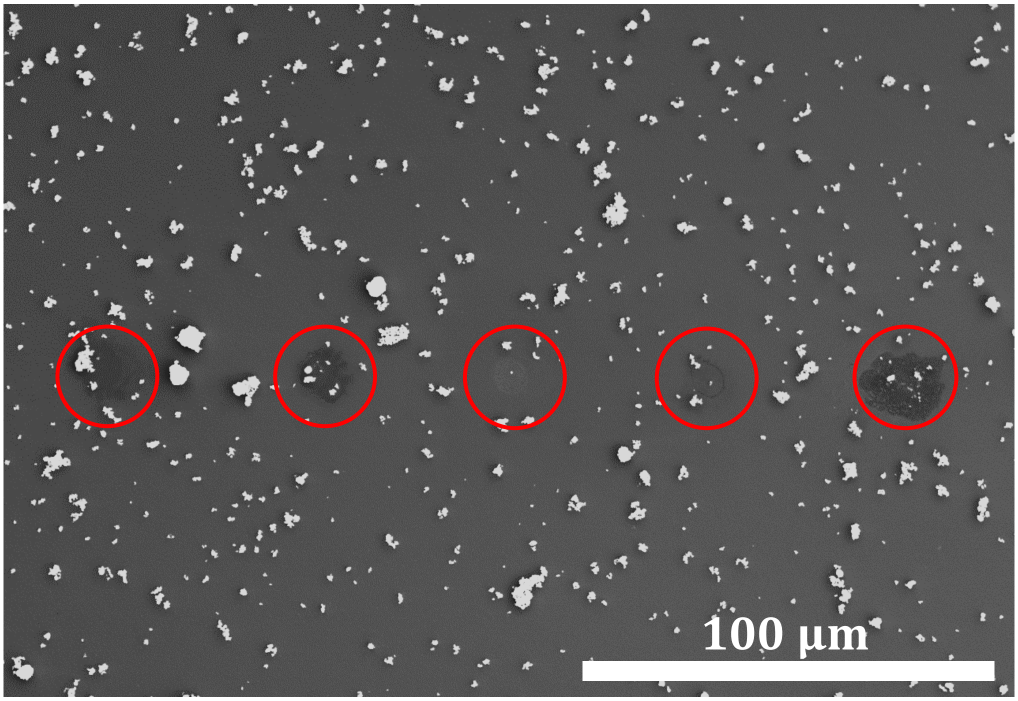

Figure C1: SEM image showing the dispersion of LFP active material on glassy carbon substrate. The red circle representing the different landing sites of the micropipette to collect the cyclic voltammograms responses.

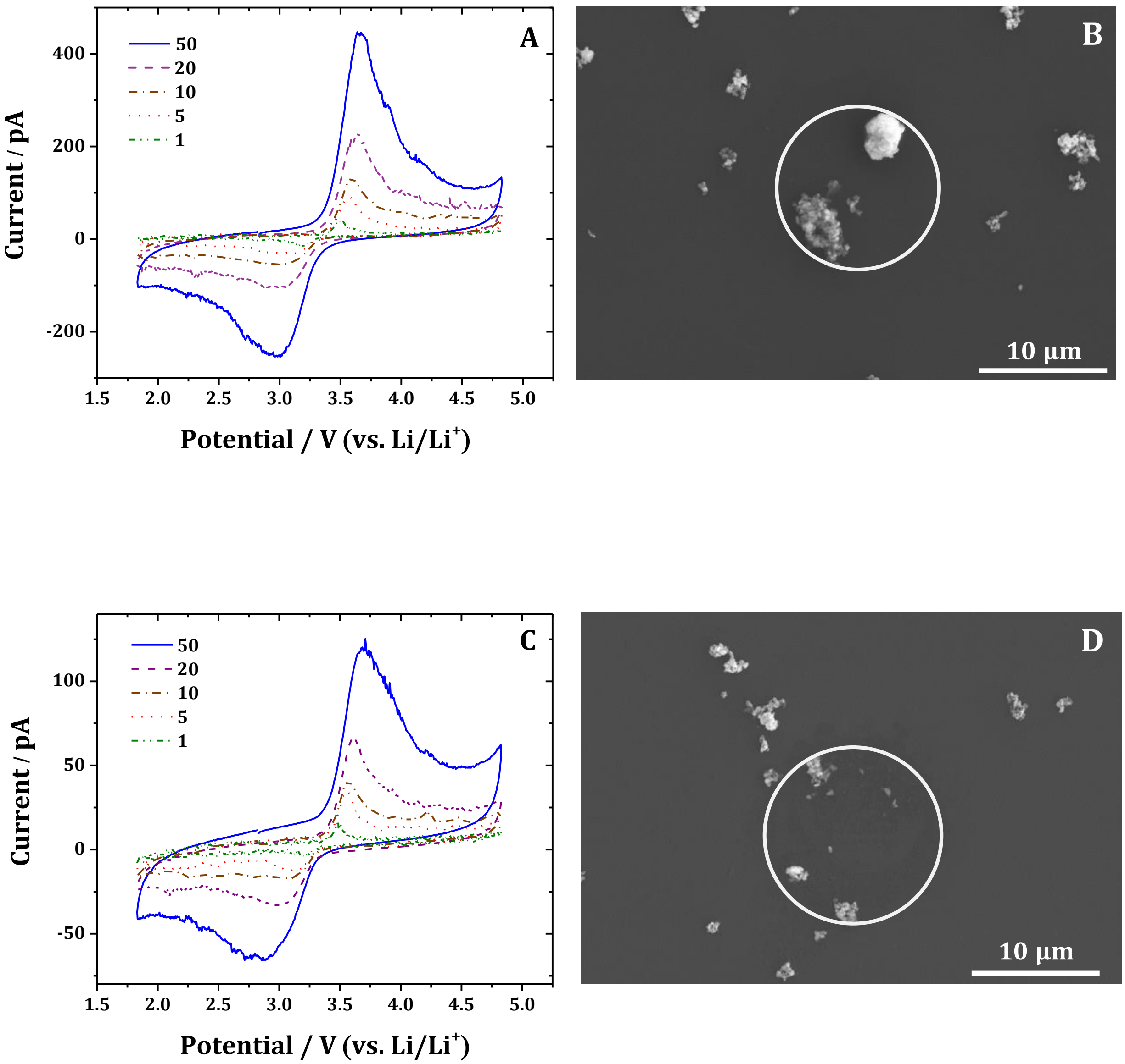

Figure C2: (A, C) The cyclic voltammetry obtained from SMCM and (B, D) the corresponding SEM image collected at different landing areas, respectively. Cyclic voltammetry was performed at different scan rates using SMCM with 0.1 M LiTFSI in EMI TFSI on LFP particles that were dispersed on a glassy carbon electrode. The legend corresponds to scan rate in mV s^{-1}. The 5th consecutive wave was reported for each scan rate, except for 1 mV s^{-1} where the 3rd wave was reported. (B, D) The SEM image shows the dispersed LFP active material within the actual landing area on a glassy carbon substrate.

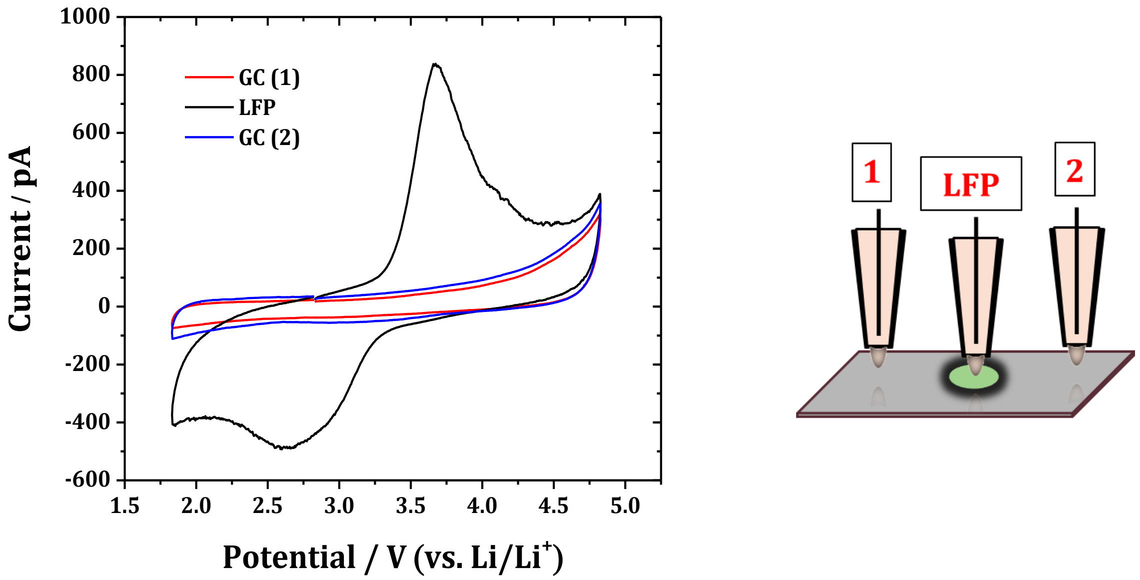

Figure C3: Cyclic voltammograms performed by SMCM on glassy carbon substrate over an area that has no active material (1–red line). The pipette was then positioned over an area decorated with LFP (black line), and then moved to a new clean area on the substrate (3–blue line). The electrochemical responses displayed in Figure C3 demonstrated that the particles are not lifted and redeposited by SMCM during the measurements.

Table C1: The coulombic efficiency for LFP oxidation/reduction calculated upon using ionic liquid (IL) (Figure C2A and C) compared to that calculated upon using PC the previous work (Chapter 3).

	Efficiency (%)		
Scan rate	**LFP in IL Point I**	**LFP in IL Point II**	**LFP in PC**
1 mV s^{-1}	97.6	95.2	68.5
5 mV s^{-1}	98.0	98.0	72.9
10 mV s^{-1}	90.1	98.4	79.3
20 mV s^{-1}	97.1	90.4	62.3
50 mV s^{-1}	91.3	98.5	67.5

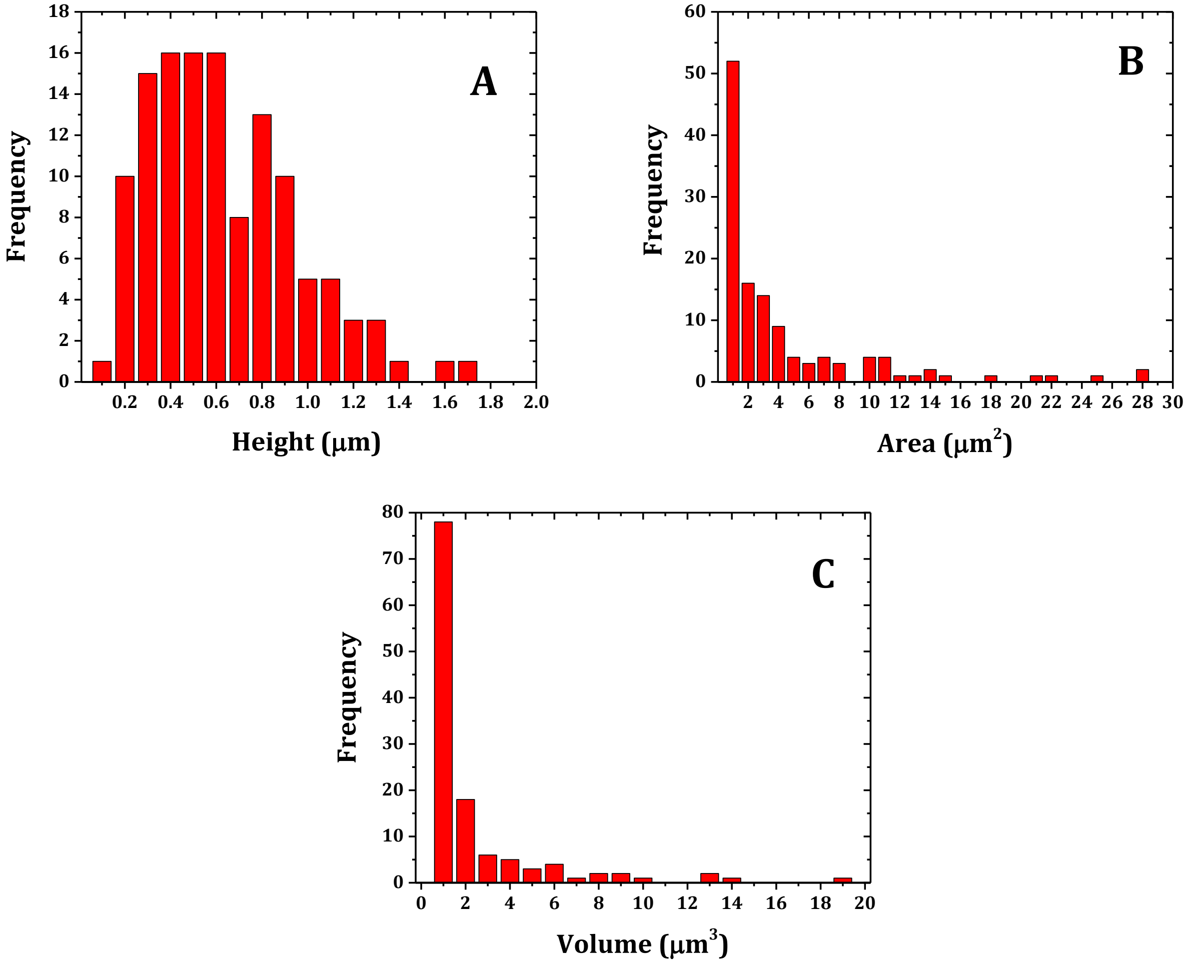

Figure C4: Histograms representing the distribution of the LFP particles' size in terms of (A) height (B) area and (C) volume.

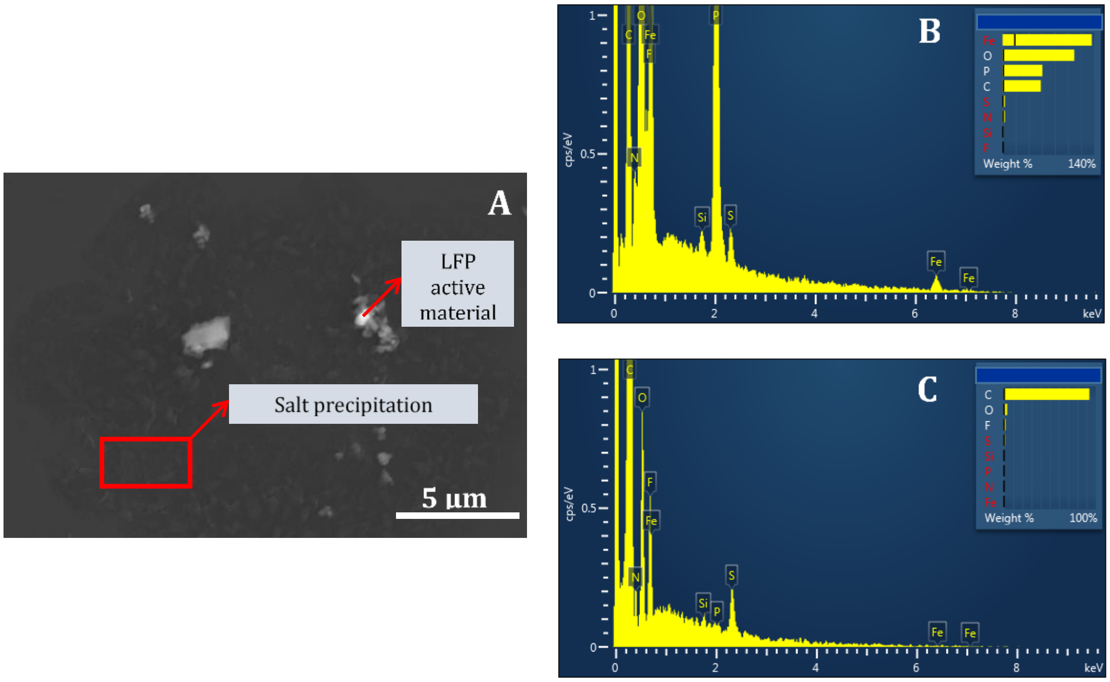

Figure C5: (A) SEM image for a landing area after long term cycling. EDX elemental analysis reveals (B) the LFP active material and (C) precipitation of LiTFSI salt.

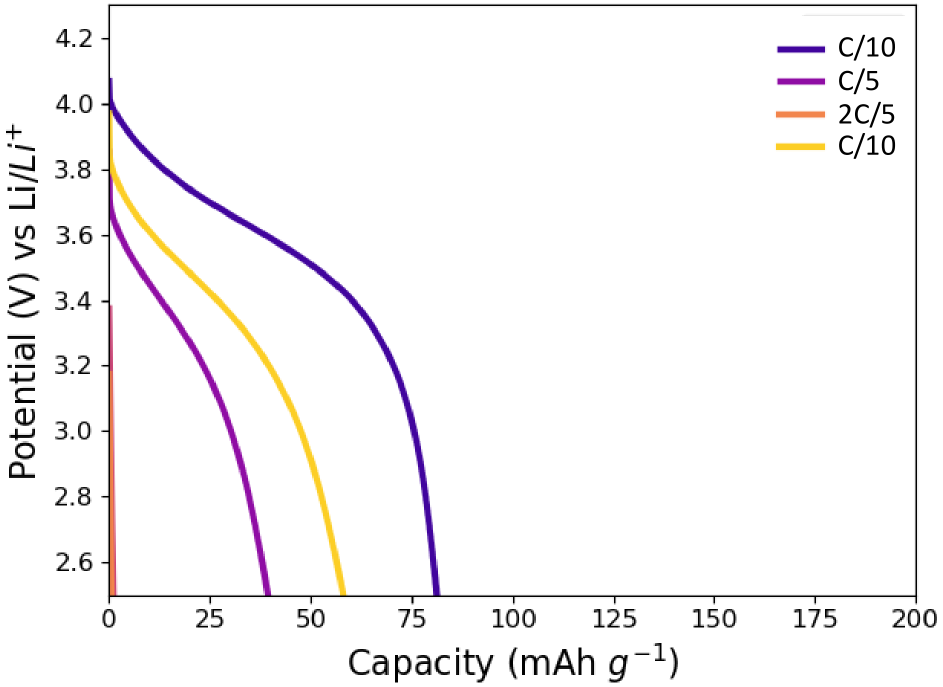

Figure C6: The discharge curves of LFP electrode in the ionic liquid EMI TFSI showing the poor electrochemical performance. The cells were cycled between 2.5-4.3 V at different C-rates. The electrode had a mass loading of ~5.7 mg/cm^2 in total (active material, binder and conductive additive).

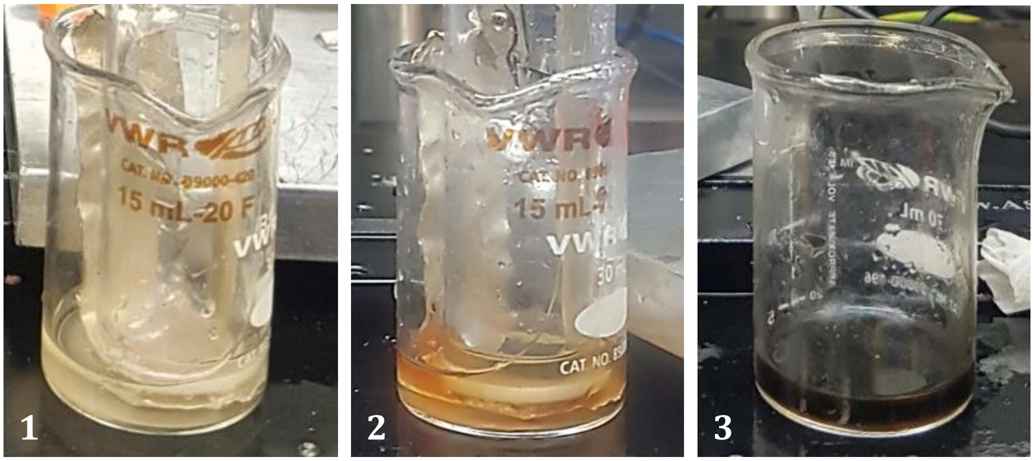

0 h **2 h** **4 h**

Figure C7: Ionic liquid samples after aging for a few hours: pure EMI TFSI (1) and lithium-metal-containing EMI TFSI (2 and 3).

Appendix D

Supporting Information for Chapter 5

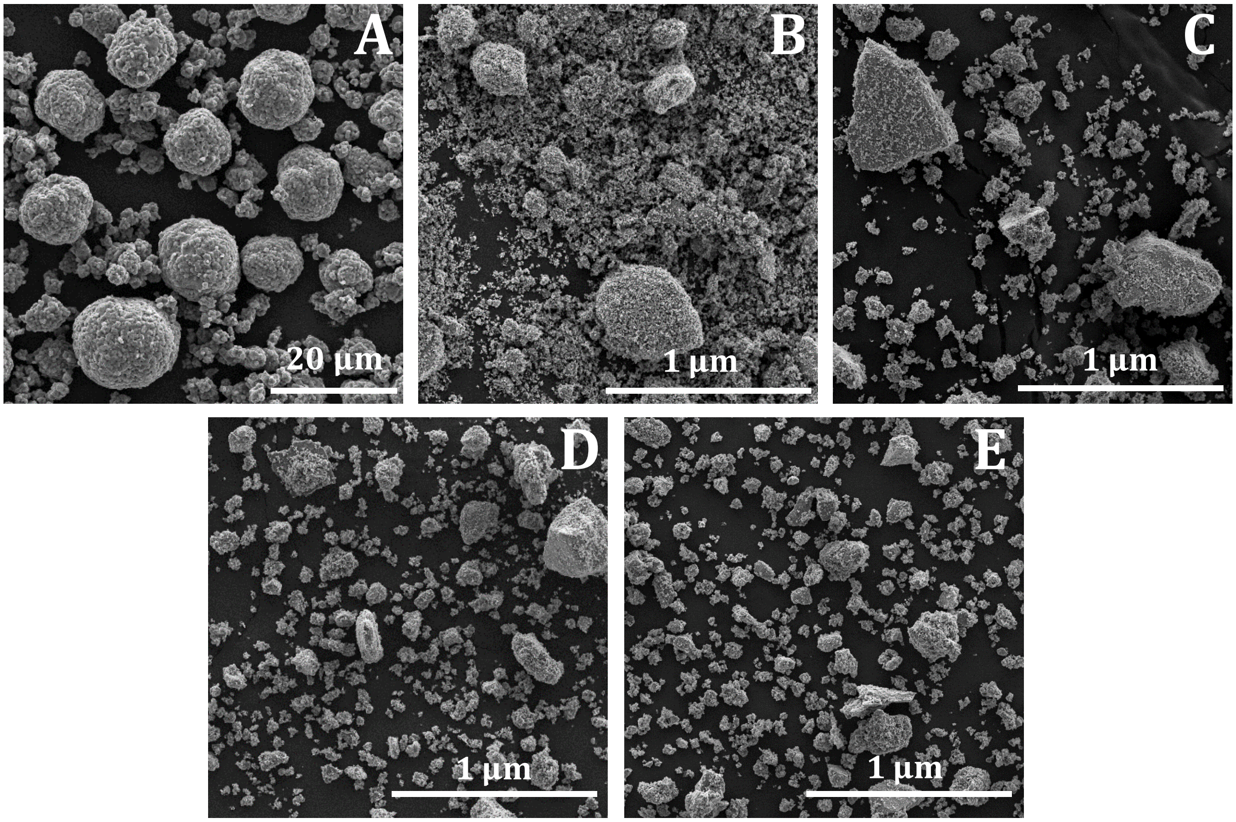

Figure D1: SEM images of the pristine NMC material (A), and ball-milled NMC samples at different conditions: NMC-20-1 (B), NMC-20-2 (C), NMC-45-1 (D), and NMC-45-2 (E). The images show the formation of aggregates after ball milling.

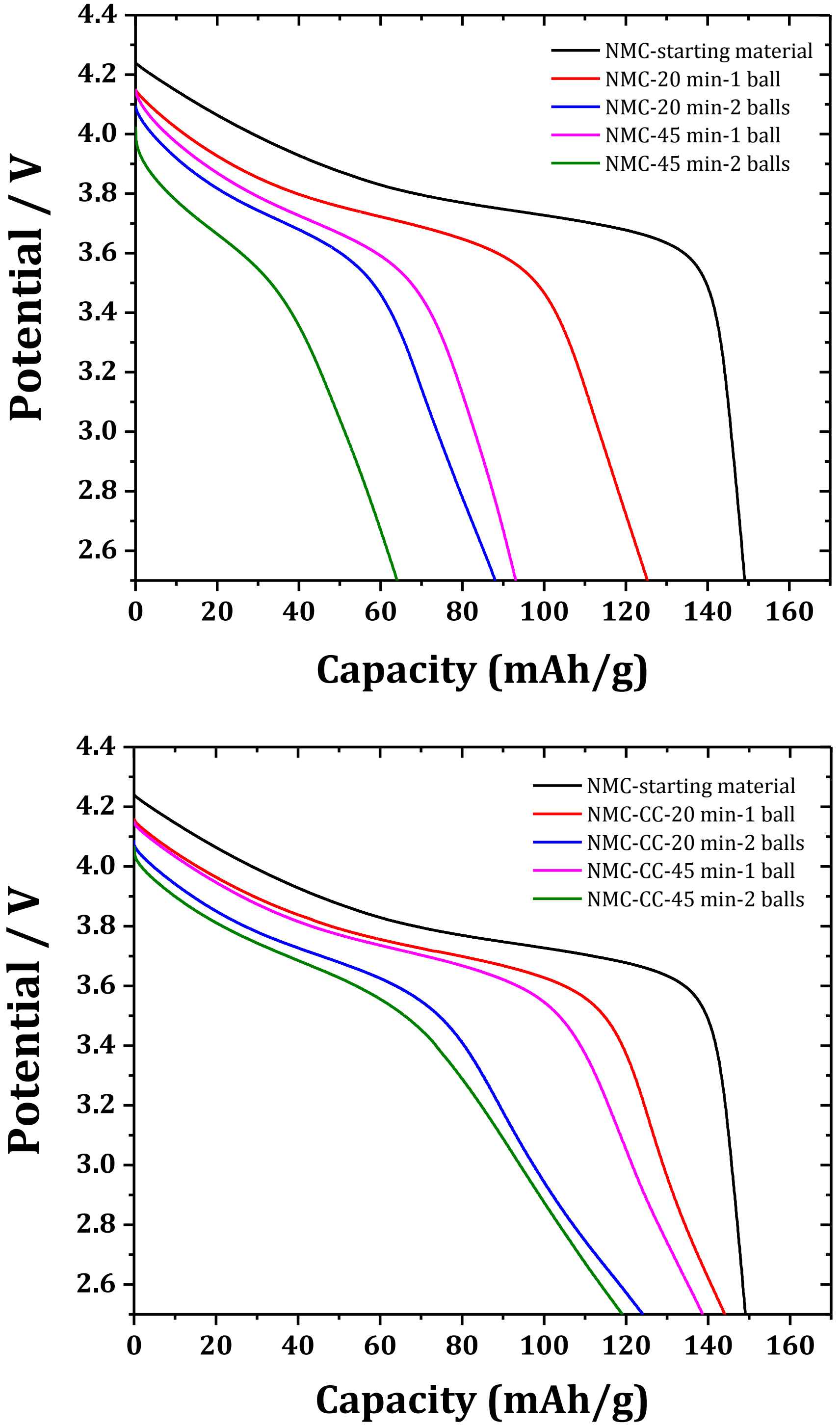

Figure D2: The discharge curves for the NMC electrodes comparing the effect of ball milling time and number of balls used before carbon addition (A) and after carbon addition (B). The cells were cycled between 2.5-4.3 V at C/10 rate.

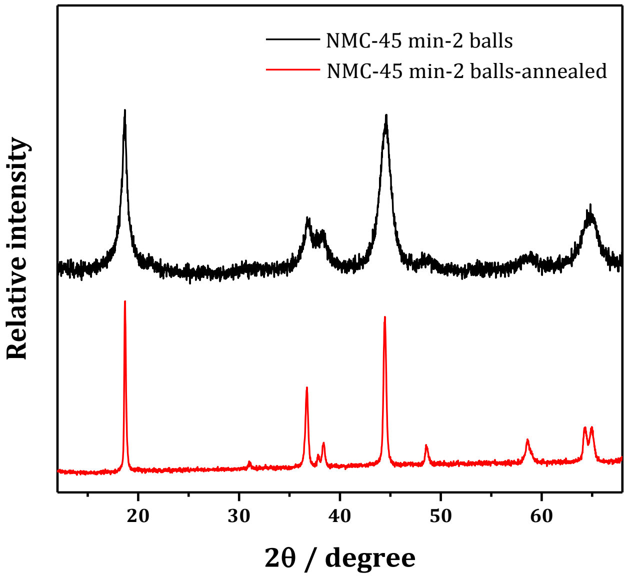

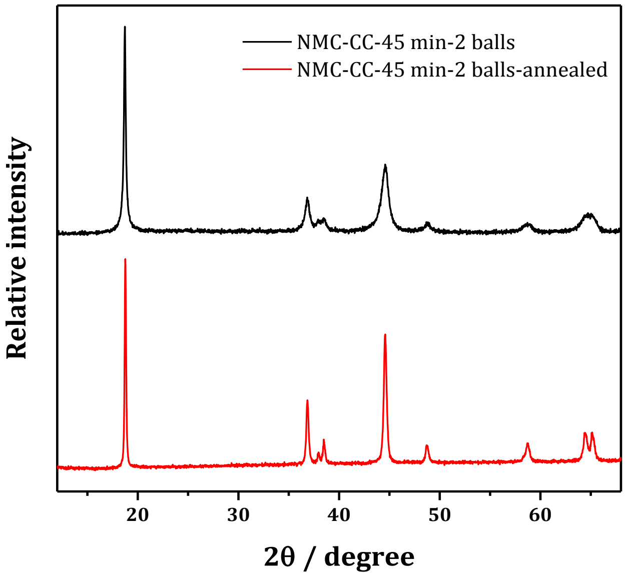

Figure D3: XRD patterns of ball-milled NMC samples before and after annealing in air at 800 °C for 6 hours.